THE UNIVERSITY OF OKLAHOMA

GRADUATE COLLEGE

DUAL-POROSITY AND DUAL-PERMEABILITY POROMECHANICS SOLUTIONS FOR PROBLEMS IN LABORATORY AND FIELD APPLICATIONS

A DISSERTATION

SUBMITTED TO THE GRADUATE FACULTY

in partial fulfillment of the requirements for the degree of

DOCTOR OF PHILOSOPHY

By

VINH XUAN NGUYEN
Norman, Oklahoma
2010

DUAL-POROSITY AND DUAL-PERMEABILITY POROMECHANICS SOLUTIONS FOR PROBLEMS IN LABORATORY AND FIELD APPLICATIONS

A DISSERTATION APPROVED FOR THE
MEWBOURNE SCHOOL OF PETROLEUM AND GEOLOGICAL ENGINEERING

BY

_____
Dr. Younane N. Abousleiman, Chair

_____
Dr. Dean S. Oliver

_____
Dr. Yucel I. Akkutlu

_____
Dr. Subhash N. Shah

_____
Dr. Roger M. Slatt

Dedicated to my family and those who love and support me!

Acknowledgements

I would like to express my wholehearted appreciation to Dr. Younane N. Abousleiman, my dissertation chair, who introduced me to the field of Poromechanics and spent a lot of times and energy teaching me the theory. I thank Dr. Abousleiman for giving me the fruitful opportunity to work at the PoroMechanics Institute and to learn from him. Without his patient guidance, technical advice and sincere encouragement, the completion of this dissertation would not be possible. Above all, I hope to maintain the scientific honesty and integrity I learnt from him and to exceed his standards of excellence in my future career.

I also would like to thank Dr. Dean Oliver, Dr. Yucel Akkutlu, Dr. Subhash Shah, and Dr. Roger Slatt for serving as my committee members.

My special thanks go to my colleagues, Mr. Son Hoang and Minh Tran for their intellectual companionship. My appreciation also goes to Ms. Carla Cates, PMI Administration and Operations Manager, for making every administrative matter go smoothly and for making my times at PMI a pleasant experience.

I am thankful to Mr. and Ms. Flanagan whom I lovingly call “Uncle Larry” and “Má Hà” for caring and loving me since the first day I arrived at OU. I also thank all of my Vietnamese friends, the “SVS community”, especially my roommate and fellow Ph.D. student Mr. Ha Mai, for spending the last nine years, sharing all the joys and tears with me.

Finally, I am deeply indebted to my parents, Mr. Nguyễn Xuân Vũ and Ms. Đặng Thị Kim Nguyên, and my sister Ms. Nguyễn Thị Kim Yến for their support and loving.

Table of Contents

List of Tables

List of Figures

Abstract

In this work, a study of anisotropic dual-porosity and dual-permeability poromechanics is presented through generalized analytical solutions for selected problems in laboratory and field applications. For example, the solution to the inclined wellbore geometry with standard applications in the oil and gas industry for drilling stability or consolidation in naturally fractured rock formations are derived and illustrated. In addition, the dual-porosity and dual-permeability poromechanics solutions to common laboratory testing setups in geomechanics and biomechanics for purposes of rock and bio-tissue characterization are developed for rectangular strip, solid and hollow cylinder geometries.

The behaviors of naturally fractured rock formations or the responses of the well known dual-porosity bone structure are modeled as dual-porosity and dual-permeability poroelastic media that fully couples the secondary porosity medium's deformation, fluid flow and interporosity exchange processes. For chemically active fractured media, e.g., clay, shale, or biomaterial, chemical interaction effects including osmotic and solute transport in both the primary porosity (matrix) and secondary porosity (fracture) are addressed based on non-equilibrium thermodynamics. Thermohydromechanical coupling under non-isothermal condition is incorporated by adopting a "single-temperature" approach in which a single representative thermodynamic continuum is argued to be sufficient to describe the thermally induced responses of a naturally fractured rock formation.

The physical and mathematical models are used to find poromechanics analytical solutions for pore pressure, fluid flux, stress, and displacement, in addition to solute flux for chemically active material or temperature for non-isothermal condition to the above problem geometries. These solutions are general and can be tailored to simulate specific field problems or experimental testing. For instance, the inclined wellbore solutions include boundary conditions for simulating openhole drilling and fluid injection or withdrawal. On the other hand, the solutions for laboratory testing of rectangular and cylinder geometries account for two primary axial loading modes, namely, stroke control or stress relaxation and load control or creep test. The rectangular strip solution is also shown to simplify to the classical one-dimensional consolidation in soil mechanics.

For non-reactive dual-porous material under isothermal condition, generic dual-poromechanics results are plotted and compared with single-poromechanics counterpart representing a homogenous isotropic medium when applicable. Parametric analyses are also carried out through the responses of a solid cylinder under unconfined compression to evaluate the effects of material anisotropy and dimensionless dual-poroelastic parameters such as permeability ratio, storage ratio, and interporosity coefficient. For chemically active fractured formation, the analyses is focused on the impacts of chemical salinity gradients via osmotic and solute transport on pore pressure and effective stress distributions near the wellbore or fluid/solute flux and displacement of solid cylinder under axial-flow-only oedometer testing setup. Finally, the effects of temperature gradients manifested through thermal expansion/contraction and conductive heat transport are assessed using the

analytical solutions for inclined wellbore and rectangular strip geometries. Furthermore, the significance of heat convection is evaluated numerically and displayed.

Application-wise, the inclined wellbore solution is used to perform time-dependent wellbore stability analysis for drilling through chemically active fractured rock formations under non-isothermal conditions. The hollow cylinder is applied to study elastic consolidation of a producing naturally fractured reservoir and associated implications on porosity and permeability reduction in the near-wellbore region. Finally, some realistic quasi-static loading conditions commonly encountered in experimental testing and field applications such as cyclic, linear ramping, and exponentially decayed are demonstrated via the solutions of unconfined solid cylinder.

Chapter 1

Introduction

1.1 Overview

Naturally fractured rocks can be found in many subsurface formations through out the world (Aguilera 1995) and are problematic when it comes to field operations in the oil and gas industry. Such formations involve various types of highly coupled hydraulic, mechanical, thermal, and chemical processes taking place simultaneously at different rate. Adding to this complexity, fractured formations usually possess a high degree of local heterogeneity that makes the task of modeling even more challenging. Understanding the coupled and transient behaviors of these fluid saturated fractured formations are critical in many petroleum engineering field applications ranging from drilling stability, hydraulic fracturing, production induced compaction to the design and analysis of laboratory rock testing procedures.

Over the years, research efforts have matured from the original dual-porosity concept of Barenblatt et al. (1960) and Warren and Root (1963) for treating fluid flow in naturally fractured reservoirs to the dual-porosity and dual-permeability isotropic poroelastic approach which can handle the fully coupled fluid flow and deformations processes

(Bowen 1976; Aifantis 1977; Berryman and Wang 1995). Although the literature is prolific, analytical solutions have been limited to the one-dimensional consolidation problem in geomechanics (Lewallen and Wang 1998) or the uncoupled fluid-flow problem in well testing and production management (Chen 1989). Furthermore, all of the previous solutions and analyses are restricted to the isotropic case in which both the rock matrix and fracture system are considered to possess the same material properties such as permeability and compressibility in all directions. In reality, geo-activities are carried out in formations that can be broadly classified transversely isotropic due to the natural deposition and compaction processes of sedimentary rocks over a geological time scale. The depositional processes lead to development of formations with similar material properties across a cross section but having different characteristics in the perpendicular direction.

On the other hand, biomaterials such as bone tissues are well known for their multi-porosity makeup and anisotropic characteristics. For example, it was suggested that a two-porosity poroelastic model is appropriate for the study of bone fluid movement and bone fluid pressures (e.g., Cowin 1999). It was also shown that the greatest degree of elastic symmetry appears to be orthotropy for bone (e.g., Dempster and Liddicoat 1952; Bird et al. 1968); however, bones are mostly modeled as transversely isotropic material (Cohen et al. 1998). Furthermore, biological tissues display osmotic swelling behavior when the surrounding fluid salinity is in the excess due to ionized charged structure, e.g., the negatively charged proteoglycans in intervertebral discs and articular cartilage (Urban et al. 1979). Similar to the modeling of naturally fractured rock in geomechanics, existing models and solutions describe biomaterials as single-porosity and single-permeability

homogeneous medium (e.g., Norwinski and Davis 1970; Armstrong et al. 1984; Cowin and Mehrabadi 2007) and thus fall short at simulating the proper responses of dual-porosity bone structure.

In this dissertation, the behaviors of these dual-porous materials are modeled as dual-porosity and dual-permeability poroelastic media that fully couples the secondary porosity medium's deformation, fluid flow and inter-porosity exchange processes, i.e., **Fig. 1.1**. In addition, chemical interaction effects including osmotic and solute transport in clay, shale or bio-tissue, and the impact of thermal loading due to temperature gradient are also incorporated.

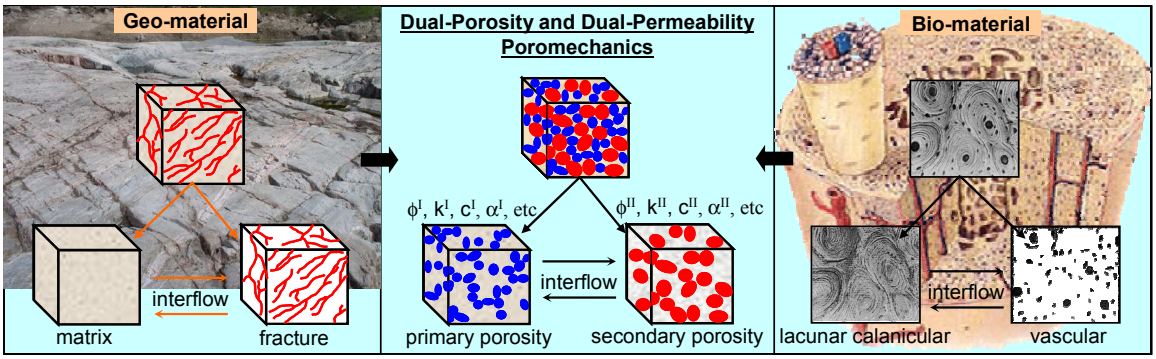

Fig. 1.1—Modeling geo-material (naturally fractured rock) or bio-material (bone tissues) as dual-porosity and dual-permeability poroelastic media (the multi-porous bone structure illustration is adapted from Cowin et al. 2009).

1.2 Literature Review

A brief review of the development of theoretical formulation and analytical solution is presented in this section. More detailed review of the literature is discussed in relevant chapters.

Biot (1941) is the first to present a consistent theory of isotropic poroelasticity to

account for the coupled diffusion-deformation processes in fully saturated porous media. Later work of Geertsma (1957, 1985), Verrujt (1969), Chen and Teufel (1997) reinterpreted Biot's theory along the line of conventional fluid flow modeling in the petroleum industry. Rice and Cleary (1976) recast Biot's theory in terms of new and straight forward physical constants and developed some general solution methods. Biot's (1941) theory was first developed for isotropic porous medium saturated with an incompressible fluid. Subsequently, this theory was generalized to account for anisotropy and compressible fluid by Biot (1955) and Biot and Willis (1957). Biot's isotropic and anisotropic poroelastic theory has been the basis for diverse application in many areas such as geo- and bio-material characterization (Armstrong et al. 1984; Hart and Wang 1995; Zhang et al. 1998; Scott and Abousleiman 2002; Al-Tahini et al. 2005), wellbore stability (Cui et al. 1998; Abousleiman et al. 2001), subsidence above compacting oil and gas reserve (Geertsma 1973), ocean wave-induced seabed's response (Rahman et al. 1994), groundwater level fluctuations (Verruijt 1969; Kim and Pariek 1997; Wang 2000), sedimentation on an impermeable basement (Gibson 1958), induced seismicity (Roeloffs 1988), and bone poroelasticity (Cowin 1999) to name a few. Two such applications are illustrated in **Fig. 1.2**. Analytical solutions of fundamental problems such as the one-dimensional consolidation problem (Biot 1941), consolidation of a rectangular strip or the Mandel's problem (Mandel 1953; Abousleiman et al. 1996), consolidation of semi-infinite stratum (Gibson and McNamee 1963), sphere (Cryer 1963), solid cylinder (Abousleiman and Cui 1998), hollow cylinder and borehole (Rice and Clearly 1976; Abousleiman and Cui 1998).

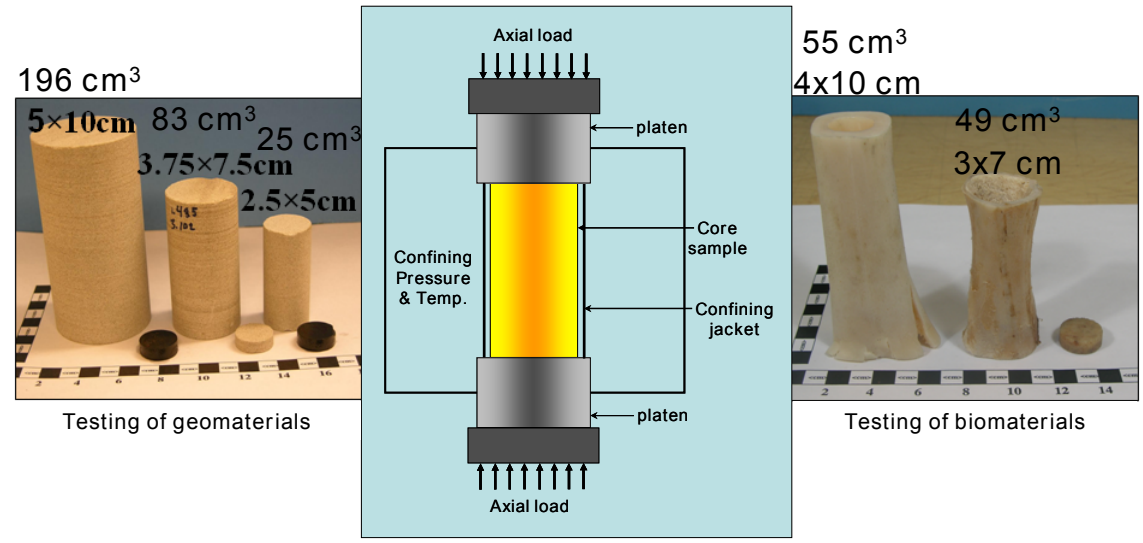

(a)

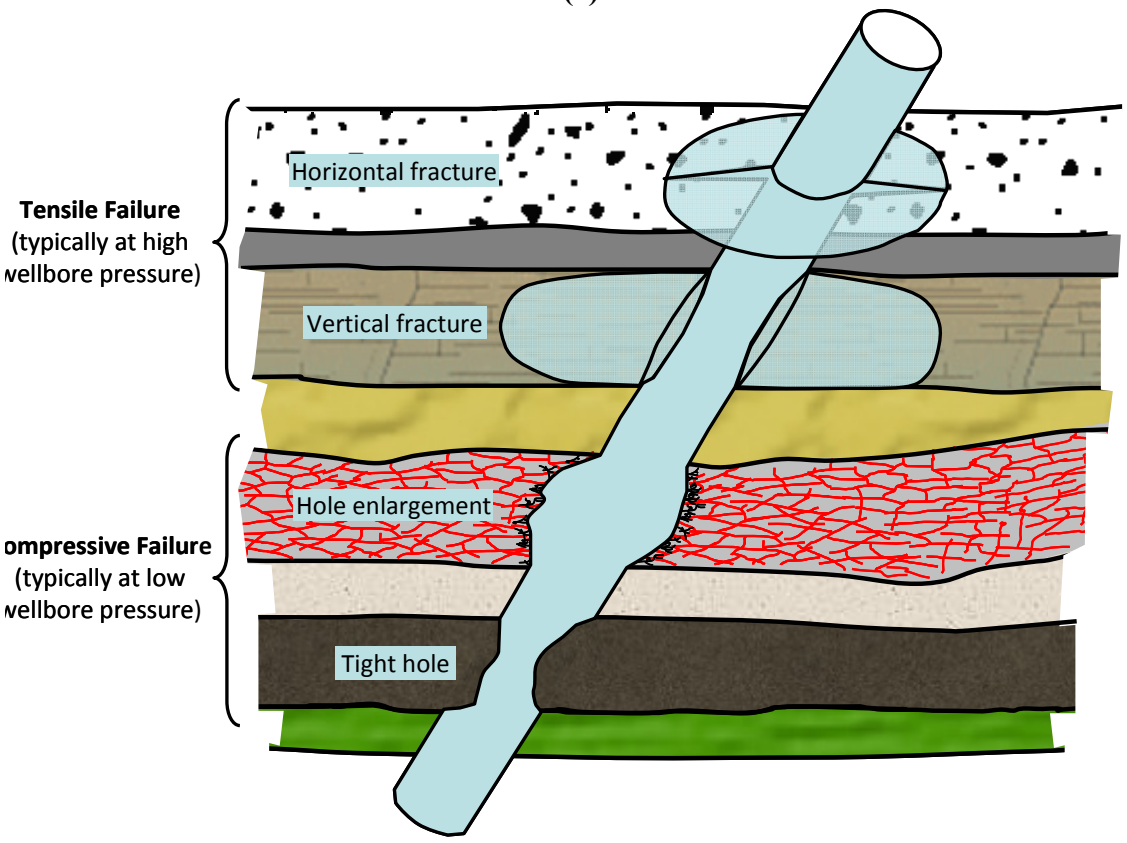

(b)

Fig. 1.2—Two applications of poroelastic theory and solutions: (a) geo- and bio-material characterization and (b) wellbore drilling stability (modified after Bradley 1979).

A unified poroelastic solution for cylindrical geometries, called the "generalized

Lamé's problem", was also reported (Kanj and Abousleiman 2004a). These analytical solutions served as basis for understanding the physical phenomena as well as benchmark for validating the integrity of numerical codes (Finol and Ali 1975; Chin et al. 2000; Jourine et al. 2004; Alassi et al. 2006; Phillips and Wheeler 2007). The characteristic behavior of the poroelastic response that is lacking in the uncoupled diffusion theory is illustrated through the pressure history at the center of a solid cylinder under sudden axial-load application in **Fig. 1.3**. The phenomenon is known as the Mandel-Cryer effect in which the pore-pressure continues to rise after its initial value instead of monotonically declines as in regular diffusion process.

In chemically active porous media such as clays, shales, and biological tissues, additional osmotic effect is generated due to physico-chemical interactions among pore-fluid's components with the invading fluid and the solid matrix that result in membrane behavior, i.e., only transport of certain pore fluid species is allowed. A chemical potential gradient will induce simultaneous flows of fluid and solute into or out of the medium. The coupled osmotic and solute transport processes can lead to material's strength weakening in addition to pore-pressure elevation or reduction. Early analyses addressing chemical osmotic effect in active shale were presented by lumping the activity-generated osmotic pressure and hydraulic pressure into a chemical potential term, ignoring the solute movement into or out of the shale (Yew et al. 1990; Hale et al. 1992; Van Oort 1994). This chemical potential is treated as an effective pressure which is used in subsequent evaluation of effective stresses. Later, the concept of a chemical potential and membrane efficiency are further woven into the poromechanics formulation (Sherwood 1993; Abousleiman et al.

2001) and have been applied in estimating the swelling effects on stress and pore pressure distributions in the vicinity of deep wellbores (Sherwood and Bailey 1994; Abousleiman et al. 2001; Chen et al. 2003).

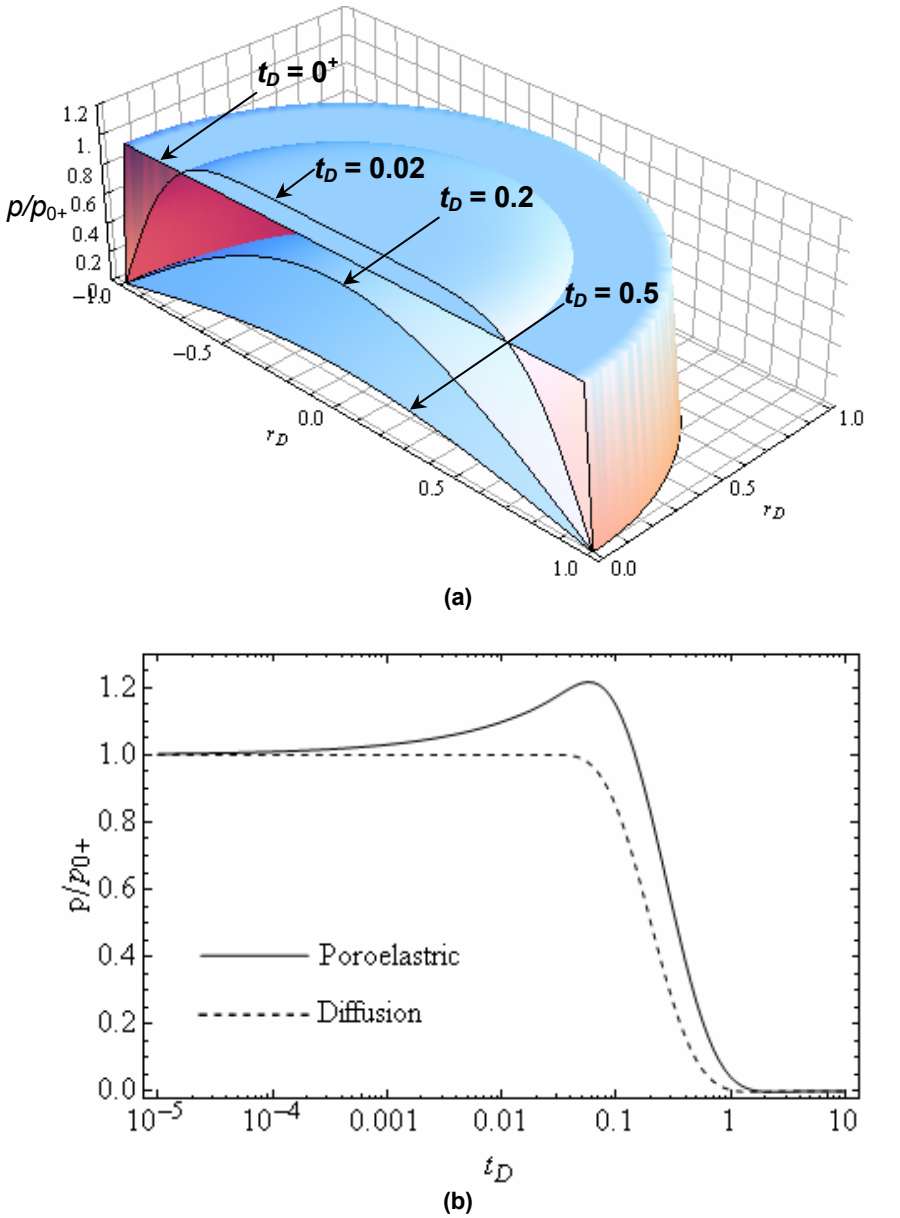

Fig. 1.3—The Mandel-Cryer's poroelastic effect: (a) evolution of pore-pressure distribution in a solid cylinder and (b) history of pore-pressure fluctuation at the center, the dashed line is the uncoupled diffusion behavior.

In more rigorous approaches, the complete chemical interaction effects including osmotic and solute transport in stressed shale or bio tissues have been formulated and addressed extensively based on mixture theory and/or non-equilibrium thermodynamics (Sachs and Grodzinsky 1987; Sherwood 1993; Heidug and Wong 1996; Huyghe and Janssen 1999). In term of field applications, Ekbote and Abousleiman (2003, 2005, and 2006) presented a linearized anisotropic porochemoelastic model and provided the general analytical solution to inclined wellbore drilling problem through shale formations.

The development of field projects that are often subjected to non-isothermal conditions such as drilling in deep and high temperature subsurface, oil recovery by steam injection, geothermal wells, and nuclear waste depository necessitates an understanding of the coupled thermo-hydro-mechanical processes. Extension of Biot's theory, incorporating both thermal expansion/contraction and heat diffusion, has been successfully studied under the isotropic porothermoelastic model (Bear and Corapcioglu 1981; McTigue 1986; Coussy 1989). Extensive analytical solutions have been developed for many problems including consolidation around spherical heat source (Booker and Savidou 1984, 1985), heating of a porothermoelastic half-space (Mc-Tigue 1986), axisymmetric borehole solutions (Mc-Tigue 1990), vertical wellbore in non-hydrostatic in-situ stress (Wang and Papamichos 1994), and inclined wellbore subjected to three-dimensional state of stress (Ekbote 2002; Chen et al. 2003; Abousleiman and Ekbote 2004; Chen and Ewy 2005). A complication in the analytical approach is due to the presence of the convective heat flow – heat transported by the pore fluid carrier – which renders the heat diffusion equation non-linear. As such, numerical solutions were also presented, e.g., thermally induced stresses in poroelastic

cylinder and hollow sphere (Kurashige 1992; Kodashima and Kurashige 1996), one-dimensional consolidation accounting for thermo-osmosis and thermal filtration (Zhou et al. 1998).

The original Biot's theory treated the saturated porous medium as a homogenous material, i.e., single-porosity and single-permeability model. However, in naturally fractured rock formations containing distributions of various distinct types of pores, from fractures or fissures to porous rock matrix, the use of an approximate average porosity over both domains, in many field cases, is inappropriate. A dual-porosity continuum approach, utilizing two distinct forms of intrinsic porosity, one corresponding to the porous matrix (primary porosity) and the other corresponding to the fracture framework pore distribution (secondary porosity), is more appropriate. To this end, Barenblatt et al. (1960), and subsequently Warren and Root (1963) presented the original ideas of representing the fluid domain in a naturally fractured reservoir by two overlapping continua. Each continuum possesses its own fluid pressure fields. A summary of the extensive literature on treating the fluid flow problems in naturally fractured reservoirs incorporating the dual-porosity and dual-permeability concept was presented by Chen (1989). All of these models have been developed for the study of fluid flow (single-phase and/or multiphase) in hydrocarbon reservoirs or ground water aquifers (Cheng et al. 1992), but the rock formation is treated as a rigid body, thus ignoring the coupling effect between fluid flow and deformation.

The extension of Biot's theory of poromechanics to fractured rock formations within the framework of the dual-porosity and dual-permeability approach was presented by

Aifantis (1977 and 1980) based on the theory of mixtures (Bowen 1976 and 1982). The quasi-static linear constitutive relation relates linearly the overall macroscopic stress to the strain and pore pressures in both the primary porosity as well as in the secondary porosity media. Berryman and Wang (1995) reformulated Aifantis's dual-porosity governing equations by exchanging the roles of the dependent and independent variables. The coefficients of the governing equations could mostly be interpreted as different storage coefficients. Using a rigorous mathematical approach, Valliappan and Khalili-Naghadeh (1990) presented a coupled dual-porosity flow-deformation formulation. One deviation from the Aifantis and Berryman and Wang formulations is that the coefficients of the governing equations were considered as variables instead of constants. Recently, Berryman and Pride (2002) presented models that allow all dual-poroelastic coefficients to be determined from the underlying constituents' properties, thus expanding the applicability of the dual-poroelastic formulation. Nevertheless, existing analytical solutions in this area are scarce, ranging from the one-dimensional consolidation (Lewallen and Wang 1998), axisymmetric borehole (Wilson and Aifantis 1982), to plane-strain wellbore (Li 2003). Lately, the a series of analytical solution for the geometries of rectangular strip, solid cylinder, hollow cylinder and inclined wellbore in naturally fractured rock formations modeled as dual-porosity and dual-permeability isotropic poroelastic continuum was published (Abousleiman and Nguyen 2005; Nguyen and Abousleiman 2009a; Nguyen and Abousleiman 2010). These solutions serve as the basis for understanding the salient features of the coupled dual-time scale response in fractured porous media.

For chemically active fractured porous media, e.g., fractured shale, additional coupled

osmotic and solute transport processes in both the porous matrix and fracture network have to be accounted. To the author's knowledge, no analytical solution exists for dual-poroelastic with chemical osmotic interaction. Available solutions are either numerical or mostly focused on the fluid and solute transport aspect of the problem, e.g., Dershowitz and Miller 1995. As a first order approach, Nguyen et al. (2009) extended the dual-poroelastic inclined wellbore solution (Abousleiman and Nguyen 2005) to include chemical osmotic potential while neglecting the solute transport effect in fractured shale formations. It was shown in this work that fractured shale modeled as dual-poroelastic formation subjected to chemical potential gradient show significantly different behavior than its compact-shale counterpart. This solution laid the foundation for the complete inclined wellbore stability solution for fractured shale accounting for chemical osmosis as well as solute transport (Nguyen and Abousleiman 2009b) which will be presented in Chapter 3 of this dissertation.

Incorporating thermal effect into the dual-poroelastic theoretical formulation is more involved due to difference in the mechanism of heat flow from that of fluid flow in constituent porosity media. Heat flow in the porous matrix is primarily driven by conductive mechanism through the compact matrix skeleton while heat convection carried by the fast diffusing fluid in the fracture network is intuitively more dominant. However, because thermal conductivity is significantly higher through the compact matrix framework than through the fracture network, comprised mostly of pore space, the dual-porosity temperature evolutions and interporosity heat exchange are most likely masked. Consequently, a single-temperature approach for naturally fractured geomaterials appears to be more practical (Master et al. 2000) than the double-temperature approach (Aifantis

and Bekos 1980). Again, for fractured porous media, despite the abundance in numerical modeling of porothermoelastic effects (e.g., Aifantis and Bekos 1980; Millard et al. 1995; Nguyen and Selvadurai 1995; Abdallah et al. 1995; Master et al. 2000; Nair et al. 2004), no analytical solution has been provided for the coupled heat and fluid flow and the resultant stress and deformation field in fractured porous media.

1.3 Objectives

Based on the preceding literature review regarding dual-poromechanics formulations and solutions, it is evident that, to date, a large number of analytically-solvable problems for dual-porous materials such as naturally fractured rock formations or bone tissues have not been addressed. Therefore, the objective of this dissertation is to present consistent theoretical formulations and analytical solution methods for problems in laboratory and field applications in a transversely isotropic dual-porosity and dual-permeability poroelastic medium incorporating the effects of chemical and thermal gradients. Given the generality and widespread applications of the following problem's geometries: rectangular strip, solid and hollow cylinder and inclined wellbore, in geo- and bio-mechanics fields, it is necessary to develop mathematical framework and obtain the corresponding analytical solutions. Finally, it is desired to carry some laboratory and field analyses to demonstrate the applications of the derived analytical solutions. For example, the inclined wellbore solution can be applied to study such problems as drilling stability, production induced consolidation, and hydraulic fracturing (Schmitt and Zoback 1992; Cui et al. 1998; Abousleiman et al. 2007). The cylinder geometry are commonly used in the design and

setups for uniaxial and triaxial laboratory testing of porous rock specimens (Schmitt et al. 1993; Cui and Abousleiman 2001; Kanj and Abousleiman 2004b; Jourine et al. 2004), sanding experiment (Papamichos et al. 2001), and in simulating sudden stress relief of a long core removed from subsurface wellbore (Detournay and Cheng 1993). The rectangular strip geometry can be used to investigate reservoir consolidation features as well as to benchmark and validate the integrity of numerical codes.

1.4 Dissertation Outline

Chapter 2 is devoted to studying the behaviors and characteristics of dual-poroelastic saturated porous media. An anisotropic dual-poroelastic formulation is presented by extending the classical elastic and single-poroelastic ones. Governing equations are specialized for a transversely isotropic as well as isotropic material under generalized plane-strain loading condition. The resulting system of equations is used to derive analytical solutions for wellbore and consolidation problems in naturally fractured rock formations. The wellbore problem is illustrated via the solution of inclined borehole geometry for various fluid-flow boundary conditions. The consolidation problem includes solutions to geometries such as rectangular strip and cylinders (solid and hollow). The results for pore pressure, stress, and displacement for each problem's geometry are plotted to highlight the dual-time-scale behaviors and the effect of fracture network as well as transverse isotropy on the overall responses.

In Chapter 3, the analytical dual-porosity and dual-permeability porochemoelastic formulation and solutions to simulate the poromechanical responses of chemically active

fractured formation are presented. First, the single-porochemoelastic governing equations, extended based on thermodynamic framework of dual-poroelasticity to incorporate the effects of fluid and solute flow in the secondary porosity, e.g., rock's fractures, are briefly presented. The constituent porous matrix and fracture media are generally modeled as imperfect semi-permeable membranes which can allows partial transport and exchange of the solutes. Separate transport equations and inter-porosity exchange are written for the porous matrix and fracture network accounting for the fully coupled flow processes including hydraulic conduction (Darcy's law), chemical osmotic flow, and solute diffusion (Fick's law). The resulting system of equations is applied to obtain the analytical solutions for the drilling of inclined wellbore and consolidation of solid cylinder under oedometer testing condition (K_0 test). Results for dual pore pressures, solute concentrations, stresses, and displacements are plotted and compared with the corresponding single-porochemoelastic counterparts or dual-poroelastic (neglecting chemical effect) to highlight the contributions of fracture, chemical osmosis and solute transport on the overall responses.

In Chapter 4, a dual-porosity and dual-permeability porothermoelastic analytical formulation and solution applicable to transversely isotropic fractured porous media is presented. First, the dual-poroelastic governing equations as presented in Chapter 2 are extended to incorporate thermal effects within the thermodynamic framework of a global temperature approach. The complete formulation includes contribution from both heat conduction and convection in the porous matrix and fracture system. Neglecting the non-linear heat convection, the resulting system of equations is applied to obtain the analytical

solutions for inclined wellbore and consolidation of rectangular strip (the Mandel's problem) subjected to thermal perturbation. The effect of heat convection is assessed numerically by finite difference solution method for a special case of vertical borehole drilled in hydrostatic in-situ stress condition. In addition, the extended non-isothermal Mandel's problem can be treated as a canonical illustration of the intricate dual-porothermoelastic interplay. The results for stress, pore pressure, displacement, and temperature are plotted and compared with the corresponding isothermal counterpart to demonstrate the effect of temperature gradient in a fractured porous saturated medium.

Chapter 5 demonstrates some practical applications of the presented wellbore and consolidation solutions, both in field cases and in laboratory testing designs. First, the various inclined wellbore solutions accounting for drilling fluid's pressure, salinity, and temperature are applied to simulate and predict time-dependent borehole stability. Next, the hollow cylinder solution is employed to study reservoir geomechanics responses of a vertical well in a naturally fractured reservoir. The analysis includes vertical consolidation and associated implication on porosity and permeability reductions due to fluid withdrawal process. Concluding the chapter, the unconfined solid cylinder solutions are used to simulate some realistic loading conditions in poromechanics testing of rocks and bio-tissues.

Finally, Chapter 6 includes a summary of this dissertation findings and recommendations for future work.

Chapter 2

Dual-Porosity and Dual-Permeability Poroelasticity: Dual-Poroelasticity

2.1 Introduction

In this chapter, the modeling of naturally fractured formations will be addressed analytically applying the dual-porosity and dual-permeability poromechanics approach accounting for the transversely isotropic nature of the rocks. For clarity of subsequent presentations, the classical elastic and single-porosity poroelastic formulations are briefly reviewed and summarized. Next, the naturally fractured rock formation is modeled within the framework of the anisotropic dual-porosity and dual-permeability poroelastic approach. Governing field equations are then developed and specialized for a transversely isotropic as well as isotropic poroelastic material under generalized plane-strain loading condition. The resulting system of equations is used to obtain analytical solutions to typical geometries such as inclined wellbore, rectangular strip, solid and hollow cylinder. Note that although the formulation and solutions are derived for naturally fractured rock formation, they are generally applicable to other dual-porous material such as bio-tissues (bone,

cartilage, etc.).

2.2 Governing Equations

2.2.1 Elasticity

In the simplest form, the deformation of a linear elastic isotropic material follows the classical Hooke's law (e.g., Timoshenko and Goodier 1951)

$$\sigma_{ij} = \frac{E}{1+\nu}\left(\varepsilon_{ij} + \frac{\nu}{1-2\nu}\varepsilon_{kk}\delta_{ij}\right), \quad (2.1)$$

where σ_{ij} is the total stress tensor, ε_{ij} is the total strain tensor, $\varepsilon_{kk} = \Delta V/V$ is the bulk volumetric strain, E is Young's modulus, ν is Poisson's ratio, and δ_{ij} is the Kronecker's delta ($\delta_{ij} = 1$ for $i = j$, $\delta_{ij} = 0$ for $i \neq j$). The elastic coefficients E and ν are related to the familiar bulk compressibility as $C_b = 3(1-2\nu)/E$. Correspondingly, Eq. 2.1 is generalized in the anisotropic form as (e.g., Saada 1974; Boresi and Chong 2000)

$$\sigma_{ij} = M_{ijkl}\varepsilon_{kl}, \quad (2.2)$$

The above equations are written in Einstein's tensor notation where repeated index denotes summation. M_{ijkl} is the symmetric elastic modulus tensor, the reciprocal of which is the compliance or compressibility tensor C_{ijkl} of the rock formation.

2.2.2 Poroelasticity

For fluid saturated porous media, e.g., subsurface rock formations, it is well-known that changes in pore pressure alter the "effective stresses" acting on the porous solid frame through a weighted effective stress coefficient (Biot 1941; Geertsma 1957). Thus, in a

poroelastic approach, the constitutive Eq. 2.2 can simply be expressed in terms of effective stress as (Biot 1955; Thompson and Willis 1991; Cheng 1997)

$$\sigma_{ij} - \alpha_{ij} p = M_{ijkl} \varepsilon_{kl} , \quad (2.3a)$$

or equivalently

$$\sigma_{ij} = M_{ijkl} \varepsilon_{kl} + \alpha_{ij} p , \quad (2.3b)$$

where α_{ij} is the Biot's effective stress coefficient tensor and compression is positive. On the other hand, the variation of the fluid content corresponding to the fluid exchange with the surroundings is governed by not only the pore-fluid pressure field but also by the rock deformation as

$$\zeta = \left(\frac{\Delta m_f}{\rho_{f,0}} \right) = -\alpha_{ij} \varepsilon_{ij} + \frac{p}{M} , \quad (2.4)$$

in which $m_f = \phi \rho_f$ is the fluid mass content per unit total reference bulk volume, ρ_f is the fluid density, and ϕ is the porosity. M is the Biot's modulus, the inverse of which is equivalent to the familiar storage coefficient in groundwater literatures. For the most general anisotropic case, the above constitutive behaviors (Eqs. 2.3 and 2.4) are described using twenty eight material constants (twenty one M_{ijkl}, six α_{ij} and one M coefficients).

The time-dependent poroelastic effect comes in under the transient nature of the fluid flow across the porous formation. The fluid flux due to the pressure gradient follows Darcy's law

$$q_i = -\kappa_{ij} \frac{\partial p}{\partial x_j} , \quad (2.5)$$

where q_i is the total volumetric fluid flux and κ_{ij} is the usual Darcy's mobility coefficient tensor defined as the ratio of the intrinsic permeability k_{ij} tensor over the dynamic fluid viscosity μ. Other governing equations are the strain-displacement relations and conservation equations which include the quasi-static stress equilibrium equation and mass balance equations written in index notation as

$$\varepsilon_{ij} = \frac{1}{2}\left(\frac{\partial u_i}{\partial x_j} + \frac{\partial u_j}{\partial x_i}\right), \quad (2.6)$$

$$\frac{\partial \sigma_{ij}}{\partial x_j} = 0, \quad (2.7)$$

$$\frac{\partial \zeta}{\partial t} + \frac{\partial q_i}{\partial x_i} = 0, \quad (2.8)$$

in which u_i is the displacement vector. Equations 2.3 to 2.8 complete the time-dependent poroelastic description of the response of anisotropic saturated porous rock formations. These equations are extended to model naturally fractured porous media using the dual-porosity and dual-permeability concept in the following.

2.2.3 Dual-Poroelasticity

Naturally fractured porous rock involves a high degree of local heterogeneity due to the presence of abnormally high permeability but low porosity flow paths (fractures). One way to model would be to account for each fracture in the computational mesh. Unfortunately, it is mathematically and physically impossible to model all the fractures in a field scale rock mass explicitly, e.g., an astounding number of 5 million fractures were estimated in a 68 cubic meter volume from mapping statistics in consideration of seepage in three-

dimensional fracture networks (Billaux et al. 1989; Pariseau 1993). A more tractable and "least damaging" approach is to realizing the fractured porous media within the frame work of the dual-porosity and dual-permeability continuum concept (Cho et al. 1991; Tom et al. 2006; Bagheri and Settari 2006).

The current approach ignores the characteristics of individual fracture such as aperture, length and toughness. In other words, the fractures are not discretely modeled but explicitly represented as a secondary porous continuum characterized by secondary porosity, compressibility and permeability. At the macroscopic level, the overall system is considered to consist of two co-located but distinct fluid-saturated porous continua: the primary one represents the porous matrix with intrinsic properties $\{M^{\mathrm{I}}_{ijkl}, \alpha^{\mathrm{I}}_{ij}, M^{\mathrm{I}}, \phi^{\mathrm{I}}, \kappa^{\mathrm{I}}_{ij}\}$ occupying volume fraction v^{I} of the total bulk volume and the secondary one represents the porous fracture network with intrinsic properties $\{M^{\mathrm{II}}_{ijkl}, \alpha^{\mathrm{II}}_{ij}, M^{\mathrm{II}}, \phi^{\mathrm{II}}, \kappa^{\mathrm{II}}_{ij}\}$ occupying the remaining bulk volume fraction $v^{II} = 1 - v^{I}$. In other word, the overall domain is envisioned as containing two distinct porous continua, each possessing a solid skeletal framework and a saturated pore network. As a result, fractured formation will exhibit dual pore-pressure evolutions when subjected to stress and pressure perturbations. The porous matrix and fracture continua can communicate and may exchange fluid mass.

In the dual-poroelastic constitutive approach, since there are two distinct effective fluid-pressure fields, the linear anisotropic constitutive equations accounting for the effect of fracture network follow naturally from the single-poroelastic formulation Eqs. 2.3 and 2.4 as

$$\sigma_{ij} = \overline{M}_{ijkl}\varepsilon_{kl} + \overline{\alpha}^{\mathrm{I}}_{ij} p^{\mathrm{I}} + \overline{\alpha}^{\mathrm{II}}_{ij} p^{\mathrm{II}}, \qquad (2.9)$$

$$\zeta^{\mathrm{I}} = -\overline{\alpha}_{ij}^{\mathrm{I}}\varepsilon_{ij} + \frac{p^{\mathrm{I}}}{\overline{M}^{\mathrm{I}}} + \frac{p^{\mathrm{II}}}{\overline{M}^{\mathrm{I,II}}}, \quad (2.10)$$

$$\zeta^{\mathrm{II}} = -\overline{\alpha}_{ij}^{\mathrm{II}}\varepsilon_{ij} + \frac{p^{\mathrm{I}}}{\overline{M}^{\mathrm{I,II}}} + \frac{p^{\mathrm{II}}}{\overline{M}^{\mathrm{II}}}, \quad (2.11)$$

where the superscript (N) = I or II represents the porous intact rock matrix and the porous fracture network, respectively; $p^{(\mathrm{N})}$ is the fluid pressure; $\zeta^{(\mathrm{N})} = \left(\mathrm{v}^{(\mathrm{N})}\phi^{(\mathrm{N})}\rho_f^{(\mathrm{N})}\right)/\rho_{f,0}^{(\mathrm{N})}$ is the variation of fluid content per unit total reference bulk volume; $\phi^{(\mathrm{N})} = V_{\mathrm{p}}^{(\mathrm{N})}/V^{(\mathrm{N})}$ is the local porosity based on individual bulk volume of the porous matrix and fracture continua. The over bar symbol denotes the overall dual-poroelastic material coefficients.

Unlike the pore-pressure fields which are distinct, the stress and strain tensors in Eqs. 2.9 to 2.11 represent the overall mechanical response of the combined matrix-fracture system. The formulation is characterized by effective material constants such as the overall drained elastic modulus tensor, $\overline{M}_{ijkl}$, the effective pore-pressure-coefficient tensors, $\overline{\alpha}_{ij}^{\mathrm{I}}$ and $\overline{\alpha}_{ij}^{\mathrm{II}}$, and the effective coupled Biot's moduli, $\overline{M}^{\mathrm{I}}$, $\overline{M}^{\mathrm{II}}$, and $\overline{M}^{\mathrm{I,II}}$. As a result, the most general anisotropic dual-poroelastic constitutive behaviors is described using thirty six constants (twenty one $\overline{M}_{ijkl}$'s, six $\overline{\alpha}_{ij}^{\mathrm{I}}$'s, six $\overline{\alpha}_{ij}^{\mathrm{II}}$'s and three Biot moduli). These overall coefficients represent the combined responses of the system and can be related to the intrinsic material constants and volume fractions of the constituting porous continua (matrix and fracture network) as described in Appendix A. The applicability of the dual-porosity and dual-compressibility continuum approach depends on the determination of the bulk properties of the fracture network and the extent of its contribution to the whole system.

The dual-permeability nature of fractured formations demands dual Darcy's laws for the fluid flow in the fracture network and in the intact rock matrix regions. Assuming that the flow in each constituting porous medium is independent of the flow in the other, separate Darcy's equation for each medium can be written as

$$q_i^{\mathrm{I}} = -\kappa_{ij}^{\mathrm{I}} \frac{\partial p^{\mathrm{I}}}{\partial x_j}; \qquad q_i^{\mathrm{II}} = -\kappa_{ij}^{\mathrm{II}} \frac{\partial p^{\mathrm{II}}}{\partial x_j}, \quad \text{.....(2.12)}$$

The system is subjected to momentum and mass balance laws. The momentum conservation is enforced by the quasi-static equilibrium equations and is the same as given by Eq. 2.6. The fluid mass balance, accounting for the fluid flow in the porous fracture network and the porous rock's matrix as well as the interporosity fluid transfer can be expressed separately as

$$\frac{\partial \zeta^{\mathrm{I}}}{\partial t} + \mathrm{v}^{\mathrm{I}} \frac{\partial q_i^{\mathrm{I}}}{\partial x_i} = \Gamma, \quad \text{.....(2.13a)}$$

$$\frac{\partial \zeta^{\mathrm{II}}}{\partial t} + \mathrm{v}^{\mathrm{II}} \frac{\partial q_i^{\mathrm{II}}}{\partial x_i} = -\Gamma, \quad \text{.....(2.13b)}$$

In the above, Γ represents the interporosity fluid flux transfer. Modeling interporosity fluid flow can be classified into two main categories: pseudo steady state and transient interporosity flow. In the simplest form, the pseudo steady-state model assumes the fluid exchange to be directly proportional to the pressure differential between the porous fracture network and porous rock matrix as (Warren and Root 1963)

$$\Gamma = \lambda (p^{\mathrm{II}} - p^{\mathrm{I}}), \quad \text{.....(2.14)}$$

where λ is a characteristics of fractured formation such as matrix's permeability, fractures' geometry, distribution, and size. Warren and Root (1963) provided some idealization for

the determination of λ assuming regular matrix block shape and fracture's pattern. It should be noticed that such assumed idealizations are no other than some averaging techniques to arrive at the macroscopic parameters as required by the continuum approach (Chen 1989).

On the other hand, the transient model is a more appropriate representation of the interporosity flow process in which the fluid exchange is proportional to the gradient of pressure difference at the fracture and matrix interface (de Swaan 1976). This fact further complicates the governing equations and solutions have to be resorted to numerical approach. Analytical solutions are restricted to cases of special fracture pattern such as slab, layer, or cubes (Chen et al. 1990). No analytical solution exists for the dual-porosity and dual-permeability case assuming a transient interporosity flow regime. In this dissertation, the pseudo steady-state model, i.e., that of Warren and Root (1963), will be used to characterize the interporosity flow process.

The above set of equations, Eqs. 2.9 to 2.14, represents the dual-porosity and dual-permeability poroelastic system in general anisotropic form. It is specialized to transversely isotropic and isotropic materials in the following section. Additionally, the corresponding field equations necessary for solutions under generalized plane-strain condition are also derived.

2.2.4 Special Anisotropic Cases

Transversely Isotropic Materials. Transversely isotropic materials are characterized by an axis of rotational symmetry. That is, they have the same properties in one plane (e.g., the x_1-x_2 plane) and different properties in the perpendicular direction to this plane (e.g., the x_3

axis). Practically, it is reasonable to assume that the axes of rotational symmetry are the same for both the intact rock matrix and the fracture network. As a result, the drained elastic modulus tensor of the combined matrix-fracture system $\overline{M}_{ijkl}$ is also transversely isotropic and characterized by five material constants. Because shear stresses do not give rise to fluid pressure generation, only two directional pore-pressure coefficients exist: one in the isotropic plane and the other in the perpendicular direction to define the effective pore-pressure-coefficient tensor (two each for $\overline{\alpha}_{ij}^{\mathrm{I}}$ and $\overline{\alpha}_{ij}^{\mathrm{II}}$). Additionally, there are three Biot's moduli $\overline{M}^{\mathrm{I}}$, $\overline{M}^{\mathrm{II}}$, and $\overline{M}^{\mathrm{I,II}}$ which signify the coupled storage capacities of the dual-porosity system under constant strain. Totally, there are twelve independent constitutive parameters to sufficiently describe the response of a transversely isotropic dual-poroelastic system. The constitutive equation expressed in matrix notation is

$$\begin{Bmatrix}\sigma_{11}\\ \sigma_{22}\\ \sigma_{33}\\ \sigma_{12}\\ \sigma_{23}\\ \sigma_{31}\end{Bmatrix}=\begin{bmatrix}\overline{M}_{11} & \overline{M}_{12} & \overline{M}_{13} & 0 & 0 & 0\\ \overline{M}_{12} & \overline{M}_{11} & \overline{M}_{13} & 0 & 0 & 0\\ \overline{M}_{13} & \overline{M}_{13} & \overline{M}_{33} & 0 & 0 & 0\\ 0 & 0 & 0 & \overline{M}_{44} & 0 & 0\\ 0 & 0 & 0 & 0 & \overline{M}_{55} & 0\\ 0 & 0 & 0 & 0 & 0 & \overline{M}_{55}\end{bmatrix}\begin{Bmatrix}\varepsilon_{11}\\ \varepsilon_{22}\\ \varepsilon_{33}\\ 2\varepsilon_{12}\\ 2\varepsilon_{23}\\ 2\varepsilon_{31}\end{Bmatrix}+\begin{bmatrix}\overline{\alpha}_{1}^{\mathrm{I}}\\ \overline{\alpha}_{1}^{\mathrm{I}}\\ \overline{\alpha}_{3}^{\mathrm{I}}\\ 0\\ 0\\ 0\end{bmatrix}p^{\mathrm{I}}+\begin{bmatrix}\overline{\alpha}_{1}^{\mathrm{II}}\\ \overline{\alpha}_{1}^{\mathrm{II}}\\ \overline{\alpha}_{3}^{\mathrm{II}}\\ 0\\ 0\\ 0\end{bmatrix}p^{\mathrm{II}}, \quad \text{.....(2.15)}$$

$$\zeta^{\mathrm{I}}=-\left[\overline{\alpha}_{1}^{\mathrm{I}}(\varepsilon_{11}+\varepsilon_{22})+\overline{\alpha}_{3}^{\mathrm{I}}\varepsilon_{33}\right]+\frac{p^{\mathrm{I}}}{\overline{M}^{\mathrm{I}}}+\frac{p^{\mathrm{II}}}{\overline{M}^{\mathrm{I,II}}}, \quad \text{.....(2.16)}$$

$$\zeta^{\mathrm{II}}=-\left[\overline{\alpha}_{1}^{\mathrm{II}}(\varepsilon_{11}+\varepsilon_{22})+\overline{\alpha}_{3}^{\mathrm{II}}\varepsilon_{33}\right]+\frac{p^{\mathrm{I}}}{\overline{M}^{\mathrm{I,II}}}+\frac{p^{\mathrm{II}}}{\overline{M}^{\mathrm{II}}}, \quad \text{.....(2.17)}$$

In the above, the components of overall elastic moduli and poroelastic coefficients are

related to individual set of material properties of the primary and secondary porosity as given in Appendix A1. Under generalized plane-strain condition where all response functions (except axial displacement) are invariant along the axis of material rotational symmetry and the out-of-plane strain components are zero or spatially uniform, i.e., $\varepsilon_{13} = \varepsilon_{23} = 0$ and $\varepsilon_{33} = \varepsilon_{33}(t)$, the stress equilibrium (Eq. 2.7) reduce to

$$\frac{\partial \sigma_{11}}{\partial x_1} + \frac{\partial \sigma_{12}}{\partial x_2} = 0; \quad \frac{\partial \sigma_{12}}{\partial x_1} + \frac{\partial \sigma_{22}}{\partial x_2} = 0 , \qquad (2.18)$$

Combining the stress-strain-pressure constitutive relations (Eq. 2.15) with the equilibrium Eq. 2.18 and strain-displacement Eq. 2.6 leads to the compatibility equation

$$\nabla^2 \left(\varepsilon_{11} + \varepsilon_{22} + \frac{\overline{\alpha}_1^{\mathrm{I}}}{\overline{M}_{11}} p^{\mathrm{I}} + \frac{\overline{\alpha}_1^{\mathrm{II}}}{\overline{M}_{11}} p^{\mathrm{II}} \right) = 0 , \qquad (2.19)$$

or in terms of stress by inverting Eqs. 2.15 and substituting into Eq. 2.18

$$\nabla^2 \left[\sigma_{11} + \sigma_{22} - \left(1 - \frac{\overline{M}_{12}}{\overline{M}_{11}} \right) \overline{\alpha}_1^{\mathrm{I}} p^{\mathrm{I}} - \left(1 - \frac{\overline{M}_{12}}{\overline{M}_{11}} \right) \overline{\alpha}_1^{\mathrm{II}} p^{\mathrm{II}} \right] = 0 , \qquad (2.20)$$

where $\nabla^2 = \partial^2 / x_1^2 + \partial^2 / x_2^2$ is the Laplacian spatial differential operator.

Isotropic Materials. Under isotropic case where the material properties are the same in all directions, the constitutive equations (Eqs. 2.9 to 2.11) simplify to

$$\sigma_{ij} = \frac{\overline{E}}{1+\overline{\nu}} \left[\varepsilon_{ij} + \frac{\overline{\nu}}{(1-2\overline{\nu})} \varepsilon_{kk} \delta_{ij} \right] + (\overline{\alpha}^{\mathrm{I}} p^{\mathrm{I}} + \overline{\alpha}^{\mathrm{II}} p^{\mathrm{II}}) \delta_{ij} , \qquad (2.21)$$

$$\zeta^{\mathrm{I}} = -\overline{\alpha}^{\mathrm{I}} \varepsilon_{kk} + \frac{p^{\mathrm{I}}}{\overline{M}^{\mathrm{I}}} + \frac{p^{\mathrm{II}}}{\overline{M}^{\mathrm{I,II}}} , \qquad (2.22)$$

$$\zeta^{\mathrm{II}} = -\overline{\alpha}^{\mathrm{II}} \varepsilon_{kk} + \frac{p^{\mathrm{I}}}{\overline{M}^{\mathrm{I,II}}} + \frac{p^{\mathrm{II}}}{\overline{M}^{\mathrm{II}}} , \qquad (2.23)$$

And the corresponding field equations under generalized plane-strain condition become

$$\nabla^2\left(\varepsilon_{kk}+\frac{\overline{\eta}^{\mathrm{I}}}{\overline{G}}p^{\mathrm{I}}+\frac{\overline{\eta}^{\mathrm{II}}}{\overline{G}}p^{\mathrm{II}}\right)=0\,, \quad (2.24)$$

$$\nabla^2\left(\sigma_{11}+\sigma_{22}+2\overline{\eta}^{\mathrm{I}}p^{\mathrm{I}}+2\overline{\eta}^{\mathrm{II}}p^{\mathrm{II}}\right)=0\,, \quad (2.25)$$

where $\varepsilon_{kk} = \varepsilon_{11} + \varepsilon_{22} + \varepsilon_{33}$ noting that $\nabla^2\varepsilon_{33} = 0$ for generalized plane strain; $\overline{\eta}^{(\mathrm{N})}$ is lumped poroelastic coefficient defined as $\overline{\eta}^{(\mathrm{N})} = \overline{\alpha}^{(\mathrm{N})}(1-2\overline{\nu})/2(1-\overline{\nu})$ and $\overline{G}$ is the overall shear modulus given as $\overline{G} = \overline{E}/2(1+\overline{\nu})$. Again, the overall material coefficients are related to the constituent properties as given in Appendix A2.

2.3 Inclined Wellbore[1]

2.3.1 Background

The inclined wellbore problem and solution have become an important tool in the simulation and prediction of wellbore stability for drilling through subsurface rock formations. The first analytical solution for a vertical borehole with unequal far-field stress was Kirsch equations (1898) based on plane-strain idealization and linear elastic modeling of rock. This solution was later generalized to inclined wellbore geometry in a three-dimensional state of stress (Hiramatsu and Oka 1968; Bradley 1979). The elastic approach in these early solutions failed to account for the transient fluid-flow effect due to drilling that will significantly alter the near-wellbore pore pressure and stress concentration. Incorporating the time-dependent fluid diffusion process, Carter and Booker (1982) presented analytical solution for circular tunnel excavated in a fluid saturated medium

[1] Part of this section was published in *J. Eng. Mech.*, **131** (11): 1170–1183 (Abousleiman and Nguyen 2005)

under the framework of Terzaghi's consolidation theory (1943) which is a special case of Biot's poroelasticity theory, i.e., when the effective pore pressure coefficient $\alpha = 1$. Based on this work, a solution for vertical wellbore in a linear poroelastic medium was provided (Detournay and Cheng 1988). The complete analytical solution for an inclined borehole, drilled in an isotropic poroelastic compact rock formation and subjected to a three-dimensional state of stress, was first published by Cui et al. (1997), employing similar boundary-condition decomposition scheme of Carter and Booker (1982). Subsequently, the solution was extended to account for formation transverse anisotropy (Abousleiman and Cui 1998) and different wellbore-fluid boundary conditions (Cui et al. 1998; Ekbote et al. 2004). It was demonstrated that the poroelastic inclined wellbore solution and its effects in this problem present quantitative and qualitative results that are very different from their elastic counterparts (Cui et al. 1999). In addition, wellbore stability analyses reveal results capturing field observations that are not explained by the conventional elastic solution, e.g., time-delayed failure (Abousleiman et al. 2001).

For fractured rock formations modeled as dual-porosity and dual-permeability porous media, Waren and Root (1963) provided the first analytical solution to the fluid flow problem for a vertical wellbore. Following this work, extensive literature was developed for the solution of fluid flow in hydrocarbon reservoirs (Mattax and Kyte 1962; Kazemi 1969; Duguid and Lee 1977; Kazemi et al. 1976; Thomas et al. 1983; Wu and Pruess 1988 and Choi et al. 1997) or ground water aquifers (Cheng et al. 1992). However, the fractured rock formation is treated as a rigid body, thus neglecting the coupling between fluid flow and deformation. Incorporating the coupled deformation process within the framework of the

dual-poroelasticity formulation, Wilson and Aifantis (1982) and Bekos and Aifantis (1986) published analytical solution for vertical wellbore under hydrostatic state of stress, without any plots or numerical results for verification and analysis. Li (2003) presented analytical solution for vertical wellbore in non-hydrostatic stress field. Based on this work and previous solutions for compact rock formations, the complete analytical solution for inclined wellbore drilled in fractured rock formations and subjected to three-dimensional state of stress was derived by Abousleiman and Nguyen (2005). This solution is for isotropic fractured formation and permeable fluid-boundary condition, e.g., openhole drilling. Analyses showed significantly different evolution of effective stress and pore pressure distributions in both the rock matrix and the fracture network, leading to more conservative failure predictions, which agree with field observations (Nguyen et al. 2009).

In this section, the isotropic inclined wellbore solution for fractured formations (Abousleiman and Nguyen 2005) is extended to account for transverse isotropy and different fluid boundary conditions across the wellbore wall.

2.3.2 Problem Descriptions

The wellbore is defined as an infinitely long cylinder created by removal of rock material from a formation with infinite lateral extent. Prior to drilling, the saturated rock formation is subjected to a three-dimensional in-situ state of stresses $\{S_V, S_H, S_h\}$ and formation fluid pressure p_0. The in-situ stresses S_V, S_H, and S_h form an orthogonal set of principal stresses where S_V is the vertical overburden stress while S_H and S_h, which generally are not equal, represent the maximum and minimum principal stresses in the horizontal plane, respectively. An inclined wellbore is one in which the borehole axis is drilled inclined to

the far-field principal in-situ three-dimensional state of stress. In addition, the borehole generator is also assumed to be perpendicular to the isotropic plane of a transversely isotropic poroelastic rock formation. A schematic of the inclined wellbore geometry and the associated in-situ stress orientation is illustrated in **Fig. 2.1**.

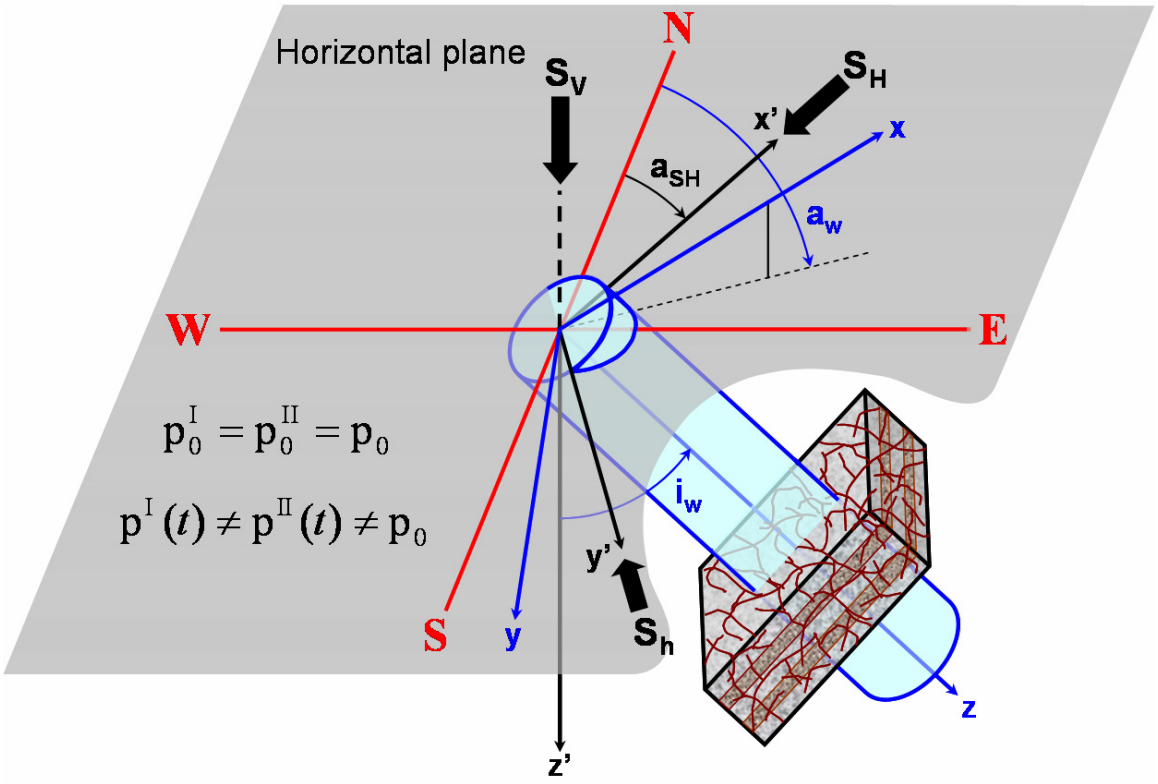

Fig. 2.1—Inclined wellbore geometry in transversely isotropic fractured formation.

Two separate right-handed coordinate systems (x, y, z) and (x', y', z') are attached to the wellbore and the in-situ principal stresses, respectively. The in-situ stress orientation is defined by the azimuth of the maximum horizontal stress direction, a_{SH}, while the borehole local coordinate are described by two angles—the wellbore inclination i_w and azimuth a_w. For practical purpose, all azimuthal angles are defined clockwise from the geographic

North direction. In **Fig. 2.2**, the far-field in-situ stress components from the vantage point of the wellbore coordinates (x, y, z) is illustrated. It is seen that the wellbore is subjected to far-field normal as well as shear stress components denoted by S_x, S_y, S_z, S_{xy}, S_{yz}, and S_{xz}. The stress transformation operation is listed in Appendix D.

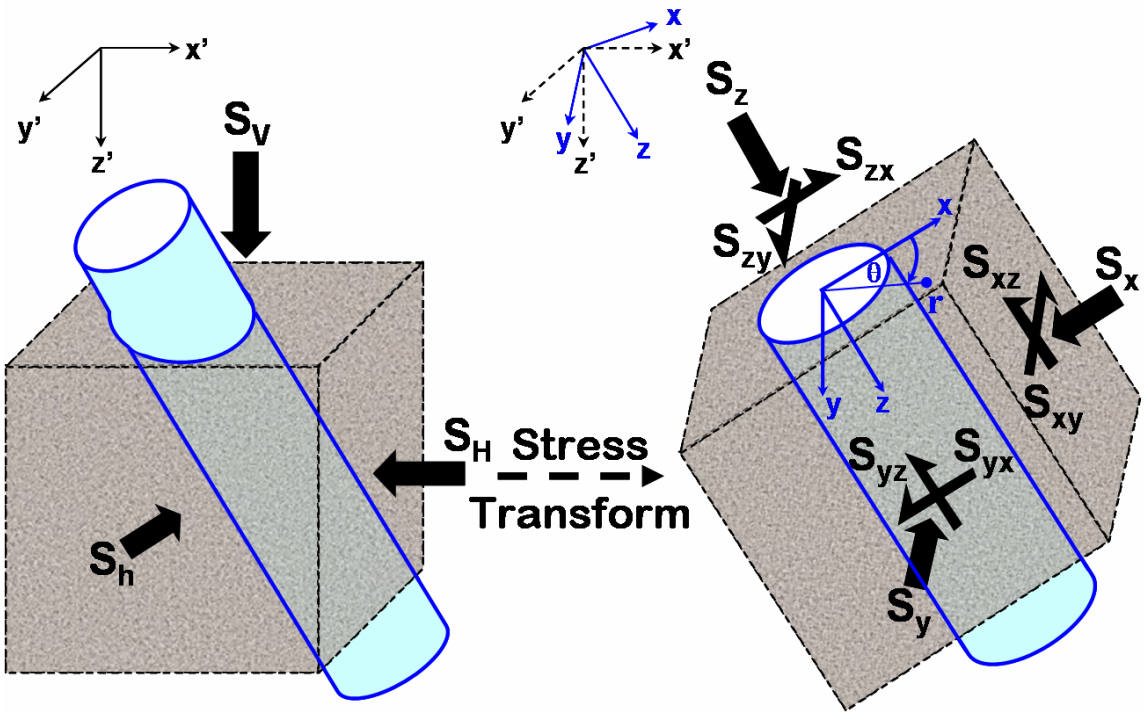

Fig. 2.2—Far-field in-situ stress components in local wellbore coordinate system (x, y, z).

As the wellbore is drilled, the hydraulic pressure of the drilling fluid replaces the support lost by the excavated column of rock. However, the mud pressure, being hydrostatic, can not exactly balance the in-situ earth stresses. As a result, the rock around the wellbore is strained due to the redistribution of stresses. In addition, the imbalance between the mud pressure and the formation fluid pressure leads to potential gradient which acts as driving force for fluid flow process that also affects near-wellbore distribution of stress and pore pressure. The boundary conditions for the problem are

imposed at far field and at the borehole wall. Because the far-field boundary is at infinite distance from the wellbore, it is assumed that there are no changes of stress and pore pressure at this boundary such that

$$\sigma_{xx} = S_x; \qquad \sigma_{yy} = S_y; \qquad \sigma_{zz} = S_z, \quad (2.26a)$$

$$\sigma_{xy} = S_{xy}; \qquad \sigma_{yz} = S_{yz}; \qquad \sigma_{xz} = S_{xz}, \quad (2.26b)$$

$$p^{\mathrm{I}} = p_0^{\mathrm{I}}; \qquad p^{\mathrm{II}} = p_0^{\mathrm{II}}, \quad (2.26c)$$

where the stress components are expressed under Cartesian coordinate system (x, y, z). $p_0^{(\mathrm{N})}$ is the far-field/initial formation pore pressure in the matrix and fractures, respectively. It is reasonable to assume that $p_0^{\mathrm{I}} = p_0^{\mathrm{II}} = p_0$.

Due to its cylindrical geometry, the boundary conditions at the wellbore wall are naturally expressed within a cylindrical coordinate system (r, θ, z) as shown in **Fig. 2.3**. At the borehole wall, $r = R_w$, all surface tractions and fluid pressure or fluxes are changed from their initial state at the instant of excavation as

$$\sigma_{rr} = [\sigma_m + \sigma_d \cos(2(\theta - \theta_r))]\,\mathrm{H}(-t) + p_w(t), \quad (2.27a)$$

$$\sigma_{r\theta} = -\sigma_d \sin(2(\theta - \theta_r))\,\mathrm{H}(-t), \quad (2.27b)$$

$$\sigma_{rz} = [S_{xz}\cos(\theta) + S_{yz}\sin(\theta)]\,\mathrm{H}(-t), \quad (2.27c)$$

$$p^{\mathrm{I}} = p^{\mathrm{II}} = p_0\,\mathrm{H}(-t) + p_w(t) \text{ pressure boundary,} \quad (2.27d)$$

or

$$q_r^{\mathrm{I}} + q_r^{\mathrm{II}} = q_w(t); \qquad p^{\mathrm{I}} = p^{\mathrm{II}} = p_0\,\mathrm{H}(-t) + p_w(q_w(t)) \text{ flux boundary,} \quad (2.27e)$$

where t is time and H(t) is the Heaviside unit step function (H(t <0) = 0 and H($t \geq 0$) = 1);

$p_w(t)$ is a time-dependent wellbore mud pressure due to mud density and/or fluid flow rate and $q_w(t)$ is a transient fluid discharge across the borehole wall. As such, the hydraulic boundary condition can be specified as either pressure-boundary condition or flux-boundary condition to simulate particular field problem such as instantaneous drilling, bottom-hole pressure-controlled production, and flow-rate-controlled injection or withdrawal.

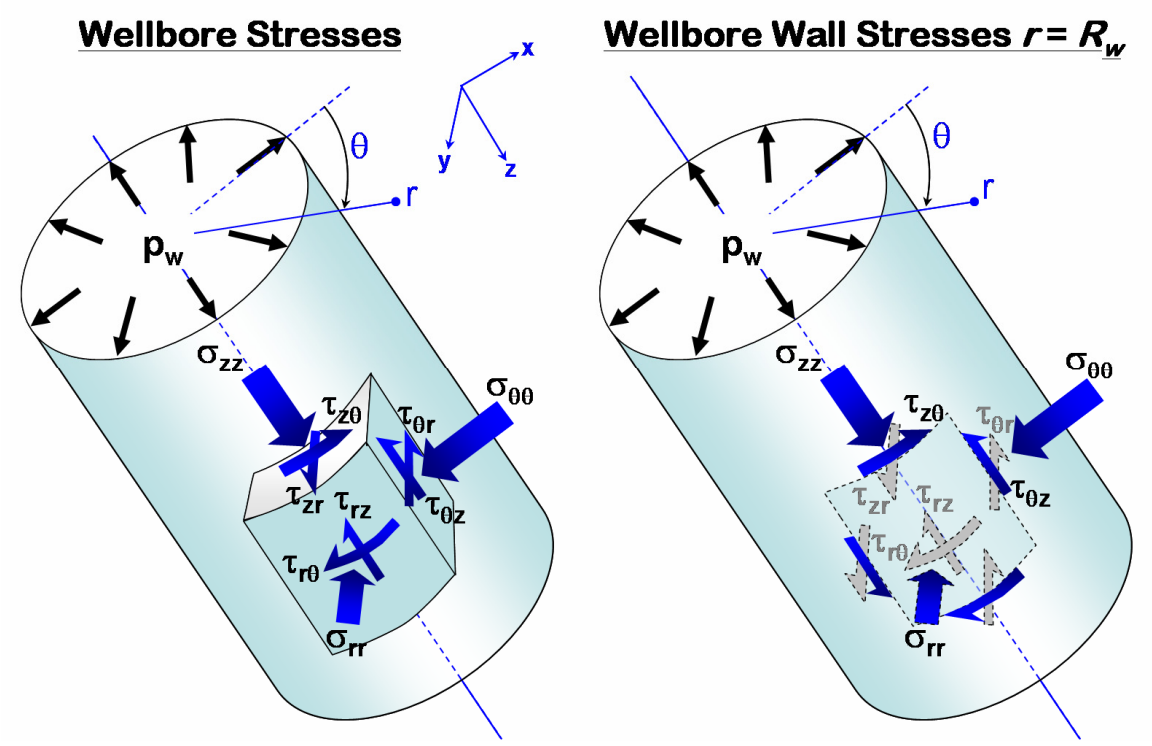

Fig. 2.3—Cylindrical stress components (*r* , *θ*, *z*) near and at the wellbore wall (grey components denote zero values).

In Eqs. 2.27a to 2.27e, terms associated with H(-*t*) represent the initial state before wellbore drilling whereas terms involved with H(*t*) correspond to conditions imposed after the instant of excavation. σ_m, σ_d, and θ_r are parts of the stress boundary condition and rotation angle in polar coordinate for a circular borehole as defined in Cui et al. (1997)

$$\sigma_m = (S_x + S_y)/2; \qquad \sigma_d = 0.5\sqrt{(S_x - S_y)^2 + 4S_{xy}^2}\ , \quad (2.28a)$$

$$\theta_r = 0.5\tan^{-1}[2S_{xy}/(S_x - S_y)], \quad (2.28b)$$

2.3.3 Analytical Solutions

Because the wellbore is infinitely long and there is no change of boundary condition along the wellbore axis, a generalized plane-strain condition can be assumed to prevail (Saada 1974). Furthermore, since all far-field quantities do not change with time, only the perturbed state needs to be solved for. As a result, the far-field boundary conditions for all perturbed variables vanish identically and drilling is simulated by applying a change in boundary condition at the borehole wall as follows

$$\sigma_{rr} = p_w(t) - [\sigma_m + \sigma_d \cos(2(\theta - \theta_r))]\ , \quad (2.29a)$$

$$\sigma_{r\theta} = \sigma_d \sin(2(\theta - \theta_r))\ , \quad (2.29b)$$

$$\sigma_{rz} = -[S_{xz}\cos(\theta) + S_{yz}\sin(\theta)]\ , \quad (2.29c)$$

$$p^{\mathrm{I}} = p^{\mathrm{II}} = p_w(t) - p_0 \text{ pressure boundary,} \quad (2.29d)$$

or

$$q_r^{\mathrm{I}} + q_r^{\mathrm{II}} = q_w(t); \qquad p^{\mathrm{I}} = p^{\mathrm{II}} = p_w(q_w(t)) - p_0 \text{ flux boundary,} \quad (2.29e)$$

Owing to the linearity of the governing equations, the problem can be decomposed into two sub-problems and solved separately. The boundary conditions and corresponding solutions to the two sub-problems are presented in the followings.

2.3.3.1 Problem I – Plane Strain

The boundary conditions for perturbed quantities in Problem I at the wall ($r = R_w$) are

$$\sigma_{rr} = p_w(t) - [\sigma_m + \sigma_d \cos(2(\theta - \theta_r))] \text{ , } \quad (2.30a)$$

$$\sigma_{r\theta} = \sigma_d \sin(2(\theta - \theta_r)) \text{ , } \quad (2.30b)$$

$$p^{\mathrm{I}} = p^{\mathrm{II}} = p_w(t) - p_0 \text{ pressure boundary, } \quad (2.30d)$$

or

$$q_r^{\mathrm{I}} + q_r^{\mathrm{II}} = q_w(t); \qquad p^{\mathrm{I}} = p^{\mathrm{II}} = p_w(q_w(t)) - p_0 \text{ flux boundary, } \quad (2.30e)$$

For plane strain condition, i.e., $\varepsilon_{zz} = \varepsilon_{33} = 0$, the fluid contents (Eqs. 2.16 and 2.17) in polar coordinate (r-θ) in terms of stress and pressures reduce to

$$\zeta^{\mathrm{I}} = -a^{\mathrm{I}}(\sigma_{rr} + \sigma_{\theta\theta} - b_{11}p^{\mathrm{I}} - b_{12}p^{\mathrm{II}}), \quad (2.31)$$

$$\zeta^{\mathrm{II}} = -a^{\mathrm{II}}(\sigma_{rr} + \sigma_{\theta\theta} - b_{21}p^{\mathrm{I}} - b_{22}p^{\mathrm{II}}), \quad (2.32)$$

where the material coefficient $a^{(\mathrm{N})}$ and dimensionless parameters $\overline{\varphi}^{(\mathrm{N})}$ and b_{ij} are

$$a^{(\mathrm{N})} = \frac{\overline{\alpha}_1^{(\mathrm{N})}}{\overline{M}_{11} + \overline{M}_{12}}, \quad (2.33)$$

$$\overline{\varphi}^{(\mathrm{N})} = \frac{\overline{\alpha}_3^{(\mathrm{N})}(\overline{M}_{11} + \overline{M}_{12}) - 2\overline{\alpha}_1^{(\mathrm{N})}\overline{M}_{13}}{\overline{\alpha}_1^{(\mathrm{N})}\overline{M}_{33}}, \quad (2.34)$$

$$b_{11} = \frac{\overline{M}_{11} + \overline{M}_{12} + 2(\overline{\alpha}_1^{\mathrm{I}})^2\overline{M}^{\mathrm{I}}}{\overline{\alpha}_1^{\mathrm{I}}\overline{M}^{\mathrm{I}}}; \qquad b_{12} = \frac{\overline{M}_{11} + \overline{M}_{12} + 2\overline{\alpha}_1^{\mathrm{I}}\overline{\alpha}_1^{\mathrm{II}}\overline{M}^{\mathrm{I,II}}}{\overline{\alpha}_1^{\mathrm{I}}\overline{M}^{\mathrm{I,II}}}, \quad (2.35a)$$

$$b_{21} = \frac{\overline{M}_{11} + \overline{M}_{12} + 2\overline{\alpha}_1^{\mathrm{I}}\overline{\alpha}_1^{\mathrm{II}}\overline{M}^{\mathrm{I,II}}}{\overline{\alpha}_1^{\mathrm{II}}\overline{M}^{\mathrm{I,II}}}; \qquad b_{22} = \frac{\overline{M}_{11} + \overline{M}_{12} + 2(\overline{\alpha}_1^{\mathrm{II}})^2\overline{M}^{\mathrm{II}}}{\overline{\alpha}_1^{\mathrm{II}}\overline{M}^{\mathrm{II}}}, \quad (2.35b)$$

Similarly, the compatibility Eq. 2.20 is rewritten in polar coordinate (r-θ) as

$$\left(\frac{\partial^2}{\partial r^2} + \frac{1}{r}\frac{\partial}{\partial r} + \frac{1}{r^2}\frac{\partial^2}{\partial \theta^2}\right)\left[\sigma_{rr} + \sigma_{\theta\theta} - \left(1 - \frac{\overline{M}_{12}}{\overline{M}_{11}}\right)\overline{\alpha}_1^{\mathrm{I}}p^{\mathrm{I}} - \left(1 - \frac{\overline{M}_{12}}{\overline{M}_{11}}\right)\overline{\alpha}_1^{\mathrm{II}}p^{\mathrm{II}}\right] = 0, \quad (2.36)$$

Based on boundary loading conditions and symmetry considerations for fluid pressures and stress, the various response functions can be decomposed as (Carter and Booker 1982)

$$[p^{(\mathrm{N})}, q_r^{(\mathrm{N})}, \sigma_{rr}, \sigma_{\theta\theta}] = [P^{(\mathrm{N})}, Q_r^{(\mathrm{N})}, S_{rr}, S_{\theta\theta}] \times \cos(n(\theta - \theta_r)), \quad (2.37a)$$

$$\sigma_{r\theta} = S_{r\theta} \sin(n(\theta - \theta_r)), \quad (2.37b)$$

where $P^{(\mathrm{N})}, S_{kk}, S_{rr}, S_{\theta\theta}$, and $S_{r\theta}$ are functions of radial distance (r) and time (t) only and n is an integer number depending on loading conditions. Incorporating Eq. 2.37a into Eq. 2.36 to eliminate θ dependency and seeking for bounded solutions gives

$$S_{rr} + S_{\theta\theta} = \bar{\gamma}^{\mathrm{I}} P^{\mathrm{I}} + \bar{\gamma}^{\mathrm{II}} P^{\mathrm{II}} + C_1(t) r^{-n}, \quad (2.38)$$

in which the dimensionless coefficient, $\bar{\gamma}^{(\mathrm{N})} = \bar{\alpha}_1^{(\mathrm{N})}(1 - \overline{M}_{12} / \overline{M}_{11})$ and $C_1(t)$ is an arbitrary time-dependent coefficients to be determined from boundary conditions. Eliminating the stress components in the fluid contents (Eqs. 2.31 and 2.32) and substituting the resulting expressions into the fluid mass balance lead to the simplified diffusion equations in terms of the decomposed fluid pressures. In compact matrix form, they are expressed as

$$\left(\mathbf{A} \frac{\partial}{\partial t} + \mathbf{\Gamma} - \mathbf{D} \nabla_r^2 \right) \begin{Bmatrix} P^{\mathrm{I}} \\ P^{\mathrm{II}} \end{Bmatrix} = \begin{Bmatrix} a^{\mathrm{I}} \\ a^{\mathrm{II}} \end{Bmatrix} \frac{\partial C_1}{\partial t} r^{-n}, \quad (2.39)$$

where $\nabla_r^2 = \partial^2 / \partial r^2 + (1/r)(\partial / \partial r)$ and the coefficient matrices **A**, **D** and **Γ** are

$$\mathbf{A} = \begin{bmatrix} A_{11} & A_{12} \\ A_{12} & A_{22} \end{bmatrix} = \begin{bmatrix} \dfrac{1}{\overline{M}^{\mathrm{I}}} + \dfrac{(\bar{\alpha}_1^{\mathrm{I}})^2}{\overline{M}_{11}} & \dfrac{1}{\overline{M}^{\mathrm{I,II}}} + \dfrac{\bar{\alpha}_1^{\mathrm{I}} \bar{\alpha}_1^{\mathrm{II}}}{\overline{M}_{11}} \\ \dfrac{1}{\overline{M}^{\mathrm{I,II}}} + \dfrac{\bar{\alpha}_1^{\mathrm{I}} \bar{\alpha}_1^{\mathrm{II}}}{\overline{M}_{11}} & \dfrac{1}{\overline{M}^{\mathrm{II}}} + \dfrac{(\bar{\alpha}_1^{\mathrm{II}})^2}{\overline{M}_{11}} \end{bmatrix}, \quad (2.40)$$

$$\mathbf{D} = \begin{bmatrix} \bar{\kappa}_1^{\mathrm{I}} & 0 \\ 0 & \bar{\kappa}_1^{\mathrm{II}} \end{bmatrix} \qquad \mathbf{\Gamma} = \lambda \begin{bmatrix} 1 & -1 \\ -1 & 1 \end{bmatrix}, \quad (2.41)$$

Introducing the following normalized parameters

$$r_D = \frac{r}{R_w}; \quad t_D = \frac{\overline{\kappa}_1^{\mathrm{I}} + \overline{\kappa}_1^{\mathrm{II}}}{(A_{11} + A_{22})R_w^2} t, \quad \text{.....(2.42)}$$

$$\overline{\kappa}_D = \frac{\overline{\kappa}_1^{\mathrm{II}}}{\overline{\kappa}_1^{\mathrm{I}} + \overline{\kappa}_1^{\mathrm{II}}}; \quad \lambda_D = \frac{\lambda R_w^2}{\overline{\kappa}_1^{\mathrm{I}} + \overline{\kappa}_1^{\mathrm{II}}}, \quad \text{.....(2.43)}$$

$$\omega = \frac{A_{22}}{A_{11} + A_{22}}; \quad \omega^{\mathrm{I,II}} = \frac{A_{12}}{A_{11} + A_{22}}, \quad \text{.....(2.44)}$$

where r_D and t_D are the dimensionless radial distance and time; $\overline{\kappa}_D$ is the macroscopic mobility ratio; λ_D is the dimensionless interporosity flow parameter; ω and $\omega^{\mathrm{I,II}}$ are the macroscopic coupled storage ratios; . The diffusion equation becomes

$$\left(\boldsymbol{\omega} \frac{\partial}{\partial t_D} + \boldsymbol{\Gamma}_{\mathbf{D}} - \overline{\boldsymbol{\kappa}}_{\mathbf{D}} \nabla^2_{n,r_D} \right) \begin{Bmatrix} P^{\mathrm{I}} \\ P^{\mathrm{II}} \end{Bmatrix} = \begin{Bmatrix} c_f^{\mathrm{I}} \\ c_f^{\mathrm{II}} \end{Bmatrix} \frac{\partial C_1}{\partial t_D} r_D^{-n}, \quad \text{.....(2.45)}$$

in which

$$\boldsymbol{\omega} = \begin{bmatrix} 1-\omega & \omega^{\mathrm{I,II}} \\ \omega^{\mathrm{I,II}} & \omega \end{bmatrix}; \quad \boldsymbol{\Gamma}_{\mathbf{D}} = \lambda_D \begin{bmatrix} 1 & -1 \\ -1 & 1 \end{bmatrix}; \quad \overline{\boldsymbol{\kappa}}_{\mathbf{D}} = \begin{bmatrix} 1-\overline{\kappa}_D & 0 \\ 0 & \overline{\kappa}_D \end{bmatrix}, \quad \text{.....(2.46)}$$

$$c_f^{(\mathrm{N})} = a^{(\mathrm{N})} / (A_{11} + A_{22}), \quad \text{.....(2.47)}$$

$$\nabla^2_{n,D} = \frac{\partial^2}{\partial r_D^2} + \frac{1}{r_D} \frac{\partial}{\partial r_D} - \frac{n^2}{r_D^2}, \quad \text{.....(2.48)}$$

The above system of partial differential equations is solved directly to obtain the general expressions for the decomposed pore-pressure fields. Applying Laplace transform to the diffusion Eq. 2.45 yields

$$\left(s\,\boldsymbol{\omega}+\boldsymbol{\Gamma}_{\mathbf{D}}-\overline{\boldsymbol{\kappa}}_{\mathbf{D}}\nabla^2_{n,r_D}\right)\begin{Bmatrix}\widetilde{P}^{\mathrm{I}}\\ \widetilde{P}^{\mathrm{II}}\end{Bmatrix}=\begin{Bmatrix}c_f^{\mathrm{I}}\\ c_f^{\mathrm{II}}\end{Bmatrix}s\,\widetilde{C}_1 r_D^{-n}\,, \quad (2.49)$$

where the tilde sign $\sim$ denotes the corresponding quantity in Laplace transform domain, s is the Laplace transform parameter, and $\widetilde{C}_1=\widetilde{C}_1(s)$. The general solutions are straightforward, noting that the pressures have to be finite as r approaches infinity

$$\widetilde{P}^{\mathrm{I}}=g^{\mathrm{I}}\widetilde{C}_1 r_D^{-n}+C_2^{\mathrm{I}}\mathrm{K}_n(\xi^{\mathrm{I}}r_D)+C_2^{\mathrm{II}}\mathrm{K}_n(\xi^{\mathrm{II}}r_D)\,, \quad (2.50)$$

$$\widetilde{P}^{\mathrm{II}}=g^{\mathrm{II}}\widetilde{C}_1 r_D^{-n}+C_2^{\mathrm{I}}m^{\mathrm{I}}\mathrm{K}_n(\xi^{\mathrm{I}}r_D)+C_2^{\mathrm{II}}m^{\mathrm{II}}\mathrm{K}_n(\xi^{\mathrm{II}}r_D)\,, \quad (2.51)$$

where $C_2^{\mathrm{I}}=C_1^{\mathrm{I}}(s)$ and $C_2^{\mathrm{II}}=C_2^{\mathrm{II}}(s)$ are arbitrary coefficients to be determined from boundary conditions; K_n is the modified Bessel functions of the second kind or order n; $\xi^{(\mathrm{N})}=\sqrt{\ell^{(\mathrm{N})}}$ where $\ell^{(\mathrm{N})}$ is the eigenvalue of the coefficient matrix $\mathbf{Y}=\overline{\boldsymbol{\kappa}}_{\mathbf{D}}^{-1}(s\,\boldsymbol{\omega}+\boldsymbol{\Gamma}_{\mathbf{D}})$; $\ell^{(\mathrm{N})}$, $g^{(\mathrm{N})}$, and $m^{(\mathrm{N})}$ are defined as

$$\ell^{\mathrm{I}},\ell^{\mathrm{II}}=\left(Y_{11}+Y_{22}\pm\sqrt{(Y_{11}-Y_{22})^2+4Y_{12}Y_{21}}\right)/2\,, \quad (2.52)$$

$$m^{\mathrm{I}}=\frac{\ell^{\mathrm{I}}-Y_{11}}{Y_{12}};\qquad m^{\mathrm{II}}=\frac{\ell^{\mathrm{II}}-Y_{11}}{Y_{12}}\,, \quad (2.53)$$

$$\begin{Bmatrix}g^{\mathrm{I}}\\ g^{\mathrm{II}}\end{Bmatrix}=\left(s\,\boldsymbol{\omega}+\boldsymbol{\Gamma}_{\mathbf{D}}\right)^{-1}\begin{Bmatrix}c_f^{\mathrm{I}}\\ c_f^{\mathrm{II}}\end{Bmatrix}s\,, \quad (2.54)$$

The decomposed radial fluid fluxes are derived using Darcy's laws (Eq. 2.12)

$$\widetilde{Q}_r^{\mathrm{I}}=-(1-\overline{\kappa}_D)[-n\,g^{\mathrm{I}}\widetilde{C}_1 r_D^{-n-1}+C_2^{\mathrm{I}}\mathrm{K'}_n(\xi^{\mathrm{I}}r_D)+C_2^{\mathrm{II}}\mathrm{K'}_n(\xi^{\mathrm{II}}r_D)]/R_w\,, \quad (2.55)$$

$$\widetilde{Q}_r^{\mathrm{II}}=-\overline{\kappa}_D[-n\,g^{\mathrm{II}}\widetilde{C}_1 r_D^{-n}+C_2^{\mathrm{I}}m^{\mathrm{I}}\mathrm{K'}_n(\xi^{\mathrm{I}}r_D)+C_2^{\mathrm{II}}m^{\mathrm{II}}\mathrm{K'}_n(\xi^{\mathrm{II}}r_D)]/R_w\,, \quad (2.56)$$

in which $\widetilde{Q}_r^{(\mathrm{N})}=-[\overline{\kappa}^{(\mathrm{N})}/(\overline{\kappa}^{\mathrm{I}}+\overline{\kappa}^{\mathrm{II}})R_w](d\widetilde{P}^{(\mathrm{N})}/dr_D)$ and $\mathrm{K'}_n(x)=d\mathrm{K}_n(x)/dx$. Once the

pressure expressions are obtained, the general solutions for stresses are easy to obtain by using the stress-strain-pressure constitutive equation (Eq. 2.15) and strain-displacement relations (Eq. 2.6) in polar coordinate. For brevity, only the final general solutions for the stress components are presented here

$$\widetilde{S}_{rr} = C_0 r_D^{-n-2} + \frac{(n+2)}{2} A_1 \widetilde{C}_1 r_D^{-n} + \\ - \sum_{(N)=I,II} A_2^{(N)} C_2^{(N)} \left[\frac{\mathrm{K}_{n-1}(\xi^{(N)} r_D)}{\xi^{(N)} r_D} + n(n+1) \frac{\mathrm{K}_n(\xi^{(N)} r_D)}{(\xi^{(N)} r_D)^2} \right], \quad (2.57)$$

$$\widetilde{S}_{\theta\theta} = -C_0 r_D^{-n-2} - \frac{(n-2)}{2} A_1 \widetilde{C}_1 r_D^{-n} \\ + \sum_{(N)=I,II} A_2^{(N)} C_2^{(N)} \left[\frac{\mathrm{K}_{n-1}(\xi^{(N)} r_D)}{\xi^{(N)} r_D} + \left(1 + \frac{n(n+1)}{(\xi^{(N)} r_D)^2} \right) \mathrm{K}_n(\xi^{(N)} r_D) \right], \quad (2.58)$$

$$\widetilde{S}_{r\theta} = C_0 r_D^{-n-2} + \frac{n}{2} A_1 \widetilde{C}_1 r_D^{-n} + \\ - \sum_{(N)=I,II} A_2^{(N)} C_2^{(N)} \left[n \frac{\mathrm{K}_{n-1}(\xi^{(N)} r_D)}{\xi^{(N)} r_D} + n(n+1) \frac{\mathrm{K}_n(\xi^{(N)} r_D)}{(\xi^{(N)} r_D)^2} \right], \quad (2.59)$$

in which $C_0 = C_0(s)$ is an additional coefficients to be determined from boundary conditions; the lumped coefficients A_1 and $A_2^{(N)}$ are expressed as

$$2A_1 = \bar{\gamma}^{I} g^{I} + \bar{\gamma}^{II} g^{II} + 1, \quad (2.60a)$$

$$A_2^{(N)} = \bar{\gamma}^{I} + \bar{\gamma}^{II} m^{(N)}, \quad (2.60b)$$

To determine the unknown constants, C_0, $\widetilde{C}_1$, C_2^{I}, and C_2^{II}, the boundary conditions for this problem are further decomposed into two contributing loading cases namely: axisymmetric and deviatoric loading cases. Case 1, the axisymmetric case, accounts for the unloading of hydrostatic part of the in-situ stress, σ_m, as well as hydraulic perturbation due

to drilling fluid pressure, $p_w(t)$. Case 2, the deviatoric case, accounts for the release of the deviatoric part of the in-plane in-situ stress, σ_d. The corresponding boundary conditions and solutions for four different wellbore-wall's fluid boundary conditions including pressure (permeable), flux, no-flow (impermeable), and impermeable-matrix and permeable-fracture boundary conditions are derived and listed in Appendix D.

2.3.3.2 Problem II – Antiplane Shear

The boundary conditions for perturbed quantities in Problem II at the wall ($r = R_w$) are

$$\sigma_{rz} = -[S_{xz}\cos(\theta) + S_{yz}\sin(\theta)] \,, \quad (2.61a)$$

$$\sigma_{rr} = \sigma_{r\theta} = 0 \,, \quad (2.61b)$$

$$p^{\mathrm{I}} = p^{\mathrm{II}} = 0 \qquad \text{or} \qquad q_r^{\mathrm{I}} = q_r^{\mathrm{II}} = 0 \,, \quad (2.61c)$$

This problem accounts for the sudden release of the out-of-plane in-situ shear stress components S_{xz} and S_{yz} at the wellbore wall. It was shown that no excess pore pressure is generated by this disturbance of shear stress. The stress state is elastic and identical to the isotropic case given as (Amadei 1983)

$$\sigma_{rz} = [S_{xz}\cos(\theta) + S_{yz}\sin(\theta)](1 - 1/r_D^2) \,, \quad (2.62a)$$

$$\sigma_{\theta z} = -[S_{xz}\sin(\theta) - S_{yz}\cos(\theta)](1 + 1/r_D^2) \,, \quad (2.62b)$$

It should be noted that the above solutions for Problem II are no longer valid if the formation material rotation symmetry axis is arbitrary.

2.3.3.3 Complete Solution

The complete solutions for stresses and pore pressures are obtained by superimposing the

non-zero solutions of the two sub-problems together with the background in-situ stress state as

$$p^{\mathrm{I}} = p_0 + p^{\mathrm{I}(1)} + p^{\mathrm{I}(2)}, \quad (2.63a)$$

$$p^{\mathrm{II}} = p_0 + p^{\mathrm{II}(1)} + p^{\mathrm{II}(2)}, \quad (2.63b)$$

$$\sigma_{rr} = \sigma_m + \sigma_d \cos(2(\theta - \theta_r)) + \sigma_{rr}^{(1)} + \sigma_{rr}^{(2)}, \quad (2.63c)$$

$$\sigma_{\theta\theta} = \sigma_m - \sigma_d \cos(2(\theta - \theta_r)) + \sigma_{\theta\theta}^{(1)} + \sigma_{\theta\theta}^{(2)}, \quad (2.63d)$$

$$\sigma_{zz} = S_z + \bar{v}_{13}(\sigma_{rr}^{(1)} + \sigma_{rr}^{(2)} + \sigma_{\theta\theta}^{(1)} + \sigma_{\theta\theta}^{(2)}) + (\bar{\alpha}_3^{\mathrm{I}} - 2\bar{v}_{13}\bar{\alpha}_1^{\mathrm{I}})(p^{\mathrm{I}(1)} + p^{\mathrm{I}(2)}) + (\bar{\alpha}_3^{\mathrm{II}} - 2\bar{v}_{13}\bar{\alpha}_1^{\mathrm{II}})(p^{\mathrm{II}(1)} + p^{\mathrm{II}(2)}), \quad (2.63e)$$

$$\sigma_{r\theta} = -\sigma_d \sin(2(\theta - \theta_r)) + \sigma_{r\theta}^{(2)}, \quad (2.63f)$$

$$\sigma_{rz} = [S_{xz}\cos(\theta) + S_{yz}\sin(\theta)](1 - 1/r_D^2), \quad (2.63g)$$

$$\sigma_{\theta z} = -[S_{xz}\sin(\theta) - S_{yz}\cos(\theta)](1 + 1/r_D^2), \quad (2.63h)$$

in which the superscript (1) and (2) denote the solutions to two loading cases of Problem I.

2.3.4 Results and Discussions

2.3.4.1 Modeling Parameters

To demonstrate the various inclined wellbore solutions presented above, the set of data for a Gulf-of-Mexico shale (Cui and Abousleiman 2001) are adopted in this analysis as

$$E = 1854\ MPa; \quad v = 0.22; \quad \alpha = 0.96; \quad M = 9100\ MPa$$
$$\phi = 0.14; \quad k = 5 * 10^{-8}\ darcy; \quad K_s = 27.6\ GPa; \quad K_f = 1744\ MPa$$

The above data are assumed to be the isotropic properties of the non-fractured porous rock matrix (I) in the dual-porosity and dual-permeability model. The fracture network in the rock modeled as the secondary porous region (II) is assumed to be more compliant than the

matrix one. Various methods for the estimation of the bulk fracture network compressibility based on individual fracture/joint characteristics, spacing, and orientation have been proposed and discussed in the rock mechanics field as summarized by Cook (1992). In this example, to highlight the contrast in stiffness, the same Poisson's ratio is assumed for both porous matrix and fracture systems while the fracture' Young modulus is specified to be 50 times smaller without loss of generality: $v^{\mathrm{I}} = v^{\mathrm{II}} = 0.22$ and $E^{\mathrm{II}} = E^{\mathrm{I}} / 50 = 37\ MPa$. The local fracture porosity ϕ^{II} is the fracture pore volume divided by the fracture total bulk volume. Since the majority of the fracture are porous flow channels, the fracture porosity are usually close to 1. On the other hand, the fracture volume fraction, v^{II}, is the fracture bulk volume divided by the total bulk volume of the combined formation. As such the fracture volume fractions depends on the fracture's spacing and geometry and usually is a small number less than 5% bulk volume as reported in the literatures (Aguilera 1995). Here, fracture porosity and volume fraction are, in here, chosen as $\phi^{\mathrm{II}} = 0.95$ and v^{II} = 1%. Subsequently, the fracture poroelastic parameters α^{II} and M^{II} can be determined using Eqs. A2.3 and A2.4, assuming that the same fluid is permeating the pore spaces $K_f^{\mathrm{I}} = K_f^{\mathrm{II}} = K_f$, $\mu^{\mathrm{I}} = \mu^{\mathrm{II}} = 0.01 Pa \cdot s$ (viscosity), and the porous matrix and porous fracture skeletons are comprised of the same mineral materials $K_s^{\mathrm{I}} = K_s^{\mathrm{II}} = K_s$. The intrinsic fracture permeability is the macroscopic permeability that is assigned to the fracture network in a given volume of rock, and thus dependent upon the fracture's width, orientation and spacing. Here, an intrinsic fracture permeability of approximately 5 milidarcy (5×10^{-15} m^2) is assumed. For isotropic modeling, the

interporosity flow geometric factor is given in term of fracture spacing d (Warren and Root 1963) and fracture's volume fraction, e.g., $\lambda = 60(v^{II}/d^2) \sim 2.4\times10^{-3}$ MPa^{-1}-s^{-1}. Other relevant data for in-situ condition and wellbore geometry are summarized below:

Depth = 1000 m, R_w = 0.1 m, well inclination = 60, well azimuth = 0

S_V = 25 MPa, S_H = 20 MPa (azimuth = 0), S_h = 18 MPa , p_0 = 10 MPa

Time is set at $t_D = 0$ when the wellbore is drilled. Four cases are considered: a constant wellbore pressure (permeable), a constant injection rate, a no-flow wellbore (impermeable), and fully permeable fracture coupled with impermeable matrix wellbore wall fluid boundary conditions. Except for the constant flux boundary condition (injection rate Q = 0.07 m^3/day/m) where the wellbore pressure varies, the wellbore pressure due to drilling mudweight for all other cases are maintained overbalanced at 1.12 g/cc or 11 MPa.

2.3.4.2 Dual-Poroelastic Responses

Due the anisotropy of in-situ stress, excavation of the wellbore will induce non uniform stress distribution near the wellbore as shown in **Fig. 2.4** for pressure boundary condition. Specifically, it is observed that there is excessive compressive tangential stress concentration along the direction of minimum horizontal stress S_h whereas the formation is more relaxed along the maximum horizontal stress direction S_H. The variation of total tangential stress concentration at and around the wellbore wall for four cases of different fluid boundary conditions is shown in **Fig. 2.5**. Obviously, the total normal stress changes significantly with locations and fluid boundary conditions. Note that even if the in-situ horizontal stresses are equal, the inclination of the wellbore will render the in-plane stress components non-hydrostatic leading to unequal stress concentration around the wellbore.

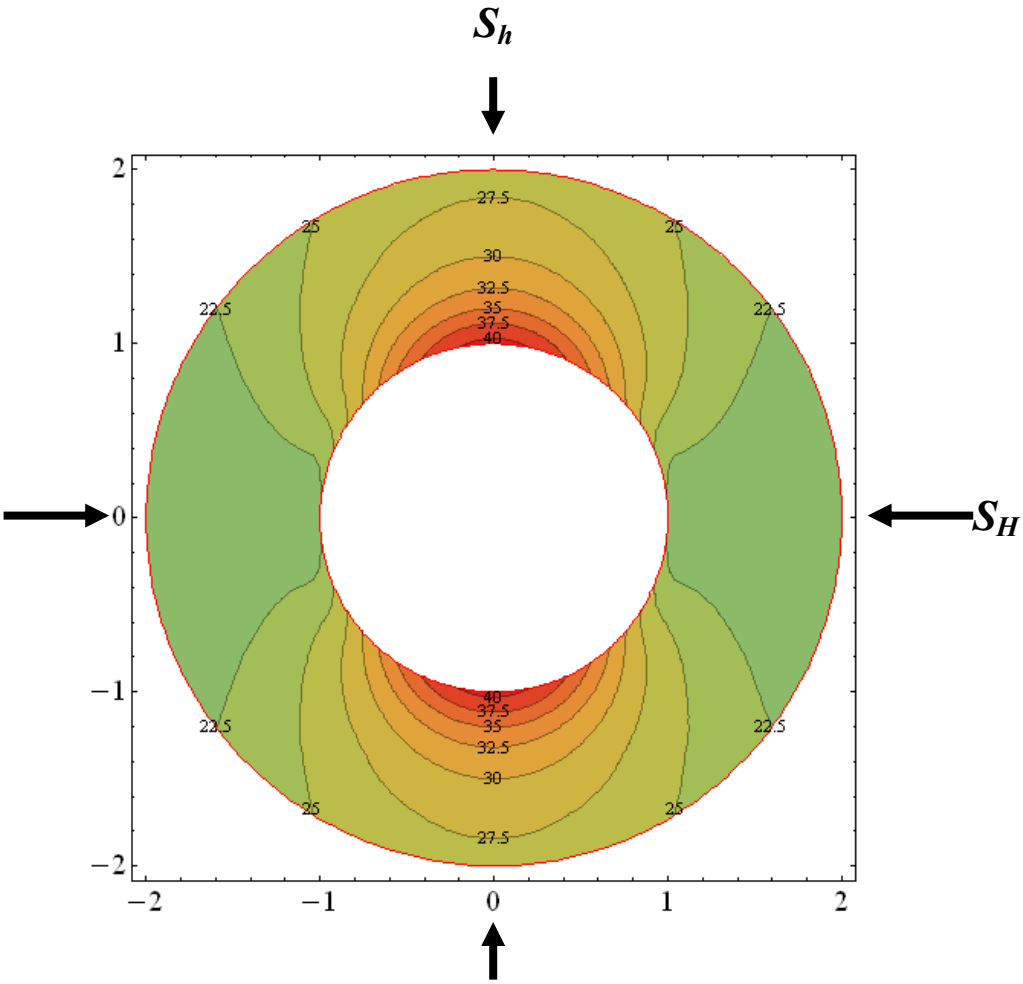

Fig. 2.4—Total tangential (hoop) stress distribution around the wellbore after t_D = 1 (~ 3.5 minutes) into drilling for pressure (permeable) boundary condition.

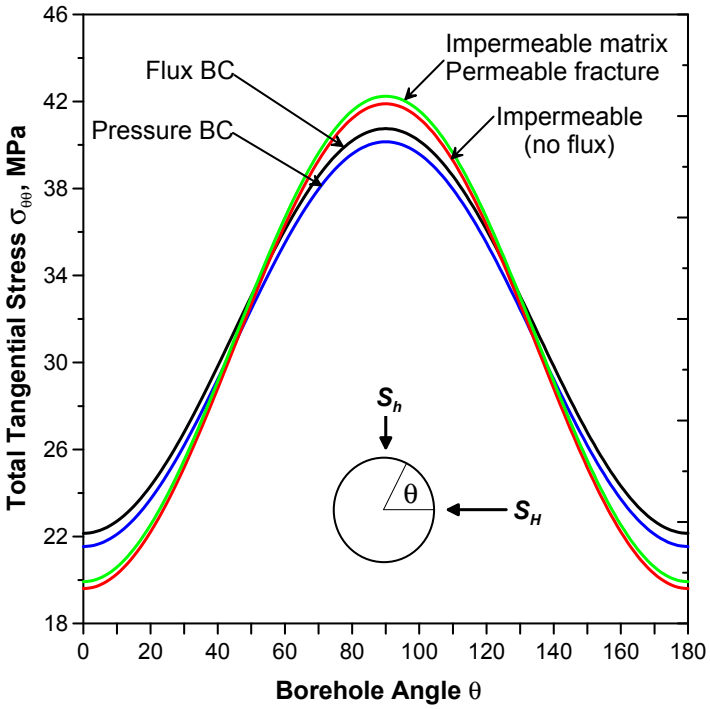

Fig. 2.5—Total tangential (hoop) stress distribution at r_D = 1 after t_D = 1 (~ 3.5 minutes) for four different fluid boundary conditions.

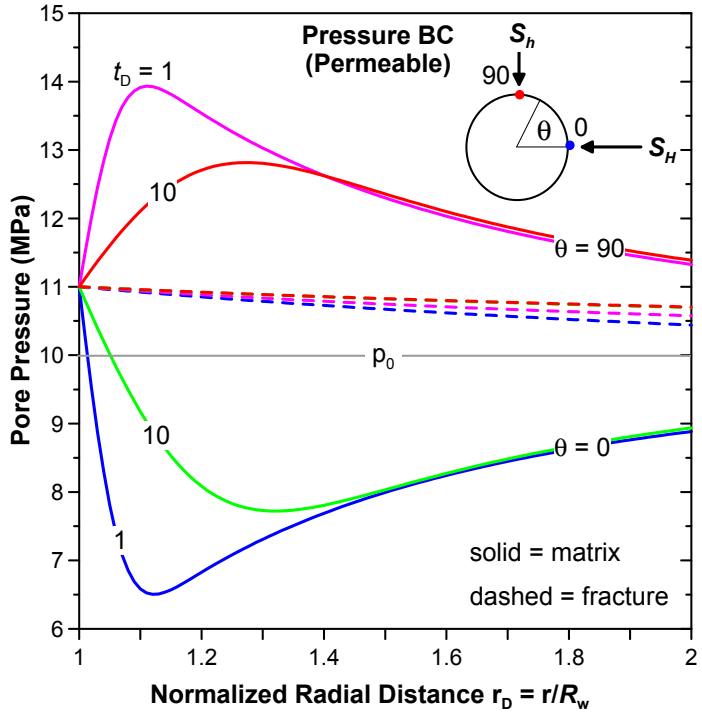

Fig. 2.6—Dual pore-pressure distributions around the wellbore after t_D = 1 (~ 3.5 minutes) and t_D = 10 (~ 35 minutes) for fluid pressure (permeable) boundary conditions.

Because pore pressure is directly coupled with the stress field, the near-wellbore pore-pressure fields are also non-uniform which is a distinct behavior of the fully coupled poroelastic theory and cannot be captured using uncoupled analysis. The evolutions of dual pore-pressure distributions are illustrated in **Figs. 2.6 to 2.12**. For all cases of fluid boundary conditions, the near-wellbore matrix pore pressure is elevated along the S_h direction (due to high stress concentration) but is depressed along the S_H direction (due to low stress concentration). As time progresses, this poroelastic effect due to unloading of the non-hydrostatic in-situ state of stress diminishes and the pore pressure distributions become more uniform around the wellbore.

In Fig. 2.6, the dual fluid-pressure penetrations through the matrix and the fracture network are shown for a permeable borehole wall subjected to a constant wellbore mud pressure. The figure clearly shows two distinct pore pressure responses in which drilling mud quickly penetrates the fracture's region and equilibrates with the applied wellbore pressure while the matrix pore pressure is still transient. This behavior signifies the domination of the flow process in the fractures to the overall matrix-fractures response.

The pressure distribution for a permeable wellbore subjected to a constant injection rate of Q = 0.07 m^3/day/m (flux boundary condition) is shown in Fig. 2.7. Unlike the constant pressure boundary condition, the fluid pressure at the borehole wall is increasing to maintain the constant fluid influx. The pore pressure distribution in the fracture network is almost uniform around the wellbore due to its high permeability.

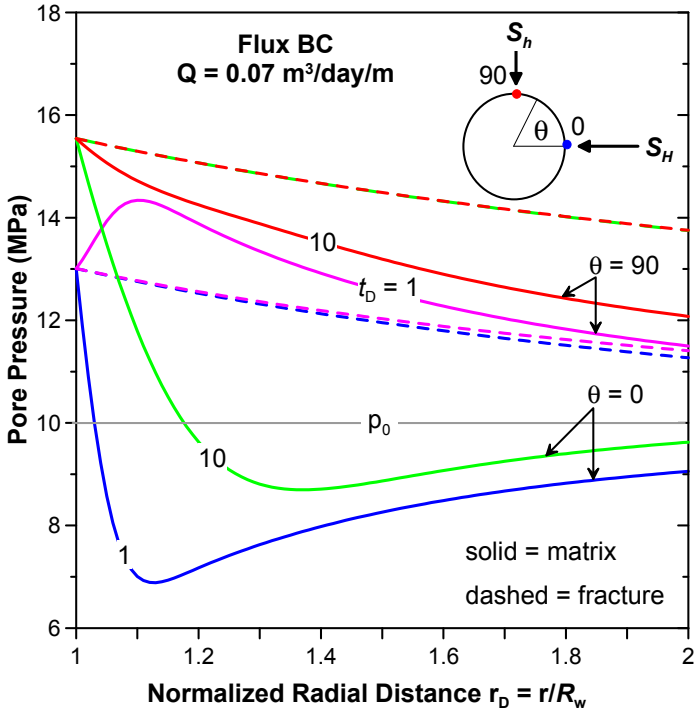

Fig. 2.7—Dual pore-pressure distributions at the wellbore after t_D = 1 (~ 3.5 minutes) and t_D = 10 (~ 35 minutes) for non-zero flux boundary conditions (Q = 0.07 m³/day/m).

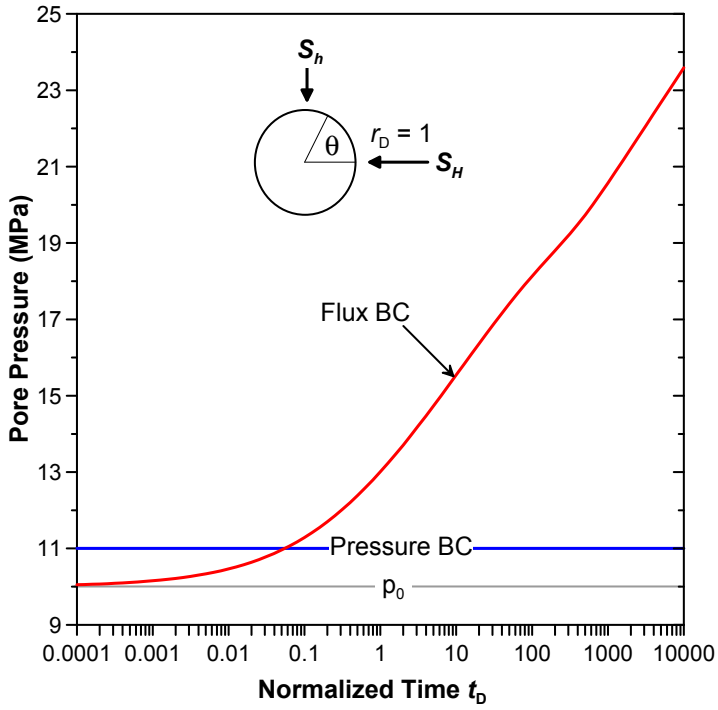

Fig. 2.8—History of pore pressure at the wellbore wall for non-zero flux (injection Q = 0.07 m³/day/m) versus pressure (permeable) boundary conditions.

The corresponding evolution of fluid pressure at the wellbore wall is plotted in Fig. 2.8. Full hydraulic communication requires that the fluid pressure be the same in both the matrix and the fracture network as well as around the wellbore wall. The pressure responses for flux boundary condition exhibits typical transient behavior as shown in the early work of Warren and Root (1963) and others.

For impermeable boundary condition, there is no flow across the wellbore wall. However, there is still pressure buildup or reduction in the matrix in the near wellbore region due to the poroelastic effect of unloading non-hydrostatic in-situ stress as shown in Fig. 2.9. Again, the perturbed pore pressure in the fracture network quickly dissipates and converges to the original formation pore pressure as displayed in Fig. 2.10. Similar behaviors are observed in Figs. 2.11 and 2.12 for the evolution of pore-pressure distribution for the case of impermeable-matrix and permeable-fracture boundary condition. Instead of converging to the original formation pore pressure, the dual responses approach the applied wellbore pressure due to full hydraulic communication between the wellbore and the fracture network as well as interporosity flow exchange.

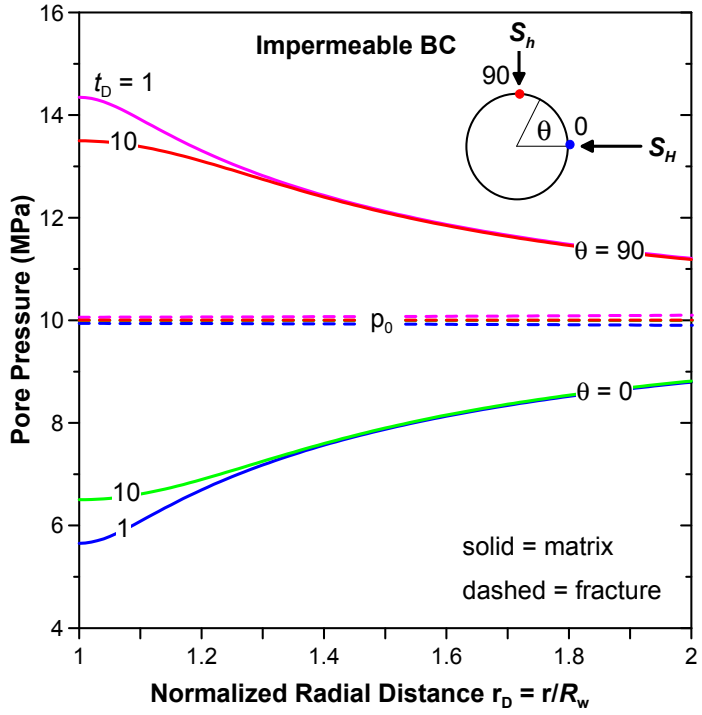

Fig. 2.9—Dual pore-pressure distributions around the wellbore after t_D = 1 (~ 3.5 minutes) and t_D = 10 (~ 35 minutes) for no-flow fluid boundary conditions.

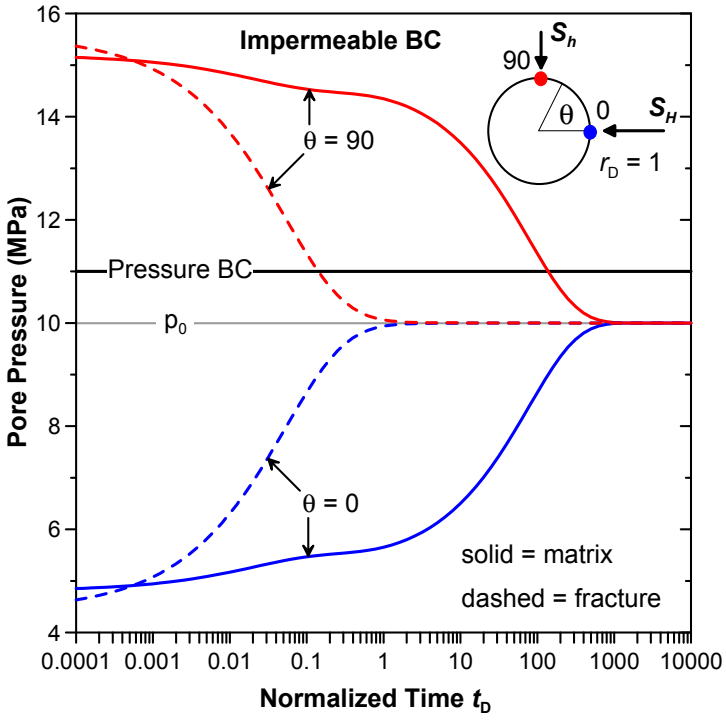

Fig. 2.10—History of pore pressure at the wellbore wall for no-flow fluid boundary condition.

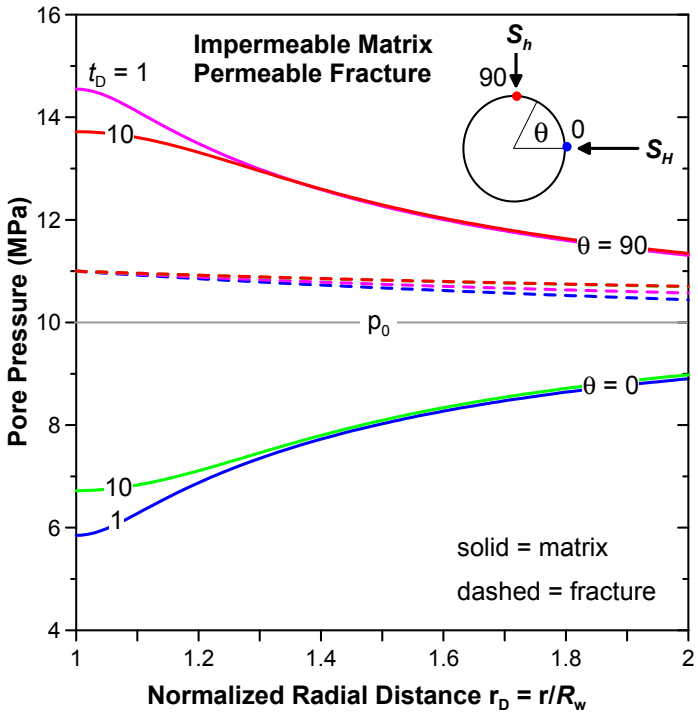

Fig. 2.11—Dual pore-pressure distributions around the wellbore after t_D = 1 (~ 3.5 minutes) and t_D = 10 (~35 minutes) for impermeable matrix and permeable fracture's fluid boundary conditions.

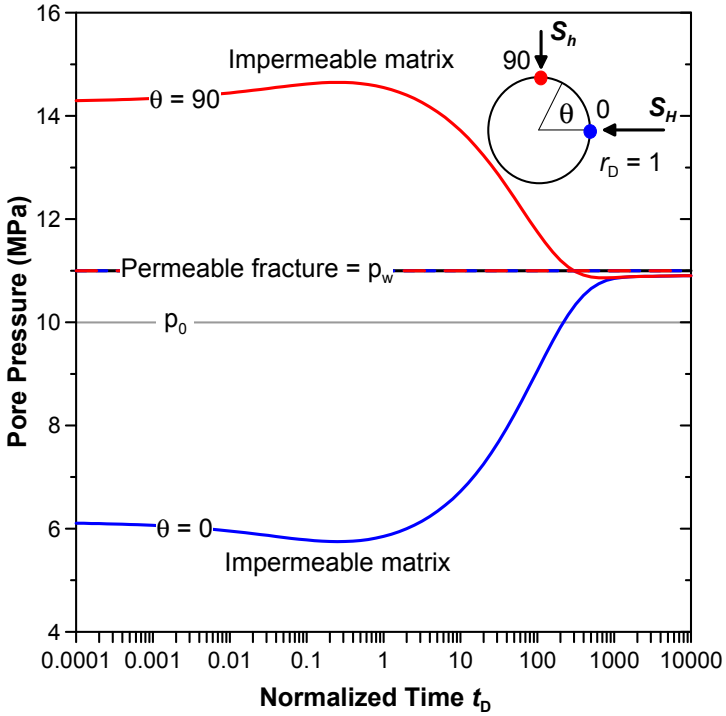

Fig. 2.12—History of pore pressure at the wellbore wall for impermeable-matrix and permeable-fracture fluid boundary condition.

Next, the evolution of effective tangential stress – total normal stress less pore pressure – at the borehole wall is demonstrated in **Figs. 2.13 to 2.15**. For pressure and flux boundary condition, both the matrix and fracture's pore pressures equal to the imposed wellbore pressure leading to the same effective stress in the matrix and fracture regions as shown in Fig. 2.13. Although the pore pressure stays constant for a pressure boundary condition, the effective tangential stress at the wall changes with time and locations. As time progresses, the effective stress increases considerably along the minimum horizontal stress direction ($\theta = 90$) which promotes compressive failure in this location but decreases along the maximum horizontal stress direction ($\theta = 0$) which makes the region more susceptible to tensile failure. On the other hand, the results for constant injection rate show reduction in effective stress all around the wellbore because the magnitude of the transient increase in total stress along $\theta = 90$ can not overcome the increase in wellbore pressure to maintain the injection rate. Along $\theta = 0$, the time-dependent reduction in effective tangential stress is more pronounced and the stress becomes tensile after $t_D = 100$ (~ 5 hours 50 mins). The result is practically helpful since it predicts the time to fracture initiation due to constant fluid injection.

For no-flow (Fig. 2.14) or impermeable-matrix and permeable-fracture boundary condition (Fig. 2.15), the pore pressure at the wall evolves differently in the porous matrix region and fracture network. Therefore, dual effective stresses, $\sigma_{\theta\theta} - p^{I}$ and $\sigma_{\theta\theta} - p^{II}$, are shown as bounds for the actual effective developed in fractured formation. It observed that the transient effective stress level is more critical in the fracture network than in the rock matrix region, i.e., higher in compression along $\theta = 90$ and closer to tension along $\theta = 0$.

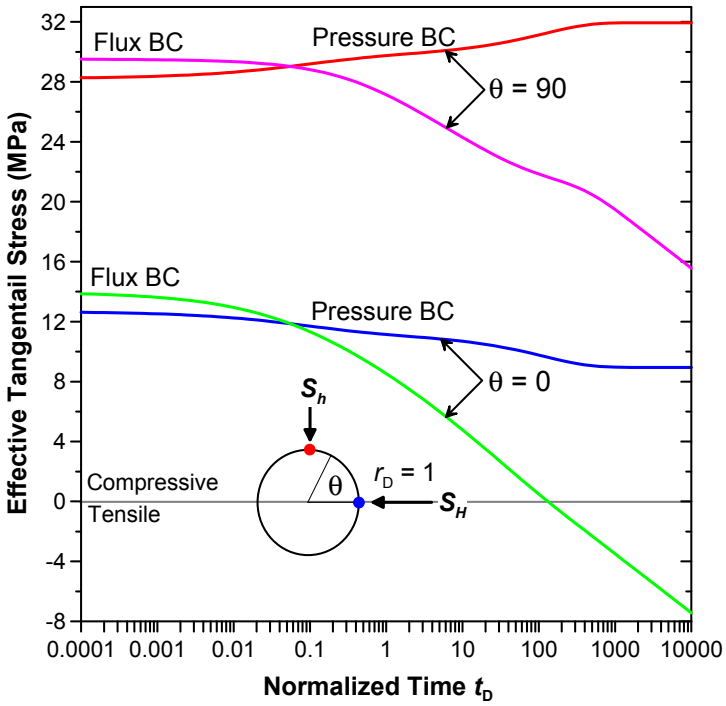

Fig. 2.13—History of effective tangential stress at the wellbore wall for flux boundary condition (injection Q = 0.07 m^3/day/m) and pressure boundary condition.

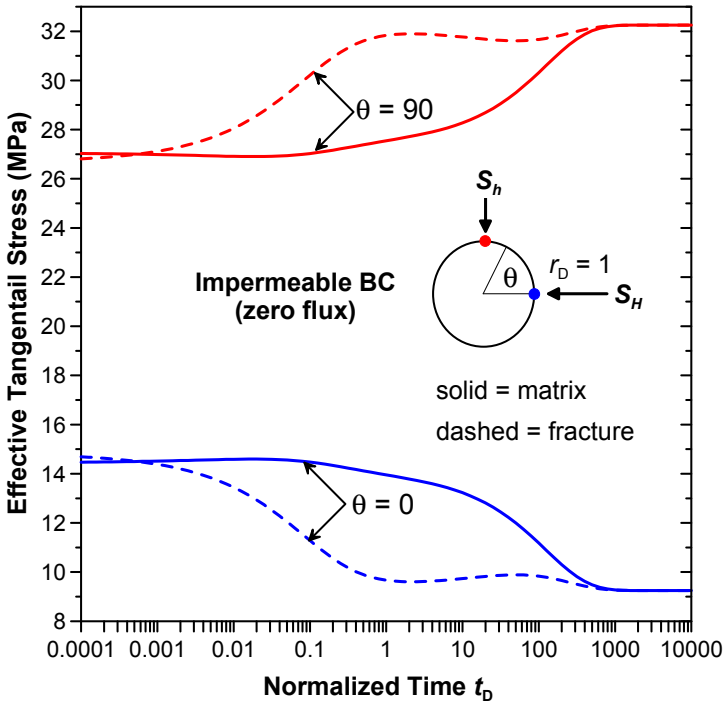

Fig. 2.14—History of effective tangential stress at the wellbore wall for impermeable (no flow) boundary condition.

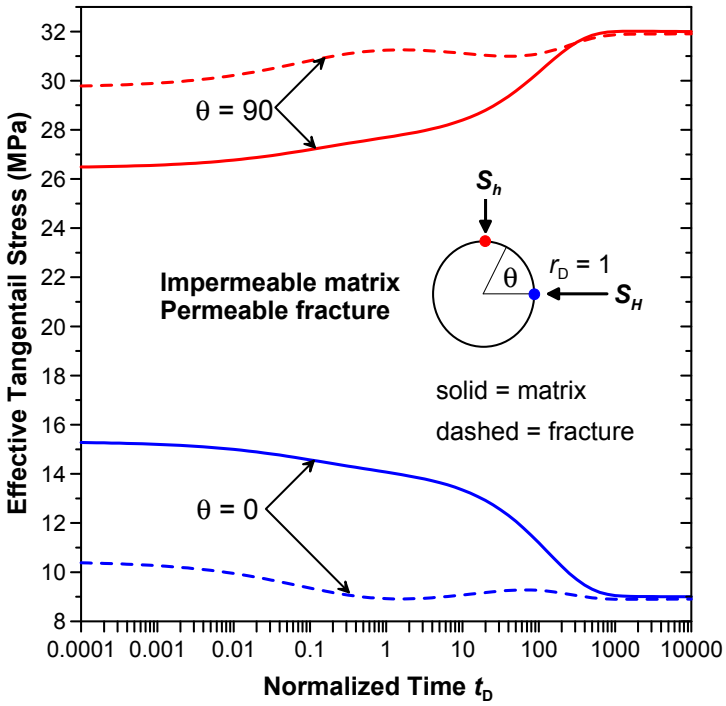

Fig. 2.15—History of effective tangential stress at the wellbore wall for impermeable-matrix and permeable-fracture boundary condition.

2.3.4.3 Comparison with Single-Poroelastic

Finally, it is also of interest to compare the dual-poroelastic response in conjunction with the single-poroelastic counterpart that model the formation as compact rock, neglecting the compressibility and fluid flow in the fracture network. As shown in **Figs. 2.16 to 2.19**, the intact rock is modeled as single-poroelastic material while the fractured rock formation is modeled as dual-poroelastic material. The transient pore pressure distribution around wellbore are shown in Figs. 2.16 and 2.17. The result for single-poroelastic has been converted to the same time scale as the dual-poroelastic using the characteristic times of the two models. It is observed that the perturbed pore pressure in a fractured rock system at a specific time is less than that in a compact one due to the faster speed of fluid dissipation. On the other hand, due to the contribution of fracture compressibility, the fractured rock

exhibits higher effective stress concentration along the S_h direction and lower effective stress level along the S_H direction as displayed in Figs. 2.18 and 2.19 for effective tangential stress. The difference in effective stress between single- and dual-poroelastic modeling approaches will translate into significant implications on wellbore stability evaluation of the mud-weight window for field planning and operations as illustrated later in Chapter 5.

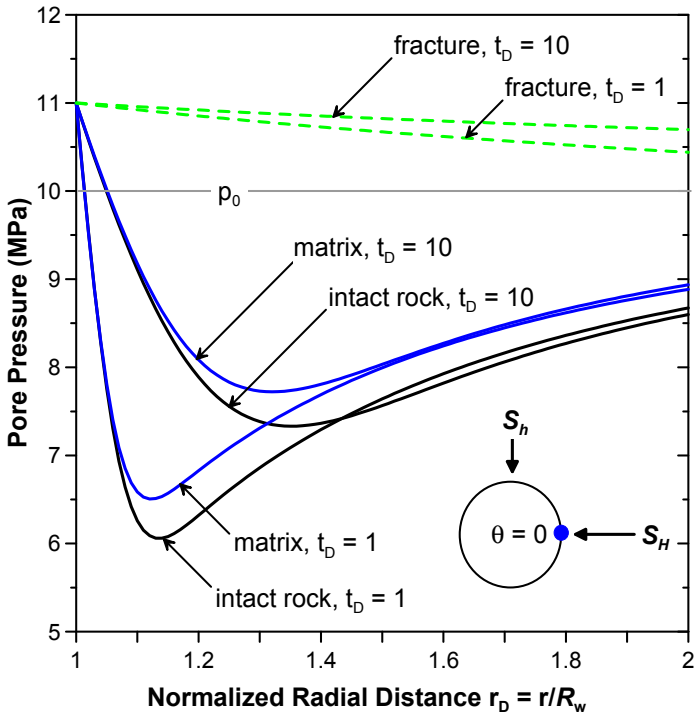

Fig. 2.16—Time-dependent pore-pressure distribution along S_H direction. The fluid boundary is constant pressure with permeable borehole wall.

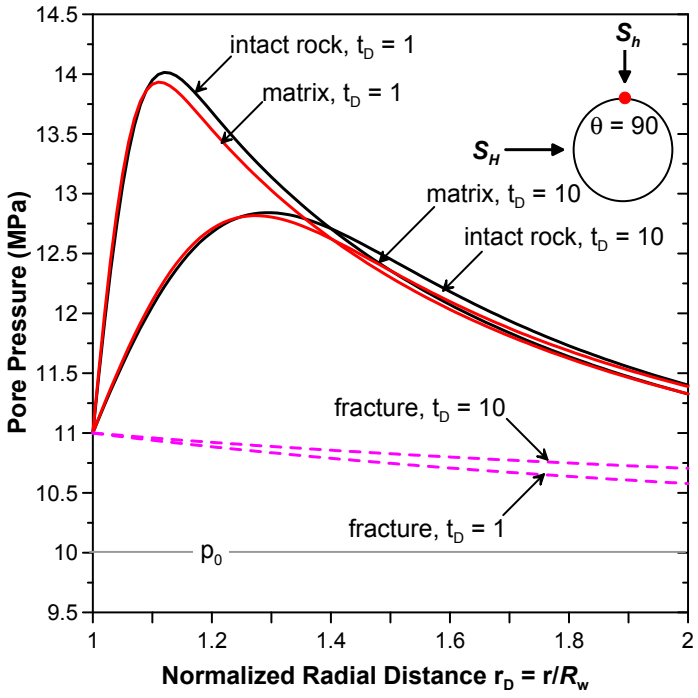

Fig. 2.17—Time-dependent pore-pressure distribution along S_h direction. The fluid boundary is constant pressure with permeable borehole wall.

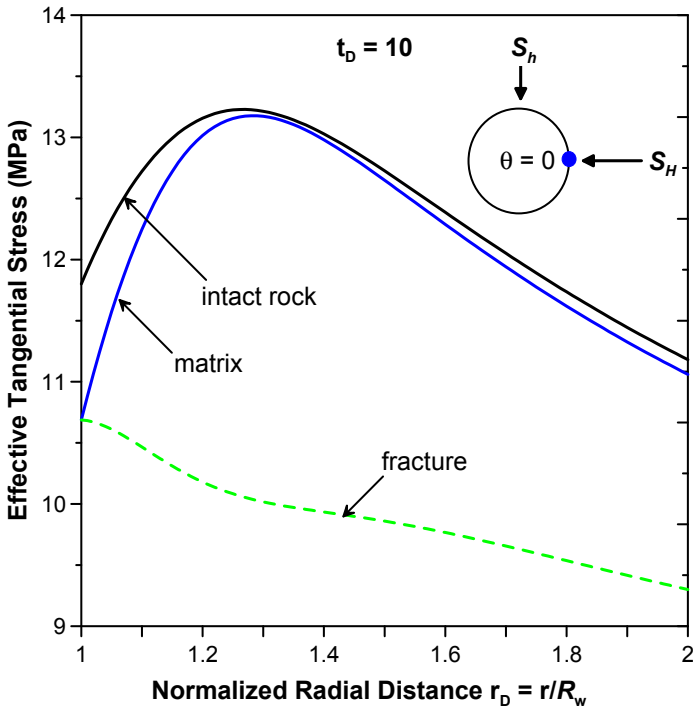

Fig. 2.18—Effective tangential stress distribution along S_H direction at t_D = 10 (~ 35 mins). The fluid boundary is constant pressure with permeable borehole wall.

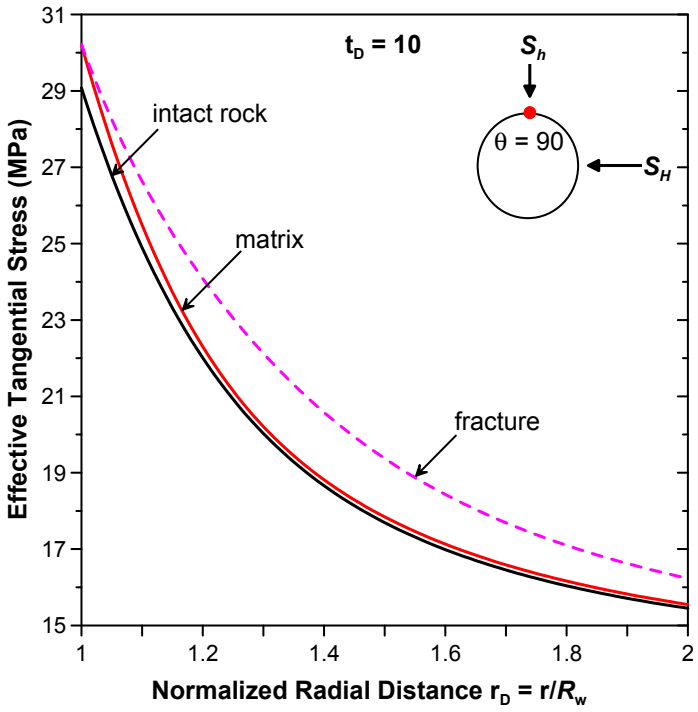

Fig. 2.19—Effective tangential stress distribution along S_h direction at t_D = 10 (~35 mins). The fluid boundary is constant pressure with permeable borehole wall.

2.4 Rectangular and Cylindrical Geometries

2.4.1 Rectangular Strip and Solid Cylinder[2]

2.4.1.1 Background

The poromechanics solutions for laboratory setups with initial and boundary conditions on prepared samples easily traverse the boundaries of various fields such as geomechanics and biomechanics. The two-dimensional Mandel-type problem geometry assumes a rectangular strip shape in Cartesian coordinate or cylindrical disk samples in polar coordinate. In geomechanics, such configurations are used in common uniaxial and triaxial testing of

[2] Part of this section was published in the *J. Appl. Mech.*, **77**(1): 011002-1-011002-18 (Nguyen and Abousleiman 2010)

porous rock specimens (Dickey et al. 1968; Abousleiman and Cui 1998) or in simulating sudden stress relief of a long core removed from subsurface wellbore (Wang 2000). Meanwhile, this problem geometry is equivalent to the popular unconfined compression test in the biomechanics society, in particular, for testing cartilages and bones (Buschmann et al. 1998). Hence, distributions and evolutions of stress, displacement, and pore pressure in the samples under these setups and conditions are of important values and have been investigated by many researchers.

Mandel (1953) presented the first solutions for the isotropic consolidation of an unconfined soil layer using Biot's theory of poroelasticity (1941), demonstrating the non-monotonic pore-water pressure response, known as the "Mandel–Cryer effect," which is a distinctive feature of the coupled consolidation theory. Kenyon (1979) provided solutions for transversely isotropic material using Terzaghi's uncoupled consolidation theory (1943), which is a limiting case of Biot's poroelasticity. Later, Abousleiman et al. (1996) extended Mandel's original solution to the full transversely isotropic case and provided the explicit expressions for stress, pore pressure, displacements, and fluid flux. Recently, Hoang and Abousleiman (2009) provided the poroviscoelastic solution accounting for the intrinsic nature of the orthotropic viscoelastic matrix structures of many porous materials such as articular cartilage. Also in biomechanics, Kameo et al. (2008) published isotropic solutions for transient response of fluid pressure under uniaxial cyclic loading. These poromechanical solutions to the original Mandel's problem have been used as a benchmark for testing the validity of numerical codes of poroelasticity (Christian and Boehmer 1970; Cui et al. 1996; Yin et al. 2006; Phillips and Wheeler 2007). In addition, the rectangular

strip geometry also matches one of the testing configurations of stiff clay samples in geomechanics (Dickey et al. 1968) or articular cartilages in biomechanics (Odgaard and Linde 1991; Wang et al. 2003).

On the other hand, testing of solid cylindrical samples subjected to load perturbation can be considered an axisymmetric Mandel type problem due to its radial symmetry and plane-strain/generalized plane-strain nature (Saada 1974). Armstrong et al. (1984), following Mandel's approach, derived the isotropic poroelastic solution simulating the unconfined compression of articular cartilage disk and showed results for step and ramp loadings. Independently in the field of geomechanics, Abousleiman and Cui (1998) published a more general cylinder solution accounting for the transversely isotropic nature of rock samples and arbitrary time-dependent loading condition. The solution was later extended to incorporate the effect of lateral confining stress and results for uniaxial and triaxial testing under ramp loading condition were demonstrated (Cui and Abousleiman 2001). Subsequently, Cowin and Mehrabadi (2007) also gave the same unconfined anisotropic poroelastic solution with results for bone testing.

This section shows the derivations of the analytical solutions for Mandel-type problems in dual-poroelastic media. By noting the parallelism between plane strain and radial symmetry, the solutions for strip and cylindrical geometries are analogously derived and expressed in closed form in the Laplace-transform domain as well as in the time-domain. The developed solutions describe the consolidation of a rectangular strip or circular disk sample under confined or unconfined compression testing setups.

2.4.1.2 Rectangular Strip (The Mandel's Problem)

2.4.1.2.1 Problem Descriptions

The original Mandel's problem involves an infinitely long rectangular specimen sandwiched between the top and bottom by two frictionless plates as illustrated in **Fig. 2.20**. It is assumed that the *y*-axis is infinitely long and the response along that direction is invariant. This geometry is represented by a perpendicular cross section (*x*-*z*) in a state of plane strain, i.e., the displacement and fluxes vanish in the *y* direction perpendicular to the paper $\varepsilon_{yy} = 0$. At time $t = 0^+$, a constant compressive force $2F$ (per unit length) is applied to the rigid plates at the top and bottom, respectively. The left and right edges of the plates are stress-free and drained. The geometry and boundary conditions imply that every horizontal plane is a plane of folding symmetry. That is, horizontal planes remain horizontal ($\varepsilon_{zz} = \varepsilon_{zz}(t)$), fluid flow is parallel to the impermeable plates ($q_z = 0$), and there are no shear stresses on the plane ($\sigma_{xz} = 0$). In addition, the responses of all quantities are symmetric about the centerline *z*-axis ($f(x) = f(-x)$) (Mandel 1953; Abousleiman et al. 1996).

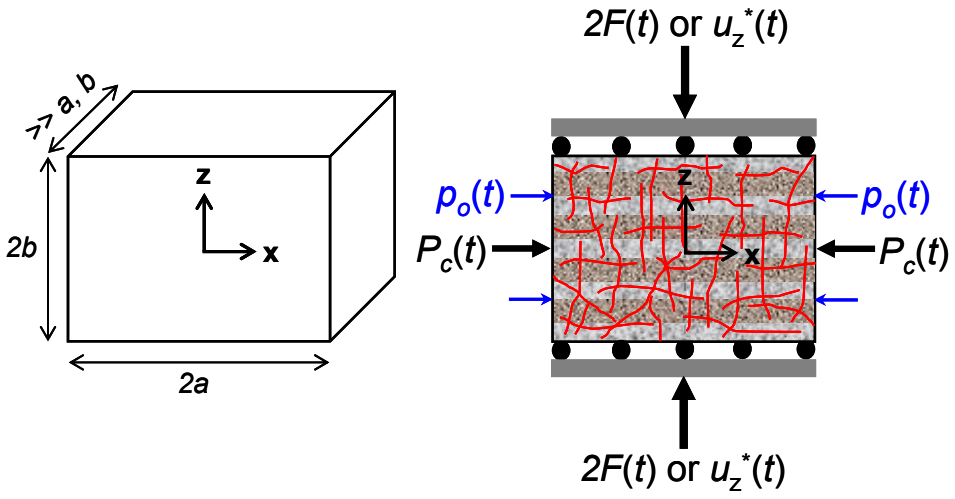

Fig. 2.20—The Mandel's problem geometry and loading setup for a rectangular strip of transversely isotropic dual-poroelastic (fractured) material.

This work extends the original Mandel's problem solution to transversely isotropic fractured rock as illustrated in Fig. 2.20. The new solution account for external boundary conditions that are generalized to time-dependent loading applications, i.e., $F = F(t)$, $P_c = P_c(t)$, and $p_o = p_o(t)$ where P_c and p_o are the confining stress and fluid pressure on the outer boundary ($x = a$). Additionally, the axial loading can represent either applied vertical strain/displacement, $\varepsilon_{zz}^{*}(t)$ or $u_z^{*}(t)$, or an applied vertical load, $2F(t)$. Mathematically, the generalized boundary conditions are expressed as

$$x = \pm a: \qquad \sigma_{xx} = P_c(t); \quad p^{\mathrm{I}} = p^{\mathrm{II}} = p_o(t); \quad \sigma_{xz} = 0, \tag{2.64}$$

$$z = 0, 2b: \qquad \sigma_{xz} = q_z^{\mathrm{I}} = q_z^{\mathrm{II}} = 0; \quad u_z = u_z(t), \tag{2.65}$$

$$z = 2b: \qquad \int_{-a}^{a} \sigma_{zz} dx = 2F(t) \text{ load control,} \tag{2.66a}$$

$$z = 2b: \qquad \varepsilon_{zz} = \varepsilon_{zz}^{*}(t) = u_z^{*}(t)/2b \text{ stroke control,} \tag{2.66b}$$

With the above boundary conditions, the governing equations is reduced to one-dimensional and all variables are at most functions of x and t only. The plane-strain condition in the y direction and the stress equilibrium (Eq. 2.18) in the x direction require that $\varepsilon_{yy} = 0$ and $\sigma_{xx} = P_c(t)$. Using these conditions into the constitutive Eqs. 2.15 and 2.16, the fluid contents are rewritten in terms of stress and fluid pressure as

$$\zeta^{\mathrm{I}} = -a^{\mathrm{I}}(\sigma_{zz} + \overline{\varphi}^{\mathrm{I}} P_c - b_{11} p^{\mathrm{I}} - b_{12} p^{\mathrm{II}}), \tag{2.67}$$

$$\zeta^{\mathrm{II}} = -a^{\mathrm{II}}(\sigma_{zz} + \overline{\varphi}^{\mathrm{II}} P_c - b_{21} p^{\mathrm{I}} - b_{22} p^{\mathrm{II}}), \tag{2.68}$$

where the material coefficient $a^{(\mathrm{N})}$ and dimensionless parameters $\overline{\varphi}^{(\mathrm{N})}$ and b_{ij} are given as

$$a^{(\mathrm{N})} = \frac{\overline{\alpha}_3^{(\mathrm{N})}\overline{M}_{11} - \overline{\alpha}_1^{(\mathrm{N})}\overline{M}_{13}}{\overline{M}_{11}\overline{M}_{33} - \overline{M}_{13}^2}, \quad (2.69)$$

$$\overline{\varphi}^{(\mathrm{N})} = \frac{\overline{\alpha}_1^{(\mathrm{N})}\overline{M}_{33} - \overline{\alpha}_3^{(\mathrm{N})}\overline{M}_{13}}{\overline{\alpha}_3^{(\mathrm{N})}\overline{M}_{11} - \overline{\alpha}_1^{(\mathrm{N})}\overline{M}_{13}}, \quad (2.70)$$

$$b_{11} = \overline{\alpha}_3^{\mathrm{I}} + \overline{\alpha}_1^{\mathrm{I}}\overline{\varphi}^{\mathrm{I}} + \frac{1}{\overline{M}^{\mathrm{I}} a^{\mathrm{I}}}; \qquad b_{12} = \overline{\alpha}_3^{\mathrm{II}} + \overline{\alpha}_1^{\mathrm{II}}\overline{\varphi}^{\mathrm{I}} + \frac{1}{\overline{M}^{\mathrm{I,II}} a^{\mathrm{I}}}, \quad (2.71a)$$

$$b_{21} = \overline{\alpha}_3^{\mathrm{I}} + \overline{\alpha}_1^{\mathrm{I}}\overline{\varphi}^{\mathrm{II}} + \frac{1}{\overline{M}^{\mathrm{I,II}} a^{\mathrm{II}}}; \qquad b_{22} = \overline{\alpha}_3^{\mathrm{II}} + \overline{\alpha}_1^{\mathrm{II}}\overline{\varphi}^{\mathrm{II}} + \frac{1}{\overline{M}^{\mathrm{II}} a^{\mathrm{II}}}, \quad (2.71b)$$

Similarly, the compatibility Eq. 2.19 simplifies to

$$\frac{\partial^2}{\partial x^2}\left[\sigma_{zz} - \left(\overline{\alpha}_3^{\mathrm{I}} - \overline{\alpha}_1^{\mathrm{I}}\frac{\overline{M}_{13}}{\overline{M}_{11}}\right)p^{\mathrm{I}} - \left(\overline{\alpha}_3^{\mathrm{I}} - \overline{\alpha}_1^{\mathrm{I}}\frac{\overline{M}_{13}}{\overline{M}_{11}}\right)p^{\mathrm{II}}\right] = 0, \quad (2.72)$$

Integrating and accounting for the symmetry about the centerline ($x = 0$) yields

$$\sigma_{zz} = \overline{\gamma}^{\mathrm{I}} p^{\mathrm{I}} + \overline{\gamma}^{\mathrm{II}} p^{\mathrm{II}} + C_1(t), \quad (2.73)$$

in which the dimensionless coefficient $\overline{\gamma}^{(\mathrm{N})} = \overline{\alpha}_3^{(\mathrm{N})} - \overline{\alpha}_1^{(\mathrm{N})}\overline{M}_{13}/\overline{M}_{11}$ and $C_1(t)$ is an integration constant depending only on time. Eliminating the stress components in the fluid contents, Eqs. 2.67 and 2.68, and substituting the resulting expressions into the fluid mass balance, Eqs. 2.13a and 2.13b, lead to the simplified diffusion equations in terms of the dual fluid pressure fields and applied stress as.

$$\left(\mathbf{A}\frac{\partial}{\partial t} + \mathbf{\Gamma} - \mathbf{D}\frac{\partial^2}{\partial x^2}\right)\begin{Bmatrix} p^{\mathrm{I}} \\ p^{\mathrm{II}} \end{Bmatrix} = \begin{Bmatrix} a^{\mathrm{I}}\overline{\varphi}^{\mathrm{I}} \\ a^{\mathrm{II}}\overline{\varphi}^{\mathrm{II}} \end{Bmatrix}\frac{\partial P_c(t)}{\partial t} + \begin{Bmatrix} a^{\mathrm{I}} \\ a^{\mathrm{II}} \end{Bmatrix}\frac{\partial C_1(t)}{\partial t}, \quad (2.74)$$

where the coefficient matrices **A**, **D** and **Γ** are defined in Eqs. 2.40 and 2.41. In compact matrix form, Eq. 2.74 is expressed as

$$\left(\boldsymbol{\omega}\frac{\partial}{\partial t_D}+\boldsymbol{\Gamma}_{\mathbf{D}}-\overline{\boldsymbol{\kappa}}_{\mathbf{D}}\frac{\partial^2}{\partial x_D^2}\right)\begin{Bmatrix}p^{\mathrm{I}}\\ p^{\mathrm{II}}\end{Bmatrix}=\begin{Bmatrix}c_f^{\mathrm{I}}\overline{\varphi}^{\mathrm{I}}\\ c_f^{\mathrm{II}}\overline{\varphi}^{\mathrm{II}}\end{Bmatrix}\frac{\partial P_c}{\partial t_D}+\begin{Bmatrix}c_f^{\mathrm{I}}\\ c_f^{\mathrm{II}}\end{Bmatrix}\frac{\partial C_1}{\partial t_D}, \quad (2.75)$$

in which the dimensionless coefficient matrixes $\boldsymbol{\omega}$, $\boldsymbol{\lambda}_{\mathbf{D}}$, $\overline{\boldsymbol{\kappa}}_{\mathbf{D}}$ and the parameter $c_f^{(\mathrm{N})}$ are given in Eqs. 2.46 and 2.47; x_D and t_D are the dimensionless distance and time. The system of Eqs. 2.73 and 2.75 together with relevant boundary conditions are sufficient for the general solution of the three variables $\{\sigma_{zz}, p^{\mathrm{I}}, p^{\mathrm{II}}\}$.

2.4.1.2.2 Analytical Solutions

Analogous to the inclined wellbore problem, the general solution to this coupled ordinary differential equation system is straightforward and admits the following form in Laplace transform domain

$$\widetilde{p}^{\mathrm{I}}=\widetilde{P}_c f^{\mathrm{I}}+\widetilde{C}_1 g^{\mathrm{I}}+C_2^{\mathrm{I}}\cosh(\xi^{\mathrm{I}}x_D)+C_2^{\mathrm{II}}\cosh(\xi^{\mathrm{II}}x_D), \quad (2.76)$$

$$\widetilde{p}^{\mathrm{II}}=\widetilde{P}_c f^{\mathrm{II}}+\widetilde{C}_1 g^{\mathrm{II}}+m^{\mathrm{I}}C_2^{\mathrm{I}}\cosh(\xi^{\mathrm{I}}x_D)+m^{\mathrm{II}}C_2^{\mathrm{II}}\cosh(\xi^{\mathrm{II}}x_D), \quad (2.77)$$

where $C_2^{\mathrm{I}}=C_2^{\mathrm{I}}(s)$ and $C_2^{\mathrm{II}}=C_2^{\mathrm{II}}(s)$ are arbitrary coefficients to be determined from boundary conditions; $\xi^{(\mathrm{N})}$, $g^{(\mathrm{N})}$, and $m^{(\mathrm{N})}$ are coefficients as given in Eqs. 2.52 to 2.54; $f^{(\mathrm{N})}$ is defined as

$$\begin{Bmatrix}f^{\mathrm{I}}\\ f^{\mathrm{II}}\end{Bmatrix}=\left(s\,\boldsymbol{\omega}+\boldsymbol{\Gamma}_{\mathbf{D}}\right)^{-1}\begin{Bmatrix}c_f^{\mathrm{I}}\overline{\varphi}^{\mathrm{I}}\\ c_f^{\mathrm{II}}\overline{\varphi}^{\mathrm{II}}\end{Bmatrix}s, \quad (2.78)$$

Next, the non-zero stress and displacement components are obtained by substituting the pressure expressions into Eqs. 2.73 and 2.15 to get

$$\widetilde{\sigma}_{zz}=A_0\widetilde{P}_c+A_1\widetilde{C}_1+A_2^{\mathrm{I}}C_2^{\mathrm{I}}\cosh(\xi^{\mathrm{I}}x_D)+A_2^{\mathrm{II}}C_2^{\mathrm{II}}\cosh(\xi^{\mathrm{II}}x_D), \quad (2.79)$$

$$\frac{\widetilde{u}_x}{a} = -(f\,\widetilde{P}_c + g\,\widetilde{C}_1)\,x_D - h^{\mathrm{I}} C_2^{\mathrm{I}} \frac{\sinh(\xi^{\mathrm{I}} x_D)}{\xi^{\mathrm{I}}} - h^{\mathrm{II}} C_2^{\mathrm{II}} \frac{\sinh(\xi^{\mathrm{II}} x_D)}{\xi^{\mathrm{II}}}, \quad (2.80)$$

$$\frac{\widetilde{u}_z}{b} = \frac{\overline{M}_{11}\widetilde{C}_1 - \overline{M}_{13}\widetilde{P}_c}{\overline{M}_{11}\overline{M}_{33} - \overline{M}_{13}^2}\, z_D, \quad (2.81)$$

where the lumped coefficients A_0, A_1, $A_2^{(\mathrm{N})}$, $h^{(\mathrm{N})}$, f, and g are given as

$$A_0 = \bar{\gamma}^{\mathrm{I}} f^{\mathrm{I}} + \bar{\gamma}^{\mathrm{II}} f^{\mathrm{II}}, \quad (2.82a)$$

$$A_1 = \bar{\gamma}^{\mathrm{I}} g^{\mathrm{I}} + \bar{\gamma}^{\mathrm{II}} g^{\mathrm{II}} + 1, \quad (2.82b)$$

$$A_2^{(\mathrm{N})} = \bar{\gamma}^{\mathrm{I}} + \bar{\gamma}^{\mathrm{II}}\, m^{(\mathrm{N})}, \quad (2.82c)$$

$$f = \frac{\overline{\alpha}_1^{\mathrm{I}} f^{\mathrm{I}} + \overline{\alpha}_1^{\mathrm{II}} f^{\mathrm{II}}}{\overline{M}_{11}} - \frac{\overline{M}_{33}}{\overline{M}_{11}\overline{M}_{33} - \overline{M}_{13}^2}, \quad (2.83)$$

$$g = \frac{\overline{\alpha}_1^{\mathrm{I}} g^{\mathrm{I}} + \overline{\alpha}_1^{\mathrm{II}} g^{\mathrm{II}}}{\overline{M}_{11}} + \frac{\overline{M}_{13}}{\overline{M}_{11}\overline{M}_{33} - \overline{M}_{13}^2}, \quad (2.84)$$

$$h^{(\mathrm{N})} = (\overline{\alpha}_1^{\mathrm{I}} + \overline{\alpha}_1^{\mathrm{II}} m^{(\mathrm{N})}) / \overline{M}_{11}, \quad (2.85)$$

The remaining three unknowns $\widetilde{C}_1(s)$, $C_2^{\mathrm{I}}(s)$ and $C_2^{\mathrm{II}}(s)$ are determined from the fluid pressure boundary conditions for p^{I} and p^{II} at the edges x_D = +/-1 and the vertical loading condition at the top z_D = 1. Detail derivations of this solution for load-control and displacement-control vertical loading are presented in Appendix B.

It is obvious that the solutions developed in here have the same functional forms as their single-poroelastic counterparts. The differences arise in the additional set of similar terms accounting for the secondary porosity coupled contributions. Requiring the secondary porosity porous medium to shrink to zero, all material parameters associated with the secondary porosity porous medium vanish and the current solution naturally

simplifies to single-porosity solution as demonstrated by Nguyen and Abousleiman (2010a) for isotropic case.

The newly developed dual-poroelastic solution in Laplace transform domain is too complicated to be inverted analytically back into the time domain. However, the time domain solution can be efficiently computed using numerical inversion methods such as the Stehfest's algorithm (1970). Though robust, the numerical inversion schemes may diverge and fall short in modeling certain loading conditions such as cyclic or piecewise loading function (Chen et al. 1994). As a result, it is of benefit to obtain a true time-domain analytical solution for using where the numerical inversion of Laplace transform fails. Derivation of the general time-domain solution in terms of infinite series was published by Nguyen and Abousleiman (2010a) in which explicit expressions for three unconfined uniaxial loading cases such as step loading, cyclic loading and linear-ramp loading were summarized. So far, the analysis applies only to strip problem in Cartesian coordinate. It will be shown in the next section that the extension to cylindrically axisymmetric problem is analogously straightforward.

2.4.1.3 Solid Cylinder (The Axisymmetric Mandel-type Problem)

2.4.1.3.1 Problem Descriptions

In this section, the compaction of a saturated solid cylinder sandwiched between a top and bottom impermeable, rigid, and frictionless plates as illustrated in **Fig. 2.21** is investigated. The cross section of the cylinder is circular. The axial loading is represented either by an applied axial displacement/strain, $\varepsilon_{zz}^{*}(t)$ or $u_z^{*}(t)$, or an applied vertical load, $F(t)$. Additionally, a confining stress $P_c(t)$ as well as a fluid pressure $p_o(t)$ can be applied on the

lateral surface. In common laboratory setting, the confining stress and fluid pressure at the outer boundary ($r = R$) are often the same, i.e., $P_c(t) = p_o(t)$.

Mathematically, the boundary conditions are expressed in cylindrical coordinate as

$$r = R: \quad \sigma_{rr} = P_c(t); \quad p^{\mathrm{I}} = p^{\mathrm{II}} = p_o(t); \quad \sigma_{r\theta} = \sigma_{rz} = 0, \qquad (2.86)$$

$$z = 0, 2h: \quad \sigma_{rz} = \sigma_{\theta z} = q_z^{\mathrm{I}} = q_z^{\mathrm{II}} = 0; \quad u_z = u_z(t), \qquad (2.87)$$

$$z = 2h: \quad \int_0^R r\sigma_{zz} dr = \frac{F(t)}{2\pi} \text{ load control}, \qquad (2.88a)$$

$$z = 2h: \quad \varepsilon_{zz} = \varepsilon_{zz}^*(t) = u_z^*(t)/2h \text{ stroke control}, \qquad (2.88b)$$

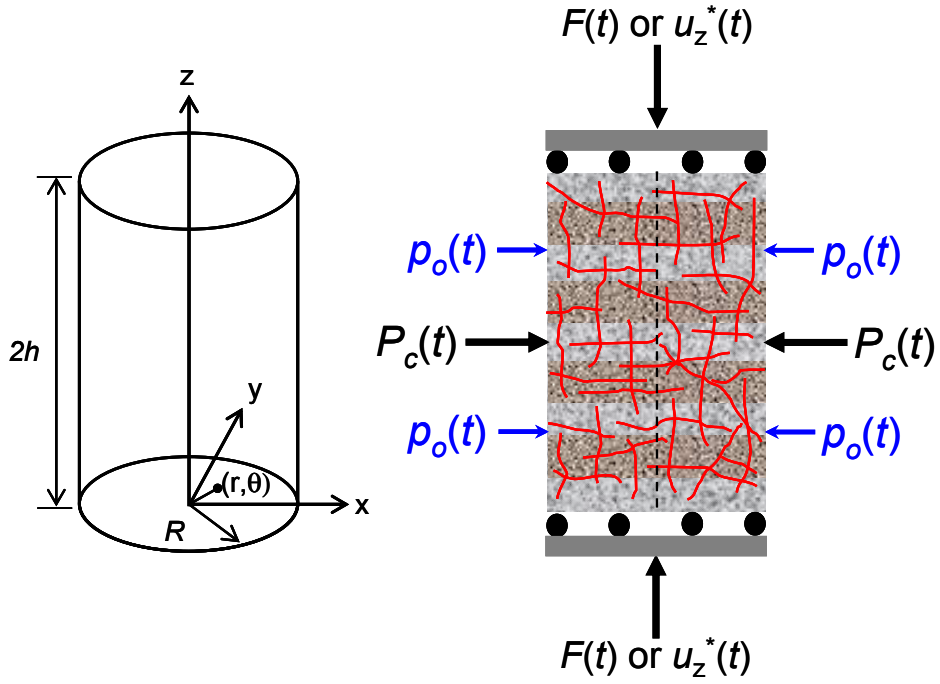

Fig. 2.21—The axisymmetric Mandel-type problem geometry and loading setup for a solid cylinder of transversely isotropic dual-poroelastic (fractured) material.

With the aforementioned setup, the problem is obviously axisymmetric providing that at any time the shear stresses and strains $\sigma_{r\theta} = \sigma_{\theta z} = 0, \varepsilon_{r\theta} = \varepsilon_{\theta z} = 0$ and all other

variables are independent of θ. The geometry and boundary conditions imply that every horizontal cross section is a plane of folding symmetry. That is, horizontal planes remain horizontal ($\varepsilon_{zz} = \varepsilon_{zz}(t)$), fluid flow is in the radial direction only ($q_z^{\mathrm{I}} = q_z^{\mathrm{II}} = 0$) and there are no shear stress on the plane ($\sigma_{rz} = 0$). Under such conditions, a generalized plane strain condition naturally manifests in any cross-sectional plane (Saada 1974). Consequently, the governing equations are reduced to one-dimensional and all variables are at most functions of r and t only. Specifically, the fluid contents are expressed in terms of stress and fluid pressure as

$$\zeta^{\mathrm{I}} = -a^{\mathrm{I}}(\sigma_{rr} + \sigma_{\theta\theta} + \overline{\varphi}^{\mathrm{I}} S_{zz} - b_{11} p^{\mathrm{I}} - b_{12} p^{\mathrm{II}}), \quad (2.89)$$

$$\zeta^{\mathrm{II}} = -a^{\mathrm{II}}(\sigma_{rr} + \sigma_{\theta\theta} + \overline{\varphi}^{\mathrm{II}} S_{zz} - b_{21} p^{\mathrm{I}} - b_{22} p^{\mathrm{II}}), \quad (2.90)$$

where $S_{zz}(t) = \overline{M}_{33}\varepsilon_{zz}(t)$; $a^{(\mathrm{N})}$, $\overline{\varphi}^{(\mathrm{N})}$ and b_{ij} are the same as defined in the inclined wellbore solution, Eqs. 2.33 to 2.35b. Similarly, the compatibility Eq. 2.20 simplifies to

$$\left(\frac{\partial^2}{\partial r^2} + \frac{1}{r}\frac{\partial}{\partial r}\right)\left[\sigma_{rr} + \sigma_{\theta\theta} - \overline{\alpha}_1^{\mathrm{I}}\left(1 - \frac{\overline{M}_{12}}{\overline{M}_{11}}\right)p^{\mathrm{I}} - \overline{\alpha}_1^{\mathrm{II}}\left(1 - \frac{\overline{M}_{12}}{\overline{M}_{11}}\right)p^{\mathrm{II}}\right] = 0, \quad (2.91)$$

Integrating twice and seeking for bounded expression yields

$$\sigma_{rr} + \sigma_{\theta\theta} = \overline{\gamma}^{\mathrm{I}} p^{\mathrm{I}} + \overline{\gamma}^{\mathrm{II}} p^{\mathrm{II}} + C_1(t), \quad (2.92)$$

in which the dimensionless coefficient $\overline{\gamma}^{(\mathrm{N})} = \overline{\alpha}_1^{(\mathrm{N})}(1 - \overline{M}_{12}/\overline{M}_{11})$ and $C_1(t)$ is an integration constant depending only on time. Eq. 2.91 is used to eliminate the in-plane stress components in the fluid contents, Eqs. 2.89 and 2.90. The resulting expressions are substituted into the fluid continuity Eqs. 2.13a and 2.13b to get the diffusion equations as

$$\left(\mathbf{A}\frac{\partial}{\partial t}+\mathbf{\Gamma}-\mathbf{D}\nabla_r^2\right)\begin{Bmatrix}p^{\mathrm{I}}\\p^{\mathrm{II}}\end{Bmatrix}=\begin{Bmatrix}a^{\mathrm{I}}\overline{\varphi}^{\mathrm{I}}\\a^{\mathrm{I}}\overline{\varphi}^{\mathrm{II}}\end{Bmatrix}\frac{\partial S_{zz}}{\partial t}+\begin{Bmatrix}a^{\mathrm{I}}\\a^{\mathrm{II}}\end{Bmatrix}\frac{\partial C_1}{\partial t}, \quad \text{.....(2.93)}$$

where $\nabla_r^2=\partial^2/\partial r^2+(1/r)(\partial/\partial r)$; **A**, **D** and **Γ** are coefficient matrices as defined in Eqs. 2.40 and 2.41. In terms of dimensionless coefficients, Eq. 2.93 is expressed as

$$\left(\boldsymbol{\omega}\frac{\partial}{\partial t_D}+\mathbf{\Gamma_D}-\overline{\boldsymbol{\kappa}}_{\mathbf{D}}\nabla_{r_D}^2\right)\begin{Bmatrix}p^{\mathrm{I}}\\p^{\mathrm{II}}\end{Bmatrix}=\begin{Bmatrix}c_f^{\mathrm{I}}\overline{\varphi}^{\mathrm{I}}\\c_f^{\mathrm{II}}\overline{\varphi}^{\mathrm{II}}\end{Bmatrix}\frac{\partial S_{zz}}{\partial t_D}+\begin{Bmatrix}c_f^{\mathrm{I}}\\c_f^{\mathrm{II}}\end{Bmatrix}\frac{\partial C_1}{\partial t_D}, \quad \text{.....(2.94)}$$

where the coefficient matrices $\boldsymbol{\omega}$, $\mathbf{\Gamma_D}$, $\overline{\boldsymbol{\kappa}}_{\mathbf{D}}$ and $c_f^{(\mathrm{N})}$ were defined in Eqs. 2.46 and 2.47. The dimensionless time t_D and the differential operator $\nabla_{n,D}^2$ are

$$t_D=\frac{\overline{\kappa}^{\mathrm{I}}+\overline{\kappa}^{\mathrm{II}}}{(A_{11}+A_{22})R^2}t; \qquad \nabla_{r_D}^2=\frac{\partial^2}{\partial r_D^2}+\frac{1}{r_D}\frac{\partial}{\partial r_D}$$

The system of Eqs. 2.92 and 2.94 together with appropriate boundary conditions are sufficient for the general solution of the three variables $\{\sigma_{rr}+\sigma_{\theta\theta}, p^{\mathrm{I}}, p^{\mathrm{II}}\}$

2.4.1.3.2 Analytical Solutions

Analogous to the strip problem, the Laplace-transform general solutions for the dual pore-pressure fields are first derived as

$$\tilde{p}^{\mathrm{I}}=\tilde{S}_{zz}f^{\mathrm{I}}+\tilde{C}_1 g^{\mathrm{I}}+C_2^{\mathrm{I}}\mathrm{I}_0(\xi^{\mathrm{I}}r_D)+C_2^{\mathrm{II}}\mathrm{I}_0(\xi^{\mathrm{II}}r_D), \quad \text{.....(2.95)}$$

$$\tilde{p}^{\mathrm{II}}=\tilde{S}_{zz}f^{\mathrm{II}}+\tilde{C}_1 g^{\mathrm{II}}+m^{\mathrm{I}}C_2^{\mathrm{I}}\mathrm{I}_0(\xi^{\mathrm{I}}r_D)+m^{\mathrm{II}}C_2^{\mathrm{II}}\mathrm{I}_0(\xi^{\mathrm{II}}r_D), \quad \text{.....(2.96)}$$

in which I_0 is the modified Bessel function of the first kind of order zero and all other parameters are the same as previously defined in the strip loading solution. Eqs. 2.95 and 2.96 also imply that both pressure field must be finite at $r_D = 0$. Making use of the pressure

expressions, other solutions for stresses, displacements, and strains follow naturally from the constitutive equation as

$$\widetilde{\sigma}_{rr} = A_0 \widetilde{S}_{zz} + A_1 \widetilde{C}_1 + A_2^{\mathrm{I}} C_2^{\mathrm{I}} \frac{\mathrm{I}_1(\xi^{\mathrm{I}} r_D)}{\xi^{\mathrm{I}} r_D} + A_2^{\mathrm{II}} C_2^{\mathrm{II}} \frac{\mathrm{I}_1(\xi^{\mathrm{II}} r_D)}{\xi^{\mathrm{II}} r_D}, \quad (2.97)$$

$$\begin{aligned}\widetilde{\sigma}_{\theta\theta} = {} & A_0 \widetilde{S}_{zz} + A_1 \widetilde{C}_1 + A_2^{\mathrm{I}} C_2^{\mathrm{I}} \left[\mathrm{I}_0(\xi^{\mathrm{I}} r_D) - \frac{\mathrm{I}_1(\xi^{\mathrm{I}} r_D)}{\xi^{\mathrm{I}} r_D} \right] \\ & + A_2^{\mathrm{II}} C_2^{\mathrm{II}} \left[\mathrm{I}_0(\xi^{\mathrm{II}} r_D) - \frac{\mathrm{I}_1(\xi^{\mathrm{II}} r_D)}{\xi^{\mathrm{II}} r_D} \right],\end{aligned} \quad (2.98)$$

$$\widetilde{\sigma}_{zz} = B_0 \widetilde{S}_{zz} + B_1 \widetilde{C}_1 + B_2^{\mathrm{I}} C_2^{\mathrm{I}} \mathrm{I}_0(\xi^{\mathrm{I}} r_D) + B_2^{\mathrm{II}} C_2^{\mathrm{II}} \mathrm{I}_0(\xi^{\mathrm{II}} r_D), \quad (2.99)$$

$$\frac{\widetilde{u}_r}{R} = -(f \widetilde{S}_{zz} + g \widetilde{C}_1)\, r_D - h^{\mathrm{I}} C_2^{\mathrm{I}} \frac{\mathrm{I}_1(\xi^{\mathrm{I}} r_D)}{\xi^{\mathrm{I}}} - h^{\mathrm{II}} C_2^{\mathrm{II}} \frac{\mathrm{I}_1(\xi^{\mathrm{II}} r_D)}{\xi^{\mathrm{II}}}, \quad (2.100)$$

$$\begin{aligned}\widetilde{\varepsilon}_{rr} = {} & -(f \widetilde{S}_{zz} + g \widetilde{C}_1) \\ & - h^{\mathrm{I}} C_2^{\mathrm{I}} \left[\mathrm{I}_0(\xi^{\mathrm{I}} r_D) - \frac{\mathrm{I}_1(\xi^{\mathrm{I}} r_D)}{\xi^{\mathrm{I}} r_D} \right] - h^{\mathrm{II}} C_2^{\mathrm{II}} \left[\mathrm{I}_0(\xi^{\mathrm{II}} r_D) - \frac{\mathrm{I}_1(\xi^{\mathrm{II}} r_D)}{\xi^{\mathrm{II}} r_D} \right],\end{aligned} \quad (2.101)$$

$$\widetilde{\varepsilon}_{\theta\theta} = -(f \widetilde{S}_{zz} + g \widetilde{C}_1) - h^{\mathrm{I}} C_2^{\mathrm{I}} \frac{\mathrm{I}_1(\xi^{\mathrm{I}} r_D)}{\xi^{\mathrm{I}} r_D} - h^{\mathrm{II}} C_2^{\mathrm{II}} \frac{\mathrm{I}_1(\xi^{\mathrm{II}} r_D)}{\xi^{\mathrm{II}} r_D}, \quad (2.102)$$

where the lumped coefficients A_0, A_1, $A_2^{(\mathrm{N})}$, B_0, B_1, $B_2^{(\mathrm{N})}$, f, g, and $h^{(\mathrm{N})}$ are

$$2A_0 = \bar{\gamma}^{\mathrm{I}} f^{\mathrm{I}} + \bar{\gamma}^{\mathrm{II}} f^{\mathrm{II}}, \quad (2.103a)$$

$$2A_1 = \bar{\gamma}^{\mathrm{I}} g^{\mathrm{I}} + \bar{\gamma}^{\mathrm{II}} g^{\mathrm{II}} + 1, \quad (2.103b)$$

$$A_2^{(\mathrm{N})} = \bar{\gamma}^{\mathrm{I}} + \bar{\gamma}^{\mathrm{II}} m^{(\mathrm{N})}, \quad (2.103c)$$

$$B_0 = \left(\bar{\alpha}_3^{\mathrm{I}} - \bar{\alpha}_1^{\mathrm{I}} \frac{\overline{M}_{13}}{\overline{M}_{11}} \right) f^{\mathrm{I}} + \left(\bar{\alpha}_3^{\mathrm{II}} - \bar{\alpha}_1^{\mathrm{II}} \frac{\overline{M}_{13}}{\overline{M}_{11}} \right) f^{\mathrm{II}} + \frac{\overline{M}_{33}(\overline{M}_{11} + \overline{M}_{12}) - 2\overline{M}_{13}^2}{\overline{M}_{33}(\overline{M}_{11} + \overline{M}_{12})}, \quad (2.104a)$$

$$B_1 = \left(\overline{\alpha}_3^{\mathrm{I}} - \overline{\alpha}_1^{\mathrm{I}} \frac{\overline{M}_{13}}{\overline{M}_{11}} \right) g^{\mathrm{I}} + \left(\overline{\alpha}_3^{\mathrm{II}} - \overline{\alpha}_1^{\mathrm{II}} \frac{\overline{M}_{13}}{\overline{M}_{11}} \right) g^{\mathrm{II}} + \frac{\overline{M}_{13}}{\overline{M}_{11} + \overline{M}_{12}}, \quad \text{.....(2.104b)}$$

$$B_2^{(\mathrm{N})} = \overline{\alpha}_3^{\mathrm{I}} - \overline{\alpha}_1^{\mathrm{I}} \frac{\overline{M}_{13}}{\overline{M}_{11}} + \left(\overline{\alpha}_3^{\mathrm{II}} - \overline{\alpha}_1^{\mathrm{II}} \frac{\overline{M}_{13}}{\overline{M}_{11}} \right) m^{(\mathrm{N})}, \quad \text{.....(2.104c)}$$

$$2f = \frac{\overline{\alpha}_1^{\mathrm{I}} f^{\mathrm{I}} + \overline{\alpha}_1^{\mathrm{II}} f^{\mathrm{II}}}{\overline{M}_{11}} + \frac{2\overline{M}_{13}}{\overline{M}_{33}(\overline{M}_{11} + \overline{M}_{12})}, \quad \text{.....(2.105)}$$

$$2g = \frac{\overline{\alpha}_1^{\mathrm{I}} g^{\mathrm{I}} + \overline{\alpha}_1^{\mathrm{II}} g^{\mathrm{II}}}{\overline{M}_{11}} - \frac{1}{\overline{M}_{11} + \overline{M}_{12}}, \quad \text{.....(2.106)}$$

$$h^{(\mathrm{N})} = (\overline{\alpha}_1^{\mathrm{I}} + \overline{\alpha}_1^{\mathrm{II}} m^{(\mathrm{N})}) / \overline{M}_{11}, \quad \text{.....(2.107)}$$

In addition to $\widetilde{C}_1(s)$, $C_2^{\mathrm{I}}(s)$ and $C_2^{\mathrm{II}}(s)$, the fourth undetermined quantity in the solution is the axial strain $\widetilde{\varepsilon}_{zz}(s) = \widetilde{S}_{zz} / \overline{M}_{33}$. All of these coefficients and variables are determined using boundary conditions of vertical stress/displacement, radial stress, and dual pressure fields. Again, details derivations are presented in Appendix C. Again, the corresponding time-domain isotropic solution in terms of infinite series is also derived and presented in Nguyen and Abousleiman (2010a).

It is easy to verify that the above solution reduce to the single-poroelastic solid cylinder solution as presented by Cui and Abousleiman (2001) by allowing either the primary or the secondary porosity porous medium to vanish. It should be noted that Cui and Abousleiman expressed the solution using a different set of material coefficients such as undrained and drained Poisson ratios $\{\nu_u, \nu\}$ and storativity coefficient S. The reduction to single-poroelastic solution in the Laplace transform domain for isotropic case is shown in Nguyen and Abousleiman (2010a).

2.4.1.4 Results and Discussions

The results for rectangular strip and solid cylinder are presented and studied in a parallel manner to highlight the different responses of the two geometries. The fractured rock's material properties are the same as listed in section 2.3.4.1. Let $P_c(t) = p_o(t) = 0$, resulting in unconfined uniaxial loading condition which is the common laboratory testing setup for geo- and bio-material. The analysis is carried out for step loading, i.e., $F(t) = F \times H(t)$ or $\varepsilon_{zz}(t) = \varepsilon_{zz}^{*} \times H(t)$. Results for other loading applications are discussed later in Chapter 5. For laboratory testing, the strip's cross section is set as $2(a \times b) = 6 \times 10$ cm while the cylinder's diameter and height are also $2(R \times H) = 6 \times 10$ cm. The transverse anisotropy is modeled by different ratios of material coefficients between the isotropic plane and the transverse direction, i.e., $n_{\bar{E}} = \bar{E}_1 / \bar{E}_3$ and $n_{\bar{\nu}} = \bar{\nu}_{12} / \bar{\nu}_{13}$. Different ratios define different degrees of anisotropy and $n_{\bar{E}} = n_{\bar{\nu}} = 1$ denote isotropic material.

2.4.1.4.1 Dual-Poroelastic Pressure and Stress Evolutions

The analytical solution shows that there are two eigenvalues, ξ^{I} and ξ^{II}, which physically correspond to the effective pressure diffusion coefficients in the porous rock matrix and the fracture network, respectively. The relative time scale among between the flow processes in fractured porous media can be assessed by calculating the diffusion coefficients from these eigenvalues neglecting the interporosity flow contribution, i.e., $c^{(\mathrm{N})} = s / \xi^{(\mathrm{N})}$ and $t_{ch}^{(\mathrm{N})} = a^2 / c^{(\mathrm{N})}$ (or $t_{ch}^{(\mathrm{N})} = R^2 / c^{(\mathrm{N})}$). This data set gives

matrix $\quad c^{\mathrm{I}} = 7.3 \times 10^{-4}\ \mathrm{cm}^2/\mathrm{s}; \quad t_{ch}^{\mathrm{I}} = 12245\ \mathrm{s} \cong 3.4\ \mathrm{hours}$

fracture $c^{II} = 1.4\,\mathrm{cm}^2/\mathrm{s}; \qquad t_{ch}^{II} = 6.4\,\mathrm{s}$

Hence, fluid diffusion process that takes only seconds in the fracture network requires hours in the porous rock matrix. The histories of dual pore-pressure changes in the center of the specimens are illustrated in conjunction with the single-poroelastic's responses in **Figs. 2.22 and 2.23**. The single-poroelastic's results are obtained by requiring the bulk volume fraction of either the fracture network or the porous matrix to vanish ($v^{II} \to 0 \Rightarrow \omega = \kappa_D = 0$ or $v^{I} \to 0 \Rightarrow \omega = \kappa_D = 1$). In Figs. 2.22 and 2.23, the dimensionless time for single-poroelastic results are scaled with respect to the effective characteristic time of the overall dual-poroelastic system t_{ch} = 19 s. The results display typical non-monotonic poroelastic behaviors in term of the Mandel-Cryer effect. After initial loading, the pore pressure near the lateral surface must dissipate due to access to drainage, effectively making the specimen more compliant near the sides and stiffer in the middle region. Therefore, there is a load transfer to the middle region, as reflected in the history of vertical stress in **Figs. 2.24**, such that the pore pressures continue to rise after the initial jumps due to Skempton's effect. At long time, the pore-pressure buildup decrease due to subsequent fluid diffusion. Clearly, there are two distinct responses, especially in the matrix' pressure, signifying the dual time scales that is not captured in the single-poroelastic solution. The first pressure peaks in both the matrix and fracture network correspond to the characteristic time scale of the fracture network. Being more fluid permeable, the pressure in the fracture dissipates faster and quickly falls below the matrix's pressure. As time progresses, the matrix's pressure seeks to build up non-monotonically again according to the matrix' time scale while simultaneously feeding fluid into the fracture network via interporosity fluid

exchange. In fact, fluid exchange with the fracture system negates the second pressure peak in the matrix. The contribution of interporosity exchange can be visualized by looking at the separation between the matrix's pressure with and without interporosity flow in both Figs. 2.22 and 2.23.

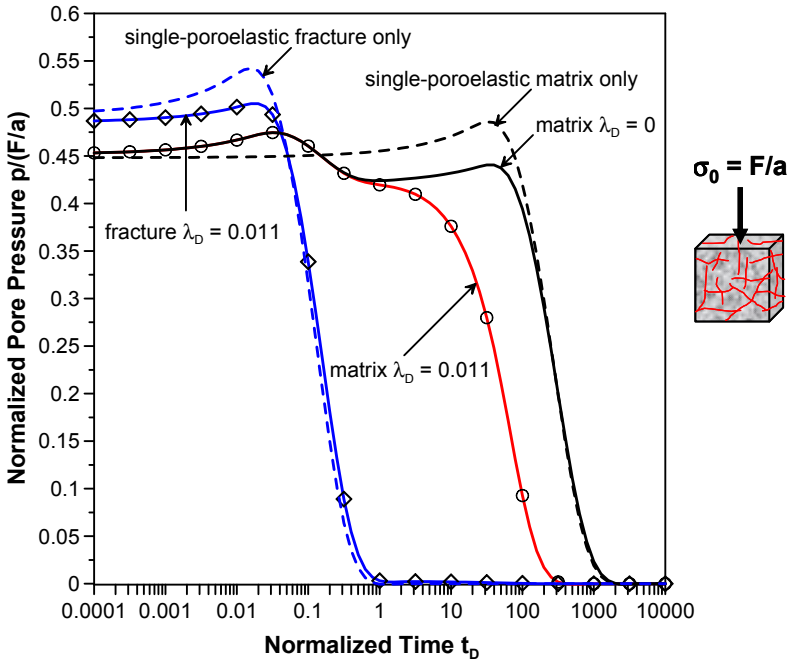

Fig. 2.22—Pore pressure histories in the center of an isotropic rectangular-strip geometry under uniaxial step loading.

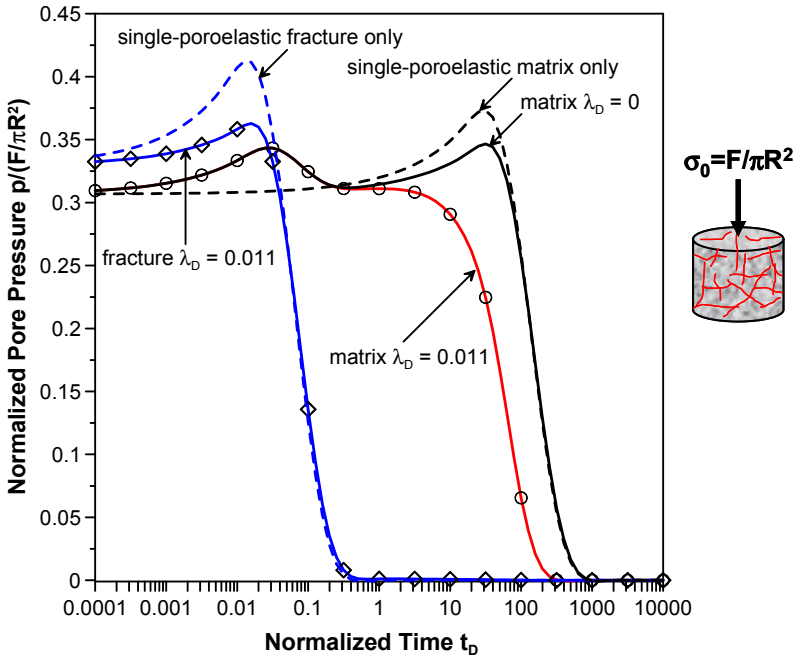

Fig. 2.23—Pore pressure histories in the center of an isotropic solid-cylinder geometry under uniaxial step loading.

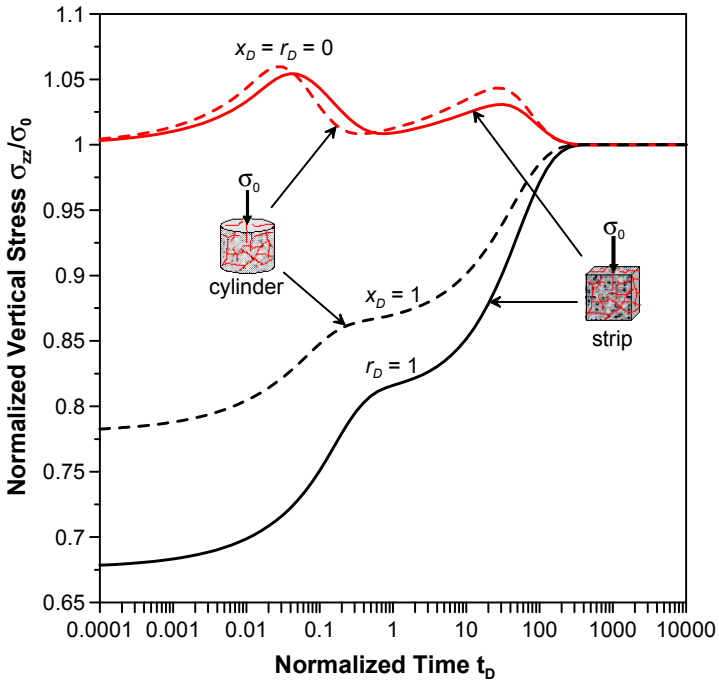

Fig. 2.24—Total vertical stress histories at $x_D = r_D = 0$ and $x_D = r_D = 1$ for both geometries under uniaxial step loading.

Next, the pore pressure responses due to a step loading of constant vertical strain for both geometries are shown in **Fig. 2.25**. The results are for the case of no interporosity flow, λ_D

= 0, and normalized by $\overline{E}_z\varepsilon_0$. It is interesting to observe that the well-known Mandel-Cryer effect, in which the pore pressures continue to rise after the initial values, does not manifest in the rectangular strip geometry. Physically, for a constant step load (σ_0), the material is effectively softened on the outside leading to redistribution of the constant applied load to the middle region and simultaneously increasing the pore pressures. Under a constant vertical strain (ε_0), the vertical stress relaxes as the material softens so that there is no extra pore pressure generation. However, this is not the case for solid cylinder geometry where the non-monotonic pore pressure behavior still exists. Mathematically, this can be explained by looking at the coupled diffusion equations for both geometries. Under unconfined vertical strain application, the stress and corresponding diffusion equations in terms of strain components of each geometry become:

Rectangular strip (Eqs. 2.73 and 2.74)

$$\sigma_{zz} = \frac{\overline{M}_{11}\overline{M}_{33} - \overline{M}_{13}^2}{\overline{M}_{11}}\varepsilon_{zz} + \bar{\gamma}^{\mathrm{I}} p^{\mathrm{I}} + \bar{\gamma}^{\mathrm{II}} p^{\mathrm{II}}, \quad \text{(2.108a)}$$

$$\left(\mathbf{A}\frac{\partial}{\partial t} - \mathbf{D}\frac{\partial^2}{\partial x^2} + \mathbf{\Gamma}\right)\begin{Bmatrix} p^{\mathrm{I}} \\ p^{\mathrm{II}} \end{Bmatrix} = \begin{Bmatrix} \bar{\gamma}^{\mathrm{I}} \\ \bar{\gamma}^{\mathrm{II}} \end{Bmatrix}\frac{\partial \varepsilon_{zz}}{\partial t}, \quad \text{(2.108b)}$$

Solid cylinder (Eqs. 2.92 and 2.93)

$$\sigma_{rr} + \sigma_{\theta\theta} = (\overline{M}_{11} + \overline{M}_{12})(\varepsilon_{rr} + \varepsilon_{\theta\theta}) + 2\overline{M}_{13}\varepsilon_{zz} + 2(\overline{\alpha}_1^{\mathrm{I}} p^{\mathrm{I}} + \overline{\alpha}_1^{\mathrm{II}} p^{\mathrm{II}}), \quad \text{(2.109a)}$$

$$\left(\mathbf{M}\frac{\partial}{\partial t} + \mathbf{\Gamma} - \mathbf{D}\nabla_r^2\right)\begin{Bmatrix} p^{\mathrm{I}} \\ p^{\mathrm{II}} \end{Bmatrix} = \begin{Bmatrix} \overline{\alpha}_1^{\mathrm{I}} \\ \overline{\alpha}_1^{\mathrm{II}} \end{Bmatrix}\frac{\partial}{\partial t}\left(\varepsilon_{rr} + \varepsilon_{\theta\theta} + \varepsilon_{zz}\right), \quad \text{(2.109b)}$$

with $\mathbf{M} = \begin{bmatrix} 1/\overline{M}^{\mathrm{I}} & 1/\overline{M}^{\mathrm{I,II}} \\ 1/\overline{M}^{\mathrm{I,II}} & 1/\overline{M}^{\mathrm{II}} \end{bmatrix}$

As a result, pressure diffusion in strip geometry is coupled with the rate of vertical strain application. When this strain rate is constant ($\varepsilon_{zz}(t) = \varepsilon_0$), the diffusion process is uncoupled from the deformation and a regular diffusion phenomenon is observed. On the other hand, diffusion in solid cylinder is governed by the radial and tangential strain rate in addition to the vertical strain rate. The non-zero volumetric strain rate, $\partial(\varepsilon_{rr} + \varepsilon_{\theta\theta} + \varepsilon_{zz})/\partial t$, acts as a source/sink term for pore pressure generation in the diffusion equation, leading to the non-monotonic pressure behavior. It is obvious that the response of strip and solid cylinder geometries are analogous and characterized by two time scales. In the following, the effects of governing parameters and material anisotropy are shown based on solid-cylinder results.

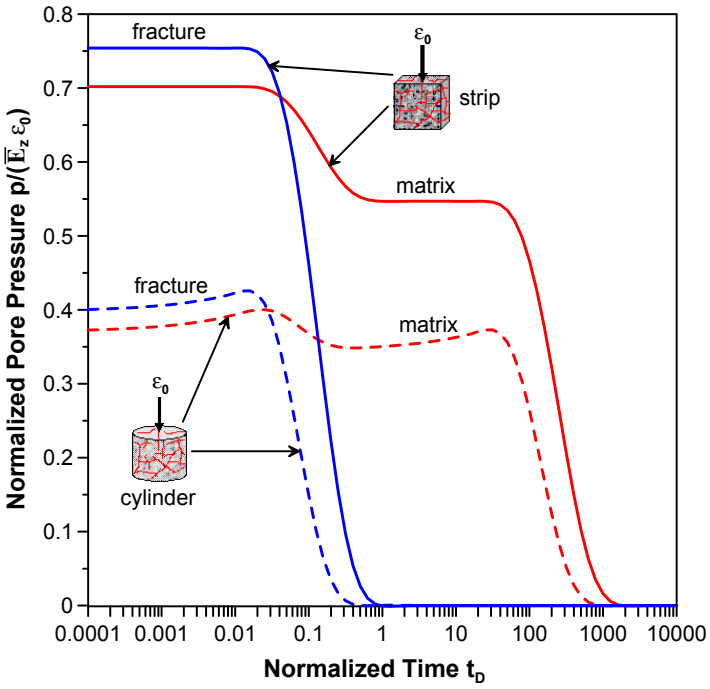

Fig. 2.25—Normalized pore pressure histories at the center ($x_D = r_D = 0$) of the sample under unconfined uniaxial step strain ($\varepsilon_{zz} = \varepsilon_0 \times H(t)$) for both rectangular strip and solid cylinder geometries ($\lambda_D = 0$).

2.4.1.4.2 Effects of Dual-Poroelastic Parameters

The analytical solutions, expressed in normalized position and time, show that pressure and stress depend on the following set of dimensionless parameters $\{\omega, \omega^{I,II}, \bar{\gamma}^{I}, \bar{\gamma}^{II}, \bar{\varsigma}^{I}, \bar{\varsigma}^{II}, \bar{\varphi}^{I}, \bar{\varphi}^{II}, \lambda_D, \bar{\kappa}_D\}$. The physical range for these coefficients are: $0 \le \omega$, $\bar{\kappa}_D$, $\bar{\gamma}_c^{I}$, $\bar{\gamma}_c^{II}$, $\bar{\varphi}^{I}, \bar{\varphi}^{II}, \bar{\varsigma}^{I}, \bar{\varsigma}^{II} \le 1$; $\lambda_D \ge 0$; and $-1 \le \omega^{I,II} \le 1$. The ratios, ω and $\omega^{I,II}$, represent relative storage of the fracture network and cross storage between the porous matrix and fracture. Although it is common to assume that $\omega^{I,II} = 0$, it has been shown that $\omega^{I,II}$ is non-zero and significant (Berryman and Wang 1995). The parameters $\bar{\gamma}^{I}$, $\bar{\gamma}^{II}$, $\bar{\varsigma}^{I}$, and $\bar{\varsigma}^{II}$ correspond to the poroelastic coupling of the system, i.e., when $\bar{\gamma}^{I}, \bar{\gamma}^{II}, \bar{\varsigma}^{I}, \bar{\varsigma}^{II} \to 1$, the solid-to-fluid and fluid-to-solid coupling are the most pronounced and vice versa. Similarly, $\bar{\varphi}^{I}$ and $\bar{\varphi}^{II}$ denote the coupling effect of axial loading on the pore pressure response. For isotropic material, $\bar{\varphi}^{I} = \bar{\varphi}^{II} = (1-2\bar{\nu})/(1-\bar{\nu})$. The dimensionless interporosity parameter, λ_D, is a measure of the flow exchange between the matrix and the fracture. The macroscopic mobility ratio, $\bar{\kappa}_D$, indicates the relative macroscopic flow ability of the fracture system and the matrix. The storage ratios and dual-poroelastic dimensionless coefficients affect the responses in two ways: they modify the magnitude and partially control the speed of evolution. The histories of pore pressure at the center of the cylinder and axial stress for different values of ω are shown in **Figs. 2.26 and 2.27**.

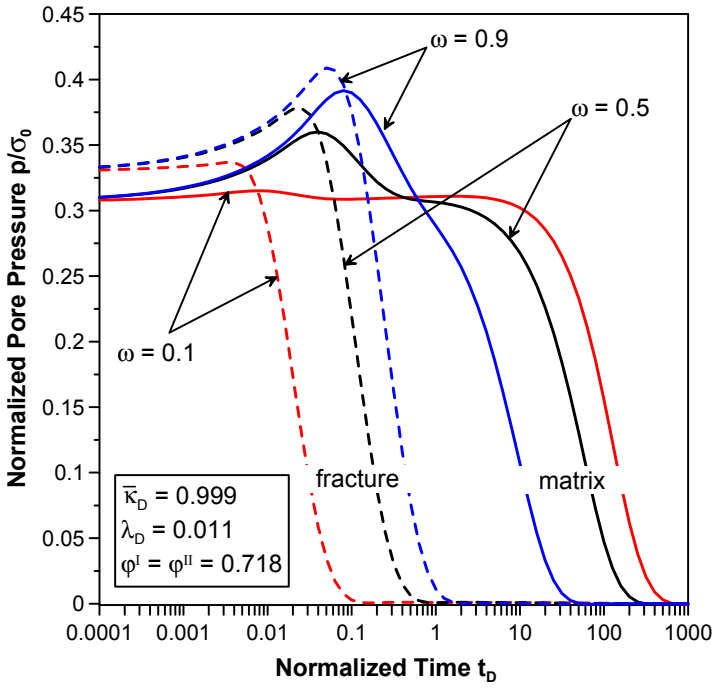

Fig. 2.26—Effect of storage ratio ω on pore-pressure histories at the center (r_D = 0) of isotropic solid cylinder sample under unconfined uniaxial step loading.

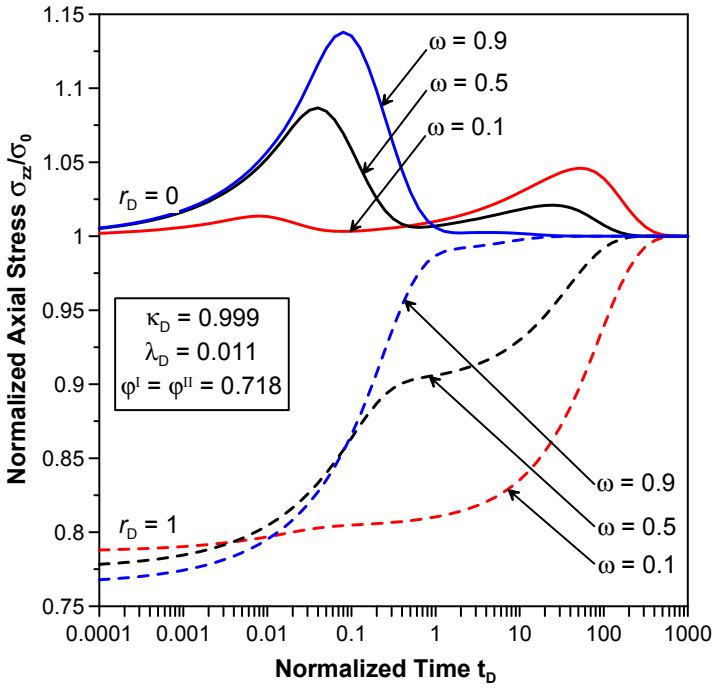

Fig. 2.27— Effect of storage ratio ω on axial stress history in isotropic solid cylinder sample under unconfined uniaxial step loading.

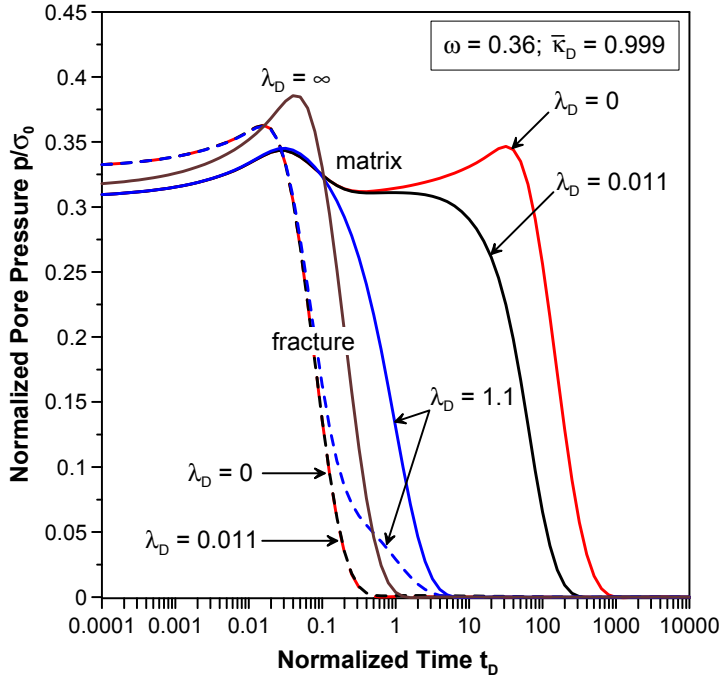

Fig. 2.28—Effect of interporosity coefficients λ_D on pore pressure histories at the center (r_D = 0) of isotropic solid cylinder sample under unconfined uniaxial step loading.

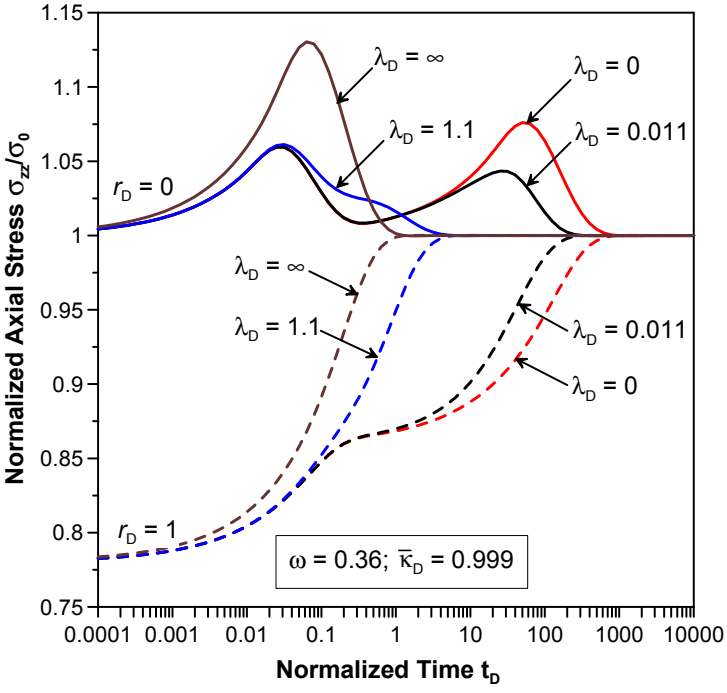

Fig. 2.29—Effect of interporosity coefficients λ_D on axial stress history in isotropic solid cylinder under unconfined uniaxial step loading.

The effect of interporosity exchange parameter, λ_D, is illustrated through the pore pressure and axial stress evolutions in **Figs. 2.28 and 2.29**. For no interflow, the dual-non-monotonic pressure buildups in the center of the cylinder are clearly observed. The higher the interflow coefficient, the closer the matrix and fracture pressure converge to each other and the less distinct the dual behavior becomes. As $\lambda_D \to \infty$, the pore pressure in the matrix is instantaneously equilibrated with the fracture's pressure which renders the system single-response. The corresponding axial stress history in Fig. 2.29 also reveals two stages of load transfer into the middle region of the cylinder for intermediate values of λ_D. In other words, interporosity exchange equilibrates the dual pore pressures and reduces the non-monotonic matrix's pressure buildup in the center of the cylinder.

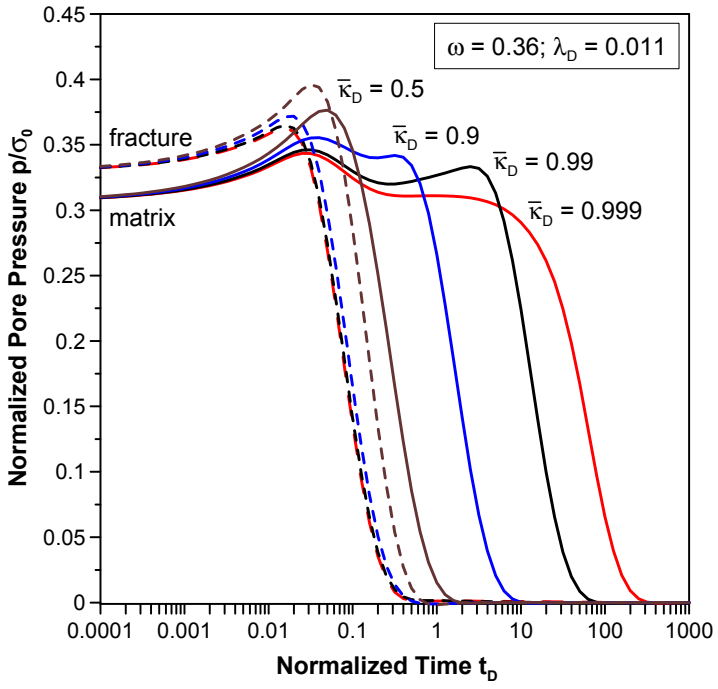

Fig. 2.30—Effect of macroscopic mobility ratios $\bar{\kappa}_D$ on pore pressure histories at the center (r_D = 0) of isotropic solid cylinder under unconfined uniaxial step loading.

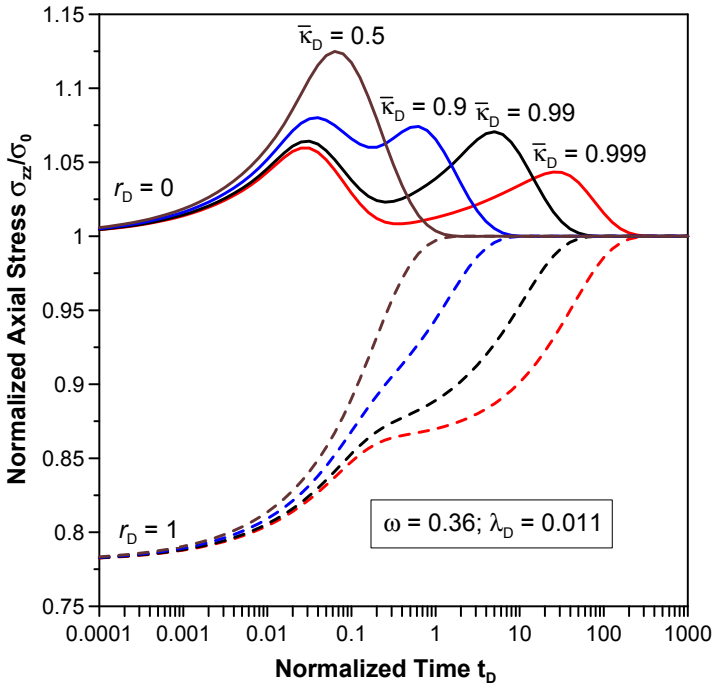

Fig. 2.31—Effect of macroscopic mobility ratios $\bar{\kappa}_D$ on axial stress history at the center of isotropic solid cylinder under unconfined uniaxial step loading.

On the other hand, the macroscopic mobility ratio directly alters the dual time scales which are shown in **Figs. 2.30 and 2.31**. It is seen that the higher the mobility ratio, the more pronounced the characteristic dual response exhibits due to the separation of the characteristic time scales. As the mobility ratio approaches 0.5, the response converges to single-permeability's one. The different matrix and fracture pore-pressure responses for $\bar{\kappa}_D$ = 0.5 in Figs. 2.30 and 2.31 is due to the effect of contrasting compressibility.

2.4.1.4.3 Effects of Material Anisotropy

The history of pore pressure at the center of the cylinder for the case of $n_{\bar{E}} = \bar{E}_1 / \bar{E}_3 = 0.5$, 1, 2 with $n_{\bar{\nu}} = \bar{\nu}_{12} / \bar{\nu}_{13} = 1$ is presented in **Fig. 2.32**. The magnitude of the initial and non-monotonic pore-pressure response varies significantly with different ratios of $n_{\bar{E}}$. The

greater the ratio $n_{\bar{E}}$ is, the higher the dual pore pressures are because more of external axial loading is transferred to the fluid when the solid frame is less stiff in the loading direction. In **Fig. 2.33**, the pore pressures are plotted for the case of $n_{\bar{\nu}}$ = 0.5, 1, 2 with $n_{\bar{E}}$ = 1. Similar trends to the previous ones are observed. The material anisotropy and time effects on displacements are shown in **Figs. 2.34 and 2.35**.

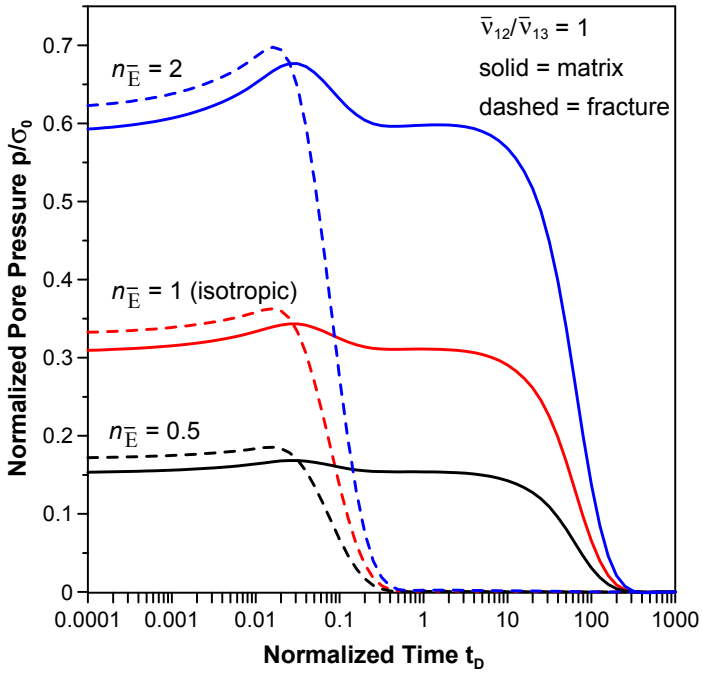

Fig. 2.32—Effect of different isotropic-to-transverse Young modulus ratios ($n_{\bar{E}} = \bar{E}_1 / \bar{E}_3$) on pore pressure history at the center (r_D = 0) of solid cylinder under unconfined uniaxial step loading.

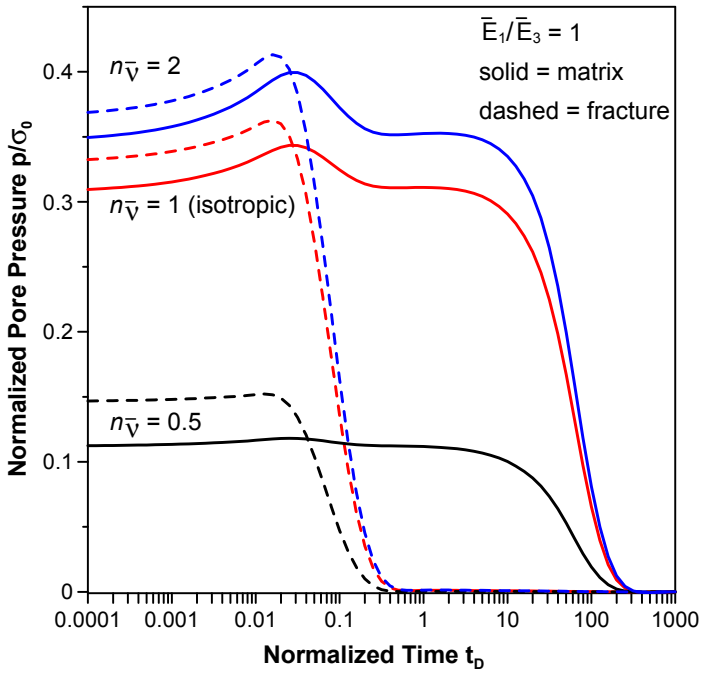

Fig. 2.33— Effect of different isotropic-to-transverse Poisson ratios ($n_{\bar{v}} = \bar{v}_{12} / \bar{v}_{13}$) on pore pressure history at the center (r_D = 0) of solid cylinder under unconfined uniaxial step loading.

In Fig. 2.34, the axial displacement is plotted for both variations in $n_{\bar{E}}$ and $n_{\bar{v}}$. It is obvious that $n_{\bar{E}}$ has more significant effect on vertical consolidation than $n_{\bar{v}}$ because $n_{\bar{E}}$ directly controls the compliance of the sample in the loading direction. On the other hand, $n_{\bar{v}}$ is related to the Poisson effect which has more impact on the lateral responses. Therefore, for the same $n_{\bar{E}}$, the final vertical consolidation is the same although the transient response are different. The corresponding radial displacement at the cylinder lateral surface is presented in Fig. 2.35 in which positive values indicate tension (expansion). As expected, varying $n_{\bar{v}}$ changes the radial displacement significantly. For all cases of $n_{\bar{E}}$ and $n_{\bar{v}}$, the sample is initially expanded then contracted because the short-time (undrained) Poisson's effect – when the sample appears to be stiffer – is higher than the long-time (drained) one.

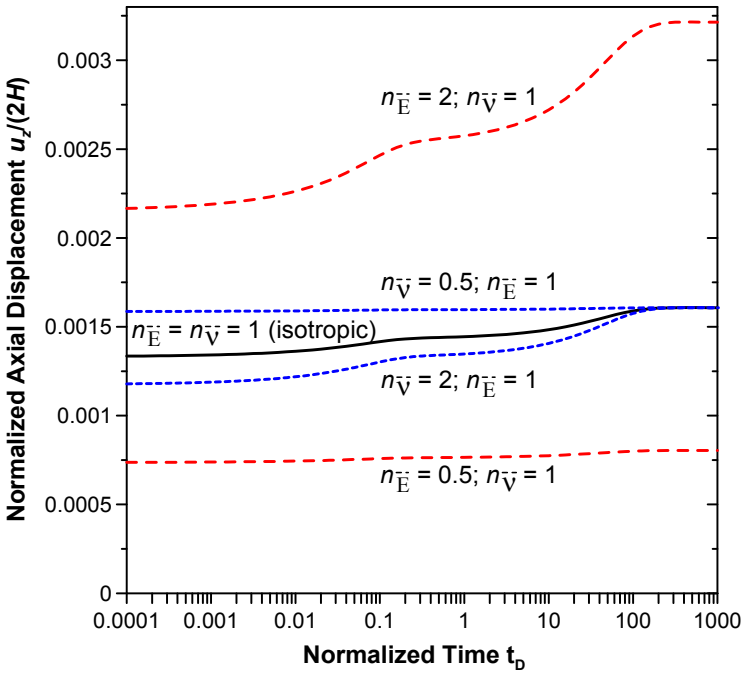

Fig. 2.34—Normalized axial displacement history of solid cylinder under unconfined uniaxial step loading for different ratios of $n_{\bar{E}} = \bar{E}_1 / \bar{E}_3$ and $n_{\bar{\nu}} = \bar{\nu}_{12} / \bar{\nu}_{13}$.

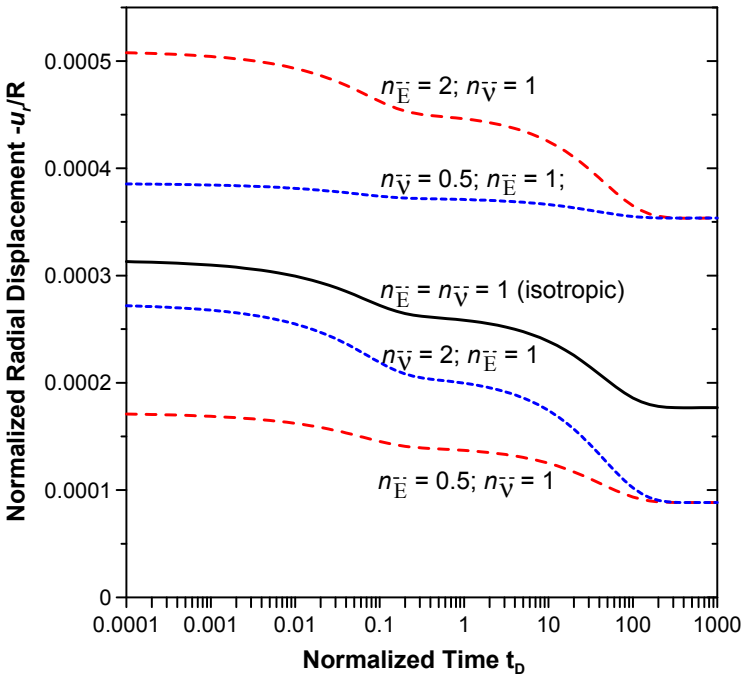

Fig. 2.35—Normalized radial displacement history at r_D = 1 of solid cylinder under unconfined uniaxial step loading for different ratios of $n_{\bar{E}} = \bar{E}_1 / \bar{E}_3$ and $n_{\bar{\nu}} = \bar{\nu}_{12} / \bar{\nu}_{13}$.

2.4.1.4.4 Special Case of One-Dimensional Consolidation

It is also of interest to demonstrate that the generalized Mandel's strip problem can be rearranged to arrive at the classical one-dimensional consolidation of a laterally constrained finite layer (Terzaghi 1943 and Biot 1941). Because $x_D = 0$ is a symmetry plane and satisfies a no-flow and no-displacement condition, half of the strip geometry can be turned on its end with external loading conditions $\varepsilon_{zz} = p_o = 0$ and $P_c \neq 0$ as depicted in **Fig. 2.36**. Here, P_c plays the role of vertical load, $p_o = 0$ implies a drained top surface, and $\varepsilon_{zz} = 0$ signifies laterally constrained condition.

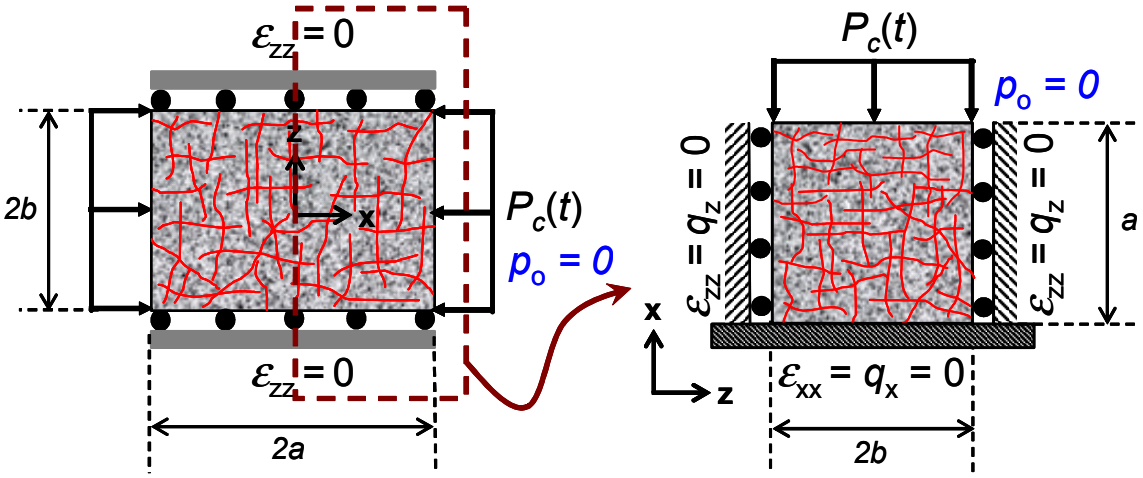

Fig. 2.36—Schematic showing the equivalency between the Mandel's problem and the one-dimensional consolidation of a finite layer by simplifying the loading condition and considering the symmetry of the problem ($P_c \neq 0$, $p_o = \varepsilon_{zz} = 0$).

The normalized dual pore-pressure distributions from top to bottom of the one-dimensional column at various times are plotted in **Fig. 2.37**. The instantaneous matrix fluid-pressure response is 86% of the applied load, lower than its fracture's counterpart at 92%. Since the column is constrained laterally, the dual pore-pressure fields are uncoupled from the stress or deformation field as derived in Eq. 2.186. Consequently, there is no non-

monotonic pressure behavior after initial loading in the column as previously shown in the work of Lewallen and Wang (1998). The histories of the matrix and fracture pore pressure at depths of $x_D = 0.1$ (near the bottom) and 0.9 (near the top) are illustrated in **Fig. 2.38**.

The corresponding settlement at the top of the column is shown in **Fig. 2.39** in conjunction with the single-poroelastic's response considering the matrix properties only. The results clearly demonstrate two phases of consolidation for a fractured medium. The difference in the final settlement denotes the contribution of fracture deformation to the overall response.

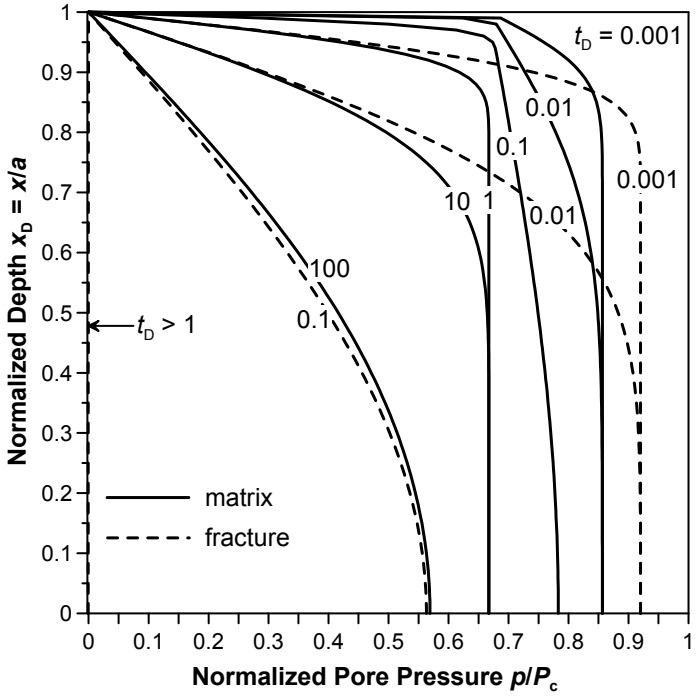

Fig. 2.37—Evolution of normalized dual pore-pressure profile in a laterally constrained finite layer under suddenly imposed constant vertical load ($P_c \neq 0$, $p_o = \varepsilon_{zz} = 0$).

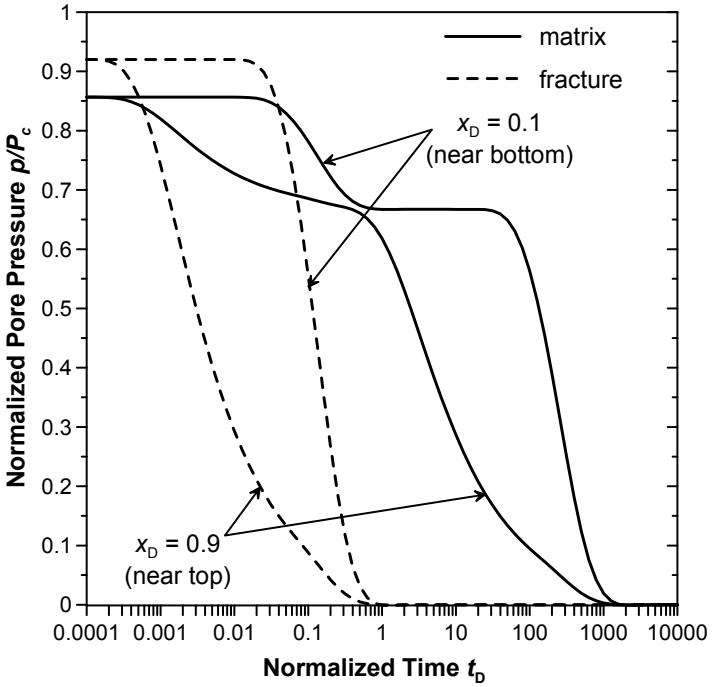

Fig. 2.38—Normalized dual pore-pressure histories at two different depths in a laterally constrained finite layer under suddenly imposed constant vertical load ($P_c \neq 0$, $p_o = \varepsilon_{zz} = 0$).

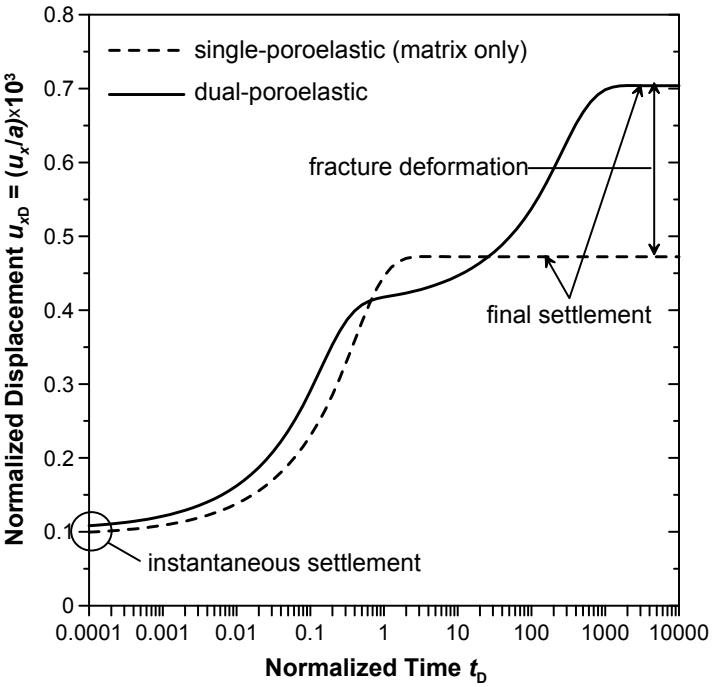

Fig. 2.39—Evolution of normalized settlement during drainage phase following a step load on finite layer ($P_c \neq 0$, $p_o = \varepsilon_{zz} = 0$).

2.4.2 Hollow Cylinder[3]

2.4.2.1 Background

Hollow cylinder geometry is the most widely used geometry in laboratory for material characterization and, particularly in petroleum engineer, for the study of field phenomena such as formation consolidation, hydraulic fracturing, breakout, and sanding, to name a few (Ewy and Cook 1990; Schmitt et al. 1993; Sherwood and Bailey 1994; Papamichos et al. 2001). The elastic solution to the Lamé problem (1852) – thick-walled cylinder under uniform, axisymmetric, external and/or internal confining pressure – have been treated extensively in classical elasticity (e.g., Kirsch 1898; Love 1944; Timoshenko and Goodier 1970; Saada 1974).

Coupling the elastic response with the transient effect of fluid flow, Rice and Cleary (1967) provided the fundamental plane-strain poroelastic solution for isotropic hollow cylinder. This solution is widely used to analyze rock formation response under rapid and intensive pressure drawdown. The solution for internal pressurization of hollow cylinder, used in laboratory testing to determine rock' tensile strength and to simulate hydraulic fracturing was presented by Detournay and Carvalho (1989) and Schmitt et al. (1993). Later, Jourine et al. (2004) gave general solution that was used to simulate laboratory experiments with realistic boundary conditions. The extension from isotropy to transverse isotropy was first carried out by Kanj et al. (2003) to evaluate uncertainties in measurements of poromechanical parameters. Recently, Abousleiman and Kanj (2004)

[3] Part of this section was presented at the Biot Conference (Nguyen and Abousleiman, June 2009, New York) and SPE ATCE (Nguyen and Abousleiman, SPE 123900, October 2009, New Orleans).

unified all analytical solutions for transversely isotropic hollow cylinder under the "umbrella" of the generalized Lamé problem. Their solutions applied to all experimental testing configurations that may be subject to stroke/load control axially and hydrostatic/non-hydrostatic laterally. Applications of these solutions encompassed a multitude of problems with cylindrical geometries ranging from solid cylinder to borehole (Kanj and Abousleiman 2004). Other notable hollow cylinder solutions in geomechanics included extension to incorporate thermal effect (Kanj and Abousleiman 2005) and chemical effect (Sherwood and Bailey; Kanj and Abousleiman 2007). In biomechanics, transversely isotropic models and solutions (Zhang et al. 1998; Rémond and Naili 2004; Gailani and Cowin 2008) were also used to simulate unconfined compression test of cortical bones or to model pore-pressure response in osteon.

All of the above solutions model the porous medium as single-poroelastic continuum and thus fall short in describing the proper response of the well-known dual-porosity porous medium and such as bone structures (Cowin 1999) or the response of naturally fractured saturated rocks modeled and simulated as dual-porosity and dual-permeability porous medium. The analytical solutions for isotropic dual-poroelastic hollow cylinder subject to vertical and/or lateral confining stress and fluid pressure was presented by Nguyen and Abousleiman (2009). This section extends that solution to transverse isotropy and generalized the lateral boundary conditions to account for radial displacement. As such, the cylinder is subject to stress and fluid pressure variations, representing all experimental configurations, yet the pore pressure responses in the medium exhibit dual and transient evolutions. Results for all testing setup are plotted to demonstrate the different behaviors.

2.4.2.2 Problem Descriptions

The schematic of a transversely isotropic fractured hollow cylinder in which the axis of material symmetry coincides with the cylinder axis is shown in **Fig. 2.40**. The sample is sandwiched between two smooth, rigid, and impervious plates. Axially, the geometry is subjected to either an applied axial load $F(t)$ or an applied axial displacement $u_z^*(t)$. Laterally, the cylinder can be subjected to inner/outer fluid pressure ($p_{\mathrm{i}}(t)$ and $p_{\mathrm{o}}(t)$) or fluid flux ($q_{\mathrm{i}}(t)$ and $q_{\mathrm{o}}(t)$) as well as inner/outer confining stress ($P_{\mathrm{i}}(t)$ and $P_{\mathrm{o}}(t)$). The generalized setups and solutions are intended for studying of various rock testing conditions and field problems by combining relevant boundary conditions. It is also important to recognize that the hollow cylinder problem reduces to the solid cylinder case when the inner radius approaches zero or converges to the vertical borehole problem in an infinite medium when the outer radius becomes very large compared to inner radius. The overall boundary conditions are generally expressed in cylindrical coordinates as follow:

At the cylinder's inner wall, $r = R_{\mathrm{i}}$

$$\sigma_{rr} = P_{\mathrm{i}}(t) \quad \text{or} \quad u_r = U_{\mathrm{i}}(t), \qquad (2.110a)$$

$$\sigma_{r\theta} = \sigma_{rz} = 0, \qquad (2.110b)$$

$$p^{\mathrm{I}} = p^{\mathrm{II}} = p_{\mathrm{i}}(t) \quad \text{or} \quad \begin{cases} q_r^{\mathrm{I}} + q_r^{\mathrm{II}} = q_{\mathrm{i}}(t) \\ p^{\mathrm{I}} = p^{\mathrm{II}} \end{cases}, \qquad (2.110c)$$

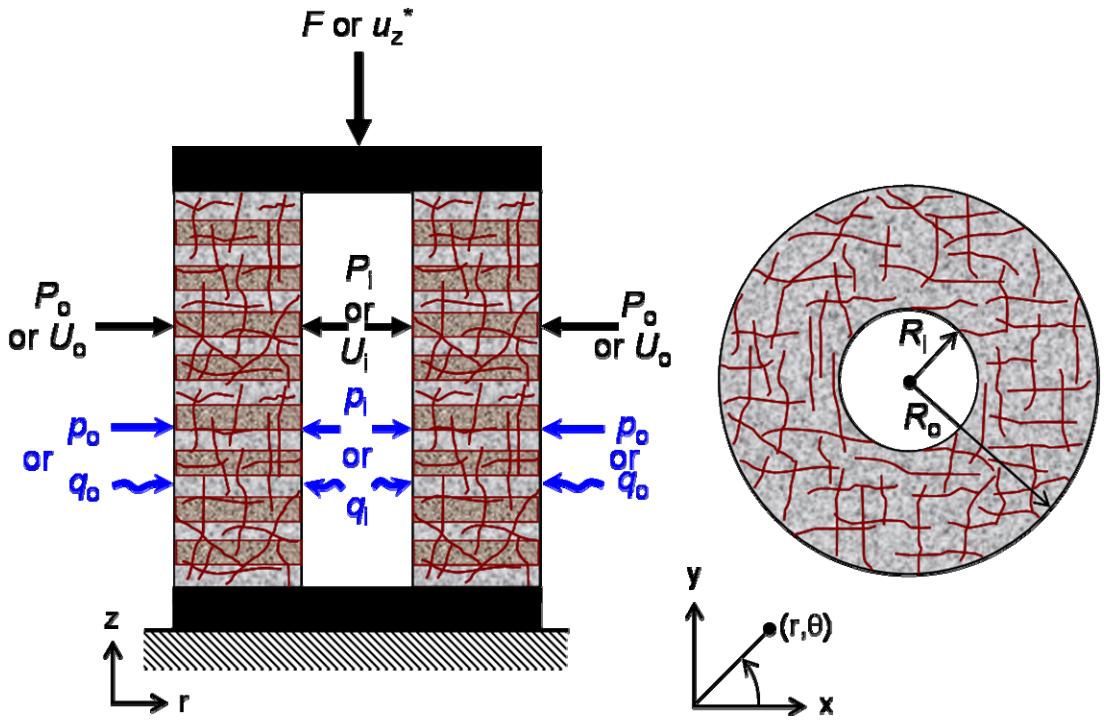

Fig. 2.40—The generalized hollow cylinder problem's geometry and boundary conditions.

At the cylinder's outer boundary, r = R_o

$$\sigma_{rr} = P_o(t) \quad \text{or} \quad u_r = U_o(t), \qquad (2.111a)$$

$$\sigma_{r\theta} = \sigma_{rz} = 0, \qquad (2.111b)$$

$$p^{I} = p^{II} = p_o(t) \quad \text{or} \quad \begin{cases} q_r^{I} + q_r^{II} = q_o(t) \\ p^{I} = p^{II} \end{cases}, \qquad (2.111c)$$

Axially at the top or bottom, z = 0 or z = H

$$\sigma_{\theta z} = \sigma_{rz} = 0; \qquad q_z^{I} = q_z^{II} = 0, \qquad (2.112a)$$

$$\varepsilon_{zz} = \varepsilon_{zz}^{*}(t) \quad \text{or} \quad \int_{R_i}^{R_o} r\sigma_{zz}\,dr = \frac{A_h}{2\pi}\sigma_{zz}^{*}(t), \qquad (2.112b)$$

In the above, the subscripts i and o denotes inner and outer boundary condition

respectively; $A_h = \pi(R_o^2 - R_i^2)$ is the cross sectional area of the hollow cylinder. ; $\varepsilon_{zz}^*(t)$ is an average axial strain due to the applied stroke/displacement $u_z^*(t)$; $\sigma_{zz}^*(t) = F(t)/A_h$ is the average axial stress applied on the cylinder.

The geometry and boundary conditions imply that every horizontal cross section is a plane of folding symmetry. That is, horizontal planes remain horizontal ($\varepsilon_{zz} = \varepsilon_{zz}(t)$). No axial fluid displacement occurs ($q_z^{\mathrm{I}} = q_z^{\mathrm{II}} = 0$) and fluid flow is in the radial direction only. The end effects of shear and torsion are negligible and there is no axial shear stress on the plane. Under such conditions, a generalized plane-strain condition naturally manifests in any cross-sectional plane. Consequently, all response functions (except axial displacement $u_z(t)$) are axially invariant and at most functions of radial distance r and time t only. Following Abousleiman and Kanj (2004), the next section discusses the generalized axisymmetric problem and presents the corresponding analytical solution.

2.4.2.3 Generalized Analytical Solutions

This is a designated generalized plane strain (z-independent) and axisymmetric problem (θ-independent). First, the general dual-poroelastic solutions of pore pressures, fluid fluxes, and stresses are derived. Then solutions applicable to specific boundary conditions such as pressure or flux boundary conditions are presented. The generalized boundary conditions for this axisymmetric problem as depicted in Fig. 2.40 are expressed as follow:

At the cylinder's inner wall, $r = R_i$

$$\sigma_{rr}^{(1)} = P_i(t) \quad \text{or} \quad u_r^{(1)} = U_i(t), \qquad (2.113a)$$

$$\sigma_{r\theta}^{(1)} = \sigma_{rz}^{(1)} = 0, \qquad (2.113b)$$

$$p^{\mathrm{I}(1)} = p^{\mathrm{II}(1)} = p_{\mathrm{i}}(t) \quad \text{or} \quad \begin{cases} q_r^{\mathrm{I}(1)} + q_r^{\mathrm{II}(1)} = q_{\mathrm{i}}(t) \\ p^{\mathrm{I}(1)} = p^{\mathrm{II}(1)} \end{cases}, \tag{2.113c}$$

At the cylinder's outer surface, $r = R_{\mathrm{o}}$

$$\sigma_{rr}^{(1)} = P_{\mathrm{o}}(t) \quad \text{or} \quad u_r^{(1)} = U_{\mathrm{o}}(t), \tag{2.114a}$$

$$\sigma_{r\theta}^{(1)} = \sigma_{rz}^{(1)} = 0, \tag{2.114b}$$

$$p^{\mathrm{I}(1)} = p^{\mathrm{II}(1)} = p_{\mathrm{o}}(t) \quad \text{or} \quad \begin{cases} q_r^{\mathrm{I}(1)} + q_r^{\mathrm{II}(1)} = q_{\mathrm{o}}(t) \\ p^{\mathrm{I}(1)} = p^{\mathrm{II}(1)} \end{cases}, \tag{2.114c}$$

Axially at the top or bottom, $z = 0$ or $z = H$

$$\sigma_{\theta z}^{(1)} = \sigma_{rz}^{(1)} = 0; \qquad q_z^{\mathrm{I}(1)} = q_z^{\mathrm{II}(1)} = 0, \tag{2.115a}$$

$$\varepsilon_{zz}^{(1)} = \varepsilon_{zz}^{*}(t) \quad \text{or} \quad \int_{R_{\mathrm{i}}}^{R_{\mathrm{o}}} r\sigma_{zz}^{(1)} dr = \frac{A_h}{2\pi}\sigma_{zz}^{*}(t), \tag{2.115b}$$

Due to the uniformity of the lateral boundary condition, the problem is obviously axisymmetric such that at any time the shear stress and strain components are identically zero ($\sigma_{r\theta} = \sigma_{\theta z} = 0$ and $\varepsilon_{r\theta} = \varepsilon_{\theta z} = 0$) and all other response functions are independent of the circumferential angle θ. Consequently, the governing equations are reduced to one-dimensional and all variables are at most functions of r and t only. Specifically, the equilibrium equation, Eq. 2.18, in polar coordinate becomes

$$\frac{\partial \sigma_{rr}}{\partial r} + \frac{\sigma_{rr} - \sigma_{\theta\theta}}{r} = 0, \tag{2.116}$$

Combining the above equilibrium equation with the stress-strain-pressure constitutive Eq. 2.15 and the strain-displacement relations, Eq. 2.6, yields the Navier-type field equation

$$\frac{\partial}{\partial r}\left[\sigma_{rr}+\sigma_{\theta\theta}-\left(1-\frac{\overline{M}_{12}}{\overline{M}_{11}}\right)\overline{\alpha}_1^{\mathrm{I}}p^{\mathrm{I}}-\left(1-\frac{\overline{M}_{12}}{\overline{M}_{11}}\right)\overline{\alpha}_1^{\mathrm{II}}p^{\mathrm{II}}\right]=0\,, \quad \text{.....(2.117)}$$

Integration with respect to *r* yields

$$\sigma_{rr}+\sigma_{\theta\theta}-\left(1-\frac{\overline{M}_{12}}{\overline{M}_{11}}\right)\overline{\alpha}_1^{\mathrm{I}}p^{\mathrm{I}}-\left(1-\frac{\overline{M}_{12}}{\overline{M}_{11}}\right)\overline{\alpha}_1^{\mathrm{II}}p^{\mathrm{II}}=C_1(t)\,, \quad \text{.....(2.118)}$$

where $C_1 = C_1(t)$ is an integration constant. Analogous to the solid cylinder problem, the fluid content constitutive equations simplify to

$$\zeta^{\mathrm{I}}=-a^{\mathrm{I}}(\sigma_{rr}+\sigma_{\theta\theta}+\overline{\varphi}^{\mathrm{I}}S_{zz}-b_{11}p^{\mathrm{I}}-b_{12}p^{\mathrm{II}})\,, \quad \text{..... (2.119))}$$

$$\zeta^{\mathrm{II}}=-a^{\mathrm{II}}(\sigma_{rr}+\sigma_{\theta\theta}+\overline{\varphi}^{\mathrm{II}}S_{zz}-b_{21}p^{\mathrm{I}}-b_{22}p^{\mathrm{II}})\,, \quad \text{..... (2.120))}$$

where $S_{zz}(t)=\overline{M}_{33}\varepsilon_{zz}^{*}(t)$; $a^{(\mathrm{N})}$, $\overline{\varphi}^{(\mathrm{N})}$, and b_{ij} are given in Eqs. 2.69 to 2.71b. Then, the diffusion equation in terms of normalized time t_D and radial distance r_D is identical to the solid cylinder's counterpart, Eq. 2.94. The Laplace transform solutions for the fluid pressures and fluid fluxes are straightforwardly expressed as

$$\widetilde{p}^{\mathrm{I}(1)}=\widetilde{S}_{zz}f^{\mathrm{I}}+\widetilde{C}_1 g^{\mathrm{I}}+\sum_{(\mathrm{N})=\mathrm{I,II}}[\,C_2^{(\mathrm{N})}\mathrm{I}_0(\xi^{(\mathrm{N})}r_D)+C_3^{(\mathrm{N})}\mathrm{K}_0(\xi^{(\mathrm{N})}r_D)]\,, \quad \text{.....(2.121)}$$

$$\widetilde{p}^{\mathrm{II}(1)}=\widetilde{S}_{zz}f^{\mathrm{II}}+\widetilde{C}_1 g^{\mathrm{II}}+\sum_{(\mathrm{N})=\mathrm{I,II}}m^{(\mathrm{N})}[\,C_2^{(\mathrm{N})}\mathrm{I}_0(\xi^{(\mathrm{N})}r_D)+C_3^{(\mathrm{N})}\mathrm{K}_0(\xi^{(\mathrm{N})}r_D)]\,, \quad \text{.....(2. 122)}$$

$$\widetilde{q}_r^{\mathrm{I}(1)}=-(1-\overline{\kappa}_D)\sum_{(\mathrm{N})=\mathrm{I,II}}\xi^{(\mathrm{N})}[\,C_2^{(\mathrm{N})}\mathrm{I}_1(\xi^{(\mathrm{N})}r_D)-C_3^{(\mathrm{N})}\mathrm{K}_1(\xi^{(\mathrm{N})}r_D)]\,, \quad \text{.....(2.123)}$$

$$\widetilde{q}_r^{\mathrm{II}(1)}=-\overline{\kappa}_D\sum_{(\mathrm{N})=\mathrm{I,II}}m^{(\mathrm{N})}\xi^{(\mathrm{N})}[\,C_2^{(\mathrm{N})}\mathrm{I}_1(\xi^{(\mathrm{N})}r_D)-C_3^{(\mathrm{N})}\mathrm{K}_1(\xi^{(\mathrm{N})}r_D)]\,, \quad \text{.....(2.124)}$$

where I_0 and K_0 are the modified Bessel functions of the first and second kind of order zero; $C_2^{(\mathrm{N})}$ and $C_3^{(\mathrm{N})}$ are coefficients to be determined from boundary conditions; other

parameters were same as previously defined in Eqs. 2.52 to 2.54. Making use of the pressure expressions, other solutions for stresses, displacements, and strains follow naturally from the constitutive equation as

$$\widetilde{\sigma}_{rr} = A_0\widetilde{S}_{zz} + A_1\widetilde{C}_1 + \sum_{(N)=I,II} A_2^{(N)}\left[C_2^{(N)}\frac{\mathrm{I}_1(\xi^{(N)}r_D)}{\xi^{(N)}r_D} - C_3^{(N)}\frac{\mathrm{K}_1(\xi^{(N)}r_D)}{\xi^{(N)}r_D}\right] + C_4 r_D^{-2}, \quad \text{.....(2.125)}$$

$$\widetilde{\sigma}_{\theta\theta}^{(1)} = A_0\widetilde{S}_{zz} + A_1\widetilde{C}_1 + \sum_{(N)=I,II} A_2^{(N)}\left\{\begin{array}{l} C_2^{(N)}\left[\mathrm{I}_0(\xi^{(N)}r_D) - \dfrac{\mathrm{I}_1(\xi^{(N)}r_D)}{\xi^{(N)}r_D}\right] \\ + C_3^{(N)}\left[\mathrm{K}_0(\xi^{(N)}r_D) + \dfrac{\mathrm{K}_1(\xi^{(N)}r_D)}{\xi^{(N)}r_D}\right] \end{array}\right\} - C_4 r_D^{-2}, \quad \text{.....(2.126)}$$

$$\widetilde{\sigma}_{zz}^{(1)} = B_0\widetilde{S}_{zz} + B_1\widetilde{C}_1 + \sum_{(N)=I,II} B_2^{(N)}[\,C_2^{(N)}\,\mathrm{I}_0(\xi^{(N)}r_D) + C_3^{(N)}\,\mathrm{K}_0(\xi^{(N)}r_D)], \quad \text{.....(2.127)}$$

$$\frac{\widetilde{u}_r^{(1)}}{R_{\mathrm{ch}}} = -(f\,\widetilde{S}_{zz} + g\,\widetilde{C}_1)\,r_D - \sum_{(N)=I,II} h^{(N)}\left[C_2^{(N)}\frac{\mathrm{I}_1(\xi^{(N)}r_D)}{\xi^{(N)}} - C_3^{(N)}\frac{\mathrm{K}_1(\xi^{(N)}r_D)}{\xi^{(N)}}\right], \quad \text{.....(2.128)}$$
$$- \frac{C_4}{\overline{M}_{11} - \overline{M}_{12}} r_D^{-1}$$

$$\widetilde{\varepsilon}_{rr}^{(1)} = -(f\,\widetilde{S}_{zz} + g\,\widetilde{C}_1) - \sum_{(N)=I,II} h^{(N)}\left\{\begin{array}{l} C_2^{(N)}\left[\mathrm{I}_0(\xi^{(N)}r_D) - \dfrac{\mathrm{I}_1(\xi^{(N)}r_D)}{\xi^{(N)}r_D}\right] \\ + C_3^{(N)}\left[\mathrm{K}_0(\xi^{(N)}r_D) - \dfrac{\mathrm{K}_1(\xi^{(N)}r_D)}{\xi^{(N)}r_D}\right] \end{array}\right\}, \quad \text{.....(2.129)}$$
$$+ \frac{C_4}{\overline{M}_{11} - \overline{M}_{12}} r_D^{-2}$$

$$\widetilde{\varepsilon}_{\theta\theta}^{(1)} = -(f\,\widetilde{S}_{zz} + g\,\widetilde{C}_1) - \sum_{(N)=I,II} h^{(N)}\left[C_2^{(N)}\frac{\mathrm{I}_1(\xi^{(N)}r_D)}{\xi^{(N)}r_D} - C_3^{(N)}\frac{\mathrm{K}_1(\xi^{(N)}r_D)}{\xi^{(N)}r_D}\right], \quad \text{.....(2.130)}$$
$$- \frac{C_4}{\overline{M}_{11} - \overline{M}_{12}} r_D^{-2}$$

in which the lumped coefficients A_0, A_1, $A_2^{(N)}$, B_0, B_1, $B_2^{(N)}$, f, g, and $h^{(N)}$ are given

previously in the solid cylinder solution, e.g., Eqs. 2.103a to 2.107.

TABLE 1—AXISYMMETRIC LOADING CONFIGURATIONS OF HOLLOW CYLINDER GEOMETRY UNDER AN AXIALLY DISPLACEMENT-CONTROLLED CONDITION

Config. No.	1	2	3	4	5	6	7	8
$(\sigma_{rr})_{\mathrm{i}}$	P_{i}	P_{i}	P_{i}	P_{i}	P_{i}	P_{i}	P_{i}	P_{i}
$(\sigma_{rr})_{\mathrm{o}}$	P_{o}	P_{o}	P_{o}	P_{o}	-	-	-	-
$(u_r)_{\mathrm{i}}$	-	-	-	-	-	-	-	-
$(u_r)_{\mathrm{o}}$	-	-	-	-	U_{o}	U_{o}	U_{o}	U_{o}
$(p^{\mathrm{I}})_{\mathrm{i}}$	p_{i}	$p^{\mathrm{I}} = p^{\mathrm{II}}$	p_{i}	$p^{\mathrm{I}} = p^{\mathrm{II}}$	p_{i}	$p^{\mathrm{I}} = p^{\mathrm{II}}$	p_{i}	$p^{\mathrm{I}} = p^{\mathrm{II}}$
$(p^{\mathrm{II}})_{\mathrm{i}}$	p_{i}	$p^{\mathrm{II}} = p^{\mathrm{I}}$	p_{i}	$p^{\mathrm{II}} = p^{\mathrm{I}}$	p_{i}	$p^{\mathrm{II}} = p^{\mathrm{I}}$	p_{i}	$p^{\mathrm{II}} = p^{\mathrm{I}}$
$(p^{\mathrm{I}})_{\mathrm{o}}$	p_{o}	p_{o}	$p^{\mathrm{I}} = p^{\mathrm{II}}$	$p^{\mathrm{I}} = p^{\mathrm{II}}$	p_{o}	p_{o}	$p^{\mathrm{I}} = p^{\mathrm{II}}$	$p^{\mathrm{I}} = p^{\mathrm{II}}$
$(p^{\mathrm{II}})_{\mathrm{o}}$	p_{o}	p_{o}	$p^{\mathrm{II}} = p^{\mathrm{I}}$	$p^{\mathrm{II}} = p^{\mathrm{I}}$	p_{o}	p_{o}	$p^{\mathrm{II}} = p^{\mathrm{I}}$	$p^{\mathrm{II}} = p^{\mathrm{I}}$
$(q_r)_{\mathrm{i}}$	-	q_{i}	-	q_{i}	-	q_{i}	-	q_{i}
$(q_r)_{\mathrm{o}}$	-	-	q_{o}	q_{o}	-	-	q_{o}	q_{o}
ε_{zz}	ε_{zz}^*	ε_{zz}^*	ε_{zz}^*	ε_{zz}^*	ε_{zz}^*	ε_{zz}^*	ε_{zz}^*	ε_{zz}^*
Config. No.	9	10	11	12	13	14	15	16
$(\sigma_{rr})_{\mathrm{i}}$	-	-	-	-	-	-	-	-
$(\sigma_{rr})_{\mathrm{o}}$	P_{o}	P_{o}	P_{o}	P_{o}	-	-	-	-
$(u_r)_{\mathrm{i}}$	U_{i}	U_{i}	U_{i}	U_{i}	U_{i}	U_{i}	U_{i}	U_{i}
$(u_r)_{\mathrm{o}}$	-	-	-	-	U_{o}	U_{o}	U_{o}	U_{o}
$(p^{\mathrm{I}})_{\mathrm{i}}$	p_{i}	$p^{\mathrm{I}} = p^{\mathrm{II}}$	p_{i}	$p^{\mathrm{I}} = p^{\mathrm{II}}$	p_{i}	$p^{\mathrm{I}} = p^{\mathrm{II}}$	p_{i}	$p^{\mathrm{I}} = p^{\mathrm{II}}$
$(p^{\mathrm{II}})_{\mathrm{i}}$	p_{i}	$p^{\mathrm{II}} = p^{\mathrm{I}}$	p_{i}	$p^{\mathrm{II}} = p^{\mathrm{I}}$	p_{i}	$p^{\mathrm{II}} = p^{\mathrm{I}}$	p_{i}	$p^{\mathrm{II}} = p^{\mathrm{I}}$
$(p^{\mathrm{I}})_{\mathrm{o}}$	p_{o}	p_{o}	$p^{\mathrm{I}} = p^{\mathrm{II}}$	$p^{\mathrm{I}} = p^{\mathrm{II}}$	p_{o}	p_{o}	$p^{\mathrm{I}} = p^{\mathrm{II}}$	$p^{\mathrm{I}} = p^{\mathrm{II}}$
$(p^{\mathrm{II}})_{\mathrm{o}}$	p_{o}	p_{o}	$p^{\mathrm{II}} = p^{\mathrm{I}}$	$p^{\mathrm{II}} = p^{\mathrm{I}}$	p_{o}	p_{o}	$p^{\mathrm{II}} = p^{\mathrm{I}}$	$p^{\mathrm{II}} = p^{\mathrm{I}}$
$(q_r)_{\mathrm{i}}$	-	q_{i}	-	q_{i}	-	q_{i}	-	q_{i}
$(q_r)_{\mathrm{o}}$	-	-	q_{o}	q_{o}	-	-	q_{o}	q_{o}
ε_{zz}	ε_{zz}^*	ε_{zz}^*	ε_{zz}^*	ε_{zz}^*	ε_{zz}^*	ε_{zz}^*	ε_{zz}^*	ε_{zz}^*

Note: For axially load-controlled condition, simply replacing the condition $\varepsilon_{zz} = \varepsilon_{zz}^*(t)$ with $\overline{\sigma}_{zz} = \sigma_{zz}^*(t)$

There are seven unknown coefficients $\widetilde{C}_1$, C_2^{I}, C_2^{II}, C_3^{I}, C_3^{II}, C_4, and $\widetilde{\varepsilon}_{zz}^*$ (or $\widetilde{S}_{zz}$) to be determined from boundary conditions. These equations may include four equations for fluid pressure or fluid fluxes and two equations for radial stress or radial displacement at the inner and outer boundaries, respectively, in addition to one equation for axial loading. Table 1 summarizes the 16 different possible axially displacement-controlled

configurations for this generalized axisymmetric loading. An equal number of configurations (17 to 32) can be listed for the axially load-controlled scenarios by simply replaced the condition $\varepsilon_{zz} = \varepsilon_{zz}^{*}(t)$ with $\overline{\sigma}_{zz} = \sigma_{zz}^{*}(t)$ in the same table.

The displacement-controlled loading condition involves a prescribed axial strain or displacement, i.e., $\varepsilon_{zz} = \varepsilon_{zz}^{*}(t)$ is known. Hence, there are only six unknown coefficients to be determined from the following system of six linear equations

$$\begin{bmatrix} c_{11} & c_{12} & c_{13} & c_{14} & c_{15} & c_{16} \\ c_{21} & c_{22} & c_{23} & c_{24} & c_{25} & c_{26} \\ c_{31} & 0 & c_{33} & c_{34} & c_{35} & c_{36} \\ c_{41} & 0 & c_{43} & c_{44} & c_{45} & c_{46} \\ c_{51} & 0 & c_{53} & c_{54} & c_{55} & c_{56} \\ c_{61} & 0 & c_{63} & c_{64} & c_{65} & c_{66} \end{bmatrix} \begin{Bmatrix} \widetilde{C}_1 \\ C_4 \\ C_2^{\mathrm{I}} \\ C_2^{\mathrm{II}} \\ C_3^{\mathrm{I}} \\ C_3^{\mathrm{II}} \end{Bmatrix} = \begin{Bmatrix} b_1 - c_{17}\widetilde{S}_{zz} \\ b_2 - c_{27}\widetilde{S}_{zz} \\ b_3 - c_{37}\widetilde{S}_{zz} \\ b_4 - c_{47}\widetilde{S}_{zz} \\ b_5 - c_{57}\widetilde{S}_{zz} \\ b_6 - c_{67}\widetilde{S}_{zz} \end{Bmatrix}, \quad \text{.....(2.131)}$$

where b_1 and b_2 correspond to the boundary conditions of the radial stress or displacement (Eqs. 2.110a and 2.111a); b_3 to b_6 represent the fluid pressure or flux boundary conditions (Eqs. 2.110c and 2.111c). The components of the coefficient matrix c_{ij} and vector b_i for specific loading configurations are listed in Appendix E with the corresponding solutions.

Under the load-control condition, the sample is subjected to a prescribed time-dependent axial force that can be expressed in term of an average axial stress $\overline{\sigma}_{zz} = \sigma_{zz}^{*}(t)$. The solution under this condition is best handled by converting the applied axial stress into an equivalent axial strain by using the general expression for vertical stress (Eq. 2.15) in conjunction with the load equilibrium equation (Eq. 2.112b). The approach yields

$$\widetilde{S}_{zz} = (\widetilde{\sigma}^{*}_{zz} - B_1 \widetilde{C}_1)/B_0 - \frac{2}{B_0 (r_{oD}^2 - r_{iD}^2)} \sum_{(N)=I,II} \frac{B_2^{(N)}}{\xi^{(N)}} \left\{ \begin{matrix} C_2^{(N)} \left[r_{oD} \mathrm{I}_1(\xi^{(N)} r_{oD}) - r_{iD} \mathrm{I}_1(\xi^{(N)} r_{iD}) \right] \\ - C_3^{(N)} \left[r_{oD} \mathrm{K}_1(\xi^{(N)} r_{oD}) - r_{iD} \mathrm{K}_1(\xi^{(N)} r_{iD}) \right] \end{matrix} \right\}, \quad (2.132)$$
$$= c_{71} \widetilde{C}_1 + c_{73} C_2^{\mathrm{I}} + c_{74} C_2^{\mathrm{II}} + c_{75} C_3^{\mathrm{I}} + c_{76} C_3^{\mathrm{II}} + c_{77} \widetilde{\sigma}^{*}_{zz}$$

The above Eq. 2.132 is then substituted into Eq. 2.131 to allow expressing boundary conditions in term of the axially applied stress, $\widetilde{\sigma}^{*}_{zz}$. As a result, the same set solution expressions for displacement-controlled condition can be used for load-controlled counterpart in which the c_{ij} coefficients are updated to

$$c_{ij} \rightarrow c_{ij} + c_{i7} c_{7j} \qquad i = 1,2,...,6;\ j = 1,3,...,6, \quad (2.133)$$

2.4.2.4 Results and Discussions

This section illustrates the poroelastic responses for various loading configurations of a fully saturated, hollow cylindrical fractured sample. The same material properties adopted earlier for a Gulf-of-Mexico shale are used in these examples.

Geometrically, the cylinder has an inner radius, R_i = 0.0127 m, and an outer radius, R_o = 0.0635 m so that R_o is five times R_i. At $t = 0^+$, the sample is subjected to a compressive Heaviside-type axial load differential, F = 1.2×10^{-2} MN, leading an average axial stress differential of 1 MPa. Laterally, the specimen can be unconfined (P_i = 0 or P_o = 0) and/or restrained (U_i = 0 or U_o = 0). The fluid can be drained on both ($p_i = p_o$ = 0) boundaries or a mixed of drained and jacketed boundaries (p_i = 0, q_o = 0 or q_i = 0, p_o = 0). These can be also numbered as configuration 17, 18, 19, 21, 22, 23, 25, 26, 27, 29, 30, and 31 in the extended form of Table 1. Cases of fully jacketed configurations (20, 24, 28, and 32) are not considered since the solutions and responses reduce to the undrained elastic ones.

Two basic poromechanical responses, namely, pore pressure and total tangential stress, are illustrated for each of the considered loading configurations. In **Fig. 2.41**, the dual pore-pressure responses at various locations in the hollow cylinder versus time are shown on the left column while the evolution of total tangential stress profile is annexed on the right side for configurations that involve only pressure boundary condition (17, 21, 25, and 29). For unconfined configuration 17, the sample is allowed to expand laterally thus induces tensile tangential stress near the two boundaries. In addition, the drained surfaces effectively soften the material on the boundaries and give rise to the Mandel-Cryer effect causing the pore-pressure response to vary non-monotonically over the course of time. Restricting the lateral movement at either or both boundaries increases the levels of stress and pore pressure responses in the cylinder. Naturally, fixing the radial displacement on the outer surface (configuration 21) leads to higher stress concentration than on the inner surface (configuration 25).

For inner jacketed or outer jacketed case under laterally unconfined condition (configuration 18 and 19), the evolutions of pore pressure and tangential stress distributions in the cylinder are illustrated in **Figs. 2.42**. The results show that compressive total stress arises at the jacketed surface while tensile total stress develops at the drained surface. However, in term of effective stress, the reverse is observed, i.e., the sample is more susceptible to tensile failure near the jacketed surface and compressive failure near the drained surface due to the corresponding effective stress concentration.

Similarly, the cases of jacketed and restrained lateral displacement on one surface (configuration 30 and 31) are displayed in **Fig. 2.43**. Again, higher total stress evolves at

the jacketed and restrained lateral surface. Finally, the responses for the rest of the loading configurations (22, 23, 26, and 27) are presented in Fig. **2.44**. These results show the capability of the solutions to be applied to various problem settings to predict the poromechanical responses of fractured or multi-porous material.

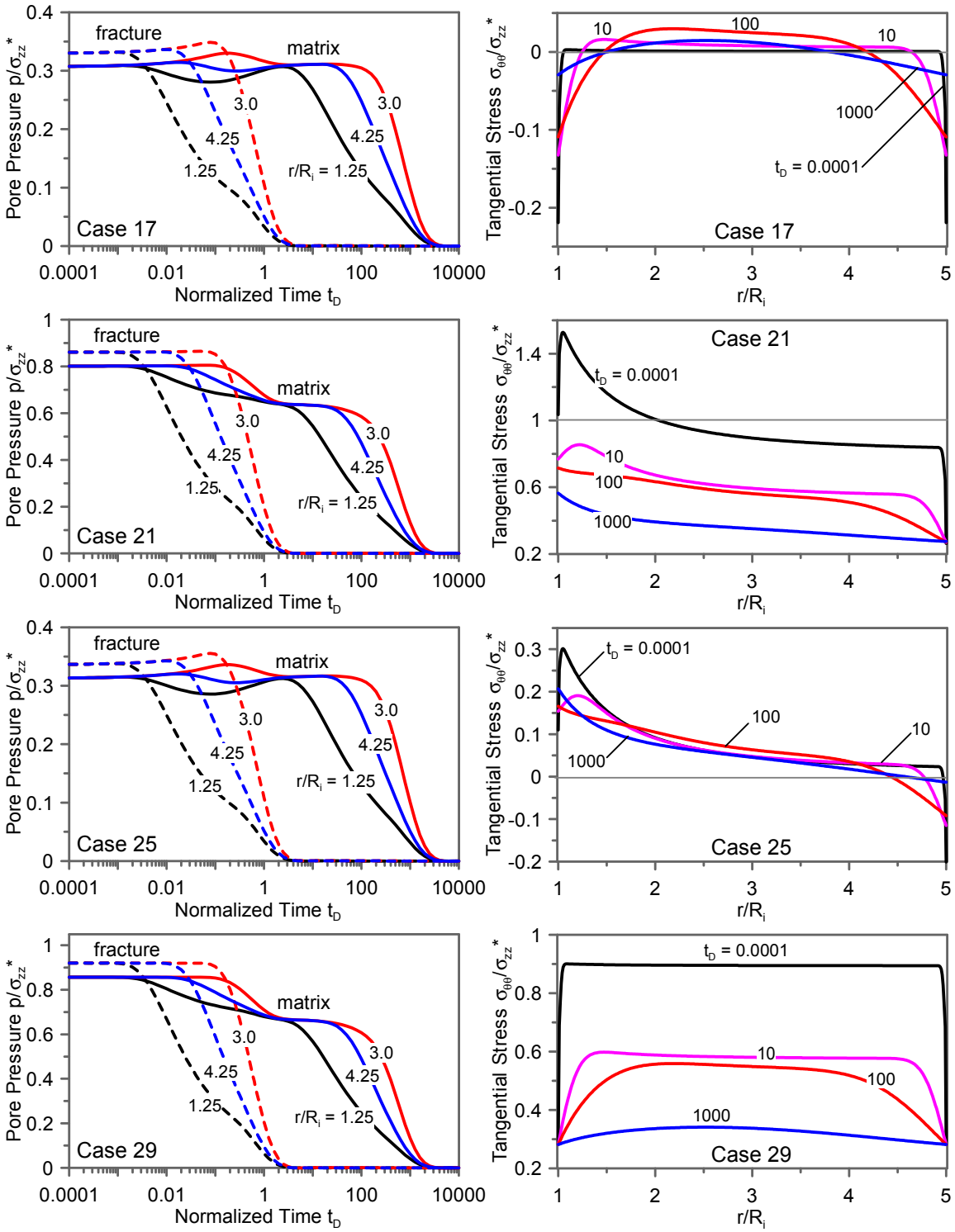

Fig. 2.41—Pore pressure and tangential stress responses for four different lateral stress/displacement configurations under fluid-pressure boundary conditions (case 17, 21, 25, and 29).

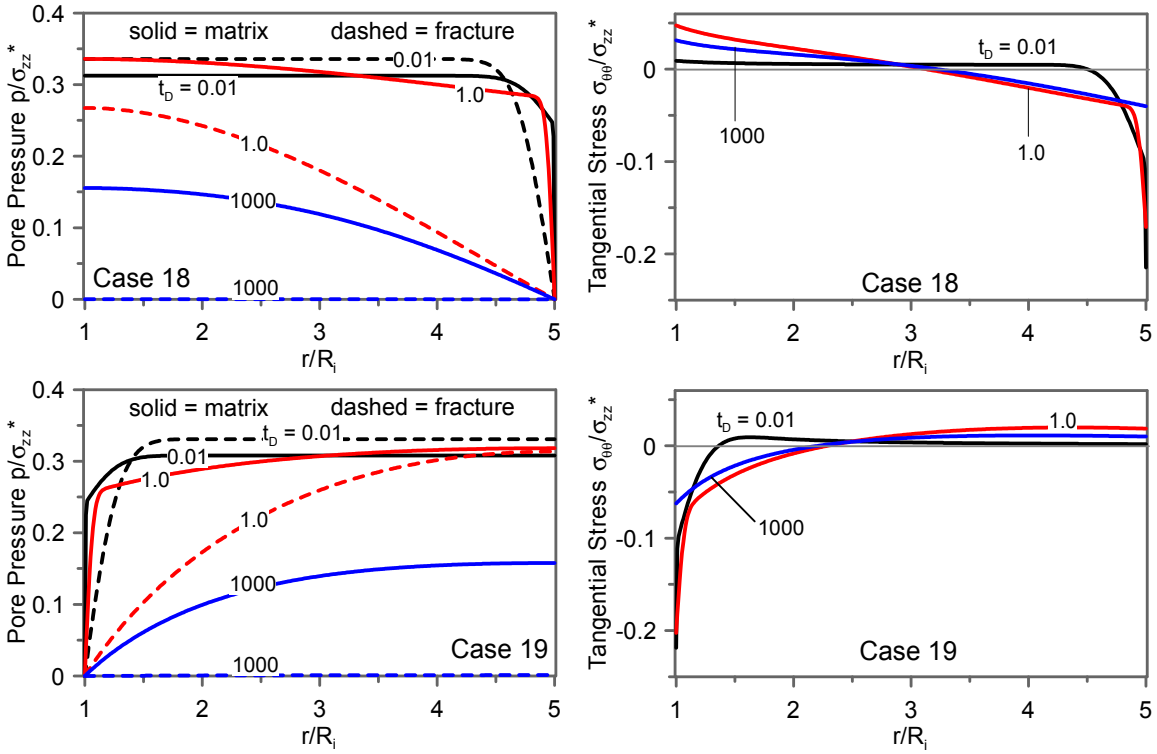

Fig. 2.42—Pore pressure and tangential stress responses for two different mixed fluid-pressure/flux boundary conditions under laterally unconfined condition (case 18 and 19).

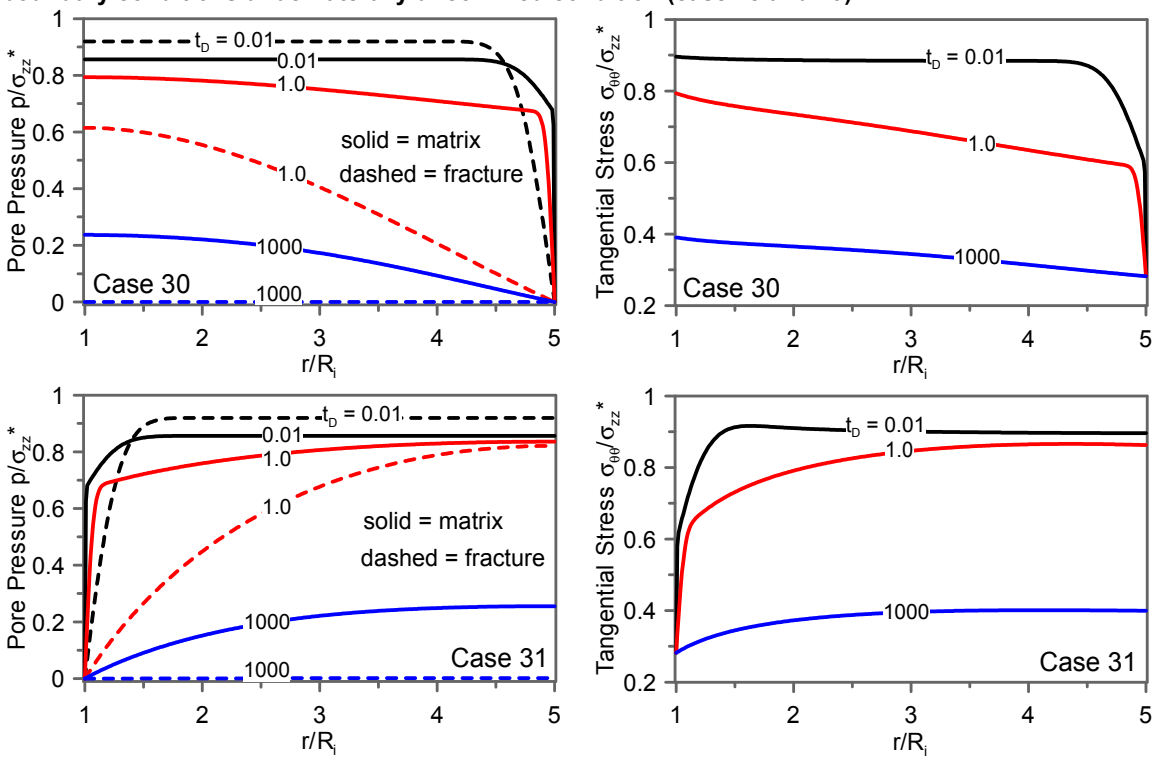

Fig. 2.43—Pore pressure and tangential stress responses for two different mixed fluid-pressure/flux boundary conditions under laterally confined displacement (case 30 and 31).

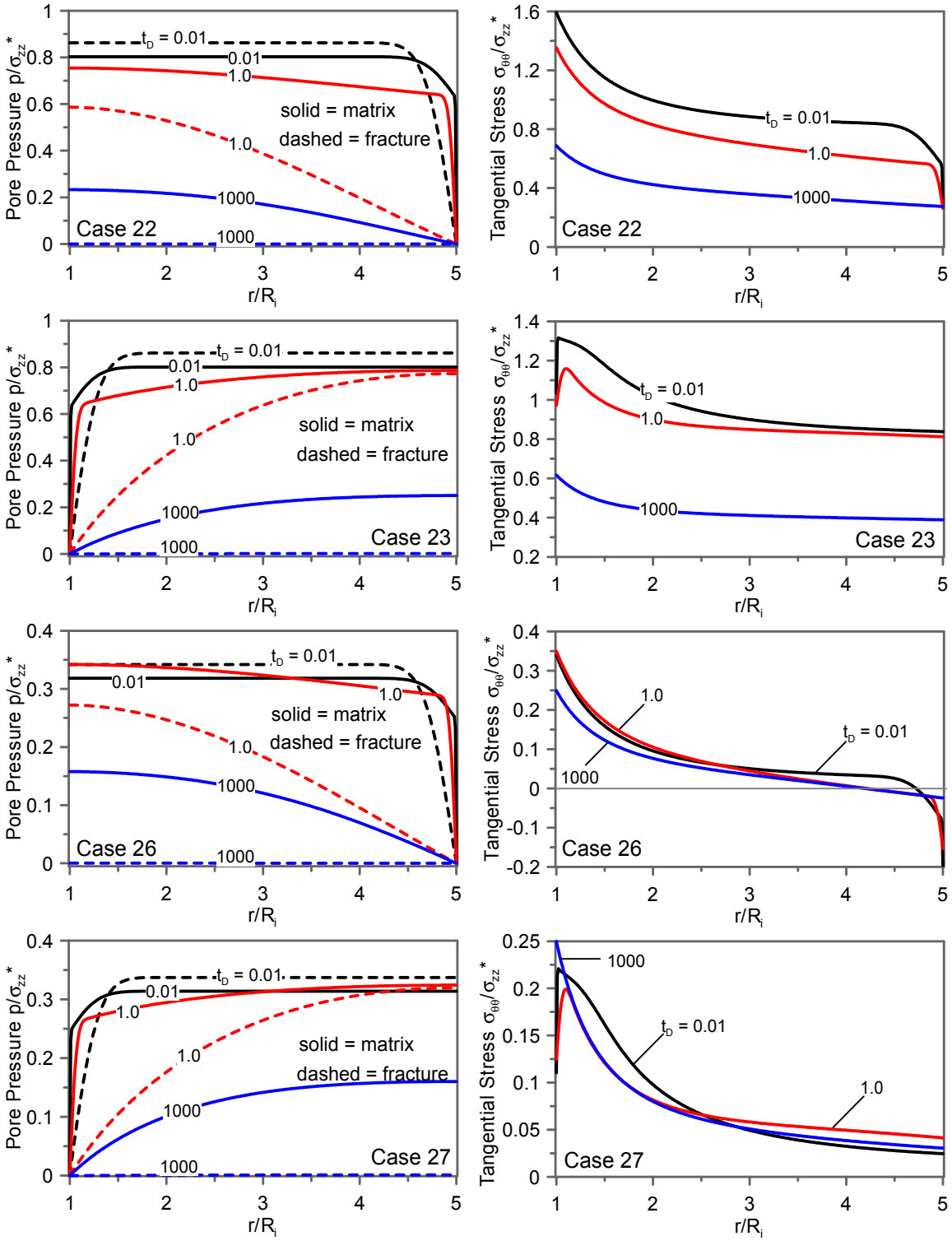

Fig. 2.44—Pore pressure and tangential stress responses for four different mixed fluid-pressure/flux and stress/displacement lateral boundary conditions (case 22, 23, 26, and 27).

2.5 Summary

In this chapter, a consistent anisotropic dual-poroelastic formulation is used to describe the proper responses of porous material exhibits multiporosity and/or multipermeability characteristics, such as secondary porosity or fracture. Specifically, the behavior of fractured rock formations is modeled as a dual-porosity and dual-permeability porous media. The model has been used to analyze the coupled responses of wellbore and consolidation through selected problem geometries including: (1) the inclined wellbore problem, which is of important applications in the field such as instantaneous drilling, pressurization of a borehole, production/injection from a reservoir; (2) the generalized Mandel-type problems, which is the canonical demonstration of poroelastic coupling, covering both rectangular and solid cylinder geometries; and (3) the hollow cylinder problem, which in the limiting case can be treated as a solid cylinder or wellbore problem.

The corresponding generalized analytical solutions to these problems are derived and presented in explicit analytical forms for both transverse and isotropic dual-porosity and dual-permeability poroelastic materials. These solutions account for arbitrary time-dependent external loading conditions, e.g., cyclic and ramping and can be tailored to simulate specific problems in laboratory testing (uniaxial, triaxial testing) or in the field (wellbore drilling, hydraulic fracturing). For ease of interpretation, the solutions are expressed in terms of dimensionless parameters such as storativity ratio, mobility ratio, dimensionless interporosity flow, etc. The model and solutions have been verified to reduce to the corresponding single-poroelastic ones.

Results for pore pressure, stress, and deformation are plotted to demonstrate the

differentiating characteristic of the dual-poroelastic behavior as well as the impact of the presence of the secondary porosity medium – or fracture network – on the overall response.

Specifically, the inclined wellbore solution shows that the different speeds of pressure dissipation in the matrix and fracture network lead to time-dependent modifications of pore pressure and stress distributions. Effective stress calculations show that the dual-poroelastic solution predictions differ substantially from single-poroelastic approach. For example, it was shown that the effective stress is higher in the compressive region and closer to tension in the tensile region around the wellbore in a fractured rock formation. Therefore, neglecting the contribution of the fracture network will likely mislead the predictions and optimization for field operations.

The dual-porous system exhibits typical dual-time-scale responses. Parametric analysis has been carried out for solid cylinder problem to study the effects of the dual characteristic time scales, poroelastic coefficients, and material anisotropy on the transient behaviors.

The rectangular Mandel's problem is shown to simplify to the classical one-dimensional consolidation problem and the results correctly reveal no non-monotonic pressure behavior after initial loading in contrast to previously published literature (Lewallen and Wang 1998).

Finally, the solutions and results for hollow cylinder's geometry provides general framework for simulating various problems spanning various fields including geomechanics and biomechanics. Particularly in the petroleum industry, this solution allows geomechanicians the ability to study the effect of fractures on the overall behaviors of naturally fractured rocks and reservoirs. In biomechanics, the same solutions can also be

applied to study the response of biological tissues well-known for their multiporosity makeup. Examples with realistic loading conditions for laboratory testing or field simulations will be provided in Chapter 5 to demonstrate the engineering applications of the presented dual-poroelastic formulation and solutions.

Chapter 3

Dual-Porosity and Dual-Permeability Porochemoelasticity: Dual-Porochemoelasticity[4]

3.1 Introduction

It has long been recognized that chemically active porous media exhibit swelling and/or shrinking when brought in contact with aqueous solutions. This phenomenon observed in clays, shales, and biological tissues is generally termed osmosis which is the non-hydraulically driven fluid flow. The chemical osmotic effect is generated from physicochemical interactions among pore fluid components with the invading fluid and the solid matrix, resulting in the membrane behavior, i.e., only transport of certain pore fluid species is allowed. A chemical potential gradient will induce simultaneous flows of fluid and solute in the porous medium. The coupled osmotic and solute transport processes can lead to strength weakening in addition to pore pressure elevation or reduction which could be very detrimental to the material integrity, in many engineering applications. Biot's poromechanical analyses addressing the coupled chemical effect, i.e., porochemoelastic,

[4] Part of this chapter was published in *J. Eng. Mech.* **135**(11): 1281-1293 (Nguyen and Abousleiman 2009)

have been formulated extensively in various fields based on mixture theory and/or non-equilibrium thermodynamic (Sachs and Grodzinsky 1987; Sherwood 1993; Heidug and Wong 1996; Huyghe and Janssen 1999).

The conventional porochemoelasticity models fluid saturated porous medium as single-porosity and single-permeability medium and thus fall short in describing the proper response of fractured rocks modeled as dual-porosity and dual-permeability porous medium (Barenblatt 1960; Warren and Root 1963; Bowen 1976; Aifantis 1977) or the behaviors of the well-known dual-porosity bone structures (Cowin 1999). Extension of Biot's theory of poroelasticity (Biot 1941) to account for the dual-porosity and dual-permeability nature of fractured porous media has been formulated by many researchers. Such formulations in the geomechanics domain (Wilson and Aifantis 1982; Valliappan and Khalili-Naghadeh 1990; Berryman and Wang 1995) only model the coupled solid deformation and fluid flow while not accounting for any chemical interaction. Recently in biomechanics, dual-porosity poroelastic models have been developed to include the effect of chemoelectrical interactions between pore fluid's species and the solid skeleton (Huyghe 1999; Simoes and Loret 2003) applicable to cartilaginous tissues. Their formulations, however, are the "dual-porosity and single-permeability" models in which the much slower transport processes in region with insignificant permeability are neglected to simplify the problem.

The time-dependent single-porochemoelastic solution, incorporating chemical osmosis and solute transport effect simulating inclined wellbore drilling stability through compact shale formation, have been presented and investigated extensively (Abousleiman et al.

2001; Ekbote and Abousleiman 2003, 2005, and 2006). Later, the analytical solution for inclined wellbores drilled in naturally fractured rock formations modeled as dual-porosity and dual-permeability continuum was published (Abousleiman and Nguyen 2005). This solution was recently extended to include chemical osmotic potential while neglecting the solute transport effect in fractured shale formations (Nguyen et al. 2009). It was found that dual-porosity and dual-permeability analyses show significantly different behaviors when compared to the single-porosity and single-permeability porochemoelastic counterparts. These solutions laid the foundation for the complete inclined wellbore stability solution for fractured shale accounting for both chemical osmosis and solute transport (Nguyen and Abousleiman 2009).

In this chapter, the analytical dual-porosity and dual-permeability porochemoelastic formulation and solution to two problem geometries, inclined wellbore and axially flow-only solid cylinder, are presented. First, the single-porosity porochemoelastic governing equations, extended based on thermodynamic framework of dual-poroelasticity to incorporate the effects of secondary porosity, e.g., rock's fractures, are briefly presented. The constituent porous matrix and fracture regions are generally modeled as imperfect semi-permeable membranes which can allows partial transport and exchange of the solutes. Individual porous matrix and fracture transport equations and inter-porosity exchange are written accounting for the fully coupled flow processes including hydraulic conduction (Darcy's law), chemical osmotic flow, and solute diffusion (Fick's law). The dissolution, deposition or chemical reaction as well as explicit modeling of electrostatic interaction between the solid skeleton and the saturating and/or invading fluid's species (Nguyen and

Abousleiman 2010b) are not considered in this work. The resulting system of equations is applied to obtain the analytical solutions of inclined wellbore drilling and uniaxial testing of solid cylinder geometries expressed in the Laplace transform domain. Results for dual pore pressures and stresses are plotted and compared with the corresponding single-porosity porochemoelastic counterparts to highlight the effects of fracture, chemical osmosis and solute transport on the overall responses.

3.2 Mathematical Formulation

This section briefly presented the governing equations describing the responses of dual-porous and chemically active media within the frame work of dual-porosity and dual-permeability porochemomechanics, hereafter termed "dual-porochemoelastic" for brevity. At the macroscopic level, the system is considered to consist of two co-located but distinct fluid-saturated porous continua: the primary one represents the porous matrix with intrinsic properties M^{I}_{ijkl} (stiffness), ϕ^{I} (porosity), and κ^{I}_{ij} (mobility) occupying volume fraction v^{I} of the total bulk volume and the secondary one represents the porous fractures with intrinsic properties M^{II}_{ijkl}, ϕ^{II}, and $\kappa^{\mathrm{II}}_{ij}$ occupying the remaining bulk volume fraction $\mathrm{v}^{\mathrm{II}} = 1 - \mathrm{v}^{\mathrm{I}}$. In other word, the overall domain is envisioned as containing two distinct porous continua, each possessing a skeletal framework and a saturated pore network. As a result, fractured formation will exhibit dual pore-pressure evolutions when subjected to stress and pressure perturbations. When the dual-porous medium is chemically active, additional coupled transport processes such as chemical osmotic and solute diffusion develop in both porous continua if there is imbalance in chemical activity or solute salinity. Additionally,

the primary and secondary porosity continua can communicate and may exchange fluid and/or solute mass.

3.2.1 Chemical Potential

The flow of fluid and its dissolving species are controlled by the total potential contribution from individual driving forces. In chemically active porous medium, the total driving force is the chemical potential which comprises of the fluid pressure and the chemical-activity-driven pressure given as (Katchalsky and Curran 1967)

$$\mu^r = V^r p + \mathrm{RT}\ln[a^r] = V^r p + i\mathrm{RT}\ln[\varsigma^r m^r] \quad \text{.....(3.1)}$$

where μ^r = chemical potential of the r^{th} fluid species (r = solvent and solutes), V^r = partial molar volume, p = thermodynamic pressure, R = universal gas constant, T = the temperature, $a^r = \varsigma^r m^r$ = chemical activity, ς^r = chemical activity coefficient, m^r = mole fraction with $\sum_r m^r = 1$, and i = number of solute's dissociating ions. Eq. 3.1 is written for electroneutral fluid components and ignores the contribution of electrostatic potential acting on the dissociating ions in solution. In an ideal or dilute solution, the activity coefficient has the property that $\varsigma^r \to 1$ as $m^r \to 0$ so $a^r \cong m^r$. For simplicity, both the primary (I) and secondary (II) porosity continua are assumed to comprise of a solid skeleton with interconnected pore space saturated with the same binary solution containing a solvent (f) and a solute (s) with mole fraction $m^{s(\mathrm{N})}$ and $m^{f(\mathrm{N})} = 1 - m^{s(\mathrm{N})}$, respectively where (N) = I, II.

3.2.2 Constitutive Equations

Because the total driving pressure is not the fluid pressure alone, the original Biot poroelasticity constitutive approach must be extended to account for the chemical potentials of all pore fluid species. The change in free energy density for a dual-porous medium completely saturated with a binary fluid solution can be expressed as (Coussy 2004)[5]

$$dW = \sigma_{ij} d\varepsilon_{ij} - \sum_{r=f,s} (M^{r\mathrm{I}} d\mu^{r\mathrm{I}} + M^{r\mathrm{II}} d\mu^{r\mathrm{II}}) \quad \text{.....(3.2)}$$

where σ_{ij} = total stress tensor, ε_{ij} = linearized total strain tensor, and $M^{r(\mathrm{N})}$ = mass content of the pore fluid species in mole per unit reference total bulk volume. The above expression is written assuming infinitesimal deformation, isothermal condition, no fluid-solid chemical reactions and dissolution or deposition processes taking place. The chemical potentials of all pore fluid components in each porosity system are not independent but related by the well known Gibbs-Duhem equation as (Katchalsky and Curran 1967)

$$-\mathrm{v}^{(\mathrm{N})}\phi^{(\mathrm{N})}\, dp^{(\mathrm{N})} + \sum_{r=f,s} M^{r(\mathrm{N})} d\mu^{r(\mathrm{N})} = 0 \quad \text{.....(3.3)}$$

In writing the above equation, it has been assumed that both primary and secondary pore-space systems are completely saturated such that $\mathrm{v}^{(\mathrm{N})}\phi^{(\mathrm{N})} = V^{f(\mathrm{N})} M^{f(\mathrm{N})} + V^{s(\mathrm{N})} M^{s(\mathrm{N})}$ where $\phi^{(\mathrm{N})} = \mathrm{V_p}^{(\mathrm{N})}/\mathrm{V}^{(\mathrm{N})}$ is the intrinsic porosity of the individual porous continua and $\mathrm{v}^{(\mathrm{N})}$ is the bulk volume fraction. Application of the Gibbs-Duhem equation into the free energy density leads to

[5] The free energy W in Eq. 3.2 is equivalent to the skeleton free energy G_s as defined in Eq. 3.66 by Coussy (2004)

$$dW = \sigma_{ij} d\varepsilon_{ij} - \mathrm{v}^{\mathrm{I}} \phi^{\mathrm{I}} dp^{\mathrm{I}} - \mathrm{v}^{\mathrm{II}} \phi^{\mathrm{II}} dp^{\mathrm{II}} \quad (3.4)$$

It is obvious that the free energy W admits ε_{ij}, p^{I} and p^{II} as state variables instead of the chemical potentials $\mu^{r(\mathrm{N})}$ of all pore fluid components. As such the linearized constitutive equations follow naturally as (compression is positive)

$$d\sigma_{ij} = \overline{M}_{ijkl} d\varepsilon_{kl} + \overline{\alpha}_{ij}^{\mathrm{I}} dp^{\mathrm{I}} + \overline{\alpha}_{ij}^{\mathrm{II}} dp^{\mathrm{II}} \quad (3.5)$$

$$d(\mathrm{v}^{\mathrm{I}} \phi^{\mathrm{I}}) = -\overline{\alpha}_{ij}^{\mathrm{I}} d\varepsilon_{ij} + \frac{dp^{\mathrm{I}}}{\overline{K}_{\phi}^{\mathrm{I}}} + \frac{dp^{\mathrm{II}}}{\overline{K}_{\phi}^{\mathrm{I,II}}} \quad (3.6)$$

$$d(\mathrm{v}^{\mathrm{II}} \phi^{\mathrm{II}}) = -\overline{\alpha}_{ij}^{\mathrm{II}} d\varepsilon_{ij} + \frac{dp^{\mathrm{I}}}{\overline{K}_{\phi}^{\mathrm{I,II}}} + \frac{dp^{\mathrm{II}}}{\overline{K}_{\phi}^{\mathrm{II}}} \quad (3.7)$$

where $\overline{M}_{ijkl}$ = overall stiffness modulus tensor, the inverse of which is the compliance tensor $\overline{C}_{ijkl}$; $\overline{\alpha}_{ij}^{(\mathrm{N})}$ = effective pore pressure coefficient; $1/\overline{K}_{\phi}^{(\mathrm{N})}$ and $1/\overline{K}_{\phi}^{\mathrm{I,II}}$ represent the apparent pore compressibility.

The intrinsic porosity, $\phi^{(\mathrm{N})}$, in Eqs. 3.6 and 3.7 can be replaced in favor of the variation in total fluid content $\zeta^{(\mathrm{N})}$ using the complete saturation condition and isothermal fluid state equation:

$$d\zeta^{(\mathrm{N})} = \frac{d\, M^{sol(\mathrm{N})}}{\rho_0^{sol(\mathrm{N})}} = \frac{d(\mathrm{v}^{(\mathrm{N})} \phi^{(\mathrm{N})}\, \rho^{sol(\mathrm{N})})}{\rho_0^{sol(\mathrm{N})}} = d(\mathrm{v}^{(\mathrm{N})} \phi^{(\mathrm{N})}) + \mathrm{v}^{(\mathrm{N})} \phi_0^{(\mathrm{N})} \frac{d\, \rho^{sol(\mathrm{N})}}{\rho_0^{sol(\mathrm{N})}} \quad (3.8)$$

$$\frac{d\, \rho^{sol(\mathrm{N})}}{\rho_0^{sol(\mathrm{N})}} = \frac{1}{K_f^{(\mathrm{N})}} dp^{(\mathrm{N})} \quad (3.9)$$

in which $M^{sol(\mathrm{N})} = M^{f(\mathrm{N})} + M^{s(\mathrm{N})}$ is the total fluid mass content (moles) and $\rho^{sol(\mathrm{N})}$ is the fluid mass density (mole/m^3); $1/K_f^{(\mathrm{N})}$ is the isothermal fluid compressibility; and the

subscript 0 denotes initial value. Using Eqs. 3.6, 3.7 and 3.9 into Eq. 3.8 yields

$$d\zeta^{\mathrm{I}} = -\overline{\alpha}_{ij}^{\mathrm{I}} d\varepsilon_{ij} + \frac{dp^{\mathrm{I}}}{\overline{M}^{\mathrm{I}}} + \frac{dp^{\mathrm{II}}}{\overline{M}^{\mathrm{I,II}}} \quad \text{.....(3.10)}$$

$$d\zeta^{\mathrm{II}} = -\overline{\alpha}_{ij}^{\mathrm{II}} d\varepsilon_{kk} + \frac{dp^{\mathrm{I}}}{\overline{M}^{\mathrm{I,II}}} + \frac{dp^{\mathrm{II}}}{\overline{M}^{\mathrm{II}}} \quad \text{.....(3.11)}$$

where $1/\overline{M}^{(\mathrm{N})} = 1/\overline{K}_{\phi}^{(\mathrm{N})} + \mathrm{v}^{(\mathrm{N})}\phi_0^{(\mathrm{N})} / K_f^{(\mathrm{N})}$ and $1/\overline{M}^{\mathrm{I,II}} = 1/\overline{K}_{\phi}^{\mathrm{I,II}}$ are the apparent storage coefficients of the dual-porous system. Additionally, it is necessary to obtain the variation of solute content by linearizing the relation

$$d\zeta^{s(\mathrm{N})} = \frac{d\,M^{s(\mathrm{N})}}{\rho_0^{sol(\mathrm{N})}} = \frac{d(m^{s(\mathrm{N})}\,M^{sol(\mathrm{N})})}{\rho_0^{sol(\mathrm{N})}} = m_0^{s(\mathrm{N})} d\zeta^{(\mathrm{N})} + \mathrm{v}^{(\mathrm{N})}\phi_0^{(\mathrm{N})} d\,m^{s(\mathrm{N})} \quad \text{.....(3.12)}$$

in which $m^{s(\mathrm{N})} = M^{s(\mathrm{N})} / M^{sol(\mathrm{N})}$ = solute mole fraction and the initial porosity is related to the initial fluid mass content and density as $\mathrm{v}^{(\mathrm{N})}\phi_0^{(\mathrm{N})} = M_0^{sol(\mathrm{N})} / \rho_0^{sol(\mathrm{N})}$. Substituting Eqs. 3.10 and 3.11 into Eq. 3.12 gives the solute content variations as

$$d\zeta^{s\mathrm{I}} = m_0^{s\mathrm{I}}\left(-\overline{\alpha}^{\mathrm{I}}\, d\varepsilon_{kk} + \frac{dp^{\mathrm{I}}}{\overline{M}^{\mathrm{I}}} + \frac{dp^{\mathrm{II}}}{\overline{M}^{\mathrm{I,II}}}\right) + \mathrm{v}^{\mathrm{I}}\phi_0^{\mathrm{I}}\, dm^{s\mathrm{I}} \quad \text{.....(3.13)}$$

$$d\zeta^{r\mathrm{II}} = m_0^{s\mathrm{II}}\left(-\overline{\alpha}^{\mathrm{II}}\, d\varepsilon_{kk} + \frac{dp^{\mathrm{II}}}{\overline{M}^{\mathrm{I,II}}} + \frac{dp^{\mathrm{II}}}{\overline{M}^{\mathrm{II}}}\right) + \mathrm{v}^{\mathrm{II}}\phi_0^{\mathrm{II}} dm^{s\mathrm{II}} \quad \text{.....(3.14)}$$

In summary, the constitutive equations for a dual-porous and chemically active medium are:

$$\sigma_{ij} = \overline{M}_{ijkl}\varepsilon_{kl} + \overline{\alpha}_{ij}^{\mathrm{I}} p^{\mathrm{I}} + \overline{\alpha}_{ij}^{\mathrm{II}} p^{\mathrm{II}} \quad \text{.....(3.15)}$$

$$\zeta^{\mathrm{I}} = -\overline{\alpha}_{ij}^{\mathrm{I}}\varepsilon_{ij} + \frac{p^{\mathrm{I}}}{\overline{M}^{\mathrm{I}}} + \frac{p^{\mathrm{II}}}{\overline{M}^{\mathrm{I,II}}} \quad \text{.....(3.16)}$$

$$\zeta^{\mathrm{II}} = -\overline{\alpha}_{ij}^{\mathrm{II}}\varepsilon_{ij} + \frac{p^{\mathrm{I}}}{\overline{M}^{\mathrm{I,II}}} + \frac{p^{\mathrm{II}}}{\overline{M}^{\mathrm{II}}} \quad \text{.....(3.17)}$$

$$\zeta^{s\mathrm{I}} = m_0^{s\mathrm{I}}\left(-\overline{\alpha}_{ij}^{\mathrm{I}}\varepsilon_{ij} + \frac{p^{\mathrm{I}}}{\overline{M}^{\mathrm{I}}} + \frac{p^{\mathrm{II}}}{\overline{M}^{\mathrm{I,II}}}\right) + \mathrm{v}^{\mathrm{I}}\phi_0^{\mathrm{I}} m^{s\mathrm{I}} \quad \text{.....(3.18)}$$

$$\zeta^{s\mathrm{II}} = m_0^{s\mathrm{II}}\left(-\overline{\alpha}_{ij}^{\mathrm{II}}\varepsilon_{ij} + \frac{p^{\mathrm{II}}}{\overline{M}^{\mathrm{I,II}}} + \frac{p^{\mathrm{II}}}{\overline{M}^{\mathrm{II}}}\right) + \mathrm{v}^{\mathrm{II}}\phi_0^{\mathrm{II}} m^{s\mathrm{II}} \quad \text{.....(3.19)}$$

where the differential operator *d* has been dropped for convenience.

Eqs. 3.18 and 3.19 show that the variation in solute contents are not only related to pore-fluid composition (solute mole fraction) but are also affected by the dual pore pressures and total volumetric strain. For dilute concentration ($m_0^{s\mathrm{I}}, m_0^{s\mathrm{II}} << 1$), the effect of fluid pressures and deformation on solute contents is small and can be neglected. On the other hand, Eqs. 3.15 to 3.17 have the same form as the dual-poroelastic formulation without chemical effect presented Chapter 2. It can be observed that the dual fluid pressures, not the chemical potentials, are important; and changing the fluid composition (or chemical activity) of the pore fluid at constant pressure will not affect the total stress, total strain and/or variation of fluid contents in the primary or secondary porosity. The chemical effect will, however, enter via the transient nature of the fluid and solute flows due to differences in the chemical potential across the dual-porous medium.

3.2.3 Coupled Transport Equations

Eq. 3.1 shows that chemical potential difference can be caused by imbalances in the fluid pressure or in the chemical activity/solute concentration. The presence of the chemical gradient results in simultaneous fluxes of the pore fluid species. Assuming that the flow in

each constituting continuum is independent of the flow in the other, separate sets of linear transport equations can be written for the primary and secondary porosity as:

$$q_i^{(\mathrm{N})} = L_{11}^{(\mathrm{N})} \frac{\partial(-p^{(\mathrm{N})})}{\partial x_i} + L_{12}^{(\mathrm{N})} \frac{i\mathrm{RT}}{m_0^{s(\mathrm{N})}} \frac{\partial(-m^{s(\mathrm{N})})}{\partial x_i} \quad \text{.....(3.20)}$$

$$J_i^{\mathrm{s,d(N)}} = L_{21}^{(\mathrm{N})} \frac{\partial(-p^{(\mathrm{N})})}{\partial x_i} + L_{22}^{(\mathrm{N})} \frac{i\mathrm{RT}}{m_0^{s(\mathrm{N})}} \frac{\partial(-m^{s(\mathrm{N})})}{\partial x_i} \quad \text{.....(3.21)}$$

where x_i = the spatial coordinates; $q_i^{(\mathrm{N})}$ = volumetric fluid flow vector through the porous medium per unit time ($\mathrm{m \cdot s^{-1}}$); $V_0^f J_i^{\mathrm{s,d(N)}} \cong q_i^{s(\mathrm{N})} - m^{s(\mathrm{N})} q_i^{(\mathrm{N})}$ = solute diffusion flux ($\mathrm{m \cdot s^{-1}}$) relative to that of the solvent in which $q_i^{s(\mathrm{N})}$ = absolute solute volumetric flux relative to the solid framework.

$L_{mn}^{(\mathrm{N})}$ = phenomenological coefficients representing coupled transport processes such as hydraulic conduction (Darcy's law), chemico-osmosis, and solute/ion diffusion (Fick's first law). According to the Onsager principle, $L_{21}^{(\mathrm{N})} = L_{12}^{(\mathrm{N})}$, which results in only three independent transport coefficients for each constituting porous medium. These transport coefficients have been well identified in the literature and can be expressed in terms of familiar field and/or laboratory measurable parameters such as permeability, $k_{ij}^{(\mathrm{N})}$, or mobility, $\kappa_{ij}^{(\mathrm{N})}$, reflection coefficient, $\chi^{(\mathrm{N})}$, solute effective diffusion coefficients, $D_{ij}^{s,eff\,(\mathrm{N})}$, as summarized in Table 2. The transport coefficients as presented in Table 1 are slightly modified from parameters as derived by Yeung and Mitchell (1993) to account for the limiting behavior of the effective solute diffusion when the material's membrane behavior is ideal (Bader and Kooi 2005), i.e., the absolute solute fluxes vanish, $q_i^{s(\mathrm{N})} = 0$, for perfect

membrane efficiency, $\chi^{(N)} = 1$. It has been shown theoretically and experimentally that the ability of membrane to hinder solute movement depend on factors such as solute concentration, particle size compared to pore scale (degree of compaction) and electrostatic interaction between the solute's dissociating ions and the charged solid skeleton [cation exchange capacity (CEC)] (Katchalsky and Curan 1967; Fritz and Marine 1983). In fact, the effect of all chemicoelectrical interactions between the fluid and the solid skeleton are lumped into the reflection coefficient. Theoretical determination the reflection coefficient in terms of concentration, compaction and CEC were provided by Hanshaw (1964) and Fritz and Marine (1983). Generally, these transport coefficients $L_{mn}^{(N)}$ are functions of solute concentration. When the system is not too far from equilibrium, i.e., when the macroscopic gradients are sufficiently small, these coefficients can be assumed to be constants.

TABLE 2—COUPLED TRANSPORT COEFFICIENTS

Coefficients	Formulas	Transport Processes
L_{11}	κ_{ij}	Hydraulic conduction – Darcy's law; $\kappa_{ij} = k_{ij}/\mu$ mobility; k_{ij} = permeability and μ = fluid viscosity.
$L_{12} = L_{21}$	$(-\chi\kappa_{ij})(m_0^s/V_0^f)$	Chemical osmosis; χ = reflection coefficient or membrane efficiency [0,1].
L_{22}	$\frac{D_{ij}^{s,eff}}{RT}\frac{m_0^s}{V_0^f} + \left(\frac{\chi m_0^s}{V_0^f}\right)^2 \kappa_{ij}$	Solute diffusion - Fick's first law $D_{ij}^{s,eff} = (1-\chi)\phi^\tau D_0^s$ where D_0^s = solute diffusion coefficient in free solution; ϕ = porosity; τ = tortuosity.

3.2.4 Other Governing Equations

Other governing equations are the strain-displacement relations (Eq. 2.6) and conservation equations which include the quasi-static stress equilibrium equation (Eq. 2.7), and mass

balance equations (Eqs. 3.22 to 3.25) accounting for interporosity fluid and solute exchange as follows

$$\frac{\partial \zeta^{\mathrm{I}}}{\partial t} = -\mathrm{v}^{\mathrm{I}} \frac{\partial q_i^{\mathrm{I}}}{\partial x_i} + \Gamma \quad \text{.....(3.22)}$$

$$\frac{\partial \zeta^{\mathrm{sI}}}{\partial t} = -\mathrm{v}^{\mathrm{I}} \frac{\partial q_i^{\mathrm{sI}}}{\partial x_i} + \Gamma^s \quad \text{.....(3.23)}$$

$$\frac{\partial \zeta^{\mathrm{II}}}{\partial t} = -\mathrm{v}^{\mathrm{II}} \frac{\partial q_i^{\mathrm{II}}}{\partial x_i} - \Gamma \quad \text{.....(3.24)}$$

$$\frac{\partial \zeta^{\mathrm{sII}}}{\partial t} = -\mathrm{v}^{\mathrm{II}} \frac{\partial q_i^{\mathrm{sII}}}{\partial x_i} - \Gamma^s \quad \text{.....(3.25)}$$

in which u_i = displacement vector and Γ and Γ^{s} = interporosity fluid and solute volumetric fluxes. The solute mass conservations are written in terms of the absolute solute fluxes defined as $q_i^{s(\mathrm{N})} \cong V_0^f J_i^{\mathrm{s,d(N)}} - m^{s(\mathrm{N})} q_i^{(\mathrm{N})}$. As such, Eqs. 3.23 and 3.25 become

$$\frac{\partial \zeta^{\mathrm{sI}}}{\partial t} = -\mathrm{v}^{\mathrm{I}} \left[V_0^f \frac{\partial J_i^{\mathrm{s,dI}}}{\partial x_i} + m^{s\mathrm{I}} \frac{\partial q_i^{\mathrm{I}}}{\partial x_i} + q_i^{\mathrm{I}} \frac{\partial m_i^{\mathrm{sI}}}{\partial x_i} \right] + \Gamma^s \quad \text{.....(3.26)}$$

$$\frac{\partial \zeta^{\mathrm{sII}}}{\partial t} = -\mathrm{v}^{\mathrm{II}} \left[V_0^f \frac{\partial J_i^{\mathrm{s,dII}}}{\partial x_i} + m^{s\mathrm{II}} \frac{\partial q_i^{\mathrm{II}}}{\partial x_i} + q_i^{\mathrm{II}} \frac{\partial m_i^{\mathrm{sII}}}{\partial x_i} \right] - \Gamma^s \quad \text{.....(3.27)}$$

The last terms in the bracket on the right-hand side of Eqs. 3.26 and 3.27 correspond to solute transport by advection and render the equations nonlinear. When the hydraulic diffusion ($\kappa_{ij}^{(\mathrm{N})}$) is smaller than the effective solute diffusion ($D_{ij}^{s,eff\,(\mathrm{N})} V_0^f / i\mathrm{RT}$), the solute diffusion mechanism dominates and advection contribution can be neglected (Yeung and Datla 1995). In addition, if the change in solute concentration is small, the solute transport

process can be linearized by taking $m^{s\mathrm{I}} \dfrac{\partial q_i^{\mathrm{I}}}{\partial x_i} \approx m_0^{s\mathrm{I}} \dfrac{\partial q_i^{\mathrm{I}}}{\partial x_i}$ and $q_i^{\mathrm{I}} \dfrac{\partial m_i^{s\mathrm{I}}}{\partial x_i} \approx 0$ leading to

$$\frac{\partial \zeta^{s\mathrm{I}}}{\partial t} = -\mathrm{v}^{\mathrm{I}}\left[D_{21}^{\mathrm{I}}\nabla^2(-p^{\mathrm{I}}) + D_{22}^{\mathrm{I}}\nabla^2(-p^{s\mathrm{I}})\right] + \Gamma^s \quad \text{.....(3.28)}$$

$$\frac{\partial \zeta^{s\mathrm{II}}}{\partial t} = -\mathrm{v}^{\mathrm{II}}\left[D_{21}^{\mathrm{II}}\nabla^2(-p^{\mathrm{II}}) + D_{22}^{\mathrm{II}}\nabla^2(-p^{s\mathrm{II}})\right] - \Gamma^s \quad \text{.....(3.29)}$$

where ∇^2 = Laplacian differential operator, $p^{s(\mathrm{N})} = (i\mathrm{RT}/V_0^f)m^{s(\mathrm{N})}$ = pressure equivalent term for solute concentration, and $D_{21}^{(\mathrm{N})}$ and $D_{22}^{(\mathrm{N})}$ are parts of a lumped transport coefficient matrix defined in terms of the original transport coefficients $L_{mn}^{(\mathrm{N})}$ as:

$$\begin{bmatrix} D_{11}^{(\mathrm{N})} & D_{12}^{(\mathrm{N})} \\ D_{21}^{(\mathrm{N})} & D_{22}^{(\mathrm{N})} \end{bmatrix} = \begin{bmatrix} \kappa_{ij}^{(\mathrm{N})} & -\chi^{(\mathrm{N})}\kappa_{ij}^{(\mathrm{N})} \\ m_0^{s(\mathrm{N})}(1-\chi^{(\mathrm{N})})\kappa_{ij}^{(\mathrm{N})} & D_{ij}^{s,eff\,(\mathrm{N})}\dfrac{V_0^f}{i\mathrm{RT}} - m_0^{s(\mathrm{N})}(1-\chi^{(\mathrm{N})})\chi^{(\mathrm{N})}\kappa_{ij}^{(\mathrm{N})} \end{bmatrix} \quad \text{.....(3.30)}$$

In the above $D_{11}^{(\mathrm{N})}$ and $D_{12}^{(\mathrm{N})}$ correspond to the transport coefficients associated with the total fluid fluxes, $q_i^{(\mathrm{N})}$. In the field, large concentration changes are usually encountered and the high hydraulic conductivity in the secondary porosity can lead to non-negligible advection effect. If these nonlinear effects are to be accounted for then numerical approaches such as finite difference or finite element are needed in subsequent solutions and analyses.

Analogous to the local coupled flow mechanism, the driving forces for the interporosity volumetric fluid and solute transfer are the chemical potential gradient at the interface between the porous primary and secondary porosity continua. Extending Warren and Root (1963) approach, the interporosity fluid and solute exchanges are hypothesized to be

dependent upon the fluid pressure and solute concentration differences between the porous regions, the transport properties of the less-conducting region, e.g., primary porosity (I), and the geometrical characteristic

$$\Gamma = \lambda\,[D_{11}^{\mathrm{I}}(p^{\mathrm{II}} - p^{\mathrm{I}}) + D_{12}^{\mathrm{I}}(p^{\mathrm{sII}} - p^{\mathrm{sI}})] \quad \text{.....(3.31)}$$

$$\Gamma^{\mathrm{s}} = \lambda\,[D_{21}^{\mathrm{I}}(p^{\mathrm{II}} - p^{\mathrm{I}}) + D_{22}^{\mathrm{I}}(p^{\mathrm{sII}} - p^{\mathrm{sI}})] \quad \text{.....(3.32)}$$

in which λ is the geometric factor accounting for the geometry, distribution and connectivity of the dual-porous structure.

The constitutive Eqs. 3.15 to 3.19, the transport Eqs. 3.20, 3.21, 3.31, and 3.32, the strain-displacement Eq. 2.6, and the conservation Eqs. 2.7 and 3.22 to 3.25 complete the governing equations for the behavior of dual-porosity and dual-permeability chemically active porous medium saturated with a binary pore fluid solution. Unlike previous work of others (Wilson and Aifantis 1982; Huyghe 1999) with appropriate simplifying assumptions regarding different time scales among various processes in the matrix or fracture, the current set of diffusion equations fully accounts for the dual-porosity, dual-permeability and dual-stiffness nature of the overall system. Therefore, the formulation can be generally applied to dual-porous system, especially where the apparent time scales are not significantly different from each other. On the other hand, because the linearized formulation do not account for any chemical reaction that would alter the mechanical behaviors of the dual-porous system, it results are limited to small range of perturbation of field variables.

3.2.5 Field and Diffusion Equations

The above governing equations are further combined to yield the field and diffusion equations that are used to solve for the coupled stress and pore-pressure responses in general anisotropic materials. In this section, they are specialized to transversely isotropic and isotropic materials for cylindrical geometry.

Transversely Isotropic Case. In the case of transverse isotropy where the z axis is assumed to coincide with the overall axis of material rotation symmetry, the constitutive relations for dual-porochemoelasticity involve twelve independent material coefficients and are given as

$$\sigma_{rr} = \overline{M}_{11}\varepsilon_{rr} + \overline{M}_{12}\varepsilon_{\theta\theta} + \overline{M}_{13}\varepsilon_{zz} + \overline{\alpha}_1^{\mathrm{I}} p^{\mathrm{I}} + \overline{\alpha}_1^{\mathrm{II}} p^{\mathrm{II}}, \quad (3.33)$$

$$\sigma_{\theta\theta} = \overline{M}_{12}\varepsilon_{rr} + \overline{M}_{11}\varepsilon_{\theta\theta} + \overline{M}_{13}\varepsilon_{zz} + \overline{\alpha}_1^{\mathrm{I}} p^{\mathrm{I}} + \overline{\alpha}_1^{\mathrm{II}} p^{\mathrm{II}}, \quad (3.34)$$

$$\sigma_{zz} = \overline{M}_{13}\varepsilon_{rr} + \overline{M}_{13}\varepsilon_{\theta\theta} + \overline{M}_{33}\varepsilon_{zz} + \overline{\alpha}_3^{\mathrm{I}} p^{\mathrm{I}} + \overline{\alpha}_3^{\mathrm{II}} p^{\mathrm{II}}, \quad (3.35)$$

$$\sigma_{r\theta} = 2\overline{M}_{44}\varepsilon_{r\theta}; \qquad \sigma_{r\theta} = 2\overline{M}_{55}\varepsilon_{rz}; \qquad \sigma_{\theta z} = 2\overline{M}_{55}\varepsilon_{\theta z}, \quad (3.36)$$

$$\zeta^{\mathrm{I}} = -\overline{\alpha}_1^{\mathrm{I}}(\varepsilon_{rr} + \varepsilon_{\theta\theta}) - \overline{\alpha}_3^{\mathrm{I}}\varepsilon_{zz} + \frac{p^{\mathrm{I}}}{\overline{M}^{\mathrm{I}}} + \frac{p^{\mathrm{II}}}{\overline{M}^{\mathrm{I,II}}}, \quad (3.37)$$

$$\zeta^{\mathrm{II}} = -\overline{\alpha}_1^{\mathrm{II}}(\varepsilon_{rr} + \varepsilon_{\theta\theta}) - \overline{\alpha}_3^{\mathrm{II}}\varepsilon_{zz} + \frac{p^{\mathrm{I}}}{\overline{M}^{\mathrm{I,II}}} + \frac{p^{\mathrm{II}}}{\overline{M}^{\mathrm{II}}}, \quad (3.38)$$

$$\zeta^{s\mathrm{I}} = m_0^{s\mathrm{I}}\left(-\overline{\alpha}_1^{\mathrm{I}}(\varepsilon_{rr} + \varepsilon_{\theta\theta}) - \overline{\alpha}_3^{\mathrm{I}}\varepsilon_{zz} + \frac{p^{\mathrm{I}}}{\overline{M}^{\mathrm{I}}} + \frac{p^{\mathrm{II}}}{\overline{M}^{\mathrm{I,II}}}\right) + \frac{\mathrm{v}^{\mathrm{I}}\phi_0^{\mathrm{I}}V_0^f}{i\mathrm{RT}} p^{s\mathrm{I}}, \quad (3.39)$$

$$\zeta^{s\mathrm{II}} = m_0^{s\mathrm{II}}\left(-\overline{\alpha}_1^{\mathrm{II}}(\varepsilon_{rr} + \varepsilon_{\theta\theta}) - \overline{\alpha}_3^{\mathrm{II}}\varepsilon_{zz} + \frac{p^{\mathrm{I}}}{\overline{M}^{\mathrm{I,II}}} + \frac{p^{\mathrm{II}}}{\overline{M}^{\mathrm{II}}}\right) + \frac{\mathrm{v}^{\mathrm{II}}\phi_0^{\mathrm{II}}V_0^f}{i\mathrm{RT}} p^{s\mathrm{II}}, \quad (3.40)$$

In the above, the subscripts 1 and 2 denote properties in the isotropic plane and 3 represents the axis of rotational symmetric. The coefficients, $\overline{M}_{11}$, $\overline{M}_{12}$, $\overline{M}_{13}$, $\overline{M}_{33}$, $\overline{M}_{44}$, and $\overline{M}_{55}$ are components of the drained overall elastic tensor for a transversely isotropic dual-porous material. $\overline{\alpha}_1^{(\mathrm{N})}$ and $\overline{\alpha}_3^{(\mathrm{N})}$ are Biot's effective stress coefficients in the isotropic plane and transverse direction, respectively.

The transversely isotropic equations are further reduced to the plane-strain (r-θ) case where all response functions are invariant along the axis of material rotational symmetry and the out-of-plane strain components are zero, i.e., $\varepsilon_{rz} = \varepsilon_{\theta z} = 0$ and $\varepsilon_{zz} = 0$. The constitutive equations for in-plane stress components reduce to

$$\sigma_{rr} = \overline{M}_{11}\varepsilon_{rr} + \overline{M}_{12}\varepsilon_{\theta\theta} + \overline{\alpha}_1^{\mathrm{I}} p^{\mathrm{I}} + \overline{\alpha}_1^{\mathrm{II}} p^{\mathrm{II}}, \quad (3.41)$$

$$\sigma_{\theta\theta} = \overline{M}_{12}\varepsilon_{rr} + \overline{M}_{11}\varepsilon_{\theta\theta} + \overline{\alpha}_1^{\mathrm{I}} p^{\mathrm{I}} + \overline{\alpha}_1^{\mathrm{II}} p^{\mathrm{II}}, \quad (3.42)$$

$$\sigma_{r\theta} = 2\overline{M}_{44}\varepsilon_{r\theta}, \quad (3.43)$$

with the strain components defined as

$$\varepsilon_{rr} = \frac{\partial u_r}{\partial r}, \qquad \varepsilon_{\theta\theta} = \frac{u_r}{r} + \frac{1}{r}\frac{\partial u_\theta}{\partial \theta}, \qquad \varepsilon_{r\theta} = \frac{1}{2}\left(\frac{1}{r}\frac{\partial u_r}{\partial \theta} + \frac{\partial u_\theta}{\partial r} - \frac{u_\theta}{r}\right), \quad (3.44)$$

The quasi-static stress equilibrium equation becomes

$$\frac{\partial \sigma_{rr}}{\partial r} + \frac{1}{r}\frac{\partial \sigma_{\theta r}}{\partial \theta} + \frac{\sigma_{rr} - \sigma_{\theta\theta}}{r} = 0, \quad (3.45)$$

$$\frac{\partial \sigma_{r\theta}}{\partial r} + \frac{1}{r}\frac{\partial \sigma_{\theta\theta}}{\partial \theta} + \frac{2\sigma_{r\theta}}{r} = 0, \quad (3.46)$$

Combining Eqs. 3.41 to 3.46 yields the compatibility equation as

$$\nabla^2\left(\varepsilon_{kk}+\frac{\overline{\alpha}_1^{\mathrm{I}}}{\overline{M}_{11}}p^{\mathrm{I}}+\frac{\overline{\alpha}_1^{\mathrm{II}}}{\overline{M}_{11}}p^{\mathrm{II}}\right)=0\,, \qquad (3.47)$$

where $\varepsilon_{kk}=\varepsilon_{rr}+\varepsilon_{\theta\theta}$ is the total volumetric strain and $\nabla^2=\frac{\partial^2}{\partial r^2}+\frac{1}{r}\frac{\partial}{\partial r}+\frac{1}{r^2}\frac{\partial^2}{\partial\theta^2}$. Next, the diffusion equations are obtained by substituting the fluid and solute content constitutive Eqs. 3.37 to 3.40 into the fluid continuity Eqs. 3.22 to 3.25 as

$$-\overline{\alpha}_1^{\mathrm{I}}\frac{\partial\varepsilon_{kk}}{\partial t}+\frac{1}{\overline{M}^{\mathrm{I}}}\frac{\partial p^{\mathrm{I}}}{\partial t}+\frac{1}{\overline{M}^{\mathrm{I,II}}}\frac{\partial p^{\mathrm{II}}}{\partial t}= \qquad (3.48)$$
$$\mathrm{v}^{\mathrm{I}}(D_{11}^{\mathrm{I}}\nabla^2p^{\mathrm{I}}+D_{12}^{\mathrm{I}}\nabla^2p^{\mathrm{sI}})+\lambda[D_{11}^{\mathrm{I}}(p^{\mathrm{II}}-p^{\mathrm{I}})+D_{12}^{\mathrm{I}}(p^{\mathrm{sII}}-p^{\mathrm{sI}})]$$

$$m_0^{s\mathrm{I}}\left(-\overline{\alpha}_1^{\mathrm{I}}\frac{\partial\varepsilon_{kk}}{\partial t}+\frac{1}{\overline{M}^{\mathrm{I}}}\frac{\partial p^{\mathrm{I}}}{\partial t}+\frac{1}{\overline{M}^{\mathrm{I,II}}}\frac{\partial p^{\mathrm{II}}}{\partial t}\right)+\frac{\mathrm{v}^{\mathrm{I}}\phi_0^{\mathrm{I}}V_0^f}{i\mathrm{RT}}\frac{\partial p^{s\mathrm{I}}}{\partial t}= \qquad (3.49)$$
$$\mathrm{v}^{\mathrm{I}}(D_{21}^{\mathrm{I}}\nabla^2p^{\mathrm{I}}+D_{22}^{\mathrm{I}}\nabla^2p^{\mathrm{sI}})+\lambda[D_{21}^{\mathrm{I}}(p^{\mathrm{II}}-p^{\mathrm{I}})+D_{22}^{\mathrm{I}}(p^{\mathrm{sII}}-p^{\mathrm{sI}})]$$

$$-\overline{\alpha}_1^{\mathrm{II}}\frac{\partial\varepsilon_{kk}}{\partial t}+\frac{1}{\overline{M}^{\mathrm{I,II}}}\frac{\partial p^{\mathrm{I}}}{\partial t}+\frac{1}{\overline{M}^{\mathrm{II}}}\frac{\partial p^{\mathrm{II}}}{\partial t}= \qquad (3.50)$$
$$\mathrm{v}^{\mathrm{II}}(D_{11}^{\mathrm{II}}\nabla^2p^{\mathrm{II}}+D_{12}^{\mathrm{II}}\nabla^2p^{\mathrm{sII}})-\lambda[D_{11}^{\mathrm{I}}(p^{\mathrm{II}}-p^{\mathrm{I}})+D_{12}^{\mathrm{I}}(p^{\mathrm{sII}}-p^{\mathrm{sI}})]$$

$$m_0^{s\mathrm{II}}\left(-\overline{\alpha}_1^{\mathrm{II}}\frac{\partial\varepsilon_{kk}}{\partial t}+\frac{1}{\overline{M}^{\mathrm{I,II}}}\frac{\partial p^{\mathrm{I}}}{\partial t}+\frac{1}{\overline{M}^{\mathrm{II}}}\frac{\partial p^{\mathrm{II}}}{\partial t}\right)+\frac{\mathrm{v}^{\mathrm{II}}\phi_0^{\mathrm{II}}V_0^f}{i\mathrm{RT}}\frac{\partial p^{s\mathrm{II}}}{\partial t}= \qquad (3.51)$$
$$\mathrm{v}^{\mathrm{II}}(D_{21}^{\mathrm{II}}\nabla^2p^{\mathrm{II}}+D_{22}^{\mathrm{II}}\nabla^2p^{\mathrm{sII}})-\lambda[D_{21}^{\mathrm{I}}(p^{\mathrm{II}}-p^{\mathrm{I}})+D_{22}^{\mathrm{I}}(p^{\mathrm{sII}}-p^{\mathrm{sI}})]$$

with $D_{ij}^{(\mathrm{N})}$ reduced to the transport coefficients in the isotropic plane, e.g.,

$$\begin{bmatrix}D_{11}^{(\mathrm{N})} & D_{12}^{(\mathrm{N})}\\ D_{21}^{(\mathrm{N})} & D_{22}^{(\mathrm{N})}\end{bmatrix}=\begin{bmatrix}\kappa_1^{(\mathrm{N})} & -\chi^{(\mathrm{N})}\kappa_1^{(\mathrm{N})}\\ m_0^{s(\mathrm{N})}(1-\chi^{(\mathrm{N})})\kappa_1^{(\mathrm{N})} & D_1^{s,eff\,(\mathrm{N})}\frac{V_0^f}{i\mathrm{RT}}-m_0^{s(\mathrm{N})}(1-\chi^{(\mathrm{N})})\chi^{(\mathrm{N})}\kappa_1^{(\mathrm{N})}\end{bmatrix}, \qquad (3.52)$$

Isotropic Case. For isotropic dual-porous material, the constitutive equations for dual-porochemoelasticity reduce to

$$\sigma_{ij} = \frac{\overline{E}}{1+\overline{\nu}}\left[\varepsilon_{ij} + \frac{\overline{\nu}}{(1-2\overline{\nu})}\varepsilon_{kk}\delta_{ij}\right] + (\overline{\alpha}^{\mathrm{I}} p^{\mathrm{I}} + \overline{\alpha}^{\mathrm{II}} p^{\mathrm{II}})\delta_{ij}, \quad (3.53)$$

$$\zeta^{\mathrm{I}} = -\overline{\alpha}^{\mathrm{I}}\varepsilon_{kk} + \frac{p^{\mathrm{I}}}{\overline{M}^{\mathrm{I}}} + \frac{p^{\mathrm{II}}}{\overline{M}^{\mathrm{I,II}}}, \quad (3.54)$$

$$\zeta^{\mathrm{II}} = -\overline{\alpha}^{\mathrm{II}}\varepsilon_{kk} + \frac{p^{\mathrm{I}}}{\overline{M}^{\mathrm{I,II}}} + \frac{p^{\mathrm{II}}}{\overline{M}^{\mathrm{II}}}, \quad (3.55)$$

$$\zeta^{s\mathrm{I}} = m_0^{s\mathrm{I}}\left(-\overline{\alpha}^{\mathrm{I}}\varepsilon_{kk} + \frac{p^{\mathrm{I}}}{\overline{M}^{\mathrm{I}}} + \frac{p^{\mathrm{II}}}{\overline{M}^{\mathrm{I,II}}}\right) + \frac{\mathrm{v}^{\mathrm{I}}\phi_0^{\mathrm{I}}V_0^f}{i\mathrm{RT}} p^{s\mathrm{I}}, \quad (3.56)$$

$$\zeta^{s\mathrm{II}} = m_0^{s\mathrm{II}}\left(-\overline{\alpha}^{\mathrm{II}}\varepsilon_{kk} + \frac{p^{\mathrm{I}}}{\overline{M}^{\mathrm{I,II}}} + \frac{p^{\mathrm{II}}}{\overline{M}^{\mathrm{II}}}\right) + \frac{\mathrm{v}^{\mathrm{II}}\phi_0^{\mathrm{II}}V_0^f}{i\mathrm{RT}} p^{s\mathrm{II}}, \quad (3.57)$$

And the compatibility relation (Eq. 3.47) becomes

$$\nabla^2\left(\varepsilon_{kk} + \frac{\overline{\eta}^{\mathrm{I}}}{\overline{G}} p^{\mathrm{I}} + \frac{\overline{\eta}^{\mathrm{II}}}{\overline{G}} p^{\mathrm{II}}\right) = 0, \quad (3.58)$$

where $\overline{\eta}^{(\mathrm{N})}$ is a lumped poroelastic coefficient defined as $\overline{\eta}^{(\mathrm{N})} = 3\overline{\alpha}^{(\mathrm{N})}(1-2\overline{\nu})/2(1-\overline{\nu})$ and $\overline{G}$ is the overall shear modulus of the system given as $\overline{G} = \overline{E}/2(1-\overline{\nu})$. Again, the overall material coefficients are related to the constituting porosity region properties as given in Appendix A. Subsequently, the diffusion equations maintain the same forms as those of transversely isotropic case (Eqs. 3.48 to 3.51) with $\overline{\alpha}_1^{(\mathrm{N})} \to \overline{\alpha}^{(\mathrm{N})}$, $\kappa_1^{(\mathrm{N})} \to \kappa^{(\mathrm{N})}$, and $D_1^{s,eff\,(\mathrm{N})} \to D^{s,eff\,(\mathrm{N})}$.

3.3 Inclined Wellbore

This section presents the development of an analytical solution to analyze the wellbore

stability in chemically active fractured shale under the framework of the above dual-porochemoelastic formulation.

3.3.1 Problem Descriptions

The inclined wellbore problem geometry is shown in **Fig. 3.1**. The undisturbed formation pore pressure and chemical activity or solute concentration are in equilibrium between the matrix and fracture and are denoted as p_0 and a_0^f or m_0^s, respectively. The single-porochemoelastic analytical solution for an inclined wellbore accounting for solute transport was published by Ekbote and Abousleiman (2006). The same approach is applicable to the current dual- porochemoelastic with solute transport model by incorporating relevant boundary conditions for stresses, dual pore pressures, and solute concentrations.

After wellbore drilling, the borehole is filled with a drilling fluid having pressure p_w and solute mole fraction m_w^s corresponding to a mud activity a_w^f. Hence, the boundary conditions to be imposed at the wellbore wall, $r = R_w$, are

$$\sigma_{rr} = [\sigma_m + \sigma_d \cos(2(\theta - \theta_r))]\,\mathrm{H}(-t) + p_w(t), \quad (3.59a)$$

$$\sigma_{r\theta} = -\sigma_d \sin(2(\theta - \theta_r))\,\mathrm{H}(-t), \quad (3.59b)$$

$$\sigma_{rz} = [S_{xz}\cos(\theta) + S_{yz}\sin(\theta)]\,\mathrm{H}(-t), \quad (3.59c)$$

$$p^{\mathrm{I}} = p^{\mathrm{II}} = p_0\mathrm{H}(-t) + p_w(t), \quad (3.59d)$$

$$p^{\mathrm{sI}} = p^{\mathrm{sII}} = (i\mathrm{RT}/V_0^f)[m_0^s\mathrm{H}(-t) + m_w^s(t)], \quad (3.59e)$$

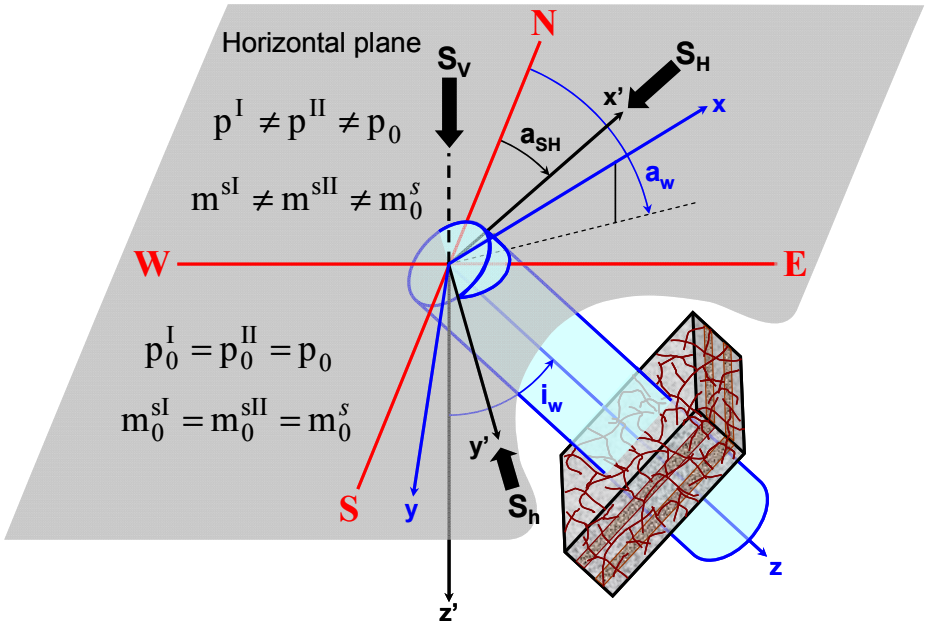

(a)

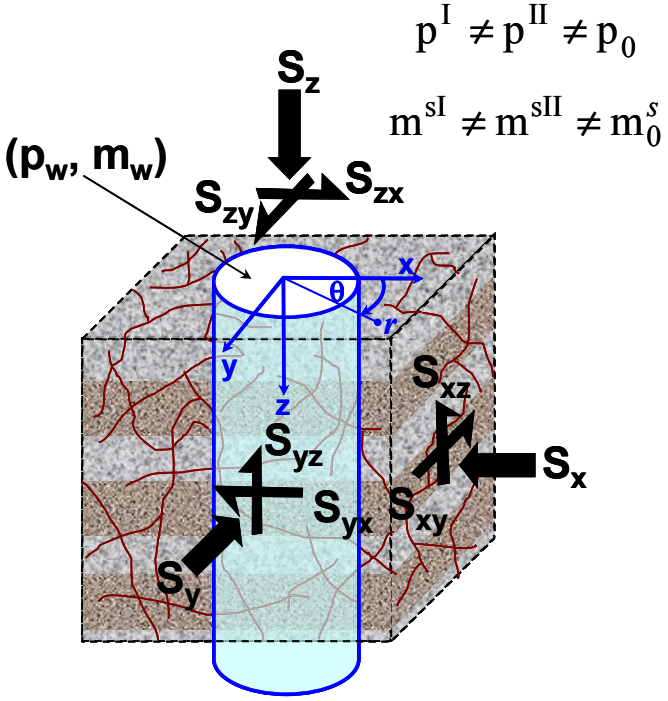

(b)

Fig. 3.1— (a) Schematic of an inclined wellbore in chemically active fractured rock formation; (b) far-field stresses, pore pressure and solute concentration in the *xyz* local wellbore coordinate system.

And at the far field, $r \to \infty$

$$\sigma_{xx} = S_x, \qquad \sigma_{yy} = S_y, \qquad \sigma_{zz} = S_z, \quad \text{.....(3.60a)}$$

$$\sigma_{xy} = S_{xy}, \qquad \sigma_{yz} = S_{yz} \qquad \sigma_{xz} = S_{xz}, \quad \text{.....(3.60b)}$$

$$p^{\mathrm{I}} = p^{\mathrm{II}} = p_0; \quad p^{\mathrm{sI}} = p^{\mathrm{sII}} = (i\mathrm{RT}/V_0^f)m_0^s \quad \text{.....(3.60c)}$$

where t is time and H(t) is the Heaviside unit step function (H(t <*0*) = 0 and H($t \geq$*0*) = 1). S_x, S_y, S_z, S_{xy}, S_{xz}, and S_{yz} are far-field in-situ stresses transformed into the local wellbore coordinate (x,y,z) as depicted in Fig. 3.1(b). In the above σ_m, σ_d, and θ_r are parts of the stress boundary condition and rotation angle in polar coordinate (r,θ) for a circular borehole as defined in Cui et al. (1997).

3.3.2 Analytical Solution

As discussed in Chapter 2, the solution approach is to solve for perturbations/changes with respect to the initial reference state so that the initial conditions and far-field boundary conditions for all variables vanish identically. The remained boundary conditions at the borehole wall are then further decomposed into two sub-problems namely: (I) the plane strain problem and (II) the antiplane shear problem. The boundary conditions and solutions in the decomposition scheme are given as follows

Problem I – Plane Strain

The boundary conditions for perturbed quantities in Problem I at the wall ($r = R_w$) are

$$\sigma_{rr} = p_w(t) - [\sigma_m + \sigma_d \cos(2(\theta - \theta_r))], \quad \text{.....(3.61a)}$$

$$\sigma_{r\theta} = \sigma_d \sin(2(\theta - \theta_r)), \quad \text{.....(3.61b)}$$

$$p^{\mathrm{I}} = p^{\mathrm{II}} = p_w(t) - p_0 \,, \quad (3.61c)$$

$$p^{\mathrm{sI}} = p^{\mathrm{sII}} = (i\mathrm{RT}/V_0^f)[m_w^s(t) - m_0^s] \,, \quad (3.61d)$$

Based on the above boundary loading conditions, the various response functions can be decomposed as (Carter and Booker 1982)

$$[p^{(\mathrm{N})}, p^{\mathrm{s(N)}}, \varepsilon_{kk}, \sigma_{rr}, \sigma_{\theta\theta}] = [P^{(\mathrm{N})}, P^{\mathrm{s(N)}}, E_{kk}, S_{rr}, S_{\theta\theta}] \times \cos(n(\theta - \theta_r)) \quad (3.62a)$$

$$\sigma_{r\theta} = S_{r\theta} \times \sin(n(\theta - \theta_r)) \quad (3.62b)$$

where $P^{(\mathrm{N})}, P^{\mathrm{s(N)}}, E_{kk}, S_{rr}, S_{\theta\theta}$, and $S_{r\theta}$ are functions of radial distance (r) and time (t) only and n is an integer number depending on loading conditions. Incorporating Eq. 3.62a into Eq. 3.47 to eliminate θ dependency and seeking bounded solutions gives

$$E_{kk} + \frac{\overline{\alpha}_1^{\mathrm{I}}}{\overline{M}_{11}} P^{\mathrm{I}} + \frac{\overline{\alpha}_1^{\mathrm{II}}}{\overline{M}_{11}} P^{\mathrm{II}} = C_0 \, r_D^{-n} \quad (3.63)$$

where $C_0 = C_0(t_D)$ is an arbitrary time-dependent coefficients to be determined from boundary conditions and $r_D = r/R_{\mathrm{w}}$ is the dimensionless radial distance. Eliminating the volumetric strain in Eqs. 3.48 to 3.51, the diffusion equations become

$$\left(\boldsymbol{\omega} \frac{\partial}{\partial t_D} + \boldsymbol{\Gamma}_{\mathbf{D}} - \overline{\boldsymbol{\kappa}}_{\mathbf{D}} \nabla_{n,D}^2 \right) \begin{Bmatrix} P^{\mathrm{I}} \\ P^{\mathrm{sI}} \\ P^{\mathrm{II}} \\ P^{\mathrm{sII}} \end{Bmatrix} = \begin{Bmatrix} c_f^{\mathrm{I}} \\ m_0^{\mathrm{s}} c_f^{\mathrm{I}} \\ c_f^{\mathrm{II}} \\ m_0^{\mathrm{s}} c_f^{\mathrm{II}} \end{Bmatrix} \frac{\partial C_0(t_D)}{\partial t_D} r_D^{-n} \,, \quad (3.64)$$

in which the dimensionless parameters are defined as follows

$$\boldsymbol{\omega} = \begin{bmatrix} 1-\omega & 0 & \omega^{\mathrm{I,II}} & 0 \\ m_0^s(1-\omega) & \omega^{\mathrm{sI}} & m_0^s \omega^{\mathrm{I,II}} & 0 \\ \omega^{\mathrm{I,II}} & 0 & \omega & 0 \\ m_0^s \omega^{\mathrm{I,II}} & 0 & m_0^s \omega & \omega^{\mathrm{sII}} \end{bmatrix}, \quad (3.65a)$$

$$\overline{\boldsymbol{\kappa}}_{\mathbf{D}} = \frac{1}{\overline{\kappa}^{\mathrm{I}} + \overline{\kappa}^{\mathrm{II}}} \begin{bmatrix} \mathrm{v}^{\mathrm{I}} D_{11}^{\mathrm{I}} & \mathrm{v}^{\mathrm{I}} D_{12}^{\mathrm{I}} & 0 & 0 \\ \mathrm{v}^{\mathrm{I}} D_{21}^{\mathrm{I}} & \mathrm{v}^{\mathrm{I}} D_{22}^{\mathrm{I}} & 0 & 0 \\ 0 & 0 & \mathrm{v}^{\mathrm{II}} D_{11}^{\mathrm{II}} & \mathrm{v}^{\mathrm{II}} D_{12}^{\mathrm{II}} \\ 0 & 0 & \mathrm{v}^{\mathrm{II}} D_{21}^{\mathrm{II}} & \mathrm{v}^{\mathrm{II}} D_{22}^{\mathrm{II}} \end{bmatrix}, \quad \text{.....(3.65b)}$$

$$\boldsymbol{\Gamma}_{\mathbf{D}} = \frac{\lambda R_w^2}{\overline{\kappa}^{\mathrm{I}} + \overline{\kappa}^{\mathrm{II}}} \begin{bmatrix} -D_{11}^{\mathrm{I}} & -D_{12}^{\mathrm{I}} & D_{11}^{\mathrm{I}} & D_{12}^{\mathrm{I}} \\ -D_{21}^{\mathrm{I}} & -D_{22}^{\mathrm{I}} & D_{21}^{\mathrm{I}} & D_{22}^{\mathrm{I}} \\ D_{11}^{\mathrm{I}} & D_{12}^{\mathrm{I}} & -D_{11}^{\mathrm{I}} & -D_{12}^{\mathrm{I}} \\ D_{21}^{\mathrm{I}} & D_{22}^{\mathrm{I}} & -D_{21}^{\mathrm{I}} & -D_{22}^{\mathrm{I}} \end{bmatrix}, \quad \text{.....(3.65c)}$$

$$t_D = \frac{\overline{\kappa}^{\mathrm{I}} + \overline{\kappa}^{\mathrm{II}}}{(A_{11} + A_{22}) R_w^2} t, \qquad \nabla_{n,D}^2 = \frac{\partial^2}{\partial r_D^2} + \frac{1}{r_D} \frac{\partial}{\partial r_D} - \frac{n^2}{r_D^2}, \quad \text{.....(3.65d)}$$

where

$$\omega = \frac{A_{22}}{A_{11} + A_{22}}, \qquad \omega^{\mathrm{I,II}} = \frac{A_{12}}{A_{11} + A_{22}}, \qquad \omega^{s(\mathrm{N})} = \frac{\mathrm{v}^{(\mathrm{N})} \phi_0^{(\mathrm{N})} V_0^f}{i \mathrm{RT} (A_{11} + A_{22})}, \quad \text{.....(3.66a)}$$

$$c_f^{\mathrm{I}} = \frac{\overline{\alpha}_1^{\mathrm{I}}}{A_{11} + A_{22}}, \qquad c_f^{\mathrm{II}} = \frac{\overline{\alpha}_1^{\mathrm{II}}}{A_{11} + A_{22}}, \quad \text{.....(3.66b)}$$

$$A_{11} = \frac{1}{\overline{M}^{\mathrm{I}}} + \frac{(\overline{\alpha}_1^{\mathrm{I}})^2}{\overline{M}_{11}}, \qquad A_{22} = \frac{1}{\overline{M}^{\mathrm{II}}} + \frac{(\overline{\alpha}_1^{\mathrm{II}})^2}{\overline{M}_{11}}, \qquad A_{12} = A_{21} = \frac{1}{\overline{M}^{\mathrm{I,II}}} + \frac{\overline{\alpha}_1^{\mathrm{I}} \overline{\alpha}_1^{\mathrm{II}}}{\overline{M}_{11}}, \quad \text{.(3.66c)}$$

$$\overline{\kappa}^{\mathrm{I}} = \mathrm{v}^{\mathrm{I}} D_{11}^{\mathrm{I}}, \qquad \overline{\kappa}^{\mathrm{II}} = \mathrm{v}^{\mathrm{II}} D_{11}^{\mathrm{II}}, \quad \text{.....(3.66d)}$$

Applying Laplace transform to Eq. 3.64 yields

$$\left(s\boldsymbol{\omega} + \boldsymbol{\Gamma}_{\mathbf{D}} - \overline{\boldsymbol{\kappa}}_{\mathbf{D}} \left(\frac{d^2}{dr_D^2} + \frac{1}{r_D} \frac{d}{dr_D} - \frac{n^2}{r_D^2} \right) \right) \begin{Bmatrix} \widetilde{P}^{\mathrm{I}} \\ \widetilde{P}^{\mathrm{sI}} \\ \widetilde{P}^{\mathrm{II}} \\ \widetilde{P}^{\mathrm{sII}} \end{Bmatrix} = \begin{Bmatrix} c_f^{\mathrm{I}} \\ m_0^{\mathrm{s}} c_f^{\mathrm{I}} \\ c_f^{\mathrm{II}} \\ m_0^{\mathrm{s}} c_f^{\mathrm{II}} \end{Bmatrix} s \widetilde{C}_0 r_D^{-n} \quad \text{.....(3.67)}$$

where the tilde sign $\sim$ denotes the corresponding quantity in Laplace transform domain and s is the Laplace transform parameter. The solution to this system of coupled ordinary

differential equations (Eq. 3.67) can be found by uncoupling the individual equations using matrix diagonalization techniques (Farlow 1993). Here, the general solutions are straightforward and given by superimposing the homogenous solution and the particular solution as

$$\widetilde{P}^{\mathrm{I}} = f_1^{\mathrm{I}}\widetilde{C}_0 r_D^{-n} + \sum_{j=1,2}\left[m_{1j}^{\mathrm{I}} C_j^{\mathrm{I}} \mathrm{K}_n(\xi_j^{\mathrm{I}} r_D) + m_{1j}^{\mathrm{II}} C_j^{\mathrm{II}} \mathrm{K}_n(\xi_j^{\mathrm{II}} r_D)\right] \quad (3.68)$$

$$\widetilde{P}^{\mathrm{sI}} = f_2^{\mathrm{I}}\widetilde{C}_0 r_D^{-n} + \sum_{j=1,2}\left[m_{2j}^{\mathrm{I}} C_j^{\mathrm{I}} \mathrm{K}_n(\xi_j^{\mathrm{I}} r_D) + m_{2j}^{\mathrm{II}} C_j^{\mathrm{II}} \mathrm{K}_n(\xi_j^{\mathrm{II}} r_D)\right] \quad (3.69)$$

$$\widetilde{P}^{\mathrm{II}} = f_1^{\mathrm{II}}\widetilde{C}_0 r_D^{-n} + \sum_{j=1,2}\left[m_{3j}^{\mathrm{I}} C_j^{\mathrm{I}} \mathrm{K}_n(\xi_j^{\mathrm{I}} r_D) + m_{3j}^{\mathrm{II}} C_j^{\mathrm{II}} \mathrm{K}_n(\xi_j^{\mathrm{II}} r_D)\right] \quad (3.70)$$

$$\widetilde{P}^{\mathrm{sII}} = f_2^{\mathrm{II}}\widetilde{C}_0 r_D^{-n} + \sum_{j=1,2}\left[m_{4j}^{\mathrm{I}} C_j^{\mathrm{I}} \mathrm{K}_n(\xi_j^{\mathrm{I}} r_D) + m_{4j}^{\mathrm{II}} C_j^{\mathrm{II}} \mathrm{K}_n(\xi_j^{\mathrm{II}} r_D)\right] \quad (3.71)$$

where $C_j^{(\mathrm{N})} = C_j^{(\mathrm{N})}(s)$ (j = 1,2) are arbitrary coefficients to be determined from boundary conditions; K_n is the modified Bessel functions of the second kind of order n; $\xi_j^{(\mathrm{N})} = \sqrt{\ell_j^{(\mathrm{N})}}$ where $\ell_j^{(\mathrm{N})}$ are the eigenvalues of the coefficient matrix $\mathbf{Y} = \overline{\boldsymbol{\kappa}}_{\mathbf{D}}^{-1}(s\,\boldsymbol{\omega} + \boldsymbol{\Gamma}_{\mathbf{D}})$ with corresponding eigenvector $\{\, m_{1j}^{(\mathrm{N})} \quad m_{2j}^{(\mathrm{N})} \quad m_{3j}^{(\mathrm{N})} \quad m_{4j}^{(\mathrm{N})} \,\}$; the coefficients $f_j^{(\mathrm{N})}$ are given as

$$\{\, f_1^{\mathrm{I}} \quad f_2^{\mathrm{I}} \quad f_1^{\mathrm{II}} \quad f_2^{\mathrm{II}} \,\}^{\mathrm{T}} = s\left(s\,\boldsymbol{\omega} - \boldsymbol{\Gamma}_{\mathbf{D}}\right)^{-1} \{\, c_f^{\mathrm{I}} \quad m_0^{\mathrm{s}} c_f^{\mathrm{I}} \quad c_f^{\mathrm{II}} \quad m_0^{\mathrm{s}} c_f^{\mathrm{II}} \,\}^{\mathrm{T}} \quad (3.72)$$

in which the superscript T denotes the transpose operation. Subsequently, the general solutions for stresses are easy to obtain by using the stress-strain-pressure constitutive equations (Eqs. 3.41 to 3.43), strain-displacement relations (Eq. 3.44) in polar coordinate, and equilibrium equation (Eqs. 3.45 and 3.46). For brevity, only the final general solutions for the stress components are presented here

$$\widetilde{S}_{rr} = -\sum_{j=1,2(\mathrm{N})=\mathrm{I,II}} \sum A_{1j}^{(\mathrm{N})} C_j^{(\mathrm{N})} \left[\frac{\mathrm{K}_{n-1}(\xi_j^{(\mathrm{N})} r_D)}{\xi_j^{(\mathrm{N})} r_D} + n(n+1) \frac{\mathrm{K}_n(\xi_j^{(\mathrm{N})} r_D)}{(\xi_j^{(\mathrm{N})} r_D)^2} \right] + \frac{(n+2)}{2} A_0 \widetilde{C}_0 r_D^{-n} + C_3 r_D^{-n-2} \quad \text{.....(3.73)}$$

$$\widetilde{S}_{\theta\theta} = \sum_{j=1,2(\mathrm{N})=\mathrm{I,II}} \sum A_{1j}^{(\mathrm{N})} C_j^{(\mathrm{N})} \left[\frac{\mathrm{K}_{n-1}(\xi_j^{(\mathrm{N})} r_D)}{\xi_j^{(\mathrm{N})} r_D} + \left(1 + \frac{n(n+1)}{(\xi^{(N)} r_D)^2} \right) \mathrm{K}_n(\xi_j^{(\mathrm{N})} r_D) \right] - \frac{(n-2)}{2} A_0 \widetilde{C}_0 r_D^{-n} - C_3 r_D^{-n-2} \quad \text{.....(3.74)}$$

$$\widetilde{S}_{r\theta} = -\sum_{j=1,2(\mathrm{N})=\mathrm{I,II}} \sum A_{1j}^{(\mathrm{N})} C_{1j}^{(\mathrm{N})} \left[n \frac{\mathrm{K}_{n-1}(\xi_j^{(\mathrm{N})} r_D)}{\xi_j^{(\mathrm{N})} r_D} + n(n+1) \frac{\mathrm{K}_n(\xi_j^{(\mathrm{N})} r_D)}{(\xi_j^{(\mathrm{N})} r_D)^2} \right] + \frac{n}{2} A_0 \widetilde{C}_0 r_D^{-n} + C_3 r_D^{-n-2} \quad \text{.....(3.75)}$$

in which $C_3 = C_3(s)$ is an additional coefficients to be determined from boundary conditions; the lumped coefficients A_0 and $A_j^{(\mathrm{N})}$ are given as follows (j = 1,2 and N = I, II)

$$A_0 = (\overline{M}_{11} - \overline{M}_{12})h/2 + \overline{M}_{11}, \qquad A_{1j}^{(\mathrm{N})} = (\overline{M}_{11} - \overline{M}_{12}) h_j^{(\mathrm{N})}, \quad \text{.....(3.76)}$$

$$h_j^{(\mathrm{N})} = (\overline{\alpha}_1^{\mathrm{I}} m_{1j}^{(\mathrm{N})} - \overline{\alpha}_1^{\mathrm{II}} m_{3j}^{(\mathrm{N})}) / \overline{M}_{11}, \qquad h = (\overline{\alpha}_1^{\mathrm{I}} f_1^{\mathrm{I}} + \overline{\alpha}_1^{\mathrm{II}} f_1^{\mathrm{II}}) / \overline{M}_{11} - 1, \quad \text{.....(3.77)}$$

To determine the unknown constants, $\widetilde{C}_0$, $C_j^{(\mathrm{N})}$ and C_3 the boundary conditions for Problem I are further decomposed into two contributing loading cases namely: axisymetric loading and deviatoric loading cases. The corresponding boundary conditions and solutions for two loading cases are listed in Appendix F.

Problem II – Antiplane Shear

The boundary conditions for perturbed quantities in Problem II at the wall ($r = R_w$) are

$$\sigma_{rz} = -[S_{xz}\cos(\theta) + S_{yz}\sin(\theta)], \quad \text{.....(3.78a)}$$

$$\sigma_{rr} = \sigma_{r\theta} = 0\,, \quad (3.78b)$$

$$p^{\mathrm{I}} = p^{\mathrm{II}} = p^{\mathrm{sI}} = p^{\mathrm{sII}} = 0\,, \quad (3.78c)$$

No disturbance of fluid or solute flow is generated by this antiplane shear stress perturbation. The solution is elastic and the same as given previously for dual-poroelastic inclined wellbore, i.e., Eqs. 2.62a and 2.62b.

The complete inclined wellbore solutions for stresses and pore pressures are obtained by superimposing the background state with non-zero solutions of the two perturbed sub-problems as given in Chapter 2, Eqs. 2.63a to 2.63h.

3.3.2 Results and Discussions

A wellbore of radius 0.1 m is assumed to be drilled in a fractured shale formation characterized by in-situ stress, pore pressure, and temperature given as: S_V = 21 MPa, S_H = 18 MPa, S_h = 16 MPa, p_0 = 10 MPa, T = 55°C at depth of 1000 meters. The formation is assumed to be saturated with a pore fluid having water activity a_0^f = 0.88 (equivalent of 150Kppm $CaCl_2$ solution or m_0^s = 0.034). The wellbore is assumed to be drilled inclined, φ_z = 60, along the maximum horizontal in-situ stress direction, φ_y = 0, and is filled with a drilling fluid (mud) maintained at constant and overbalance pressure p_w = 11 MPa with solute salinity m_w^s. The same set of material properties for a Gulf-of-Mexico shale as listed in section 2.6.1 is used to model the formation as compact and fractured rock. Other relevant data include membrane efficiency and effective solute diffusion coefficient. The effective solute diffusion coefficients, $D^{\mathrm{s,eff(N)}}$, can be simply estimated based on the

Fickian's solute diffusion coefficient in free solution, D_0^s, tortuosity, $\tau^{(N)}$, and membrane efficiency, $\chi^{(N)}$, of the porous shale structure as (Bader and Kooi 2005): $D^{s,eff(N)} = (1-\chi^{(N)})(\phi^{(N)})^{\tau^{(N)}} D_0^s$. For the porous matrix region, a membrane efficiency of $\chi^{I} = 0.4$ and a mean tortuosity of $\tau^{I} = 2$ (Gillham and Cherry 1982) are used to demonstrate the chemical osmotic and solute transport effects. On the other hand, it is reasonable to assume non tortuous flow paths $\tau^{II} = 1$ and zero membrane efficiency $\chi^{II} = 0$ for the porous fracture network. All modeling parameters are summarized in Table 3.

TABLE 3—DUAL-POROCHEMOELASTIC MODELING PARAMETERS

Parameters	Values
Matrix Young modulus (E^{I})	1854 MPa
Fracture Young modulus (E^{II})	37 Mpa
Poisson's ratio ($\nu^{I} = \nu^{II}$)	0.22
Grain bulk modulus (K_s)	27.6 GPa
Fluid bulk modulus (K_f)	1744 MPa
Matrix local porosity (ϕ^{I})	0.14
Fracture local porosity (ϕ^{II})	0.95
Matrix local permeability (k^{I})	5.0×10^{-5} mD (~ 5.0×10^{-20} m^2)
Fracture local permeability (k^{II})	5.0 mD (~ 5.0×10^{-15} m^2)
Fluid viscosity (μ)	1 cp (0.01 Pa·s)
Matrix membrane efficiency (χ^{I})	0.2
Fracture membrane efficiency (χ^{II})	0.0
Solute diffusion coeff. in free solution (D_0^s)	1.75×10^{-4} m^2/day
Interporosity geometric factor (λ)	60 m^{-2}
Fracture's bulk volume fraction ($\nu^{II} = 1 - \nu^{I}$)	0.01
Drilling-mud activity (a_w^f)	0.986 (~ 50Kppm $CaCl_2$ = 0.008 mole fraction)

Numerical results are presented in **Figs. 3.2 to 3.7**, in which positive values of stresses indicate compression. For illustration purpose, comparisons with the corresponding single-porosity and single-permeability porochemoelastic cases plotted in dashed lines are made

to highlight the coupled dual-porosity and dual-permeability and chemical effects on the results obtained. The single-porochemoelastic solution is obtained by letting the fracture space to vanish ($v^{II} \rightarrow 0$).

The dual-porochemoelastic formulation reduces to four diffusion equations, Eqs. 3.48 to 3.51, each of which is associated with an effective diffusion coefficient. The analytical solution shows that there are four eigenvalues, ξ_1^{I}, ξ_2^{I}, ξ_1^{II}, and ξ_2^{II} which physically correspond to the pressure and solute diffusion coefficients in the porous matrix and fracture continua, respectively. These eigenvalues indicate the characteristic time scales of individual diffusion processes. Due to the contribution of interporosity flow, these effective diffusion coefficients are not constant but time-dependent. The relative time scales of these coupled transport processes are estimated by calculating these eigenvalues neglecting interporosity term. From this data set, the effective diffusion coefficients, $c_j^{(N)}$, and their associated characteristic times $t_j^{(N)} = R_w^2 / c_j^{(N)}$ ($j = 1, 2$) are

$$c_1^{I} = 6.3\text{e-}03\ m^2/day; \quad c_2^{I} = 1.9\text{e-}05\ m^2/day$$
$$t_1^{I} = 1.6\ day; \quad t_2^{I} = 526\ days$$
$$c_1^{II} = 12\ m^2/day; \quad c_2^{II} = 1.7\text{e-}04\ m^2/day$$
$$t_1^{II} = 8.3e-04\ day; \quad t_2^{II} = 59\ days$$

Hence, there is about one order of magnitude in relative difference among the diffusion processes. This is so because the diffusion coefficients are proportional to not only the transport parameters such as permeability but also the stiffness of the system. Therefore, although the intrinsic fracture permeability is 10^5 times higher than the matrix permeability, the smaller fracture stiffness (50 times) reduces the relative difference among diffusion

coefficients. Since these time scales are not substantially separated, different flow processes are expected to interact and compete with each other during drilling operations.

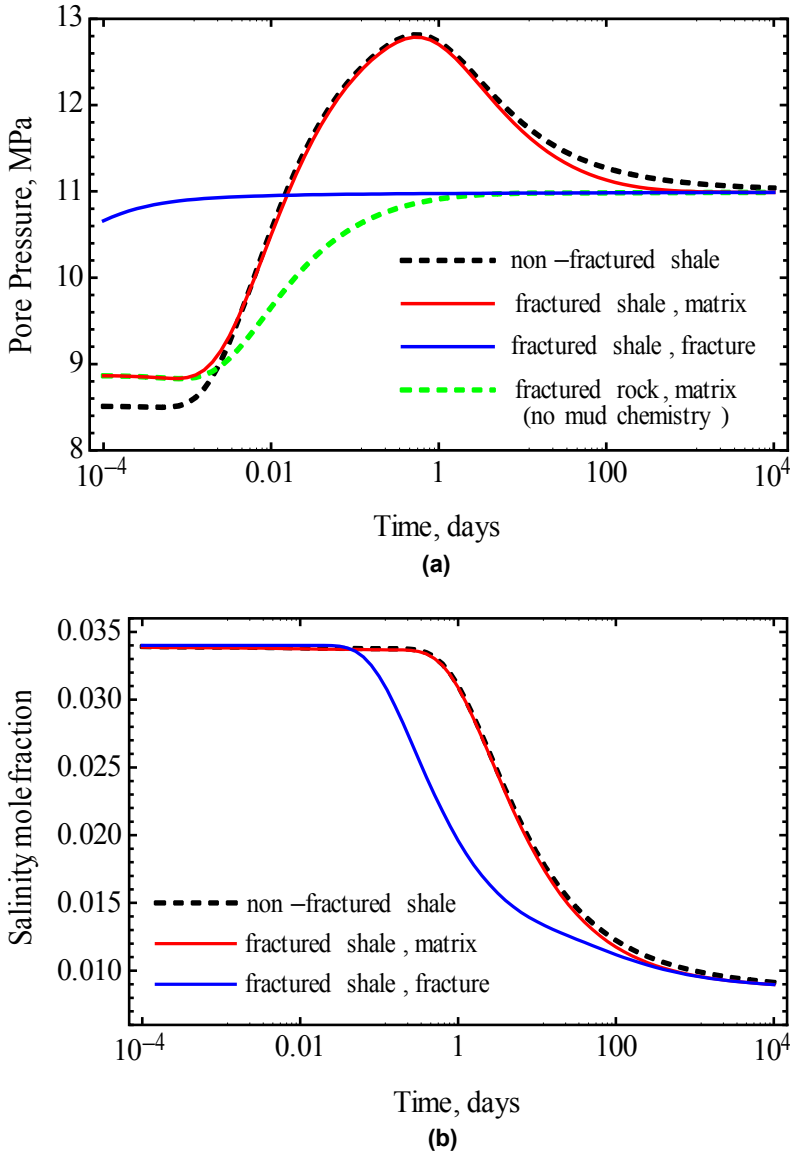

Fig. 3.2—Pore pressure and solute salinity evolutions at radial distance r = 1.10 R_w and θ = 0 (along S_H direction).

Figs. 3.2 show the history of dual pore pressure and solute concentration at radial distance r/R_w = 1.10, parallel to S_H direction (θ = 0) and for low drilling mud salinity of m_w^s = 0.008 (50Kppm $CaCl_2$). Clearly, there are four distinct responses in the pressure and

solute concentration evolutions, corresponding to the four time scales of the system as estimated above. Initially, both the matrix and fracture pressure are reduced below the formation pore pressure due to the Skempton's effect under the sudden release of non-hydrostatic in-situ stresses. With smaller effective characteristic times (t_1^{II} and t_1^{I}), fluid flow due to hydraulic pressure gradient dominates the small time pressure responses in fractured formation. The porous fracture, being more fluid-permeable, reacts first to the driving wellbore mud pressure resulting in a higher pressure in the fracture than in the matrix. As time progresses, the matrix pressure - enhanced by the inter-porosity flow from the fracture and the osmotic pressure contribution - gradually catches up with and eventually grows larger than the fracture pressure. In fact, since the mud salinity is lower than the formation salinity, an osmotic flow of fluid from the wellbore into the formation is expected. This osmotic flux will induce additional fluid pressure increase in the near-wellbore region. Hence, the matrix pressure peak at about 12.80 MPa (at 0.5 day) higher than the applied wellbore mud pressure of 11 MPa is due to the mud/shale osmotic effect. To visualize the osmotic contribution, the corresponding dual-permeability matrix pressure without chemical effect is also plotted in dash-dot in Fig. 3.2. The matrix pressure buildup above the no-chemical-effect curve quantifies the osmotic contribution. There is no osmotic contribution in the fracture pressure since it has been assumed that the porous fracture network exhibits no membrane behavior that hinders solute diffusion ($\chi^{II} = 0$). At long time, e.g., $t \rightarrow \infty$, when all pore pressures and solute concentrations equilibrate due to subsequent fluid and solute transport, the dual fluid-pressure responses converge to the single-porosity and single-permeability one.

Figs. 3.3a and 3.3b show snapshots of dual-pressure distribution along radial direction $\theta = 0^o$ (parallel to S_H) at time intervals t = 15 minutes and 0.5 day after drilling. Again, the peak in pressure responses in Fig. 3.3b is due to chemical osmotic effect. At t = 15 minutes, the dual fluid pressures mostly react to the invading wellbore mud pressure, leading to higher pressure magnitude than the single-permeability counterpart.

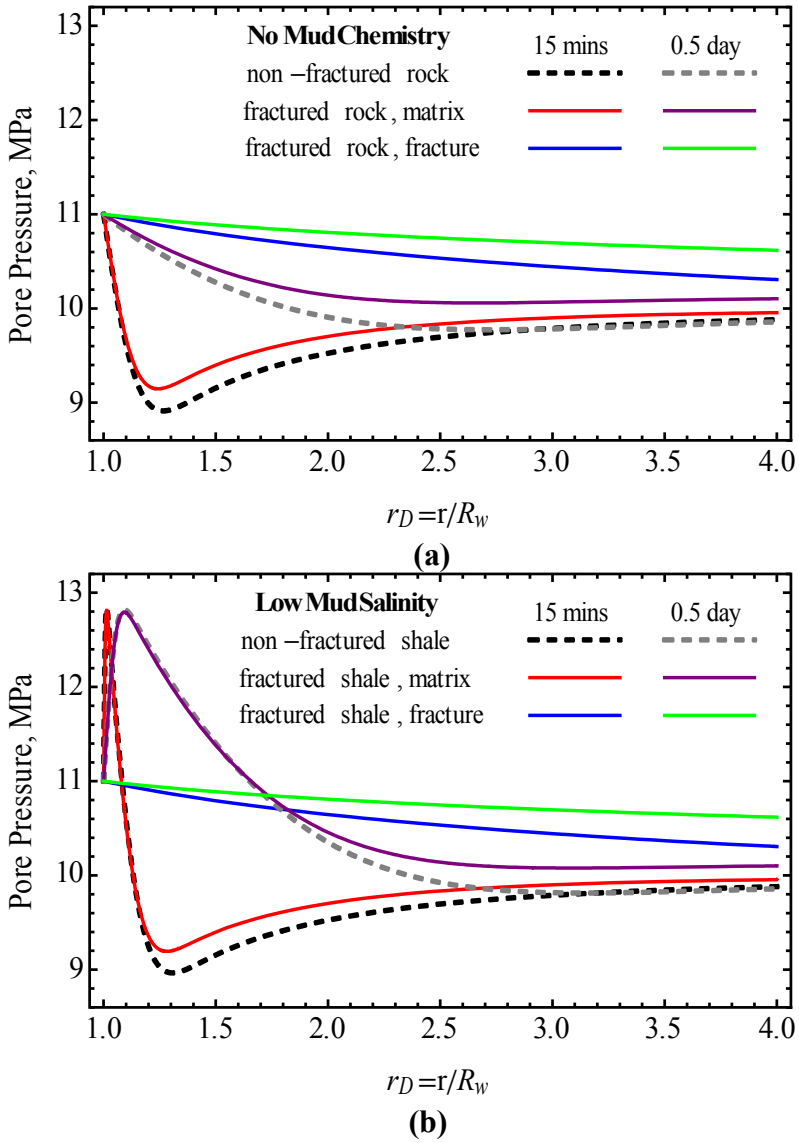

Fig. 3.3—Time-dependent pore-pressure profile along the maximum horizontal stress direction (θ = 0) for (a) without mud chemistry effect and (b) with low mud salinity (50K).

As time elapses, the slowly-diffusing osmotic pressure starts to contribute while the fast-diffusing hydraulic pressure heads, due to the presence of fracture network, are competing and partially negating the osmotic pressure rise in the porous matrix. Consequently, after t = 0.5 day the dual pressure responses are lower than single-porochemoelastic one where the induced osmotic pressure is sustained longer.

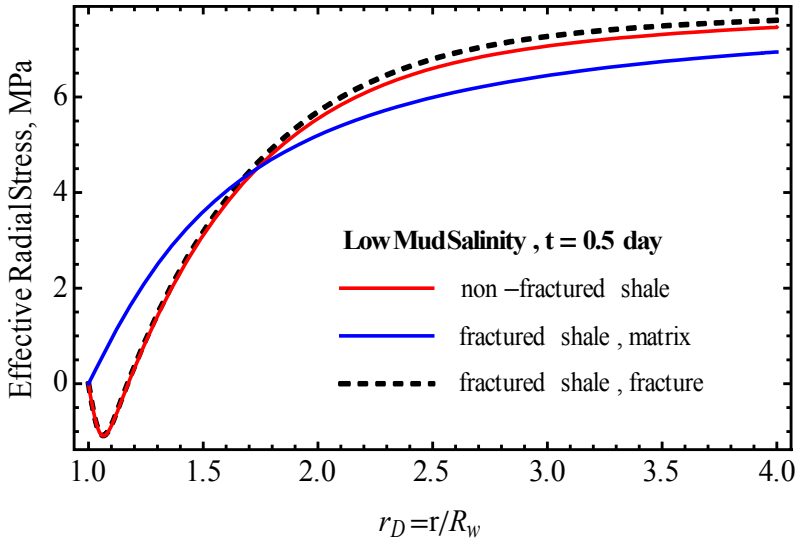

Fig. 3.4—Effective radial stress profile along the maximum horizontal stress direction (θ = 0).

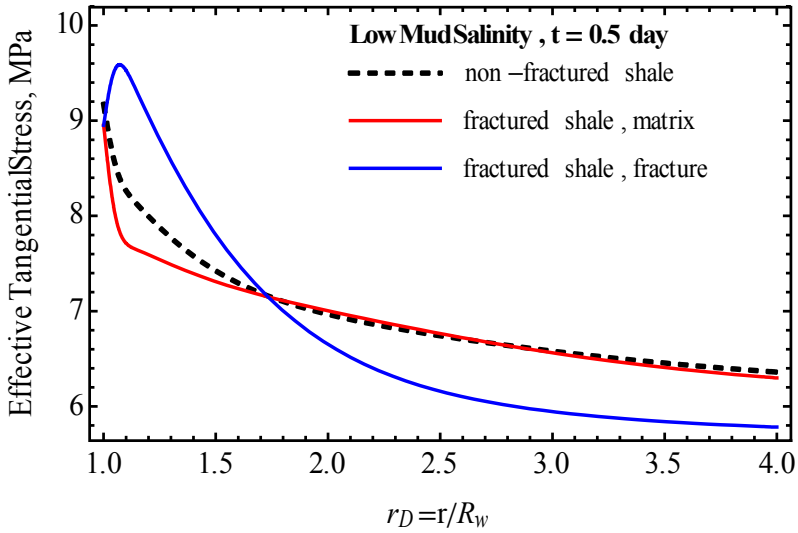

Fig. 3.5—Effective tangential stress profile along the maximum horizontal stress direction (θ = 0).

The induced dual pore-pressure leads to modifications in effective stress, i.e., normal stress less pore pressure. **Figs. 3.4 and 3.5** plot the corresponding effective radial and tangential stresses distributions in which negative values denote tension. As seen in Fig. 3.4, the effective radial stress mirrors the pressure responses shown in Fig. 3.3. There is a tensile region, $R_w < r < 1.2R_w$, developed due to mud/shale chemical osmotic effect. Similarly, low mud salinity also reduces effective tangential stress which controls borehole fracturing initiation pressure as shown in Fig. 3.5.

As a result, the transient responses of chemically active porous medium incorporating the effects of fracture network, chemical osmotic and solute transport are substantially different from those approaches that neglect the dual-porosity and dual-permeability nature of the material.

3.4 Oedometer Test of Solid Cylinder

The problem and solutions of solid cylinder subjected to radial-only or axial-only fluid-diffusion are used to simulate uniaxial reservoir depletion and subsequent consolidation. In addition, the axial-only fluid diffusion mode, the K_0 laboratory testing setups, is often considered more realistic and practical scenario for conventional triaxial testing of conventional solid core plugs. Kanj and Abousleiman (2007) presented an isotropic solution for K_0 testing to assess the osmotic effect on the response of chemically active intact rock material. This section focuses on deriving and demonstrating the solid cylinder's solution for chemically fractured samples subjected to axial-only fluid and solute flow condition. The radial-only fluid-flow solution can be obtained following similar

methodology for solid cylinder presented previously in Chapter 2, section 2.4.1.3.

3.4.2 Problem Description

The K_0 testing setup is illustrated in **Fig. 3.6** in which the fluid-saturated fractured-rock sample is sandwiched between two rigid and frictionless platens. The applied axial stress on the core plug is a result of either a time-dependent stroke control or a time-dependent load control. Moreover, the applied pore-pressure and/or solute-concentration differentials at either the upstream and downstream ends of the sample can be zero, constant, or function of time. Laterally, the outer surface of the cylinder is maintained at zero radial displacement by applying a time-dependent confining stress or using a rigid outer boundary control. Mathematically, the problem boundary conditions are written as

At the outer surface, $r = R$:

$$u_r = \sigma_{r\theta} = \sigma_{rz} = q_r^{\mathrm{I}} = q_r^{\mathrm{II}} = 0, \quad (3.79)$$

At the upstream end, $z = 0$:

$$\int_0^R r\sigma_{zz}\,dr = \frac{F(t)}{2\pi} = \frac{\pi R^2}{2\pi}\sigma_{zz}^*, \text{ load control} \quad (3.80)$$

or

$$\varepsilon_{zz} = \frac{u_z(t)}{H} = \varepsilon_{zz}^*, \text{ stroke control} \quad (3.81)$$

and

$$\sigma_{\theta z} = \sigma_{rz} = 0; \qquad p^{\mathrm{I}} = p^{\mathrm{II}} = p_u(t); \qquad p^{\mathrm{sI}} = p^{\mathrm{sII}} = (i\mathrm{RT}/V_0^f)\,m_u^s(t), \quad (3.82)$$

At the downstream end, $z = H$:

$$u_z = \sigma_{\theta z} = \sigma_{rz} = 0; \qquad p^{\mathrm{I}} = p^{\mathrm{II}} = p_d(t); \qquad p^{\mathrm{sI}} = p^{\mathrm{sII}} = (i\mathrm{RT}/V_0^f)\,m_d^s(t), \quad (3.83)$$

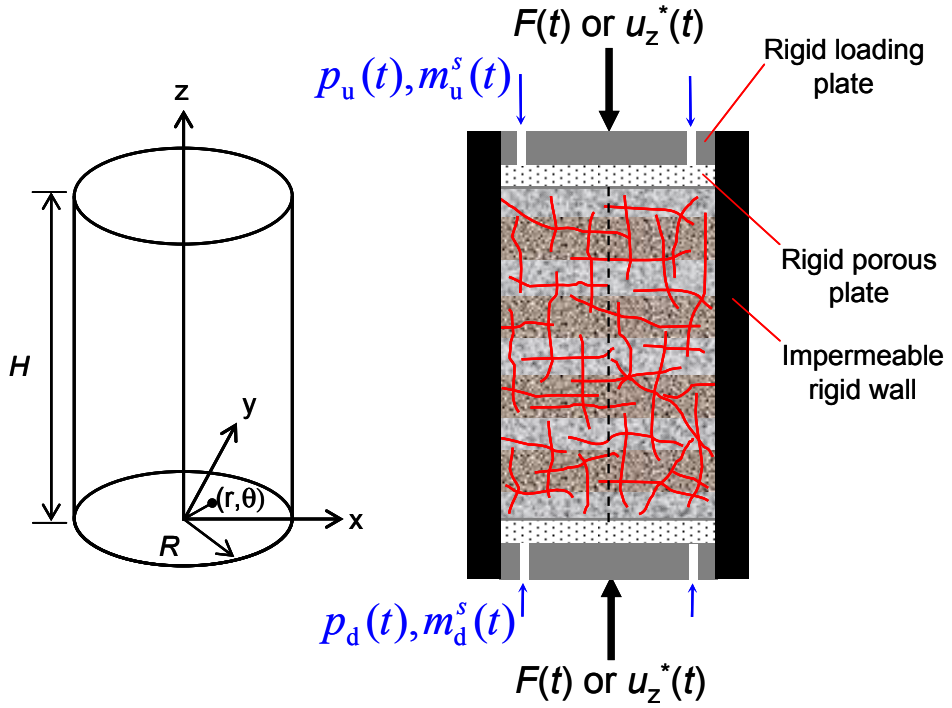

Fig. 3.6—Schematic of oedometer test (K_0) of transversely isotropic cylindrical fractured samples incorporating chemical solute salinity loading.

in which $\{p_u(t), m_u^s(t)\}$ and $\{p_d(t), m_d^s(t)\}$ are the imposed upstream and downstream fluid pressure and solute concentration, respectively. The axial-only fluid-flow constraint imposes a z-dependent variation and all variables are at most functions of z and t only. In this case, $\varepsilon_{rr} = \varepsilon_{\theta\theta} = q_r^{(N)} = q_\theta^{(N)} = 0$ and $\sigma_{zz} = \sigma_{zz}^*(t)$ due to stress equilibrium requirement in the z direction. As a result, the diffusion equations, Eqs. 3.48 to 3.51, can be rewritten compactly in terms of the applied average axial stress, pore pressure and solute concentration as

$$\left(\boldsymbol{\omega}\frac{\partial}{\partial t_D} + \boldsymbol{\Gamma}_{\mathbf{D}} - \overline{\boldsymbol{\kappa}}_{\mathbf{D}}\frac{\partial^2}{\partial z_D^2}\right)\begin{Bmatrix} p^{\mathrm{I}} \\ p^{\mathrm{sI}} \\ p^{\mathrm{II}} \\ p^{\mathrm{sII}} \end{Bmatrix} = \begin{Bmatrix} c_f^{\mathrm{I}} \\ m_0^{\mathrm{s}} c_f^{\mathrm{I}} \\ c_f^{\mathrm{II}} \\ m_0^{\mathrm{s}} c_f^{\mathrm{II}} \end{Bmatrix} \frac{\partial \sigma_{zz}^*(t_D)}{\partial t_D} \quad \text{.....(3.84)}$$

in which the dimensionless coefficient matrices, $\boldsymbol{\omega}$, $\bar{\boldsymbol{\kappa}}_{\mathbf{D}}$, and $\boldsymbol{\Gamma}_{\mathbf{D}}$, are the same as defined previously in Eqs. 3.65a to 3.65c. The dimensionless parameters, t_{D}, z_{D}, c_f^{I}, and c_f^{II}, are redefined as

$$t_D = \frac{\bar{\kappa}^{\mathrm{I}} + \bar{\kappa}^{\mathrm{II}}}{(A_{11} + A_{22})H^2} t, \qquad z_D = \frac{z}{H}, \tag{3.85}$$

$$c_f^{\mathrm{I}} = \frac{\bar{\alpha}_3^{\mathrm{I}}}{(A_{11} + A_{22})\bar{M}_{33}}, \qquad c_f^{\mathrm{II}} = \frac{\bar{\alpha}_3^{\mathrm{II}}}{(A_{11} + A_{22})\bar{M}_{33}}, \tag{3.86}$$

$$A_{11} = \frac{1}{\bar{M}^{\mathrm{I}}} + \frac{(\bar{\alpha}_3^{\mathrm{I}})^2}{\bar{M}_{33}}, \qquad A_{22} = \frac{1}{\bar{M}^{\mathrm{II}}} + \frac{(\bar{\alpha}_3^{\mathrm{II}})^2}{\bar{M}_{33}}, \qquad A_{12} = A_{21} = \frac{1}{\bar{M}^{\mathrm{I,II}}} + \frac{\bar{\alpha}_3^{\mathrm{I}}\bar{\alpha}_3^{\mathrm{II}}}{\bar{M}_{33}}, \tag{3.87}$$

3.4.3 Analytical Solution

Applying Laplace transform to the diffusion equation, Eq. 3.84, the general solution for fluid pressure and solute concentration perturbation are

$$\tilde{p}^{\mathrm{I}} = f_1^{\mathrm{I}}\tilde{\sigma}_{zz}^{*} + \sum_{j=1,2}\begin{Bmatrix} m_{1j}^{\mathrm{I}}[B_j^{\mathrm{I}}\cosh(\xi_j^{\mathrm{I}} z_D) + C_j^{\mathrm{I}}\sinh(\xi_j^{\mathrm{I}} z_D)] \\ + m_{1j}^{\mathrm{II}}[B_j^{\mathrm{II}}\cosh(\xi_j^{\mathrm{II}} z_D) + C_j^{\mathrm{II}}\sinh(\xi_j^{\mathrm{II}} z_D)] \end{Bmatrix} \tag{3.88}$$

$$\tilde{p}^{\mathrm{sI}} = f_2^{\mathrm{I}}\tilde{\sigma}_{zz}^{*} + \sum_{j=1,2}\begin{Bmatrix} m_{2j}^{\mathrm{I}}[B_j^{\mathrm{I}}\cosh(\xi_j^{\mathrm{I}} z_D) + C_j^{\mathrm{I}}\sinh(\xi_j^{\mathrm{I}} z_D)] \\ + m_{2j}^{\mathrm{II}}[B_j^{\mathrm{II}}\cosh(\xi_j^{\mathrm{II}} z_D) + C_j^{\mathrm{II}}\sinh(\xi_j^{\mathrm{II}} z_D)] \end{Bmatrix} \tag{3.89}$$

$$\tilde{p}^{\mathrm{II}} = f_1^{\mathrm{II}}\tilde{\sigma}_{zz}^{*} + \sum_{j=1,2}\begin{Bmatrix} m_{3j}^{\mathrm{I}}[B_j^{\mathrm{I}}\cosh(\xi_j^{\mathrm{I}} z_D) + C_j^{\mathrm{I}}\sinh(\xi_j^{\mathrm{I}} z_D)] \\ + m_{3j}^{\mathrm{II}}[B_j^{\mathrm{II}}\cosh(\xi_j^{\mathrm{II}} z_D) + C_j^{\mathrm{II}}\sinh(\xi_j^{\mathrm{II}} z_D)] \end{Bmatrix} \tag{3.90}$$

$$\tilde{p}^{\mathrm{sII}} = f_2^{\mathrm{II}}\tilde{\sigma}_{zz}^{*} + \sum_{j=1,2}\begin{Bmatrix} m_{4j}^{\mathrm{I}}[B_j^{\mathrm{I}}\cosh(\xi_j^{\mathrm{I}} z_D) + C_j^{\mathrm{I}}\sinh(\xi_j^{\mathrm{I}} z_D)] \\ + m_{4j}^{\mathrm{II}}[B_j^{\mathrm{II}}\cosh(\xi_j^{\mathrm{II}} z_D) + C_j^{\mathrm{II}}\sinh(\xi_j^{\mathrm{II}} z_D)] \end{Bmatrix} \tag{3.91}$$

where $B_j^{(\mathrm{N})} = B_j^{(\mathrm{N})}(s)$ and $C_j^{(\mathrm{N})} = C_j^{(\mathrm{N})}(s)$ (j = 1,2) are arbitrary coefficients to be

determined from fluid boundary conditions at the two ends, e.g., Eqs. 3.82 and 3.83, and are given as

$$\begin{Bmatrix} B_1^{\mathrm{I}} \\ B_2^{\mathrm{I}} \\ B_1^{\mathrm{II}} \\ B_2^{\mathrm{II}} \end{Bmatrix} = \begin{bmatrix} m_{11}^{\mathrm{I}} & m_{12}^{\mathrm{I}} & m_{11}^{\mathrm{II}} & m_{12}^{\mathrm{II}} \\ m_{21}^{\mathrm{I}} & m_{22}^{\mathrm{I}} & m_{21}^{\mathrm{II}} & m_{22}^{\mathrm{II}} \\ m_{31}^{\mathrm{I}} & m_{32}^{\mathrm{I}} & m_{31}^{\mathrm{II}} & m_{32}^{\mathrm{II}} \\ m_{41}^{\mathrm{I}} & m_{42}^{\mathrm{I}} & m_{41}^{\mathrm{II}} & m_{42}^{\mathrm{II}} \end{bmatrix}^{-1} \begin{Bmatrix} \widetilde{p}_d - f_1^{\mathrm{I}} \sigma_{zz}^* \\ \widetilde{p}_d^s - f_2^{\mathrm{I}} \sigma_{zz}^* \\ \widetilde{p}_d - f_1^{\mathrm{II}} \sigma_{zz}^* \\ \widetilde{p}_d^s - f_2^{\mathrm{II}} \sigma_{zz}^* \end{Bmatrix}, \quad \text{.....(3.92)}$$

$$\begin{Bmatrix} C_1^{\mathrm{I}} \\ C_2^{\mathrm{I}} \\ C_1^{\mathrm{II}} \\ C_2^{\mathrm{II}} \end{Bmatrix} = \begin{bmatrix} d_{11}^{\mathrm{I}} & d_{12}^{\mathrm{I}} & d_{11}^{\mathrm{II}} & d_{12}^{\mathrm{II}} \\ d_{21}^{\mathrm{I}} & d_{22}^{\mathrm{I}} & d_{21}^{\mathrm{II}} & d_{22}^{\mathrm{II}} \\ d_{31}^{\mathrm{I}} & d_{32}^{\mathrm{I}} & d_{31}^{\mathrm{II}} & d_{32}^{\mathrm{II}} \\ d_{41}^{\mathrm{I}} & d_{42}^{\mathrm{I}} & d_{41}^{\mathrm{II}} & d_{42}^{\mathrm{II}} \end{bmatrix}^{-1} \begin{Bmatrix} g_1^{\mathrm{I}} \\ g_2^{\mathrm{I}} \\ g_1^{\mathrm{II}} \\ g_2^{\mathrm{II}} \end{Bmatrix}, \quad \text{.....(3.93)}$$

with $i, j = 1,2$ and (N) = I, II

$$d_{ij}^{(\mathrm{N})} = m_{ij}^{(\mathrm{N})} \sinh(\xi_j^{(\mathrm{N})}); \qquad d_{(i+2)j}^{(\mathrm{N})} = m_{(i+2)j}^{(\mathrm{N})} \sinh(\xi_j^{(\mathrm{N})}), \quad \text{.....(3.94)}$$

$$g_1^{\mathrm{I}} = \widetilde{p}_d - f_1^{\mathrm{I}} \widetilde{\sigma}_{zz}^* - \sum_{j=1,2\mathrm{N}=\mathrm{I,II}} \sum m_{1j}^{(\mathrm{N})} B_j^{(\mathrm{N})} \cosh(\xi_j^{(\mathrm{N})}), \quad \text{.....(3.95a)}$$

$$g_2^{\mathrm{I}} = \widetilde{p}_d^s - f_2^{\mathrm{I}} \widetilde{\sigma}_{zz}^* - \sum_{j=1,2\mathrm{N}=\mathrm{I,II}} \sum m_{2j}^{(\mathrm{N})} B_j^{(\mathrm{N})} \cosh(\xi_j^{(\mathrm{N})}), \quad \text{.....(3.95b)}$$

$$g_1^{\mathrm{II}} = \widetilde{p}_d - f_1^{\mathrm{II}} \widetilde{\sigma}_{zz}^* - \sum_{j=1,2\mathrm{N}=\mathrm{I,II}} \sum m_{3j}^{(\mathrm{N})} B_j^{(\mathrm{N})} \cosh(\xi_j^{(\mathrm{N})}), \quad \text{.....(3.95c)}$$

$$g_2^{\mathrm{II}} = \widetilde{p}_d^s - f_2^{\mathrm{II}} \widetilde{\sigma}_{zz}^* - \sum_{j=1,2\mathrm{N}=\mathrm{I,II}} \sum m_{4j}^{(\mathrm{N})} B_j^{(\mathrm{N})} \cosh(\xi_j^{(\mathrm{N})}), \quad \text{.....(3.95d)}$$

Eqs. 3.88 to 3.91 and the governing equations (transport equations and constitutive equations) are used to determined the rest of the unknown components of fluid and solute fluxes, stresses, strains, and displacements

$$\widetilde{q}_z^{(\mathrm{N})} = -\kappa_{33}^{(\mathrm{N})} \frac{d\widetilde{p}^{(\mathrm{N})}}{dz} + \chi^{(\mathrm{N})} \kappa_{33}^{(\mathrm{N})} \frac{d\widetilde{p}^{s(\mathrm{N})}}{dz} \quad \text{.....(3.96)}$$

$$\widetilde{q}_z^{s(\mathrm{N})} = -D_{21}^{(\mathrm{N})}\frac{d\widetilde{p}^{(\mathrm{N})}}{dz} - D_{22}^{(\mathrm{N})}\frac{d\widetilde{p}^{s(\mathrm{N})}}{dz}, \quad (3.97)$$

$$\widetilde{\sigma}_{rr} = \widetilde{\sigma}_{\theta\theta} = \frac{\overline{M}_{13}}{\overline{M}_{33}}\widetilde{\sigma}_{zz}^{*} + \left(\overline{\alpha}_1^{\mathrm{I}} - \frac{\overline{M}_{13}}{\overline{M}_{33}}\overline{\alpha}_3^{\mathrm{I}}\right)\widetilde{p}^{\mathrm{I}} + \left(\overline{\alpha}_1^{\mathrm{II}} - \frac{\overline{M}_{13}}{\overline{M}_{33}}\overline{\alpha}_3^{\mathrm{II}}\right)\widetilde{p}^{\mathrm{II}}, \quad (3.98)$$

$$\widetilde{\varepsilon}_{zz} = \frac{1}{\overline{M}_{33}}\left(\widetilde{\sigma}_{zz}^{*} - \overline{\alpha}_3^{\mathrm{I}}\widetilde{p}^{\mathrm{I}} - \overline{\alpha}_3^{\mathrm{II}}\widetilde{p}^{\mathrm{II}}\right), \quad (3.99)$$

$$\frac{\widetilde{u}_z}{H} = \widetilde{\sigma}_{zz}^{*} h z_D - \sum_{j=1,2}\left\{\begin{array}{l} h_j^{\mathrm{I}}\left[B_j^{\mathrm{I}}\left(\sinh(\xi_j^{\mathrm{I}} z_D) - \sinh(\xi_j^{\mathrm{I}})\right) + C_j^{\mathrm{I}}\left(\cosh(\xi_j^{\mathrm{I}} z_D) - \cosh(\xi_j^{\mathrm{I}})\right)\right] \\ + h_j^{\mathrm{II}}\left[B_j^{\mathrm{II}}\left(\sinh(\xi_j^{\mathrm{II}} z_D) - \sinh(\xi_j^{\mathrm{II}})\right) + C_j^{\mathrm{II}}\left(\cosh(\xi_j^{\mathrm{II}} z_D) - \cosh(\xi_j^{\mathrm{II}})\right)\right] \end{array}\right\}, \quad (3.100)$$

where $u_z = 0$ at the middle due to top and bottom symmetry; $h_j^{(\mathrm{N})}$ and h are given as

$$h_j^{(\mathrm{N})} = \frac{\overline{\alpha}_3^{\mathrm{I}} m_{1j}^{(\mathrm{N})} + \overline{\alpha}_3^{\mathrm{II}} m_{3j}^{(\mathrm{N})}}{\overline{M}_{33}}; \qquad h = \frac{1 - \overline{\alpha}_3^{\mathrm{I}} f_1^{\mathrm{I}} - \overline{\alpha}_3^{\mathrm{II}} f_1^{\mathrm{II}}}{\overline{M}_{33}}, \quad (3.101)$$

For load-control mode, the average axial stress, $\widetilde{\sigma}_{zz}^{*}$, is known and the above solution is applicable. For stroke-control mode, the average axial strain, $\widetilde{\varepsilon}_{zz}^{*}$, is prescribed. From Eq. 3.99, the expression for average axial stress in term of the average axial strain is

$$\widetilde{\sigma}_{zz}^{*} = -\frac{1}{h}\left(\widetilde{\varepsilon}_{zz}^{*} - \sum_{j=1,2}\left\{h_j^{\mathrm{I}} C_j^{\mathrm{I}}[1 - \cosh(\xi_j^{\mathrm{I}})] + h_j^{\mathrm{II}} C_j^{\mathrm{II}}[1 - \cosh(\xi_j^{\mathrm{II}})]\right\}\right), \quad (3.102)$$

Therefore, the stroke-control solution can be obtained simply by substituting Eq. 3.102 into the load-control mode solutions, i.e., Eqs. 3.88 to 3.91 and Eqs. 3.96 to 3.98.

3.4.4 Results and Discussions

A comparative study between dual-poroelastic and dual-porochemoelastic of an isotropic, fractured shale sample subjected to K_0 testing and an assumed axial-only fluid flow

constraint is shown in the following. In addition, comparison with single-porochemoelastic approach for intact shale is also displayed. The fractured shale material properties are the same as listed in Table 3. The solid core is assumed to have radius of 0.025 m and a height of 0.1 m. The sample is subjected to a step application of an average axial stress of 1 MPa and both ends are drained. Moreover, the upstream end of the sample is subjected to a salinity or activity differential. This is achieved through setting the salinity of the upstream fluid of 0.008 mole fraction (50K $CaCl_2$) or 0.06 mole fraction (250K $CaCl_2$) while the original salinity in the shale is 0.034 mole fraction (150K $CaCl_2$). The fractured shale's matrix membrane efficient is 0.1, interporosity geometric coefficient is 240, and the testing temperature is 25 ^{o}C.

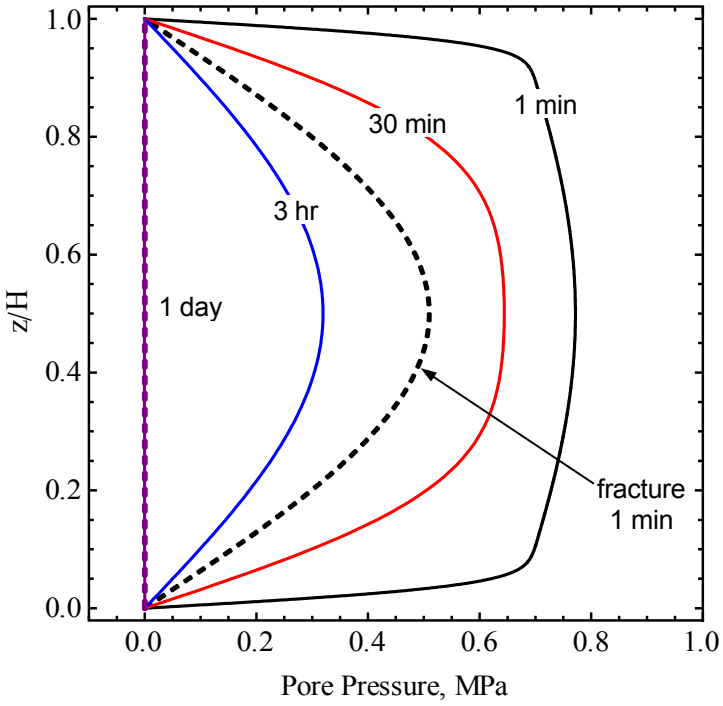

Fig. 3.7—Evolution of dual pore pressure distributions along the core without external salinity differential.

Numerical comparison between dual-poroelastic and dual-porochemoelastic is shown for

pore pressure, fluid flux and axial displacement in **Figs. 3.7 to 3.13**. The purpose is to illustrate the importance of considering proper porochemical coupling in the analysis.

The pore pressure responses along the core are plotted in Figs. 3.7 to 3.9. For dual-poroelasticity (Fig. 3.7), the dual pressure diffuse normally following instantaneous jump due to step loading of axial stress. The perturbed pore pressure in the fracture network – dashed lines – quickly dissipates and equilibrates after 30 minutes while the matrix pore pressure – solid lines – is still diffusing. Accounting for upstream salinity gradient, the osmotic effect generates additional pore pressure increment (e.g., low salinity in Fig. 3.8) or reduction (e.g., high salinity in Fig. 3.9) in the shale matrix. As time progresses, the osmotic pressure front moves down the sample and diminishes in magnitude due to subsequent solute diffusion, highlighting the leaky membrane behavior.

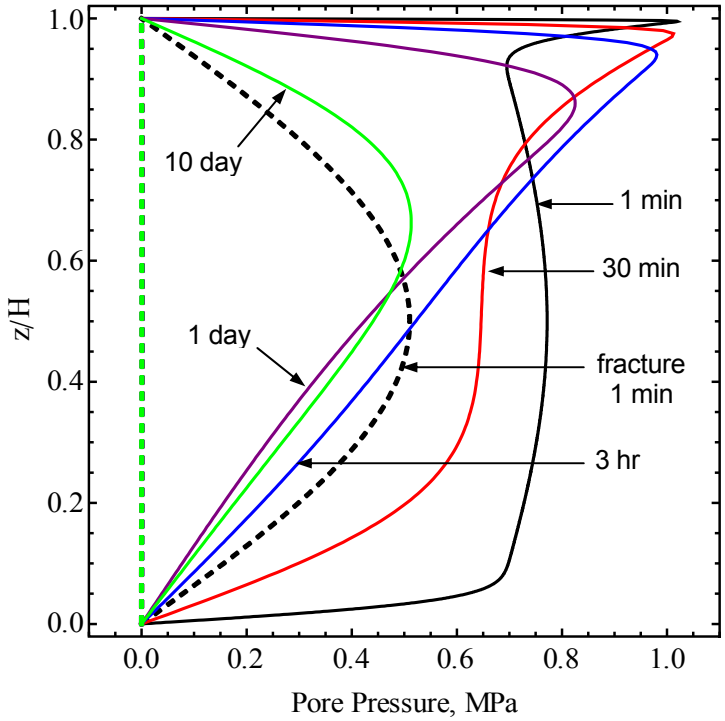

Fig. 3.8—Evolution of pore pressure distribution along the core for low upstream salinity.

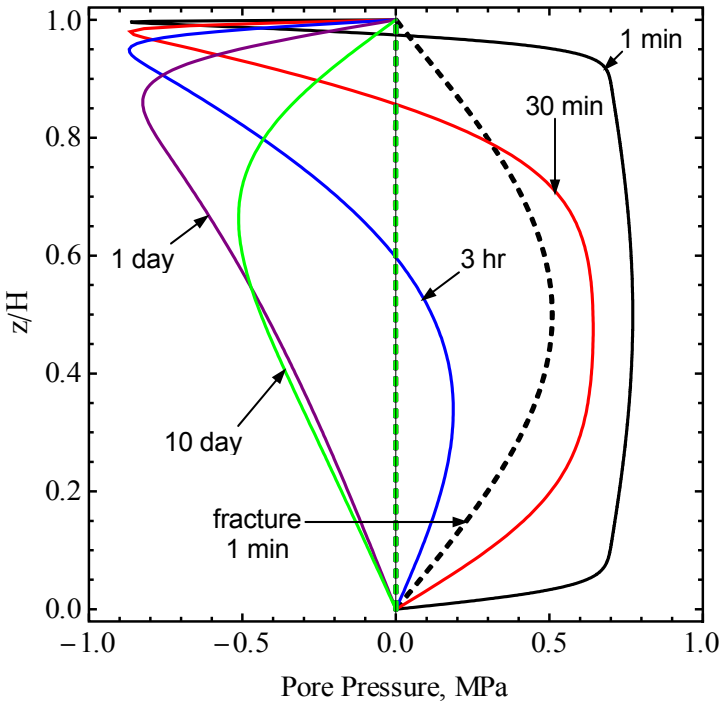

Fig. 3.9—Evolution of pore pressure distribution along the core for high upstream salinity.

The corresponding fluid fluxes at two ends of the sample are plotted in Figs. 3.10 to 3.13. Without chemical effect, dual-poroelasticity (Fig. 3.10) shows draining behavior, i.e., fluid flux out of the sample as a result of axial load application. It is seen that the same amount of fluid flows across both ends and the majority of the flow is through the fracture network. For low upstream salinity (Fig. 3.11), the bulk of the fluid are squeezed out through the fracture network at both ends. However, there is an induced osmotic flow into the matrix region at the upstream end reducing the total out-flow fluid flux at this end. On the other hand, high upstream salinity leads to additional osmotic out-flow as shown in Fig. 3.12.

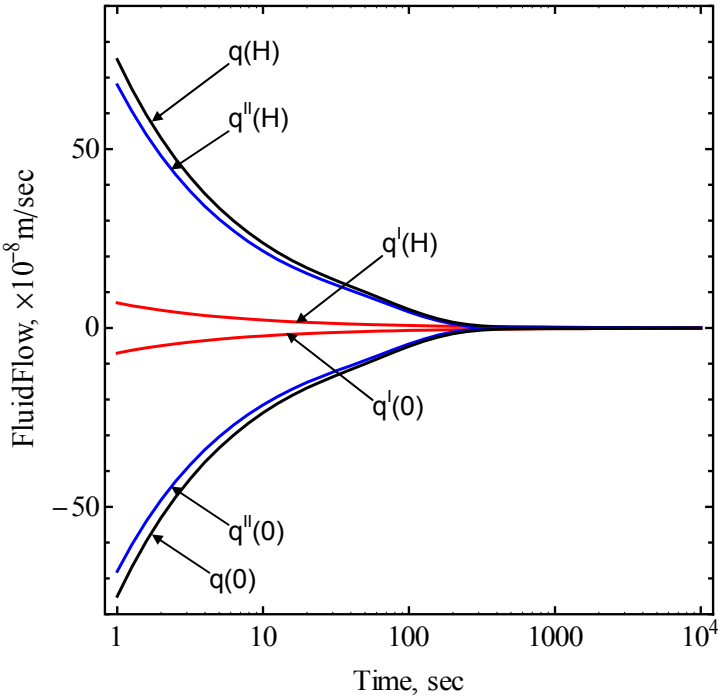

Fig. 3.10—History of fluid flux at the two ends of fractured sample without salinity gradient effect.

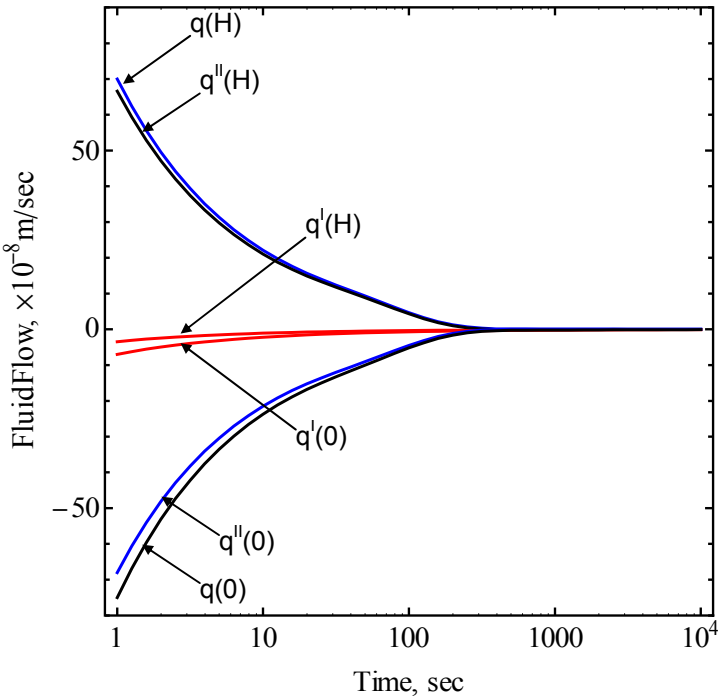

Fig. 3.11—History of fluid flux at the two ends of fractured shale sample subjected to low upstream salinity.

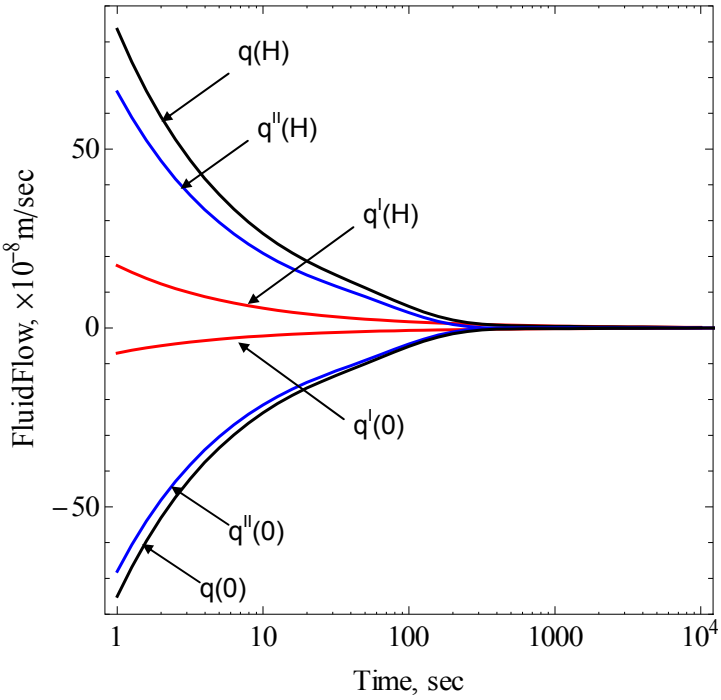

Fig. 3.12—History of total fluid flux at the two ends of fractured shale sample subjected to high upstream salinity.

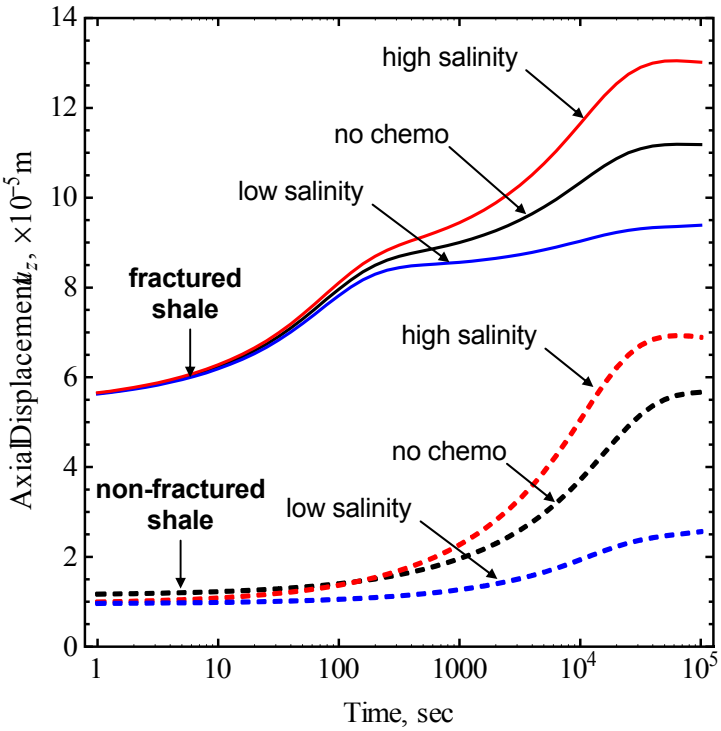

Fig. 3.13—History of axial displacement at the top of fractured shale sample subjected to different upstream salinity gradients.

Finally, the axial displacement is plotted in Fig. 3.13. The osmotic drainage due to high applied salinity promotes shrinkage, leading to higher consolidation. For low salinity differential, the osmotic inflow reduces the compaction. Compared with intact shale modeling using single-poromechanics approach, the difference in axial displacement can be attributed to deformation in the fracture network.

3.5 Summary

The dual-porosity and dual-permeability poromechanics formulation has been extended to incorporate the dual chemical osmotic and solute transport effects in the overall response of dual porous medium. The corresponding analytical solution for the drilling of inclined wellbore or the oedometer test of solid cylinder (K_0 testing configuration) of chemically active naturally fractured rock have been derived and presented in this chapter.

Via the inclined wellbore solution, effective stress and pore pressure analyses were carried out to study the dual-porosity and chemical effects on the overall poromechanics response. It is seen that the dual-porosity and dual-permeability effect is to develop dual pore-pressure responses in the shale formations. Meanwhile, the chemical osmotic effect is to modify the stress and pore pressure magnitudes in the vicinity of wellbore wall, e.g., drilling mud with lower mud salinity will induce an osmotic diffusive flow from the wellbore into the formation. In contrast to previous studies ignoring solute transport phenomenon, the developed osmotic pressure eventually dissipates due to subsequent fluid and solute diffusion processes since the shale membrane behavior is not perfect. The resultant pore pressure response leads to corresponding modifications in the effective stress

field. Effective stress calculations show that the dual-porochemoelastic solution predictions differ substantially from single-porochemoelastic approach.

Numerical applications of the solution of solid cylinder subjected to a K_0 test indicates that neglecting osmotic and solute transport effects can mislead the test results for fluid flux. In addition, neglecting the contribution of fracture network will lead to erroneous results for fluid flux as well as axial displacement.

Chapter 4

Dual-Porosity and Dual-Permeability Porothermoelasticity: Dual-Porothermoelasticity

4.1 Introduction

Geomechanical analyses of field problems are often subjected to non-isothermal conditions occurring in such cases as deep subsurface drilling, geothermal wells, and nuclear waste depository. In saturated porous media, the coupled interaction between the transient fluid flow and the deformation processes under pressure or stress perturbations are well known and investigated through the theory of poroelasticity first introduced by Biot (1941). On the other hand, a temperature gradient will lead to not only induced thermal stresses but also transient thermo-induced pore pressure responses. The thermohydromechanical effects on the mechanical response of porous media have been successfully studied under the porothermoelastic model (Bear and Corapcioglu 1981; McTigue 1986; Coussy 1989). When viewed at the microscale, thermal gradients result in differential expansion or contraction of the solid and fluid constituents within a porous saturated medium. The volume changes associated with the expansion/contraction lead to significant modification

of both the total stress and pore pressure distributions. Therefore, in addition to the transient pressure changes due to Darcy flow, thermal deformation and diffusion also induced additional pressure and effective stress alteration. In solid materials, heat transport is analogous to fluid transport where the heat is conducted through the interconnected grain structure. In a saturated porous medium, the diffusing fluid also acts as a heat carrier, introducing another heat flow mechanism via convection. Practically, temperature equilibrium between the solid and fluid constituents is assumed to be instantaneous in comparison to heat conduction and convection processes leading to a single-temperature thermodynamic continuum (Bear and Corapcioglu 1981).

In fractured rock formations, the mechanism of heat flow in the constituent porosity regions may be different from fluid mass transport. In particular, fractured rock formation is modeled as a dual-porosity and dual-permeability continuum which is comprised of a primary porosity (matrix) with low fluid conductivity and a secondary porosity (fracture network) with highly permeable flow paths. As a result, dual-porosity and dual-permeability continuum will exhibit dual pore pressure evolutions when subjected to stress and pressure perturbations. The two constituting porous regions can exchange fluid mass due to pressure differential at the interface between them. On the other hand, heat flow in the porous matrix is primarily driven by conductive mechanism through the compact matrix skeleton while heat convection carried by the fast diffusing fluid in the fracture network is intuitively more dominant. Because thermal conductivity is significantly higher through the compact matrix framework than through the fracture network comprised mostly of pore space, the dual-porosity temperature evolutions and interporosity heat

exchange are most likely masked. Consequently, a single-temperature approach for fractured porous continuum (Master et al. 2000) appears to be more practical than the double-temperature approach (Aifantis and Bekos 1980).

Analytical solutions and analyses of the porothermoelastics coupling in single-porosity medium have been well established (McTigue 1990; Wang and Papamichos 1994; Ekbote 2002; Abousleiman and Ekbote 2004; Chen and Ewy 2005). In fractured porous media, despite the abundance in numerical modeling of porothermoelastic effects (Aifantis and Bekos 1980; Millard et al. 1995; Nguyen and Selvadurai 1995; Abdallah et al. 1995; Master et al. 2000; Nair et al. 2004), no analytical solution has been provided for the coupling of heat and fluid flow and the resultant stress and deformation field in fractured porous media.

In this chapter, a dual-porosity and dual-permeability porothermoelastic analytical formulation and solution applicable to transversely isotropic fractured porous media is presented. First, the dual-porosity and dual permeability poroelastic governing equations as presented in Chapter 2 are extended to incorporate thermal effects within the framework of a single-temperature approach. The complete formulation includes contribution from both heat conduction and convection in the porous matrix and fracture system. Neglecting the non-linear heat convection, the resulting system of equations is applied to obtain the analytical solution for inclined wellbore subjected to non hydrostatic in-situ state of stress. The effect of heat convection is accessed numerically by finite difference method for a special case of vertical borehole drilled in hydrostatic in-situ stress condition.

4.2 Mathematical Formulation

4.2.1 Constitutive Equations

Thermal effect in fractured porous formation can be modeled by extending the dual-poroelastic formulation in Chapter 2 to account for non-isothermal condition. Assuming instantaneous local thermal equilibrium among all system constituents, i.e., common temperature for all constituents of the dual porous system, and infinitesimal deformation, the change in free energy density of skeleton is expressed as follows (Coussy 2004)[6]

$$dW = \sigma_{ij} d\varepsilon_{ij} - \mathrm{v}^{\mathrm{I}}\phi^{\mathrm{I}} dp^{\mathrm{I}} - \mathrm{v}^{\mathrm{II}}\phi^{\mathrm{II}} dp^{\mathrm{II}} - S^s dT \,, \quad (4.1)$$

where σ_{ij} is the total stress tensor; ε_{ij} is the linearized strain tensor; $\phi^{(\mathrm{N})}$ is the intrinsic porosity of the individual porous continua and $\mathrm{v}^{(\mathrm{N})}$ is the bulk volume fraction; $S^s = S^{s\mathrm{I}} + S^{s\mathrm{II}}$ is the total solid skeleton's entropy per unit bulk volume; and T is the temperature.

From the above equation, it is obvious that W admits ε_{ij}, p^{I}, p^{II}, and T as state variables and the linearized constitutive equations follow naturally as (compression is positive)

$$d\sigma_{ij} = \overline{M}_{ijkl} d\varepsilon_{kl} + \overline{\alpha}^{\mathrm{I}}_{ij} dp^{\mathrm{I}} + \overline{\alpha}^{\mathrm{II}}_{ij} dp^{\mathrm{II}} + \overline{\beta}^{s}_{ij} dT \quad (4.2)$$

$$d(\mathrm{v}^{\mathrm{I}}\phi^{\mathrm{I}}) = -\overline{\alpha}^{\mathrm{I}}_{ij} d\varepsilon_{ij} + \frac{dp^{\mathrm{I}}}{\overline{K}^{\mathrm{I}}_{\phi}} + \frac{dp^{\mathrm{II}}}{\overline{K}^{\mathrm{I,II}}_{\phi}} - \overline{\beta}^{\mathrm{I}}_{\phi} dT \quad (4.3)$$

$$d(\mathrm{v}^{\mathrm{II}}\phi^{\mathrm{II}}) = -\overline{\alpha}^{\mathrm{II}}_{ij} d\varepsilon_{ij} + \frac{dp^{\mathrm{I}}}{\overline{K}^{\mathrm{I,II}}_{\phi}} + \frac{dp^{\mathrm{II}}}{\overline{K}^{\mathrm{II}}_{\phi}} - \overline{\beta}^{\mathrm{II}}_{\phi} dT \quad (4.4)$$

$$dS^s = -\overline{\beta}^{s}_{ij} d\varepsilon_{ij} + \overline{\beta}^{\mathrm{I}}_{\phi} dp^{\mathrm{I}} + \overline{\beta}^{\mathrm{II}}_{\phi} dp^{\mathrm{II}} + (\overline{C}^s / T_0) dT \quad (4.5)$$

where the overbar notation indicates overall material properties; $\overline{C}^s$ is the lumped

[6] The free energy density W in Eq. 4.1 is analogous to the energy function G_s as defined in Eq. 4.3 by Coussy (2004)

volumetric heat capacity of the solid constituents in the primary and secondary porous region, i.e., $\overline{C}^{s} = \mathrm{v}^{\mathrm{I}}(1-\phi_0^{\mathrm{I}})\rho_0^{s\mathrm{I}}c^{s\mathrm{I}} + \mathrm{v}^{\mathrm{II}}(1-\phi_0^{\mathrm{II}})\rho_0^{s\mathrm{II}}c^{s\mathrm{II}}$ in which $c^{s(\mathrm{N})}$ is the specific heat and $\rho^{s(\mathrm{N})}$ is the solid grain density; and $\overline{\beta}_{ij}^{s}$ and $\overline{\beta}_{\phi}^{(\mathrm{N})}$ are thermal coefficient tensor and scalar related to the overall solid skeleton and individual pore systems, respectively. Considering unconfined condition and assuming self-similar thermal expansion/contraction for solid and pore systems, the thermal coefficients $\overline{\beta}_{ij}^{s}$ and $\overline{\beta}_{\phi}^{(\mathrm{N})}$ can be identified in terms of thermal expansion coefficients as

$$\overline{\beta}_{ij}^{s} = \overline{M}_{ijkl}\overline{\alpha}_{kl}^{s} = \overline{M}_{ijkl}(\mathrm{v}^{\mathrm{I}}\alpha_{kl}^{s\mathrm{I}} + \mathrm{v}^{\mathrm{II}}\alpha_{kl}^{s\mathrm{II}}), \quad (4.6a)$$

$$\overline{\beta}_{\phi}^{(\mathrm{N})} = \overline{\alpha}_{ij}^{(\mathrm{N})}\overline{\alpha}_{ij}^{s} - \mathrm{v}^{(\mathrm{N})}\phi_0^{(\mathrm{N})}\alpha_{kk}^{s(\mathrm{N})}, \quad (4.6b)$$

in which $\overline{\alpha}_{kl}^{s}$, $\alpha_{kl}^{s(\mathrm{N})}$ are the solid's linear thermal expansion coefficient tensor of the overall and constituting porous regions, respectively.

Following Coussy (2004), the intrinsic porosity $\phi^{(\mathrm{N})}$ and the solid's skeleton's entropy S^{s} are replaced in favor of the fluid mass content $m^{f(\mathrm{N})} = \mathrm{v}^{(\mathrm{N})}\phi^{(\mathrm{N})}\rho^{f(\mathrm{N})}$ and the total entropy $S = S^{s} + S^{f\mathrm{I}} + S^{f\mathrm{II}}$ by linearizing the saturation condition and the following state equations

$$d\zeta^{(\mathrm{N})} = \frac{dm^{f(\mathrm{N})}}{\rho_0^{f(\mathrm{N})}} = d(\mathrm{v}^{(\mathrm{N})}\phi^{(\mathrm{N})}) + \mathrm{v}^{(\mathrm{N})}\phi_0^{(\mathrm{N})}\frac{d\rho^{f(\mathrm{N})}}{\rho_0^{f(\mathrm{N})}}, \quad (4.7)$$

$$dS^{f(\mathrm{N})} = d(m^{f(\mathrm{N})}\, s^{f(\mathrm{N})}) = m_0^{f(\mathrm{N})}ds^{f(\mathrm{N})} + s_0^{f(\mathrm{N})}dm^{f(\mathrm{N})}, \quad (4.8)$$

$$\frac{d\rho^{f(\mathrm{N})}}{\rho_0^{f(\mathrm{N})}} = \frac{dp^{(\mathrm{N})}}{K_f^{(\mathrm{N})}} - \alpha^{f(\mathrm{N})}dT, \qquad ds^{f(\mathrm{N})} = -\alpha^{f(\mathrm{N})}dp^{(\mathrm{N})} + c^{f(\mathrm{N})}\frac{dT}{T_0}, \quad (4.9)$$

where $\rho^{f(\mathrm{N})}$ is the fluid density; $\alpha^{f(\mathrm{N})}$ is the volumetric thermal expansion coefficient of

the pore fluid (a scalar); $1/K_f^{(\mathrm{N})}$ is the isothermal fluid compressibility; $s^{f(\mathrm{N})}$ is the specific entropy; and $c^{f(\mathrm{N})}$ is the fluid specific heat capacity. Equations 4.3 to 4.5 become

$$d\zeta^{\mathrm{I}} = -\overline{\alpha}_{ij}^{\mathrm{I}} d\varepsilon_{kk} + \frac{dp^{\mathrm{I}}}{\overline{M}^{\mathrm{I}}} + \frac{dp^{\mathrm{II}}}{\overline{M}^{\mathrm{I,II}}} - \overline{\beta}_{fs}^{\mathrm{I}} dT \,, \quad (4.10)$$

$$d\zeta^{\mathrm{II}} = -\overline{\alpha}_{ij}^{\mathrm{II}} d\varepsilon_{kk} + \frac{dp^{\mathrm{I}}}{\overline{M}^{\mathrm{I,II}}} + \frac{dp^{\mathrm{II}}}{\overline{M}^{\mathrm{II}}} - \overline{\beta}_{fs}^{\mathrm{II}} dT \,, \quad (4.11)$$

$$dS - \sum_{(\mathrm{N})=\mathrm{I,II}} s_0^{f(\mathrm{N})} dm^{f(\mathrm{N})} = -\overline{\beta}_{ij}^{s} d\varepsilon_{ij} + \overline{\beta}_{fs}^{\mathrm{I}} dp^{\mathrm{I}} + \overline{\beta}_{fs}^{\mathrm{II}} dp^{\mathrm{II}} + (\overline{C}/T_0) dT \,, \quad (4.12)$$

where the apparent fluid storage $1/\overline{M}^{(\mathrm{N})}$, $1/\overline{M}^{\mathrm{I,II}}$, lumped thermal coefficient $\overline{\beta}_{fs}^{(\mathrm{N})}$, and total heat capacity $\overline{C}$ are given as

$$1/\overline{M}^{(\mathrm{N})} = 1/\overline{K}_{\phi}^{(\mathrm{N})} + \mathrm{v}^{(\mathrm{N})}\phi_0^{(\mathrm{N})}/K_f^{(\mathrm{N})}; \qquad 1/\overline{M}^{\mathrm{I,II}} = 1/\overline{K}_{\phi}^{\mathrm{I,II}}, \quad (4.13)$$

$$\overline{\beta}_{fs}^{(\mathrm{N})} = \overline{\beta}_{\phi}^{(\mathrm{N})} + \mathrm{v}^{(\mathrm{N})}\phi_0^{(\mathrm{N})}\alpha^{f(\mathrm{N})} = \overline{\alpha}_{ij}^{(\mathrm{N})}\overline{\alpha}_{ij}^{s} + \mathrm{v}^{(\mathrm{N})}\phi_0^{(\mathrm{N})}(\alpha^{f(\mathrm{N})} - \alpha_{kk}^{s(\mathrm{N})}), \quad (4.14)$$

$$\overline{C} = \overline{C}^{s} + \sum_{(\mathrm{N})=\mathrm{I,II}} \mathrm{v}^{(\mathrm{N})}\phi_0^{(\mathrm{N})}\rho_0^{f(\mathrm{N})}c^{f(\mathrm{N})} \,, \quad (4.15)$$

The first three terms on the right of Eq. 4.12 represent entropy or heat changes due to adiabatic deformation of the solid and the fluid. It is often negligible (Coussy 2004) and will be neglected in this work. In summary, the porothermoelastic constitutive equations for a dual-porosity medium are

$$\sigma_{ij} = \overline{M}_{ijkl}\varepsilon_{kl} + \overline{\alpha}_{ij}^{\mathrm{I}} p^{\mathrm{I}} + \overline{\alpha}_{ij}^{\mathrm{II}} p^{\mathrm{II}} + \overline{\beta}_{ij}^{s} T \quad (4.16)$$

$$\zeta^{\mathrm{I}} = -\overline{\alpha}_{ij}^{\mathrm{I}}\varepsilon_{kk} + \frac{p^{\mathrm{I}}}{\overline{M}^{\mathrm{I}}} + \frac{p^{\mathrm{II}}}{\overline{M}^{\mathrm{I,II}}} - \overline{\beta}_{fs}^{\mathrm{I}} T \,, \quad (4.17)$$

$$\zeta^{\mathrm{II}} = -\overline{\alpha}_{ij}^{\mathrm{II}}\varepsilon_{kk} + \frac{p^{\mathrm{I}}}{\overline{M}^{\mathrm{I,II}}} + \frac{p^{\mathrm{II}}}{\overline{M}^{\mathrm{II}}} - \overline{\beta}_{fs}^{\mathrm{II}} T \,, \quad (4.18)$$

$$S - \sum_{(N)=I,II} s_0^{f(N)} m^{f(N)} = \frac{\overline{C}}{T_0} T \,, \quad (4.19)$$

where the incremental form *d* has been dropped for convenient.

4.2.2 Balance Equations

Momentum Balance. The momentum balance of the whole system assuming quasi-static evolution and neglecting inertia and body force yields the equilibrium equations which is given as

$$\frac{\partial \sigma_{ij}}{\partial x_j} = 0 \,, \quad (4.20)$$

Fluid Mass Balance. The fluid mass balance, accounting for the interporosity fluid exchange, Γ, and the fluid flow, $q_i^{(N)}$, within the porous primary and secondary porosity medium, are written separately as

$$\frac{\partial \zeta^{I}}{\partial t} + v^{I} \frac{\partial q_i^{I}}{\partial x_i} = \Gamma \,, \quad (4.21a)$$

$$\frac{\partial \zeta^{II}}{\partial t} + v^{II} \frac{\partial q_i^{II}}{\partial x_i} = -\Gamma \,, \quad (4.21b)$$

Under isothermal condition, separate Darcy's equations are written for each porosity region in which the fluid flux is proportional to the individual pressure gradient (Eq. 2.12). For non-isothermal condition, fluid transport within the system can be caused by gradients in both the pore-fluid pressure as well as temperature. A generalized expression for fluid specific discharge, $q_i^{(N)}$, is given as

$$q_i^{(\mathrm{N})} = -\kappa_{ij}^{(\mathrm{N})} \frac{\partial p^{(\mathrm{N})}}{\partial x_j} + D_{ij}^{T(\mathrm{N})} \frac{\partial T}{\partial x_j}, \quad (4.22)$$

where $\kappa_{ij}^{(\mathrm{N})}$ is the mobility coefficient tensor and $D_{ij}^{T(\mathrm{N})}$ is the thermo-osmosis coefficient tensor. The first term on the right hand side of Eq. 4.22 corresponds to fluid transport caused by the Darcy effect and the second term is associated with thermo-osmosis effect which is fluid flux generated by a temperature gradient. The thermo-osmosis effect is ignored in this analysis and Eq. 4.22 results in the well-known Darcy's law.

Generally, the interporosity fluid exchange, Γ, in Eqs. 4.21a and 4.21b includes contribution from both hydro and thermo driving force. However, the assumption of a single-temperature for the overall dual-porous system effectively eliminates the thermally induced interporosity fluid transfer. As a result, interporosity exchange is the same as isothermal case which in the simplest case is proportional to the pressure differential as given in Eq. 2.14.

Energy Balance. The energy balance expressing the change of heat can be written in term of the change in entropy of the system. Neglecting viscous dissipation effect, the thermal equation is expressed as (Coussy 2004)

$$T_0 \left[\frac{\partial S}{\partial t} - \sum_{(\mathrm{N})=\mathrm{I,II}} s_0^{f(\mathrm{N})} \frac{\partial m^{f(\mathrm{N})}}{\partial t} \right] = -\frac{\partial q_i^h}{\partial x_i} - \sum_{(\mathrm{N})=\mathrm{I,II}} \rho_0^{f(\mathrm{N})} c^{f(\mathrm{N})} \mathrm{v}^{(\mathrm{N})} q_i^{(\mathrm{N})} \frac{\partial T}{\partial x_i}, \quad (4.23)$$

where q_i^h is the heat flux. In the above equations, the first term on the right hand side corresponds to heat transport by conduction, whereas the second term represents the heat transport by convection. Analogous to the fluid mass transport, the heat flux in the most

general case can be caused by gradients of both pressure and temperature. A generalized equation for the heat flux is given by

$$q_i^h = -\lambda_{ij}^T \frac{\partial T}{\partial x_j} + \sum_{(N)=I,II} D_{ij}^{p(N)} \frac{\partial p^{(N)}}{\partial x_j}, \quad (4.24)$$

in which λ_{ij}^T is the effective thermal conductivity coefficient tensor for the whole dual-porous system and $D_{ij}^{p(N)}$ is the coefficient tensor associated with the heat flux generated by the pressure gradients. The first term on the right hand side in Eq. 4.24 is the heat flux caused by the Fourier effect, whereas the second term gives the heat flux resulting from the Dufour effect. The Dufour effect is ignored in this analysis, thus giving the governing equation for the heat flux also known as Fourier's law. The effective thermal conductivity is given as a volumetric weighted average of the constituents' conductivity as

$$\lambda_{ij}^T = \sum_{(N)=I,II} v^{(N)} [(1-\phi_0^{(N)}) \lambda_{ij}^{Ts(N)} + \phi_0^{(N)} \lambda_{ij}^{Tf(N)}], \quad (4.25)$$

where $\lambda_{ij}^{Ts(N)}$ and $\lambda_{ij}^{Tf(N)}$ are the thermal conductivity of the solid and fluid constituents, respectively.

4.2.3 Field and Diffusion Equations

The above governing equations are further combined to yield the field and diffusion equations that are used to solve for the coupled stress and pore-pressure responses in general anisotropic dual-porous materials. In this section, they are specialized to transversely isotropic and isotropic materials under the generalized plane strain condition.

Transversely Isotropic Case. In the case of transverse isotropy where the *z* axis is

assumed to coincide with the overall axis of material rotation symmetry, the constitutive relations for dual-porochemoelasticity involve twelve independent material coefficients and are given as

$$\sigma_{11} = \overline{M}_{11}\varepsilon_{11} + \overline{M}_{12}\varepsilon_{22} + \overline{M}_{13}\varepsilon_{33} + \overline{\alpha}_1^{\mathrm{I}} p^{\mathrm{I}} + \overline{\alpha}_1^{\mathrm{II}} p^{\mathrm{II}} + \overline{\beta}_1^{s} T \,, \quad (4.26)$$

$$\sigma_{22} = \overline{M}_{12}\varepsilon_{11} + \overline{M}_{11}\varepsilon_{22} + \overline{M}_{13}\varepsilon_{33} + \overline{\alpha}_1^{\mathrm{I}} p^{\mathrm{I}} + \overline{\alpha}_1^{\mathrm{II}} p^{\mathrm{II}} + \overline{\beta}_1^{s} T \,, \quad (4.27)$$

$$\sigma_{33} = \overline{M}_{13}\varepsilon_{11} + \overline{M}_{13}\varepsilon_{22} + \overline{M}_{33}\varepsilon_{33} + \overline{\alpha}_3^{\mathrm{I}} p^{\mathrm{I}} + \overline{\alpha}_3^{\mathrm{II}} p^{\mathrm{II}} + \overline{\beta}_3^{s} T \,, \quad (4.28)$$

$$\sigma_{12} = 2\overline{M}_{44}\varepsilon_{12}; \qquad \sigma_{13} = 2\overline{M}_{55}\varepsilon_{13}; \qquad \sigma_{23} = 2\overline{M}_{55}\varepsilon_{23} \,, \quad (4.29)$$

$$\zeta^{\mathrm{I}} = -\overline{\alpha}_1^{\mathrm{I}}(\varepsilon_{11} + \varepsilon_{22}) - \overline{\alpha}_3^{\mathrm{I}}\varepsilon_{33} + \frac{p^{\mathrm{I}}}{\overline{M}^{\mathrm{I}}} + \frac{p^{\mathrm{II}}}{\overline{M}^{\mathrm{I,II}}} - \overline{\beta}_{fs}^{\mathrm{I}} T \,, \quad (4.30)$$

$$\zeta^{\mathrm{II}} = -\overline{\alpha}_1^{\mathrm{II}}(\varepsilon_{11} + \varepsilon_{22}) - \overline{\alpha}_3^{\mathrm{II}}\varepsilon_{33} + \frac{p^{\mathrm{I}}}{\overline{M}^{\mathrm{I,II}}} + \frac{p^{\mathrm{II}}}{\overline{M}^{\mathrm{II}}} - \overline{\beta}_{fs}^{\mathrm{II}} T \,, \quad (4.31)$$

In the above, the subscripts 1 and 2 denote properties in the isotropic plane (*x*-*y* or *r*-θ plane) and 3 represents the axis of rotational symmetric (*z* axis). The coefficients $\overline{M}_{11}$, $\overline{M}_{12}$, $\overline{M}_{13}$, $\overline{M}_{33}$, $\overline{M}_{44}$, and $\overline{M}_{55}$ are components of the drained overall elastic tensor for a transversely isotropic dual-porous material. $\overline{\alpha}_1^{(\mathrm{N})}$ and $\overline{\alpha}_3^{(\mathrm{N})}$ are Biot's effective stress coefficients in the isotropic plane and transverse direction, respectively. These overall coefficients are related to individual set of material properties of the primary and secondary porosity as given in Appendix A. The expressions for $\overline{\beta}_1^{s}$, $\overline{\beta}_3^{s}$, and $\overline{\beta}_{fs}^{(\mathrm{N})}$ are obtained as follows

$$\overline{\beta}_1^{s} = (\overline{M}_{11} + \overline{M}_{12})\overline{\alpha}_1^{s} + \overline{M}_{13}\overline{\alpha}_3^{s}; \qquad \overline{\beta}_3^{s} = 2\overline{M}_{13}\overline{\alpha}_1^{s} + \overline{M}_{33}\overline{\alpha}_3^{s} \,, \quad (4.32)$$

$$\overline{\beta}_{fs}^{(\mathrm{N})} = 2\overline{\alpha}_1^{(\mathrm{N})}\overline{\alpha}_1^{s} + \overline{\alpha}_3^{(\mathrm{N})}\overline{\alpha}_3^{s} + \mathrm{v}^{(\mathrm{N})}\phi_0^{(\mathrm{N})}(\alpha^{f(\mathrm{N})} - 2\alpha_1^{s(\mathrm{N})} - \alpha_3^{s(\mathrm{N})}) \,, \quad (4.33)$$

The transversely isotropic equations are further reduced to the generalized plane strain case where all response functions (except axial displacement) are invariant along the axis of material rotational symmetry and the out-of-plane strain components are either zero or spatially uniform, i.e., $\varepsilon_{13} = \varepsilon_{23} = 0$ and $\varepsilon_{33} = \varepsilon_{33}(t)$. The constitutive equations for in-plane stress components reduce to

$$\sigma_{11} = \overline{M}_{11}\varepsilon_{11} + \overline{M}_{12}\varepsilon_{22} + \overline{M}_{13}\varepsilon_{33} + \overline{\alpha}_1^{\mathrm{I}} p^{\mathrm{I}} + \overline{\alpha}_1^{\mathrm{II}} p^{\mathrm{II}} + \overline{\beta}_1^{s} T \,, \quad (4.34)$$

$$\sigma_{22} = \overline{M}_{12}\varepsilon_{11} + \overline{M}_{11}\varepsilon_{22} + \overline{M}_{13}\varepsilon_{33} + \overline{\alpha}_1^{\mathrm{I}} p^{\mathrm{I}} + \overline{\alpha}_1^{\mathrm{II}} p^{\mathrm{II}} + \overline{\beta}_1^{s} T \,, \quad (4.35)$$

$$\sigma_{12} = 2\overline{M}_{44}\varepsilon_{12} \,, \quad (4.36)$$

with the corresponding equilibrium equations given in Eq. 2.18. Combining these equations yields the compatibility equation as

$$\nabla^2 \left(\varepsilon_{11} + \varepsilon_{22} + \frac{\overline{\alpha}_1^{\mathrm{I}}}{\overline{M}_{11}} p^{\mathrm{I}} + \frac{\overline{\alpha}_1^{\mathrm{II}}}{\overline{M}_{11}} p^{\mathrm{II}} + \frac{\overline{\beta}_1^{s}}{\overline{M}_{11}} T \right) = 0 \,, \quad (4.37)$$

or in terms of stress

$$\nabla^2 \left[\sigma_{11} + \sigma_{22} - \left(1 - \frac{\overline{M}_{12}}{\overline{M}_{11}} \right) \overline{\alpha}_1^{\mathrm{I}} p^{\mathrm{I}} - \left(1 - \frac{\overline{M}_{12}}{\overline{M}_{11}} \right) \overline{\alpha}_1^{\mathrm{II}} p^{\mathrm{II}} - \left(1 - \frac{\overline{M}_{12}}{\overline{M}_{11}} \right) \overline{\beta}_1^{s} T \right] = 0 \,, \quad (4.38)$$

where $\nabla^2 = \partial^2 / x_1^2 + \partial^2 / x_2^2$ is the Laplacian spatial differential operator. Next, the fluid diffusion equations are obtained by substituting the fluid content constitutive equations (Eqs. 4.18 and 4.19) and Darcy's law (Eq. 4.22) into the fluid mass balance (Eqs. 4.21a to 4.21b) as follows

$$-\overline{\alpha}_1^{\mathrm{I}}\frac{\partial(\varepsilon_{11}+\varepsilon_{22})}{\partial t}-\overline{\alpha}_3^{\mathrm{I}}\frac{\partial\varepsilon_{33}}{\partial t}-\overline{\beta}_{fs}^{\mathrm{I}}\frac{\partial T}{\partial t}$$
$$+\frac{1}{\overline{M}^{\mathrm{I}}}\frac{\partial p^{\mathrm{I}}}{\partial t}+\frac{1}{\overline{M}^{\mathrm{I,II}}}\frac{\partial p^{\mathrm{II}}}{\partial t}=\overline{\kappa}_1^{\mathrm{I}}\nabla^2 p^{\mathrm{I}}+\lambda(p^{\mathrm{II}}-p^{\mathrm{I}}) \quad \text{,.....(4.39)}$$

$$-\overline{\alpha}_1^{\mathrm{II}}\frac{\partial(\varepsilon_{11}+\varepsilon_{22})}{\partial t}-\overline{\alpha}_3^{\mathrm{II}}\frac{\partial\varepsilon_{33}}{\partial t}$$
$$+\frac{1}{\overline{M}^{\mathrm{I,II}}}\frac{\partial p^{\mathrm{I}}}{\partial t}+\frac{1}{\overline{M}^{\mathrm{II}}}\frac{\partial p^{\mathrm{II}}}{\partial t}-\overline{\beta}_{fs}^{\mathrm{II}}\frac{\partial T}{\partial t}=\overline{\kappa}_1^{\mathrm{II}}\nabla^2 p^{\mathrm{II}}-\lambda(p^{\mathrm{II}}-p^{\mathrm{I}}) \quad \text{,.....(4.40)}$$

with $\overline{\kappa}_1^{(\mathrm{N})}=\mathrm{v}^{(\mathrm{N})}\kappa_1^{(\mathrm{N})}$. Combining the energy balance relation (Eq. 4.23), Fourier's law (Eq. 4.24), and Darcy's law (Eq. 4.22) with the constitutive change in entropy (Eq. 4.19) yields the heat diffusion equation

$$\frac{\partial T}{\partial t}=c_h^T\nabla^2 T+\sum_{(\mathrm{N})=\mathrm{I,II}}c_{hf}^{T(\mathrm{N})}\nabla p^{(\mathrm{N})}\nabla T \text{ , ...(4.41)}$$

where ∇ is the gradient operator, c_{hf}^T is the heat conduction diffusivity and $c_{hf}^{T(\mathrm{N})}$ is the heat convection coefficients given as

$$c_h^T=\lambda_1^T/\overline{C};\qquad c_{hf}^{T(\mathrm{N})}=\rho_0^{f(\mathrm{N})}c^{f(\mathrm{N})}\overline{\kappa}_1^{(\mathrm{N})}/\overline{C} \text{ ,.....(4.42)}$$

The summation terms on the right-hand side of Eq. 4.41 correspond to heat transport by convection and render the equations nonlinear. In low-permeability porous media such as shale, heat conduction mechanism via the intact rock matrix is dominant and convective heat transport due to fluid flow can be neglected. Hence, the heat equation is completely linearized and analytical solution can be obtained. However, in dual-porous formations such as fractured rock, the high fracture's hydraulic conductivity may lead to non-negligible heat convection contribution. If the non-linear convective effect is included, then numerical approaches such as finite difference or finite element are needed in subsequent

solutions and analyses.

Isotropic Case. For isotropic dual-porous material, the constitutive equations for dual-porothermoelasticity reduce to

$$\sigma_{ij} = \frac{\overline{E}}{1+\overline{\nu}}\left[\varepsilon_{ij} + \frac{\overline{\nu}}{(1-2\overline{\nu})}\varepsilon_{kk}\delta_{ij}\right] + (\overline{\alpha}^{\mathrm{I}} p^{\mathrm{I}} + \overline{\alpha}^{\mathrm{II}} p^{\mathrm{II}} + \overline{\beta}^{\mathrm{s}} T)\delta_{ij}\,, \quad (4.43)$$

$$\zeta^{\mathrm{I}} = -\overline{\alpha}^{\mathrm{I}}\varepsilon_{kk} + \frac{p^{\mathrm{I}}}{\overline{M}^{\mathrm{I}}} + \frac{p^{\mathrm{II}}}{\overline{M}^{\mathrm{I,II}}} - \overline{\beta}_{fs}^{\mathrm{I}} T\,, \quad (4.44)$$

$$\zeta^{\mathrm{II}} = -\overline{\alpha}^{\mathrm{II}}\varepsilon_{kk} + \frac{p^{\mathrm{I}}}{\overline{M}^{\mathrm{I,II}}} + \frac{p^{\mathrm{II}}}{\overline{M}^{\mathrm{II}}} - \overline{\beta}_{fs}^{\mathrm{II}} T\,, \quad (4.45)$$

where $\overline{\beta}^{s}$ and $\overline{\beta}_{fs}^{(\mathrm{N})}$ are given in terms of the volumetric thermal expansion coefficients $\overline{\alpha}^{s}$ and $\overline{\alpha}^{s(\mathrm{N})}$ as

$$\overline{\beta}^{s} = \frac{\overline{\alpha}^{s}\overline{E}}{3(1-2\overline{\nu})}, \qquad \overline{\beta}_{fs}^{(\mathrm{N})} = \overline{\alpha}^{(\mathrm{N})}\overline{\alpha}^{s} + \mathrm{v}^{(\mathrm{N})}\phi_0^{(\mathrm{N})}(\alpha^{f(\mathrm{N})} - \alpha^{s(\mathrm{N})})\,, \quad (4.46)$$

And the compatibility relation in plane strain, Eq. 4.37 or Eq. 4.38, becomes

$$\nabla^2\left(\varepsilon_{kk} + \frac{\overline{\eta}^{\mathrm{I}}}{\overline{G}} p^{\mathrm{I}} + \frac{\overline{\eta}^{\mathrm{II}}}{\overline{G}} p^{\mathrm{II}} + \frac{\overline{\eta}^{\mathrm{T}}}{\overline{G}} T\right) = 0\,, \quad (4.47)$$

$$\nabla^2\left(\sigma_{11} + \sigma_{22} + 2\overline{\eta}^{\mathrm{I}} p^{\mathrm{I}} + 2\overline{\eta}^{\mathrm{II}} p^{\mathrm{II}} + 2\overline{\eta}^{\mathrm{T}} T\right) = 0\,, \quad (4.48)$$

where $\varepsilon_{kk} = \varepsilon_{11} + \varepsilon_{22} + \varepsilon_{33}$ is the volumetric strain, $\overline{G}$ is the overall shear modulus of the system, $\overline{\eta}^{(\mathrm{N})}$ and $\overline{\eta}^{T}$ are lumped poroelastic coefficients defined as

$$\overline{G} = \frac{\overline{E}}{2(1+\overline{\nu})}; \qquad \overline{\eta}^{(\mathrm{N})} = \overline{\alpha}^{(\mathrm{N})}\frac{1-2\overline{\nu}}{2(1-\overline{\nu})}; \qquad \overline{\eta}^{T} = \overline{\beta}^{s}\frac{1-2\overline{\nu}}{2(1-\overline{\nu})}\,, \quad (4.49)$$

Subsequently, the fluid and heat diffusion equations maintain the same forms as those of

transversely isotropic case (Eqs. 4.39 to 4.41) with $\overline{\alpha}_1^{(\mathrm{N})} \to \overline{\alpha}^{(\mathrm{N})}$, $\kappa_1^{(\mathrm{N})} \to \kappa^{(\mathrm{N})}$, and $\lambda_1^T \to \lambda^T$.

4.3 Inclined Wellbore

This section presents the development of solutions to determine the stress and pressure redistribution due to drilling activities through high pressure and high temperature (HPHT) fractured rock formations under the framework of the above dual-porothermoelastic formulation.

4.3.1 Problem Descriptions

The inclined wellbore problem geometry is shown in Fig. 4.1. The undisturbed formation's pore pressure and temperature are in equilibrium between the matrix and fracture and are denoted as p_0 and T_0, respectively.

After excavation, the borehole is filled with a drilling fluid having pressure, p_w, and temperature, T_w. Therefore, the boundary conditions to be imposed at the wellbore wall, $r = R_w$, are

$$\sigma_{rr} = [\sigma_m + \sigma_d \cos(2(\theta - \theta_r))]\,\mathrm{H}(-t) + p_w(t), \quad (4.50a)$$

$$\sigma_{r\theta} = -\sigma_d \sin(2(\theta - \theta_r))\,\mathrm{H}(-t), \quad (4.50b)$$

$$\sigma_{rz} = [S_{xz}\cos(\theta) + S_{yz}\sin(\theta)]\,\mathrm{H}(-t), \quad (4.50c)$$

$$p^{\mathrm{I}} = p^{\mathrm{II}} = p_0\mathrm{H}(-t) + p_w(t), \quad (4.50d)$$

$$T = T_0\,\mathrm{H}(-t) + T_w(t), \quad (4.50e)$$

And at the far field, $r \to \infty$

$$\sigma_{xx} = S_x, \qquad \sigma_{yy} = S_y, \qquad \sigma_{zz} = S_z, \quad \text{(4.51a)}$$

$$\sigma_{xy} = S_{xy}, \qquad \sigma_{yz} = S_{yz} \qquad \sigma_{xz} = S_{xz}, \quad \text{(4.51b)}$$

$$p^{\mathrm{I}} = p^{\mathrm{II}} = p_0; \qquad T = T_0, \quad \text{(4.51c)}$$

It should be noted that the heat diffusion including convection effect, Eq. 4.41, is non-linear and demands numerical approaches. While realistically modeling field conditions, these numerical methods are computationally intensive and require extensive analytical validation. The complete linearization by neglecting heat convection allows analytical approach to an otherwise complex problem and provides the engineers with a tool for quick assessment of thermal effect. The porothermoelastic analytical solution for an inclined wellbore drilled in intact rock formation was published by Ekbote and Abousleiman (2005). By the same token, the approach is applicable to the current dual-porosity and dual-permeability porothermoelastic by incorporating relevant boundary conditions for stresses, dual pore pressures, and temperature as shown in the following section.

4.3.2 Analytical Solution

By neglecting the non-linear heat convection term in Eq. 4.41, the thermal diffusion equation is fully linearized. As discussed in Chapter 2, the linearity of the governing equations allows the problem to be solved by the superposition of the initial state and two sub-problems of the perturbed state: (I) the strain problem and (II) the antiplane shear stress problem. The boundary conditions and solutions in the decomposition scheme are given as follows

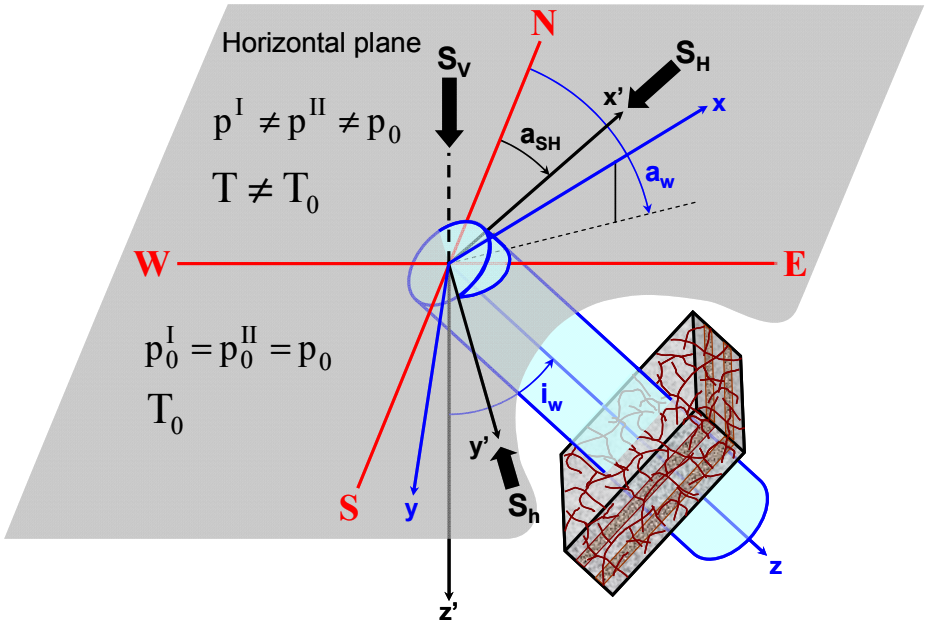

(a)

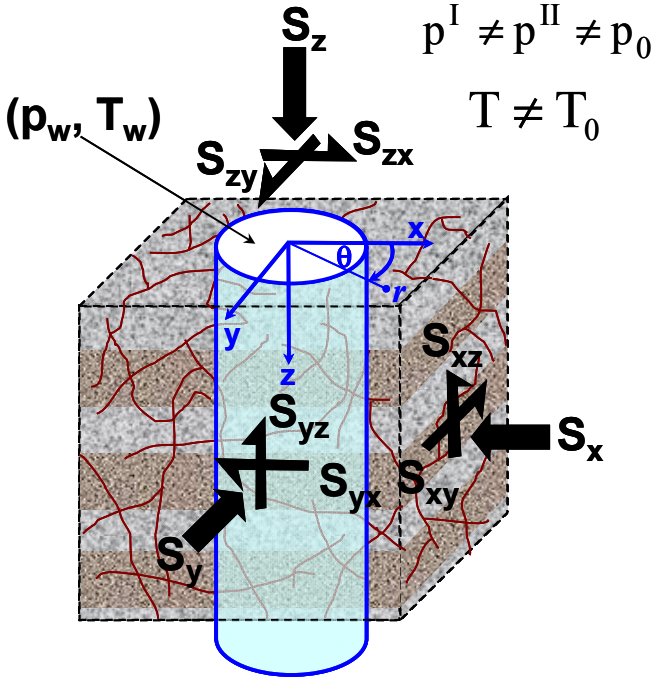

(b)

Fig. 4.1— (a) Schematic of an inclined wellbore in fractured rock formation under non-isothermal condition, (b) far-field stresses, pore pressure and temperature in the *xyz* local wellbore coordinate system.

Problem I – Plane Strain

The boundary conditions for perturbed quantities in Problem I at the wall ($r = R_w$) are

$$\sigma_{rr} = p_w(t) - [\sigma_m + \sigma_d \cos(2(\theta - \theta_r))] \,, \quad (4.52a)$$

$$\sigma_{r\theta} = \sigma_d \sin(2(\theta - \theta_r)) \,, \quad (4.52b)$$

$$p^{\mathrm{I}} = p^{\mathrm{II}} = p_w(t) - p_0 \,, \quad (4.52c)$$

$$T = T_w(t) - T_0 \,, \quad (4.52d)$$

It is obvious to recognize that the loading condition can be separated into an axisymmetric case (θ-independent) and deviatoric case (θ-dependent) as follow

Case 1: Axisymmetric Loading. The perturbed boundary conditions at the wellbore ($r = R_w$) are

$$\sigma_{rr} = p_w(t) - \sigma_m; \qquad \sigma_{r\theta} = 0 \,, \quad (4.53a)$$

$$p^{\mathrm{I}} = p^{\mathrm{II}} = p_w(t) - p_0 \,, \quad (4.53b)$$

$$T = T_w(t) - T_0 \,, \quad (4.53c)$$

Under axisymmetric condition, the compatibility relation, Eq. 4.37, becomes

$$\left(\frac{\partial^2}{\partial r^2} + \frac{1}{r}\frac{\partial}{\partial r}\right)\left(\varepsilon_{kk} + \frac{\overline{\alpha}_1^{\mathrm{I}}}{\overline{M}_{11}} p^{\mathrm{I}} + \frac{\overline{\alpha}_1^{\mathrm{II}}}{\overline{M}_{11}} p^{\mathrm{II}} + \frac{\overline{\beta}_1^{s}}{\overline{M}_{11}} T\right) = 0 \,, \quad (4.54)$$

In the above, $\varepsilon_{kk} = \varepsilon_{rr} + \varepsilon_{\theta\theta}$ since $\varepsilon_{zz} = 0$ for plane strain. Integration of the above noting that all quantities must vanish at far field ($r \to \infty$) yields

$$\varepsilon_{kk} = -\frac{\overline{\alpha}_1^{\mathrm{I}}}{\overline{M}_{11}} p^{\mathrm{I}} - \frac{\overline{\alpha}_1^{\mathrm{II}}}{\overline{M}_{11}} p^{\mathrm{II}} - \frac{\overline{\beta}_1^{s}}{\overline{M}_{11}} T \,, \quad (4.55)$$

Eliminating the volumetric strain in Eqs. 4.39 and 4.40 gives the fluid diffusion equation as

$$\left[[\mathbf{A}]\frac{\partial}{\partial t}+[\mathbf{\Gamma}]-[\mathbf{D}]\left(\frac{\partial^2}{\partial r^2}+\frac{1}{r}\frac{\partial}{\partial r}\right)\right]\begin{Bmatrix}p^{\mathrm{I}}\\ p^{\mathrm{II}}\end{Bmatrix}=\begin{Bmatrix}\overline{\beta}_{fs}^{\mathrm{I}}-\overline{\alpha}_1^{\mathrm{I}}\overline{\beta}_1^{s}/\overline{M}_{11}\\ \overline{\beta}_{fs}^{\mathrm{II}}-\overline{\alpha}_1^{\mathrm{II}}\overline{\beta}_1^{s}/\overline{M}_{11}\end{Bmatrix}\frac{\partial T}{\partial t}, \quad (4.56)$$

where the coefficient matrix [**A**], [**Γ**], and [**D**] are given in Eqs. 2.37 and 2.38. In term of dimensionless coefficients, Eq. 4.56 becomes

$$\left[[\boldsymbol{\omega}]\frac{\partial}{\partial t_D}+[\mathbf{\Gamma_D}]-[\overline{\boldsymbol{\kappa}}_{\mathbf{D}}]\left(\frac{\partial^2}{\partial r_D^2}+\frac{1}{r_D}\frac{\partial}{\partial r_D^2}\right)\right]\begin{Bmatrix}p^{\mathrm{I}}\\ p^{\mathrm{II}}\end{Bmatrix}=\begin{Bmatrix}c_{hf}^{\mathrm{I}}\\ c_{hf}^{\mathrm{II}}\end{Bmatrix}\frac{\partial T}{\partial t_D}, \quad (4.57)$$

with the dimensionless coefficient matrix [**ω**], [$\mathbf{\Gamma_D}$] and [$\overline{\boldsymbol{\kappa}}_{\mathbf{D}}$] given in Eq. 2.43 and the coefficient $c_{hf}^{(\mathrm{N})}$ defined as

$$c_{hf}^{(\mathrm{N})}=(\overline{\beta}_{fs}^{(\mathrm{N})}-\overline{\alpha}_1^{(\mathrm{N})}\overline{\beta}_1^{s}/\overline{M}_{11})/(A_{11}+A_{22}), \quad (4.58)$$

It can be seen that in axisymmetric loading of the wellbore geometry with infinite extent, the fluid diffusion equation is uncoupled and can be solved separately from the stress/displacement field. The fluid flow, however, is still coupled with the temperature variation. On the other hand, the thermal equation simplifies to a classical heat conduction equation which is uncoupled from both the stress and pore-pressure field as

$$\frac{\partial T}{\partial t_D}=\overline{\kappa}_D^T\left(\frac{\partial^2 T}{\partial r_D^2}+\frac{1}{r_D}\frac{\partial T}{\partial r_D}\right), \quad (4.59)$$

in which the dimensionless thermal coefficient $\overline{\kappa}_D^T$ is given as

$$\overline{\kappa}_D^T=\frac{(A_{11}+A_{22})c_h^T}{\overline{\kappa}^{\mathrm{I}}+\overline{\kappa}^{\mathrm{II}}}, \quad (4.60)$$

Using the boundary condition, Eq. 4.53c, the solution for temperature field is obtained independently and expressed in Laplace transform domain as

$$\widetilde{T}^{(1)} = \Delta\widetilde{T}\,\Phi(\xi_h r_D) = (\widetilde{T}_w - T_0/s)\frac{\mathrm{K}_0(\xi_h r_D)}{\mathrm{K}_0(\xi_h)}, \quad (4.61)$$

where $\xi_h = \sqrt{s/\overline{\kappa}_D^T}$; the tilde sign $\widetilde{\ }$ denotes the corresponding quantity in Laplace transform domain; s is the Laplace transform parameter; K_0 is the modified Bessel functions of the second kind of order zero; the superscript $^{(1)}$ denotes loading case number. Next, the expressions for the dual pressure fields are derived by solving Eq. 4.57. Equation 4.57 is a non-homogeneous partial differential equation system and its general solution is obtained as a summation of the homogeneous and particular solutions and given as

$$\widetilde{p}^{\mathrm{I}(1)} = g_T^{\mathrm{I}}\widetilde{T}^{(1)} + \sum_{(\mathrm{N})=\mathrm{I,II}} C_1^{(\mathrm{N})}\mathrm{K}_0(\xi^{(\mathrm{N})} r_D) \quad (4.62)$$

$$\widetilde{p}^{\mathrm{II}(1)} = g_T^{\mathrm{II}}\widetilde{T}^{(1)} + \sum_{(\mathrm{N})=\mathrm{I,II}} m^{(\mathrm{N})} C_1^{(\mathrm{N})}\mathrm{K}_0(\xi^{(\mathrm{N})} r_D) \quad (4.63)$$

where $C_1^{(\mathrm{N})} = C_1^{(\mathrm{N})}(s)$ is arbitrary coefficient to be determined from boundary conditions; $\xi^{(\mathrm{N})} = \sqrt{\ell^{(\mathrm{N})}}$ with the coefficients $\ell^{(\mathrm{N})}$ and $m^{(\mathrm{N})}$ given in Eqs. 2.48 and 2.49; the parameters $g_T^{(\mathrm{N})}$ is defined as

$$g_T^{(\mathrm{N})} = \left(s\left([\boldsymbol{\omega}] - \frac{[\overline{\boldsymbol{\kappa}}_{\mathbf{D}}]}{\overline{\kappa}_D^T} \right) + [\boldsymbol{\Gamma}_{\mathbf{D}}] \right)^{-1} \begin{Bmatrix} c_{hf}^{\mathrm{I}} \\ c_{hf}^{\mathrm{II}} \end{Bmatrix} s, \quad (4.64)$$

Applying the pressure boundary condition (Eq. 4.53b) yields

$$\widetilde{p}^{\mathrm{I}(1)} = g_T^{\mathrm{I}}\Delta\widetilde{T}\,\Phi(\xi_h r_D) + \sum_{(\mathrm{N})=\mathrm{I,II}} \Delta_{pT}^{(\mathrm{N})}\Phi(\xi^{(\mathrm{N})} r_D), \quad (4.65)$$

$$\widetilde{p}^{\mathrm{II}(1)} = g_T^{\mathrm{II}}\Delta\widetilde{T}\,\Phi(\xi_h r_D) + \sum_{(\mathrm{N})=\mathrm{I,II}} m^{(\mathrm{N})}\Delta_{pT}^{(\mathrm{N})}\Phi(\xi^{(\mathrm{N})} r_D), \quad (4.66)$$

where the lumped parameters $\Delta_{pT}^{(\mathrm{N})}$ is defined in terms of $\Delta\widetilde{p} = \widetilde{p}_w - p_0/s$ and

$\Delta\widetilde{T} = \widetilde{T}_w - T_0 / s$ as

$$\Delta^{\mathrm{I}}_{pT} = [(1-m^{\mathrm{II}})\Delta\widetilde{p} - (g^{\mathrm{II}}_T - g^{\mathrm{I}}_T m^{\mathrm{II}})\Delta\widetilde{T}]/(m^{\mathrm{I}} - m^{\mathrm{II}}) \quad \text{.....(4.67a)}$$

$$\Delta^{\mathrm{II}}_{pT} = -[(1-m^{\mathrm{I}})\Delta\widetilde{p} - (g^{\mathrm{II}}_T - g^{\mathrm{I}}_T m^{\mathrm{I}})\Delta\widetilde{T}]/(m^{\mathrm{I}} - m^{\mathrm{II}}) \text{ , ...(4.67b)}$$

After obtaining the solution of $\widetilde{p}^{(\mathrm{N})}$ and $\widetilde{T}$, the radial displacement is readily obtained by integration of the volumetric strain, Eq. 4.55, noting that $\varepsilon^{(1)}_{kk} = [(1/r_D)\partial(r_D u^{(1)}_r)/\partial r_D]/R_{\mathrm{w}}$

$$\frac{u^{(1)}_r}{R_w} = \frac{C_2}{r_D} - \frac{1}{r_D}\int r_D \left(\frac{\overline{\alpha}^{\mathrm{I}}_1}{\overline{M}_{11}} p^{\mathrm{I}(1)} + \frac{\overline{\alpha}^{\mathrm{II}}_1}{\overline{M}_{11}} p^{\mathrm{II}(1)} + \frac{\overline{\beta}^{s}_1}{\overline{M}_{11}} T^{(1)} \right) dr_D \text{ , ...(4.68)}$$

where C_2 is another coefficient to be determined from stress or displacement boundary condition. From Eq. 4.68, the polar stress components are straightforward

$$\sigma^{(1)}_{rr} = -(\overline{M}_{11} - \overline{M}_{12}) \left[\frac{C_2}{r^2_D} - \frac{1}{r^2_D}\int r_D \left(\frac{\overline{\alpha}^{\mathrm{I}}_1}{\overline{M}_{11}} p^{\mathrm{I}(1)} + \frac{\overline{\alpha}^{\mathrm{II}}_1}{\overline{M}_{11}} p^{\mathrm{II}(1)} + \frac{\overline{\beta}^{s}_1}{\overline{M}_{11}} T^{(1)} \right) dr_D \right], \text{.....(4.69)}$$

$$\sigma^{(1)}_{\theta\theta} = (\overline{M}_{11} - \overline{M}_{12}) \left[\begin{array}{l} \dfrac{C_2}{r^2_D} - \dfrac{1}{r^2_D}\displaystyle\int r_D \left(\frac{\overline{\alpha}^{\mathrm{I}}_1}{\overline{M}_{11}} p^{\mathrm{I}(1)} + \frac{\overline{\alpha}^{\mathrm{II}}_1}{\overline{M}_{11}} p^{\mathrm{II}(1)} + \frac{\overline{\beta}^{s}_1}{\overline{M}_{11}} T^{(1)} \right) dr_D \\ + \dfrac{\overline{\alpha}^{\mathrm{I}}_1}{\overline{M}_{11}} p^{\mathrm{I}(1)} + \dfrac{\overline{\alpha}^{\mathrm{II}}_1}{\overline{M}_{11}} p^{\mathrm{II}(1)} + \dfrac{\overline{\beta}^{s}_1}{\overline{M}_{11}} T^{(1)} \end{array} \right], \text{.....(4.70)}$$

$$\sigma^{(1)}_{r\theta} = 0 \text{ , ...(4.71)}$$

Using the stress boundary condition, Eq 4.53a, the solution for stress is

$$\widetilde{\sigma}^{(1)}_{rr} = -\sum_{(\mathrm{N})=\mathrm{I},\mathrm{II}} A^{(\mathrm{N})}_1 \Delta^{(\mathrm{N})}_{pT} \Pi(\xi^{(\mathrm{N})} r_D) - A^T \Delta\widetilde{T}\, \Pi(\xi_h r_D) + \Delta\widetilde{\sigma}/r^2_D \text{ , ...(4.72)}$$

$$\begin{array}{l} \widetilde{\sigma}^{(2)}_{\theta\theta} = \displaystyle\sum_{(\mathrm{N})=\mathrm{I},\mathrm{II}} A^{(\mathrm{N})}_1 \Delta^{(\mathrm{N})}_{pT} [\Pi(\xi^{(\mathrm{N})} r_D) + \Phi(\xi^{(\mathrm{N})} r_D)] \\ \quad + A^T \Delta\widetilde{T}\, [\Pi(\xi_h r_D) + \Phi(\xi_h r_D)] - \Delta\widetilde{\sigma}/r^2_D \end{array} \text{ , ...(4.73)}$$

where the coefficient $A^{(\mathrm{N})}_1$ is defined in Eq. 2.71b; the lumped parameter A^T and the

functions Π and $\Delta\widetilde{\sigma}$ are given as

$$A^T = (1-\overline{M}_{12}/\overline{M}_{11})(\overline{\alpha}_1^{\mathrm{I}} g_T^{\mathrm{I}} + \overline{\alpha}_1^{\mathrm{II}} g_T^{\mathrm{II}} + \overline{\beta}_1^{s}), \quad (4.74)$$

$$\Delta\widetilde{\sigma} = \widetilde{p}_w - \sigma_m / s; \qquad \Pi(x r_D) = \frac{\mathrm{K}_1(x r_D)}{x r_D \mathrm{K}_0(x)} - \frac{\mathrm{K}_1(x)}{x r_D^2 \mathrm{K}_0(x)}, \quad (4.75)$$

Case 2: Deviatoric Loading. The perturbed boundary condition at the borehole wall (r_D = 1) are

$$\sigma_{rr}^{(2)} = -\sigma_d \cos(2(\theta-\theta_r)), \qquad \sigma_{r\theta}^{(2)} = \sigma_d \sin(2(\theta-\theta_r)), \quad (4.76a)$$

$$p^{\mathrm{I}(2)} = p^{\mathrm{II}(2)} = T^{(2)} = 0, \quad (4.76b)$$

Under this mode of loading, the heat equation yields trivial temperature solution $T^{(2)} = 0$. As a result, the stress and pore pressure responses are the same as those for the case without thermal effect given by Eqs. D1.12 to D1.16 in Appendix D1.

Problem II: Antiplane Shear Stress

The boundary conditions for perturbed quantities in Problem II at the wall ($r = R_w$) are

$$\sigma_{rz} = -[S_{xz}\cos(\theta) + S_{yz}\sin(\theta)], \quad (4.77a)$$

$$\sigma_{rr} = \sigma_{r\theta} = 0, \quad (4.77b)$$

$$p^{\mathrm{I}} = p^{\mathrm{II}} = T = 0, \quad (4.77c)$$

No disturbance of fluid or temperature is generated by this antiplane shear stress perturbation. The solution is elastic and the same as given previously for dual-poroelastic inclined wellbore, i.e., Eqs. 2.107a and 2.107b.

Complete Solution

The complete solutions are obtained by superimposing the background state with non-zero

solutions of the two perturbed sub-problems given as

$$p^{\mathrm{I}} = p_0 + p^{\mathrm{I}(1)} + p^{\mathrm{I}(2)}, \quad (4.78)$$

$$p^{\mathrm{II}} = p_0 + p^{\mathrm{II}(1)} + p^{\mathrm{II}(2)}, \quad (4.79)$$

$$T = T_0 + T^{(1)}, \quad (4.80)$$

$$\sigma_{rr} = \sigma_m + \sigma_d \cos(2(\theta - \theta_r)) + \sigma_{rr}^{(1)} + \sigma_{rr}^{(2)}, \quad (4.81)$$

$$\sigma_{\theta\theta} = \sigma_m - \sigma_d \cos(2(\theta - \theta_r)) + \sigma_{\theta\theta}^{(1)} + \sigma_{\theta\theta}^{(2)}, \quad (4.82)$$

$$\begin{aligned}\sigma_{zz} = {} & S_z + \bar{v}_{13}(\sigma_{rr}^{(1)} + \sigma_{rr}^{(2)} + \sigma_{\theta\theta}^{(1)} + \sigma_{\theta\theta}^{(2)}) + (\bar{\beta}_3^{\mathrm{s}} - 2\bar{v}_{13}\bar{\beta}_1^{\mathrm{s}})T^{(1)} \\ & + (\bar{\alpha}_3^{\mathrm{I}} - 2\bar{v}_{13}\bar{\alpha}_1^{\mathrm{I}})(p^{\mathrm{I}(1)} + p^{\mathrm{I}(2)}) + (\bar{\alpha}_3^{\mathrm{II}} - 2\bar{v}_{13}\bar{\alpha}_1^{\mathrm{II}})(p^{\mathrm{II}(1)} + p^{\mathrm{II}(2)})\end{aligned}, \quad (4.83)$$

$$\sigma_{r\theta} = -\sigma_d \sin(2(\theta - \theta_r)) + \sigma_{r\theta}^{(2)}, \quad (4.84)$$

$$\sigma_{rz} = [S_{xz}\cos(\theta) + S_{yz}\sin(\theta)](1 - 1/r_D^2), \quad (4.85)$$

$$\sigma_{\theta z} = -[S_{xz}\sin(\theta) - S_{yz}\cos(\theta)](1 + 1/r_D^2), \quad (4.86)$$

4.3.3 Numerical Solution

Thus far, the inclined wellbore solution has been obtained analytically by neglecting the non-linear thermal convection. This section presents a quantitative analysis for the effect of thermal convection via numerical solution method. It was shown in the previous section that the pressure and temperature diffusion equations are uncoupled from the stress/deformation field under the special case of axisymmetric loading, i.e., vertical wellbore subjected to hydrostatic in-situ stress condition. Therefore, the pore-pressure and temperature distributions accounting for non-linear thermal convection effect can be obtained independently using finite difference scheme. The finite-difference solutions for

pore pressure and temperature are then substituted into Eqs. 4.69 and 4.70 to get the resultant stress field. The axisymmetric fluid and heat diffusion equations accounting for heat convection effect are

$$\left[[\boldsymbol{\omega}]\frac{\partial}{\partial t_D}+[\boldsymbol{\Gamma}_{\mathbf{D}}]-[\overline{\boldsymbol{\kappa}}_{\mathbf{D}}]\left(\frac{\partial^2}{\partial r_D^2}+\frac{1}{r_D}\frac{\partial}{\partial r_D^2}\right)\right]\begin{Bmatrix}p^{\mathrm{I}}\\ p^{\mathrm{II}}\end{Bmatrix}=\begin{Bmatrix}c_{hf}^{\mathrm{I}}\\ c_{hf}^{\mathrm{II}}\end{Bmatrix}\frac{\partial T}{\partial t_D}, \quad (4.87)$$

$$\frac{\partial T}{\partial t_D}=\overline{\kappa}_D^T\left(\frac{\partial^2 T}{\partial r_D^2}+\frac{1}{r_D}\frac{\partial T}{\partial r_D}\right)+\left(\overline{\kappa}_{hf}^{T\mathrm{I}}\frac{\partial p^{\mathrm{I}}}{\partial r_D}+\overline{\kappa}_{hf}^{T\mathrm{II}}\frac{\partial p^{\mathrm{II}}}{\partial r_D}\right)\frac{\partial T}{\partial r_D}, \quad (4.88)$$

in which the thermal convective coefficient $\overline{\kappa}_{hf}^{T(\mathrm{N})}$ is defined as

$$\overline{\kappa}_{hf}^{T(\mathrm{N})}=\frac{(A_{11}+A_{22})c_{hf}^{T(\mathrm{N})}}{\overline{\kappa}^{\mathrm{I}}+\overline{\kappa}^{\mathrm{II}}}, \quad (4.89)$$

The above diffusion equations are solved using the fully implicit Crank-Nicholson finite difference scheme. Eqs. 4.87 and 4.88 are discretized using small spatial and temporal stepsize. The Crank-Nicholson method transforms each component of the partial differential equations into the followings

$$\frac{\partial X}{\partial t_D}=\frac{X_i^{j+1}-X_i^j}{\Delta t_D}, \quad (4.90a)$$

$$\frac{\partial^2 X}{\partial r_D^2}=\frac{1}{2(\Delta r_D)^2}\left[(X_{i+1}^{j+1}-2X_i^{j+1}+X_{i-1}^{j+1})+(X_{i+1}^j-2X_i^j+X_{i-1}^j)\right], \quad (4.90b)$$

$$\frac{\partial X}{\partial r_D}=\frac{1}{2}\left[\frac{(X_{i+1}^{j+1}-X_{i-1}^{j+1})}{2\Delta r_D}+\frac{(X_{i+1}^j-X_{i-1}^j)}{2\Delta r_D}\right], \quad (4.90c)$$

$$\frac{1}{r_D}\frac{\partial X}{\partial r_D}=\frac{1}{2(1+i*\Delta r_D)}\left[\frac{(X_{i+1}^{j+1}-X_{i-1}^{j+1})}{2\Delta r_D}+\frac{(X_{i+1}^j-X_{i-1}^j)}{2\Delta r_D}\right], \quad (4.90d)$$

$$X = \frac{X_i^{j+1} + X_i^j}{2}, \quad (4.90e)$$

where i, j denote position and time, respectively; X represents either pore pressure or temperature. Application of Eqs. 4.95a to 4.95d into Eqs. 4.92 and 4.93 leads to a nonlinear system of algebraic equations. The boundary conditions at the wellbore wall ($r_D = 1$) and at the far field (taken at a sufficiently large distance, $r_D >> 1$, so as to minimize boundary effect) are used for the first and last equations

$$p_1^{(N)j+1} = p_1^{(N)j} = p_w - p_0; \qquad T_1^{j+1} = T_1^j = T_w - T_0, \quad (4.91)$$

$$p_{nr}^{(N)j+1} = p_{nr}^{(N)j} = 0; \qquad T_{nr}^{j+1} = T_{nr}^j = 0, \quad (4.92)$$

where nr is the total number of spatially discretized points. As such, the task of solving for the unknowns, $p_i^{(N)j+1}$ and T_i^{j+1}, in terms of the knowns, $p_i^{(N)j}$ and T_i^j, reduces to finding the solution to the system of 3×(nr-2) nonlinear algebraic equations given in matrix form as

$$[\mathbf{L}^{j+1}][\mathbf{X}^{j+1}] = [\mathbf{R}^j][\mathbf{X}^j] + [\mathbf{BC}], \quad (4.93)$$

where [**X**] is the solution vector; [**BC**] is the vector containing boundary conditions; [$\mathbf{L}^{j+1}$] and [$\mathbf{R}^j$] are banded matrices made of six tridiagonal submatrices. These matrices and their components are listed in Appendix G. The solution is obtained by iterating Eq. 4.93 with an error tolerance of $\varepsilon = 10^{-3}$.

4.3.4 Results and Discussions

In this section, the combined time-dependent effects of fracture and mud temperature will be analyzed through simulated downhole drilling condition using the presented analytical solution. To focus on the thermally induced responses, the effects of perturbation due to

hydraulic pressure gradient and release of non-hydrostatic in-situ stress are isolated. This is achieved by assuming a vertical wellbore, drilled in a fractured rock formation with balance mudweight, i.e., $p_w = p_0$, and subjected to hydrostatic in-situ state of stress. The formation's material data are summarized in Table 4. Other relevant data include

S_V = 24 MPa, S_H = 18 MPa (azimuth = 0), S_h = 18 MPa , p_0 = 10 MPa, T_0 = 40 ^{o}C

R_w = 0.1 m , Drilling mud pressure = 10 MPa (balanced drilling)

TABLE 4—DUAL-POROTHERMOELASTIC MODELING PARAMETERS

Parameters	Values
Matrix Young modulus (E^{I})	9600 MPa
Fracture Young modulus (E^{II})	192 Mpa
Poisson's ratio ($\nu^{I} = \nu^{II}$)	0.20
Grain bulk modulus (K_s)	42.0 GPa
Fluid bulk modulus (K_f)	2300 MPa
Matrix local porosity (ϕ^{I})	0.20
Fracture local porosity (ϕ^{II})	0.95
Matrix local permeability (k^{I})	1.0×10^{-4} mD (~ 1.0×10^{-19} m^2)
Fracture local permeability (k^{II})	1.0 mD (~ 1.0×10^{-15} m^2)
Fluid viscosity (μ)	1 cp (0.01 Pa·s)
Solid volumetric thermal expansion coeff. ($\overline{\alpha}^{s}$)	3.0×10^{-5} ^{o}C^{-1}
Fluid volumetric thermal expansion coeff. (α^{f})	3.0×10^{-4} ^{o}C^{-1}
Bulk heat capacity ($\overline{C}$)	2732 kJ/m^3 -^{o}C
Thermal conductivity (λ^{T})	353 kJ/m-day-^{o}C
Fracture's bulk volume fraction ($\nu^{II} = 1 - \nu^{I}$)	0.01

In this case, downhole drilling is simulated for heating or cooling with a constant wellbore/formation temperature difference of $\Delta T = T_w - T_0$ = +/-30 ^{o}C. Due to the isotropy of horizontal in-situ stress, there is no stress-induced pore pressure. In addition, in balance drilling, there is no hydraulically-induced fluid diffusion between the wellbore drilling mud and the formation pore fluid. The temperature gradient results in differential expansion or contraction of the solid and fluid constituents within the porous saturated fractured rock

formation. The volume changes associated with thermal expansion/contraction lead to significant modification of both pore pressure and total stress distributions in the near-wellbore region as shown in **Figs. 4.2 to 4.4**. Moreover, heat diffusion process dictates the responses time-dependent.

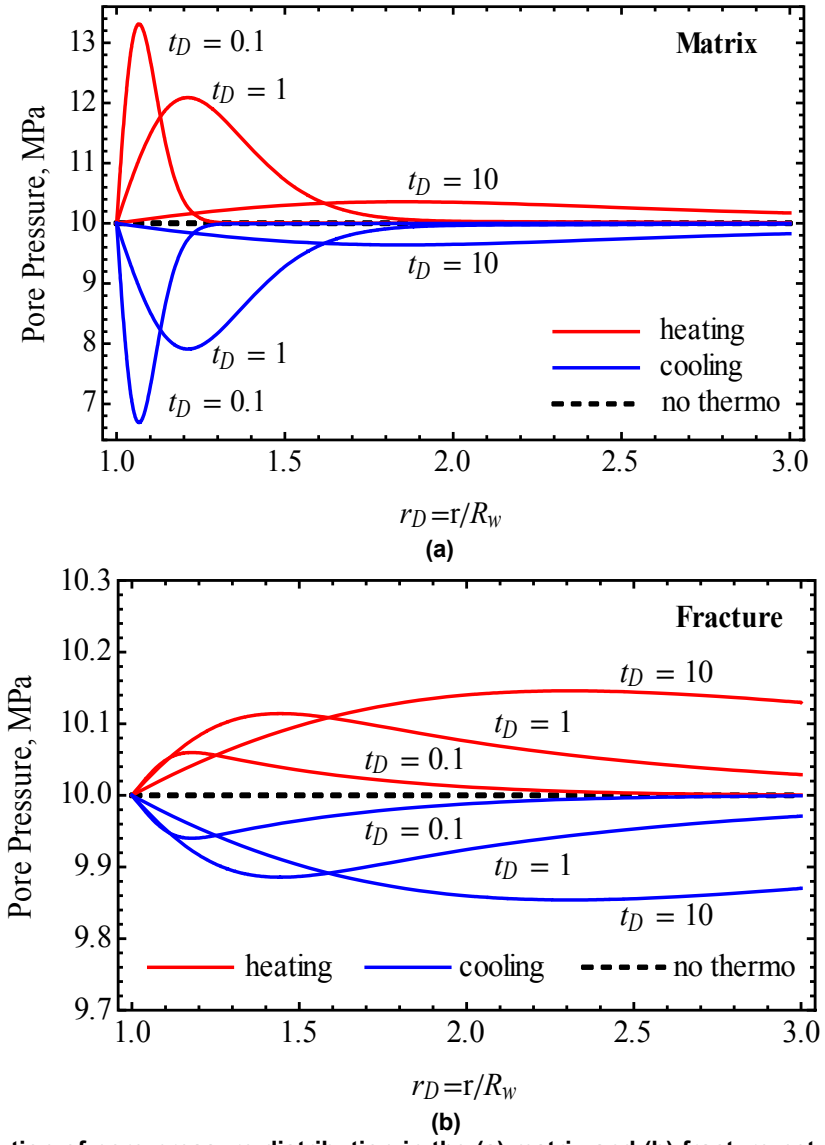

Fig. 4.2—Evolution of pore-pressure distribution in the (a) matrix and (b) fracture network under the effect of heating and cooling in conjunction with no-thermo effect (dashed lines).

From Fig. 4.2, it is seen that heating expands the pore fluid and induce increment in

pore pressure in both the matrix and fracture network. As time progresses, the peaks of thermally induced pore pressure advances into the formation and decreases due to subsequent heat diffusion. The thermal effect on pore pressure is not significant in the fracture network due to its high permeability such that all build-ups will quickly dissipate. For cooling, the near-wellbore pore pressure is reduced in a reverse analogy to heating.

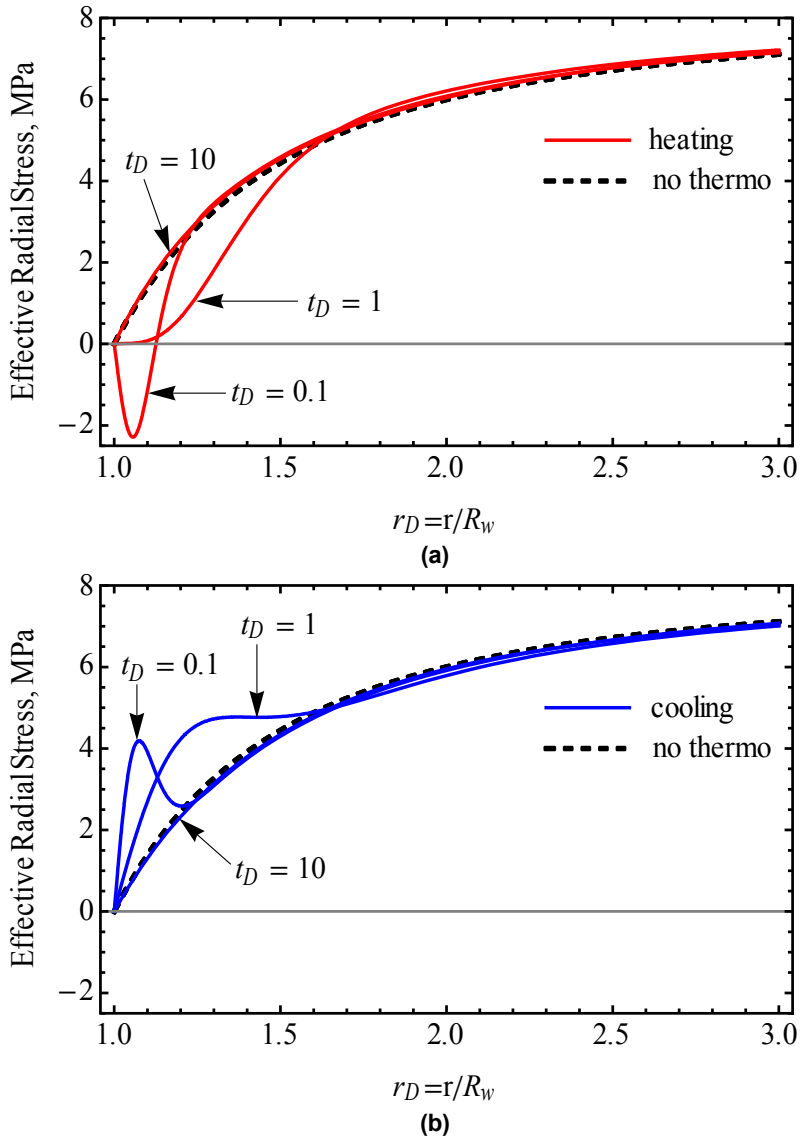

Fig. 4.3—Evolution of effective radial stress distribution in the porous matrix region under the effect of (a) heating and (b) cooling in conjunction with no-thermo effect (dashed lines).

The evolutions of the corresponding effective radial and tangential stress distributions are shown in Figs. 4.3 and 4.4. For isothermal case, the effective stresses are not functions of time due to the axisymmetric loading. The effective radial stress inversely mirrors the response of pore-pressure. As such, heating will reduce effective radial stress and develop a tensile region near the wellbore wall that will diminish with time (Figure 4.3a).

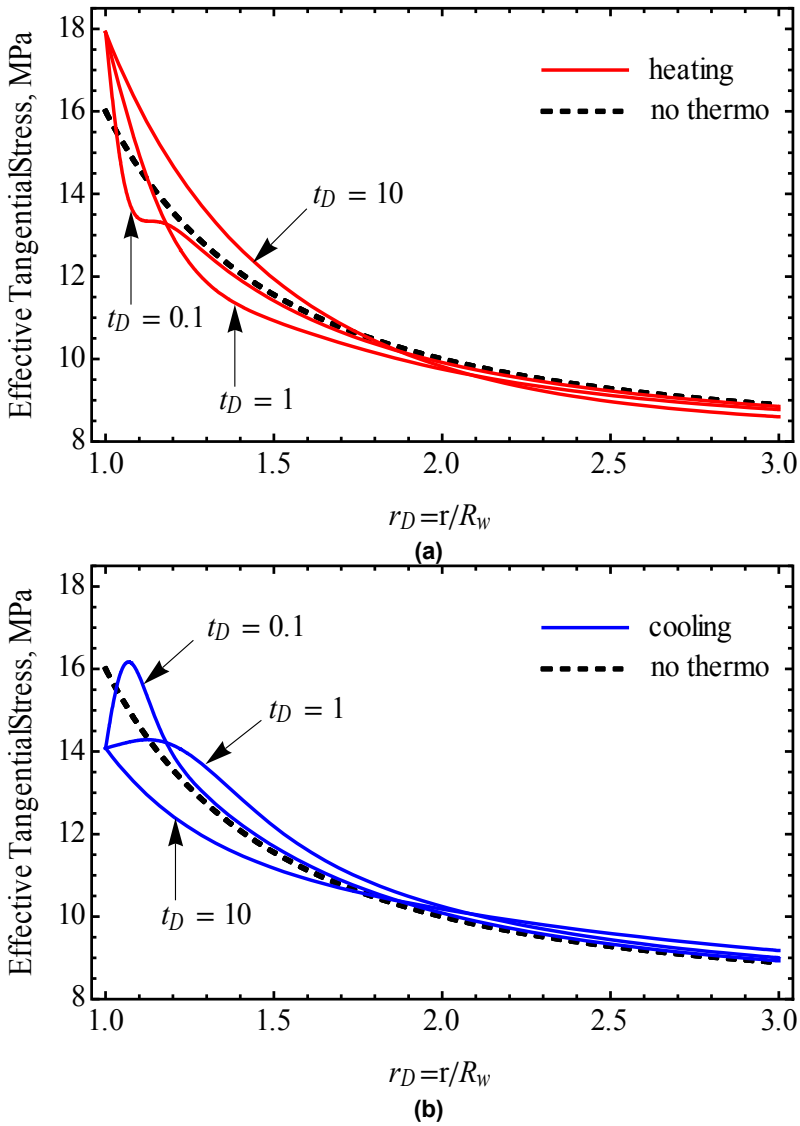

Fig. 4.4—Evolution of effective tangential stress distribution in the porous matrix region under the effect of (a) heating and (b) cooling in conjunction with no-thermo effect (dashed lines).

On the other hand, high mud temperature increases the effective normal stress at and in a short distance from the wellbore wall but decreases the effective normal stresses away from the wellbore compared to isothermal response (Fig. 4.4a). Qualitatively, the variation can be explained as followed: due to heating, there are both thermally-induced compressive tangential stress and pore pressure. In this case, the thermal expansion coefficient of the fluid is larger than the rock matrix leading to higher induced pore pressure which simultaneously lowers the effective normal stress away from the wellbore wall. On the other hand, at the borehole wall, the pore pressure is fixed due to fluid communication while the compressive total tangential stress is increased by a constant amount, leading to higher effective stress at the borehole wall. Analogously, the effects of cooling due to low mud temperature shows reduction in effective stress concentration at or near borehole wall but increase away from the wall.

From the above analysis, it is observed that the thermal expansion coefficients for solid and fluid play an important and significant role in the near-wellbore stress and pore pressure. **Figs. 4.5 and 4.6** show the effect of solid and fluid thermal expansion coefficients on pore pressure and effective tangential stress. Obviously, the solid thermal expansion coefficient dominates the stress responses while the fluid thermal expansion coefficient has more influence on pore pressure. Finally, anisotropic implications of the solid thermal expansion coefficient are displayed for heating case in **Fig. 4.7**. It is shown that for higher the ratio of $\overline{\alpha}_3^s / \overline{\alpha}_1^s$, the induced pore pressure is smaller and the effective stress is larger.

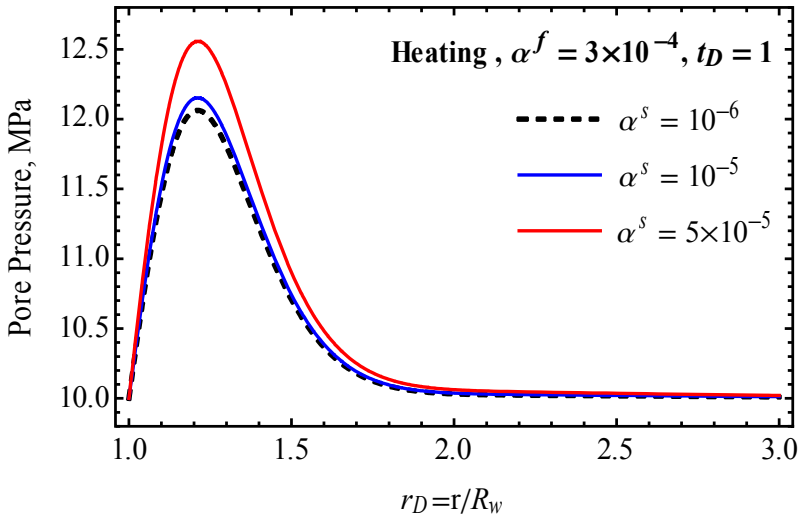

(a)

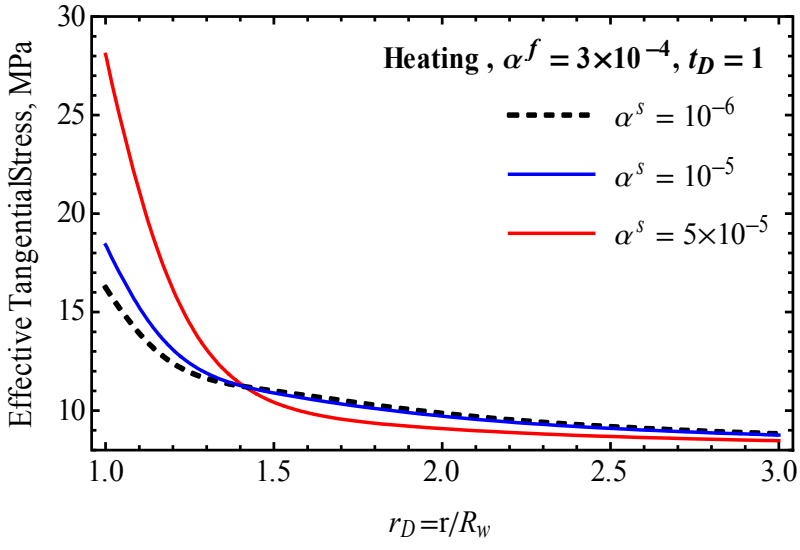

(b)

Fig. 4.5—Distribution of (a) pore pressure and (b) effective tangential stress in the porous matrix region due to heating for different values of solid thermal expansion coefficient, α^s.

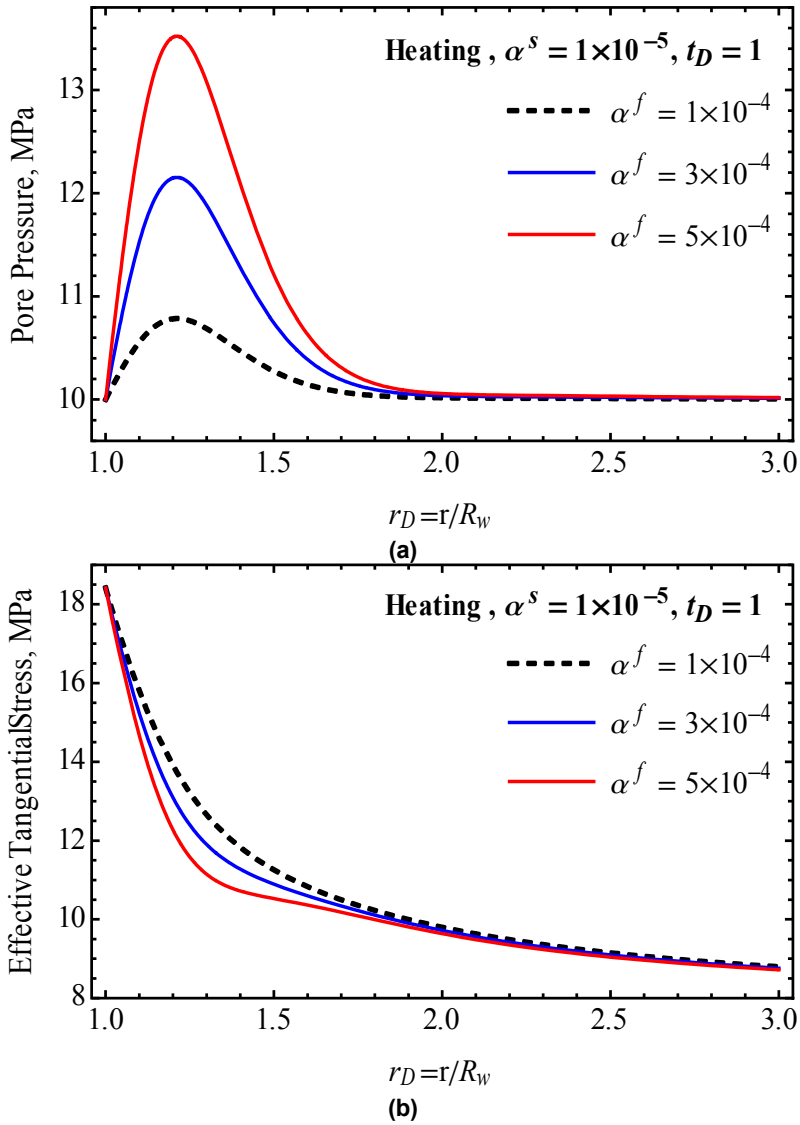

Fig. 4.6—Distribution of (a) pore pressure and (b) effective tangential stress in the porous matrix region due to heating for different values of fluid thermal expansion coefficient, α^f.

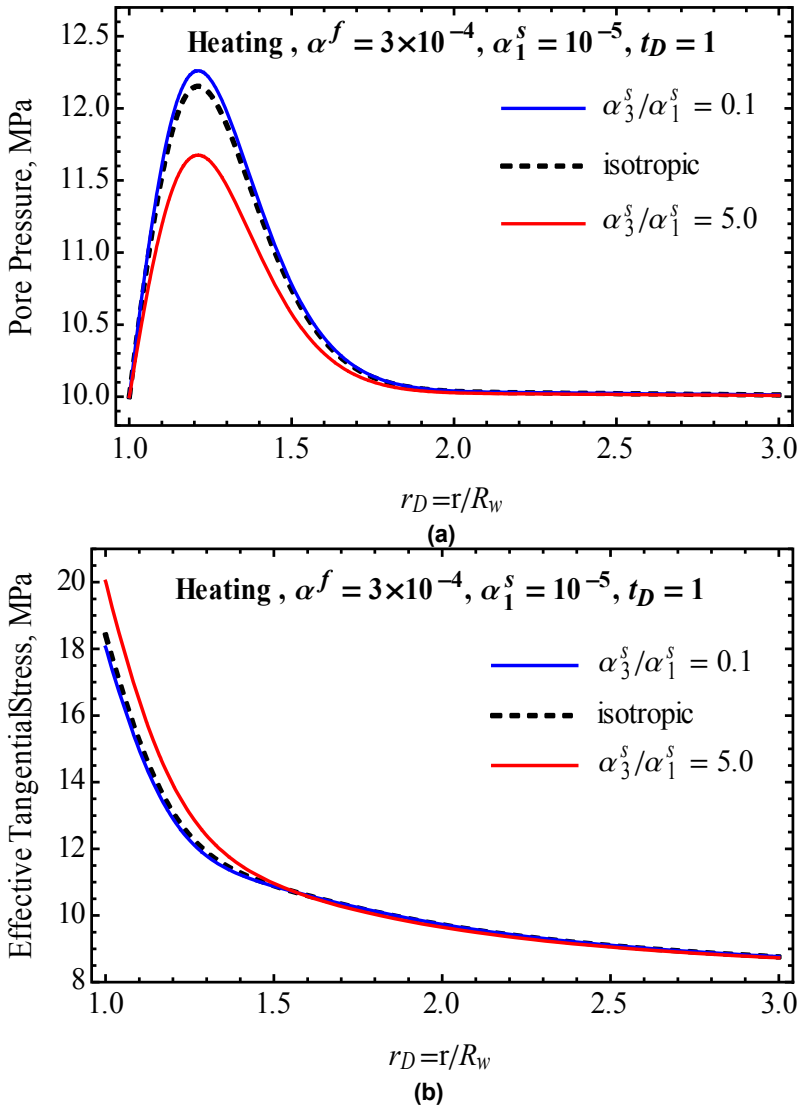

Fig. 4.7—Distribution of (a) pore pressure and (b) effective tangential stress in the porous matrix region due to heating for different ratios of solid thermal expansion coefficient in the transverse direction and isotropic plane, $\overline{\alpha}_3^s / \overline{\alpha}_1^s$.

Next, the effect of heat convection is investigated numerically for the special case of vertical wellbore subjected to hydrostatic in-situ state of stress. Instead of balance drilling, an overbalance mudweight of p_w = 11 MPa > p_0 = 10 MPa is assumed in this simulation. The case of drilling mud cooling the formation is considered since this is often the case in drilling deep rock formations. First, the finite difference scheme is validated against

analytical solutions for heat conduction in non-fractured rock (single-porothermoelastic) and fractured rock (dual-porothermoelastic) as illustrated in **Fig. 4.8**. The results show excellent agreements between the numerical and analytical solutions. At a given time, the fast fluid diffusion in the fracture network dissipates the thermally induced matrix pore pressure.

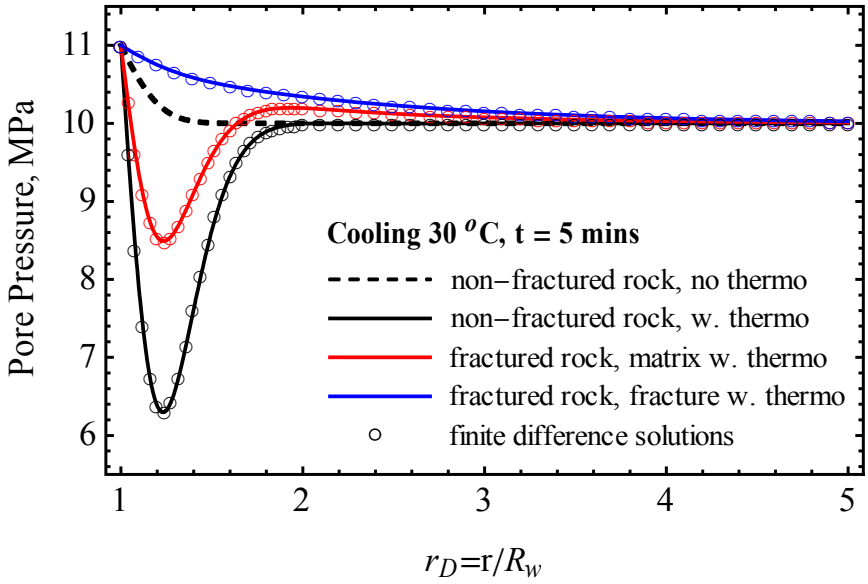

Fig. 4.8—Validation of finite difference scheme against analytical solutions for heat conduction.

The effects of heat convection are illustrated via the profile of temperature and pore pressure in the matrix in **Figs. 4. 9 and 4.10**. Heat convection carries the temperature front faster into the formation and as a result modifies the magnitude and distribution of pore pressure response in the near-wellbore region. For this data set, the solution predicts noticeable contribution from heat convection.

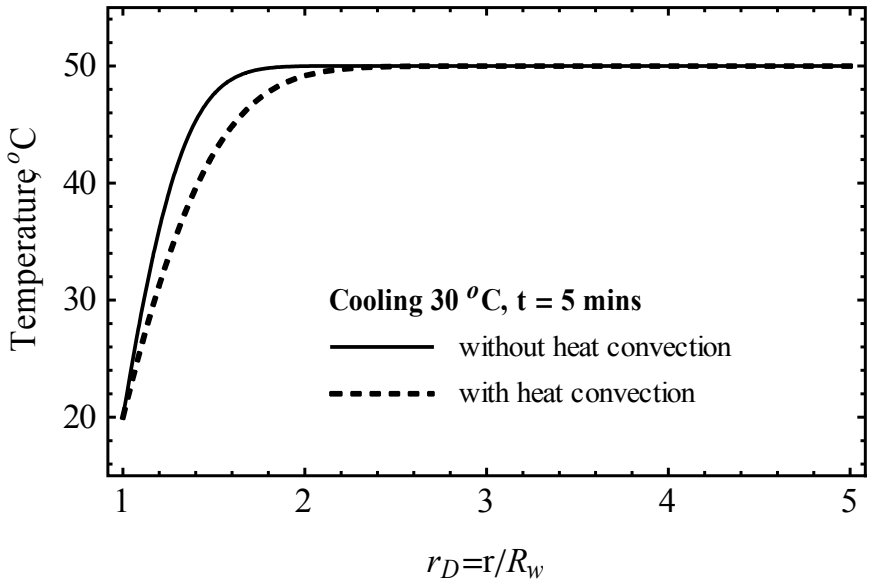

Fig. 4.9—Heat convective effects on temperature distribution.

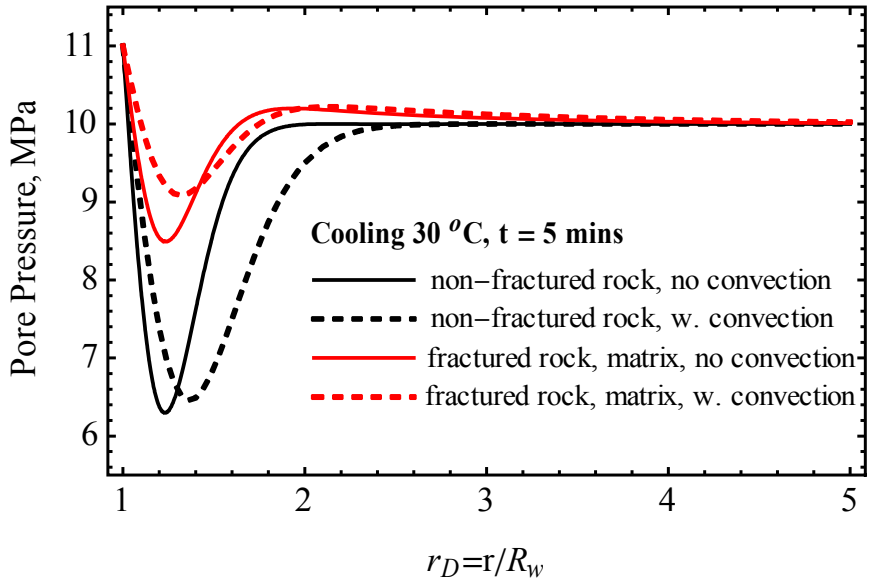

Fig. 4.10—Heat convective effects on pore pressure distributions.

4.4 Rectangular Strip

As displayed in the inclined wellbore problem, the impact of the extra coupling of a temperature gradient in fractured porous medium can be substantial and complex. The Mandel's problem and solution for dual-poroelastic media (Chapter 2), extended to include

the effect of temperature gradient, can be treated as a canonical illustration of the intricate dual-porothermoelastic coupling. This section shows the derivations of the analytical solutions for the consolidation of a rectangular strip under non-isothermal and unconfined compression condition. The analytical solution are derived and given in closed form in the Laplace transform domain. The results for stress, pore pressure, and displacements are plotted and compared with the corresponding isothermal counterpart to highlight the effect of temperature gradient in a dual-porosity and dual-permeability porous saturated medium.

4.4.1 Problem Descriptions

As illustrated in **Fig 4.11**, the original Mandel's problem involves an infinitely long rectangular specimen sandwiched between the top and bottom by two rigid, adiabatic, and frictionless plates. At time t=0^+, a generalized axial loading representing either an applied vertical strain/displacement, $\varepsilon_{zz}^*(t)$ or $u_z^*(t)$, or an applied vertical load, $2F(t)$ (per unit length) is applied to the rigid plates at the top and bottom, respectively. Simultaneously, the left and right edges of the plates are imposed with time-dependent fluid pressure $p_o(t)$, and temperature $T_o(t)$. Mathematically, the generalized boundary conditions are expressed as

$$x = \pm a: \quad \sigma_{xx} = P_c(t); \quad \sigma_{xz} = 0; \quad p^{\mathrm{I}} = p^{\mathrm{II}} = p_o(t); \quad T = T_o(t), \qquad (4.94a)$$

$$z = \pm b: \quad \sigma_{xz} = q_z^{\mathrm{I}} = q_z^{\mathrm{II}} = q_z^h = 0; \quad u_z = u_z(t), \qquad (4.94b)$$

$$z = \pm b: \quad \int_{-a}^{a} \sigma_{zz}\, dx = 2F(t) \text{ load control}, \qquad (4.94c)$$

$$z = \pm b: \quad \varepsilon_{zz} = \varepsilon_{zz}^*(t) = u_{zz}^*(t)/2b \text{ stroke control}, \qquad (4.94d)$$

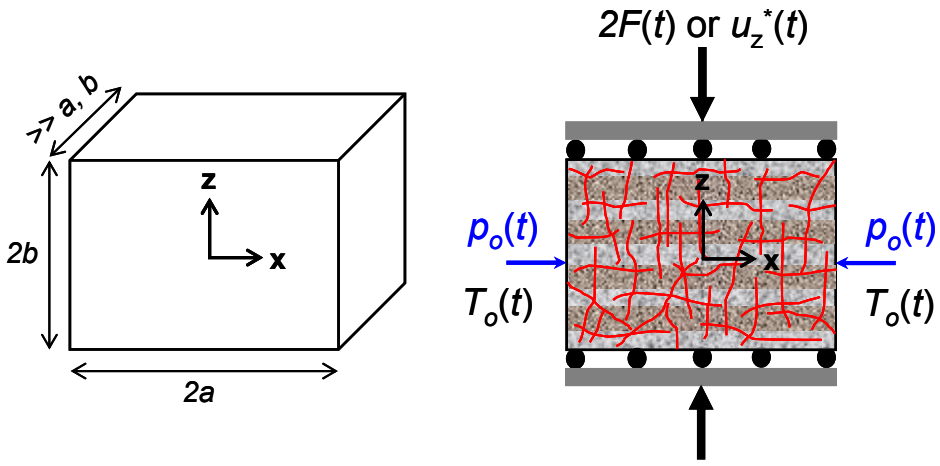

Fig. 4.11—The Mandel's problem geometry and setups incorporating temperature loading.

With the above boundary conditions, the governing equations is reduced to one-dimensional and all variables are at most functions of x and t only. The plane-strain condition in the y direction and the stress equilibrium in the x direction require that $\varepsilon_{yy} = 0$ and $\sigma_{xx} = P_c(t)$. Using these conditions into the constitutive Eqs. 4.30 and 4.31, the fluid contents are rewritten in terms of stress, fluid pressure, and temperature as

$$\zeta^{\mathrm{I}} = -a^{\mathrm{I}}(\sigma_{zz} + \overline{\varphi}^{\mathrm{I}} P_c - b_{11} p^{\mathrm{I}} - b_{12} p^{\mathrm{II}} - \overline{\beta}^{\mathrm{I}} T), \quad (4.95)$$

$$\zeta^{\mathrm{II}} = -a^{\mathrm{II}}(\sigma_{zz} + \overline{\varphi}^{\mathrm{II}} P_c - b_{21} p^{\mathrm{I}} - b_{22} p^{\mathrm{II}} - \overline{\beta}^{\mathrm{II}} T), \quad (4.95)$$

where $a^{(\mathrm{N})}$, $\overline{\varphi}^{(\mathrm{N})}$, and b_{ij} are given in Eqs. 2.34 to 2.35b. $\overline{\beta}^{(\mathrm{N})}$ is expressed as

$$\overline{\beta}^{\mathrm{I}} = \overline{\beta}_3^s + \overline{\beta}_1^s \overline{\varphi}^{\mathrm{I}} - \frac{\overline{\beta}_{fs}^{\mathrm{I}}}{a^{\mathrm{I}}}; \qquad \overline{\beta}^{\mathrm{II}} = \overline{\beta}_3^s + \overline{\beta}_1^s \overline{\varphi}^{\mathrm{I}} - \frac{\overline{\beta}_{fs}^{\mathrm{II}}}{a^{\mathrm{II}}}, \quad (4.95)$$

Similarly, the compatibility Eq. 4.38 changes to

$$\frac{\partial^2}{\partial x^2}\left[\sigma_{zz} - \left(\overline{\alpha}_3^{\mathrm{I}} - \overline{\alpha}_1^{\mathrm{I}} \frac{\overline{M}_{13}}{\overline{M}_{11}}\right) p^{\mathrm{I}} - \left(\overline{\alpha}_3^{\mathrm{I}} - \overline{\alpha}_1^{\mathrm{I}} \frac{\overline{M}_{13}}{\overline{M}_{11}}\right) p^{\mathrm{II}} - \left(\overline{\beta}_3^s - \overline{\beta}_1^s \frac{\overline{M}_{13}}{\overline{M}_{11}}\right) T\right] = 0, \quad (4.96)$$

Integrating and accounting for the symmetry about the centerline ($x = 0$) yields

$$\sigma_{zz} = \bar{\gamma}^{\mathrm{I}} p^{\mathrm{I}} + \bar{\gamma}^{\mathrm{II}} p^{\mathrm{II}} + \bar{\gamma}^{\mathrm{T}} T + C_1(t), \quad (4.97)$$

in which the dimensionless coefficient $\bar{\gamma}^{(\mathrm{N})} = \bar{\alpha}_3^{(\mathrm{N})} - \bar{\alpha}_1^{(\mathrm{N})} \bar{M}_{13} / \bar{M}_{11}$, $\bar{\gamma}^{\mathrm{T}} = \bar{\beta}_3^{s} - \bar{\beta}_1^{s} \bar{M}_{13} / \bar{M}_{11}$ and $C_1(t)$ is an integration constant depending only on time. As a result, the fluid diffusion equation with normalized parameters becomes

$$\left(\boldsymbol{\omega} \frac{\partial}{\partial t_D} + \boldsymbol{\Gamma}_{\mathbf{D}} - \bar{\boldsymbol{\kappa}}_{\mathbf{D}} \frac{\partial^2}{\partial x_D^2} \right) \begin{Bmatrix} p^{\mathrm{I}} \\ p^{\mathrm{II}} \end{Bmatrix} = \begin{Bmatrix} c_f^{\mathrm{I}} \bar{\varphi}^{\mathrm{I}} \\ c_f^{\mathrm{II}} \bar{\varphi}^{\mathrm{II}} \end{Bmatrix} \frac{\partial P_c}{\partial t_D} + \begin{Bmatrix} c_f^{\mathrm{I}} \\ c_f^{\mathrm{II}} \end{Bmatrix} \frac{\partial C_1}{\partial t_D} + \begin{Bmatrix} c_{hf}^{\mathrm{I}} \\ c_{hf}^{\mathrm{II}} \end{Bmatrix} \frac{\partial T}{\partial t_D}, \quad (4.98)$$

Neglecting the nonlinear convective term in the heat diffusion equation, the classical heat conduction equation is recovered as

$$\frac{\partial T}{\partial t_D} = \bar{\kappa}_D^T \frac{\partial^2 T}{\partial x_D^2}, \quad (4.99)$$

in the above, $[\boldsymbol{\omega}]$, $[\boldsymbol{\Gamma}_{\mathbf{D}}]$, $[\bar{\boldsymbol{\kappa}}_{\mathbf{D}}]$, and $c_f^{(\mathrm{N})}$ are given in Eqs. 2.46 and 2.47; $c_{hf}^{(\mathrm{N})}$ and $\bar{\kappa}_D^T$ are defined in Eqs. 4.58 and 4.60.

4.4.2 Analytical Solution

The heat diffusion equation, Eq. 4.99, is uncoupled from the stress and pressure field and can be solved separately. Using the temperature boundary condition, the solution for temperature field is obtained and expressed in Laplace transform domain as

$$\widetilde{T} = (\widetilde{T}_o - T_0 / s) \frac{\cosh(\xi_h x_D)}{\cosh(\xi_h)} = \Delta \widetilde{T} \frac{\cosh(\xi_h x_D)}{\cosh(\xi_h)}, \quad (4.100)$$

where $\xi_h = \sqrt{s / \bar{\kappa}_D^T}$. Next, the expressions for the dual pressure fields are derived by solving Eq. 4.98. This is a non-homogeneous partial differential equation system and its

general solution is obtained as a summation of the homogeneous and particular solutions and given as

$$\widetilde{p}^{\mathrm{I}} = \widetilde{P}_c f^{\mathrm{I}} + \widetilde{T} g_T^{\mathrm{I}} + \widetilde{C}_1 g^{\mathrm{I}} + C_2^{\mathrm{I}} \cosh(\xi^{\mathrm{I}} x_D) + C_2^{\mathrm{II}} \cosh(\xi^{\mathrm{II}} x_D), \quad (4.101)$$

$$\widetilde{p}^{\mathrm{II}} = \widetilde{P}_c f^{\mathrm{II}} + g_T^{\mathrm{II}} \widetilde{T} + \widetilde{C}_1 g^{\mathrm{II}} + C_2^{\mathrm{I}} m^{\mathrm{I}} \cosh(\xi^{\mathrm{I}} x_D) + C_2^{\mathrm{II}} m^{\mathrm{II}} \cosh(\xi^{\mathrm{II}} x_D), \quad (4.102)$$

where $C_2^{(\mathrm{N})} = C_2^{(\mathrm{N})}(s)$ is additional arbitrary coefficient to be determined from boundary conditions; $\xi^{(\mathrm{N})} = \sqrt{\ell^{(\mathrm{N})}}$ with the coefficients $\ell^{(\mathrm{N})}$, $m^{(\mathrm{N})}$, $f^{(\mathrm{N})}$, and $g^{(\mathrm{N})}$ as given in Eqs. 2.51 to 2.54; $g_T^{(\mathrm{N})}$ are defined in Eqs. 4.64. Subsequently, using the equilibrium, constitutive and strain-displacement equations, it is easy to solve for the stresses and displacements in terms of the fluid pressures and temperature as

$$\widetilde{\sigma}_{zz} = A_0 \widetilde{P}_c + A_1 \widetilde{C}_1 + A_2^{\mathrm{I}} C_2^{\mathrm{I}} \cosh(\xi^{\mathrm{I}} x_D) + A_2^{\mathrm{II}} C_2^{\mathrm{II}} \cosh(\xi^{\mathrm{II}} x_D) + A^T \widetilde{T}, \quad (4.103)$$

$$\frac{\widetilde{u}_x}{a} = -\left(f \widetilde{P}_c + g \widetilde{C}_1\right) x_D - h^T \Delta \widetilde{T} \frac{\sinh(\xi_h x_D)}{\xi_h \cosh(\xi_h)} - h^{\mathrm{I}} C_2^{\mathrm{I}} \frac{\sinh(\xi^{\mathrm{I}} x_D)}{\xi^{\mathrm{I}}} - h^{\mathrm{II}} C_2^{\mathrm{II}} \frac{\sinh(\xi^{\mathrm{II}} x_D)}{\xi^{\mathrm{II}}}, \quad (4.104)$$

$$\frac{\widetilde{u}_z}{b} = \frac{\overline{M}_{11} \widetilde{C}_1 - \overline{M}_{13} \widetilde{P}_c}{\overline{M}_{11} \overline{M}_{33} - \overline{M}_{13}^2} z_D, \quad (4.105)$$

where the lumped coefficients A_0, A_1, $A_2^{(\mathrm{N})}$, $h^{(\mathrm{N})}$, f, and g are given in Eqs. 2.82a to 2.85. A^T and h^T are defined as

$$A^T = \overline{\gamma}^{\mathrm{I}} g_T^{\mathrm{I}} + \overline{\gamma}^{\mathrm{II}} g_T^{\mathrm{II}} + \overline{\gamma}^{\mathrm{T}}, \quad (4.106a)$$

$$h^T = (\overline{\alpha}_1^{\mathrm{I}} g_T^{\mathrm{I}} + \overline{\alpha}_1^{\mathrm{II}} g_T^{\mathrm{II}} + \overline{\beta}_1^{s}) / \overline{M}_{11}, \quad (4.106b)$$

The remaining three unknowns $\widetilde{C}_1(s)$, $C_2^{\mathrm{I}}(s)$ and $C_2^{\mathrm{II}}(s)$ are determined from the fluid

pressure boundary conditions for p^{I} and p^{II} at the edges x = +/-a and the vertical loading condition on top and bottom at z = +/-b.

4.4.3 Results and Discussions

This section illustrates the response of a rectangular strip under temperature gradient loading. The following set of data are used: $\overline{E}$ = 1244 MPa, $\overline{\nu}$ = 0.22 , $\overline{\alpha}^{I}$ = 0.64, $\overline{\alpha}^{I}$ = 0.33, $\overline{\beta}^{s}$ = 1.33×10^{-2} MPa/^{o}C, $\overline{\beta}_{fs}^{I}$ = 5.05×10^{-5} ^{o}C^{-1}, $\overline{\beta}_{fs}^{II}$ = 8.71×10^{-6} ^{o}C^{-1}, k^{I} = 5×10^{-5} md, k^{II} = 5 md, μ = 1 cp, and c_h = 7.18×10^{-2} m^2/day.

Figs. 4.12 and 4.13 show the evolutions of pore pressures and vertical stress distribution with the application of a +/-5 ^{o}C temperature gradient across the sample lateral boundaries. The behavior of pore pressure in the fracture network essentially stays the same under the additional thermal effect due to fast fluid diffusion. However, the pore pressure in the matrix seems to display a counter-intuitive behavior, i.e., decreasing for heating and increasing for cooling. This can be explained through the transient redistribution of vertical stress in Fig. 4.13. For isothermal case, compatibility condition requires a stress transfer to the middle region due to the apparently softer drained edges (the Mandel-Cryer's effect). Heating will induce additional compressive stress at the edges, effectively making the sides stiffer than the center. Consequently, the stress is redistributed from the center to the sides, leading to lower pore pressure at the center. The dual evolutions of pore pressure at the center of the sample are displayed prominently in **Fig. 4.14**. Because thermal expansion counteracts vertical loading near the edges (**Fig. 4.15**), the strip starts out consolidating but quickly turns to rebounding for heating as shown in **Fig. 4.16**. Laterally, the reduction in

vertical displacement allows the strip to contract more than the isothermal counterpart as depicted in **Fig. 4.17**. The responses for cooling can be explained in opposite analogy.

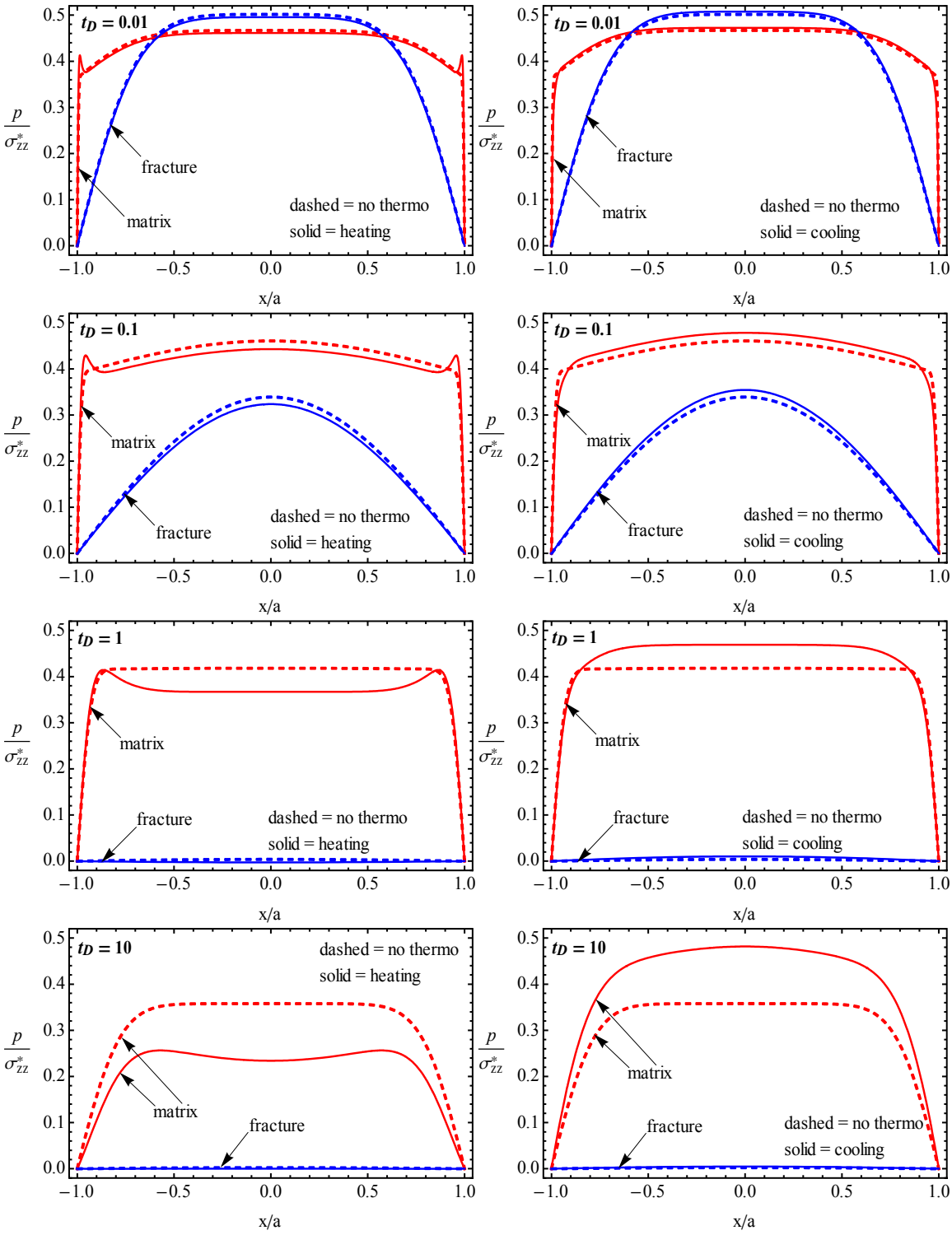

Fig. 4.12—Evolution of pore-pressure distribution in the cross section under the effect of heating (left column) and cooling (right column) in conjunction with no-thermo effect (dashed lines).

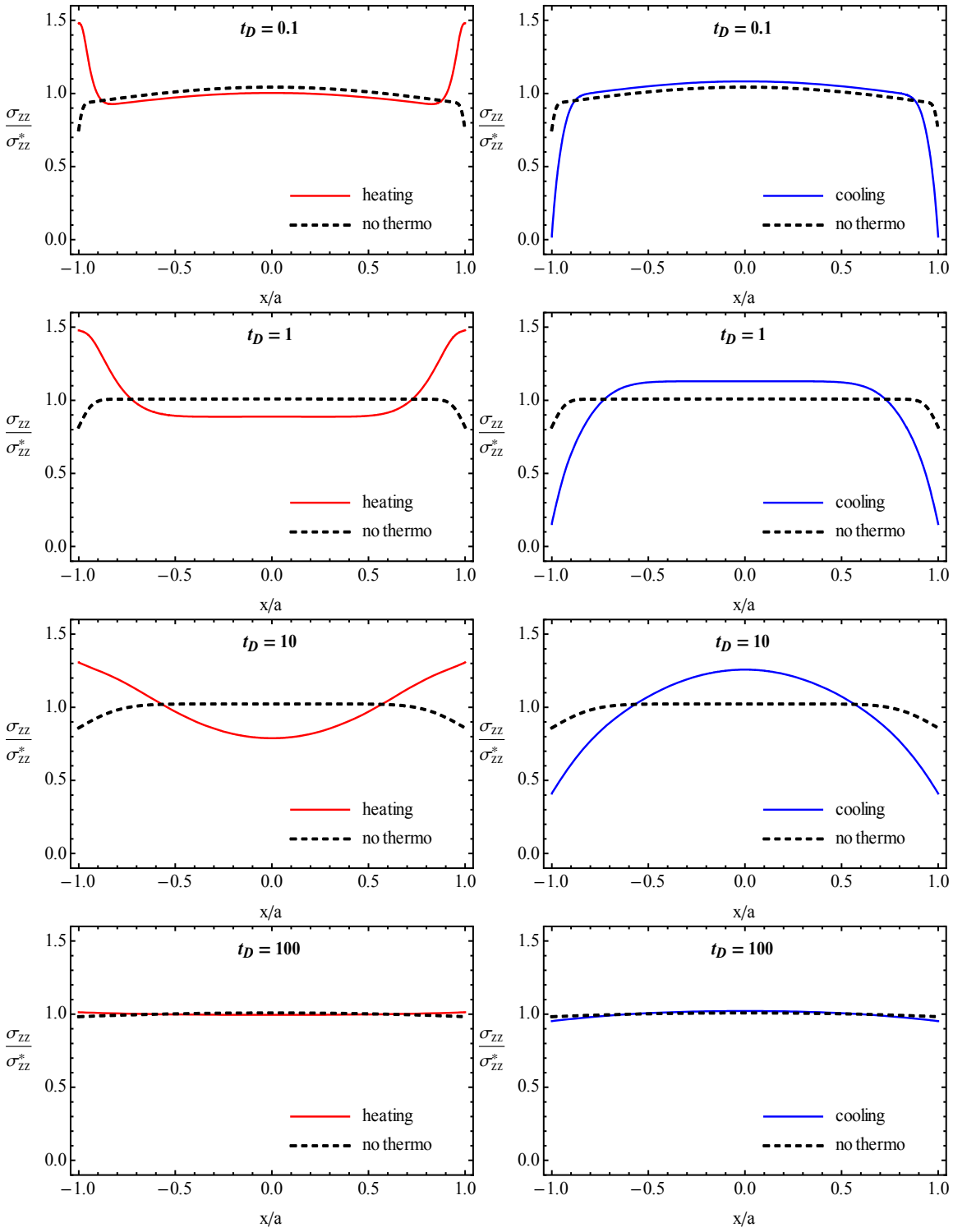

Fig. 4.13—Evolution of vertical stress distribution in the cross section under the effect of heating (left column) and cooling (right column) in conjunction with no-thermo effect (dashed lines).

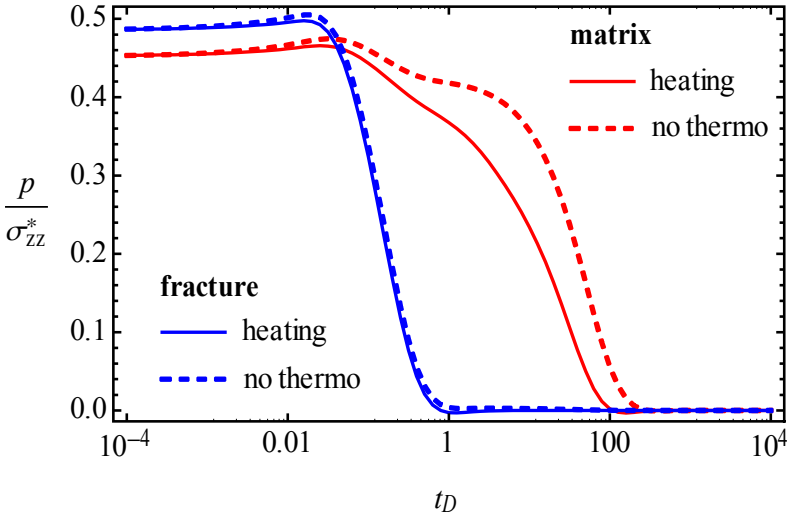

(a)

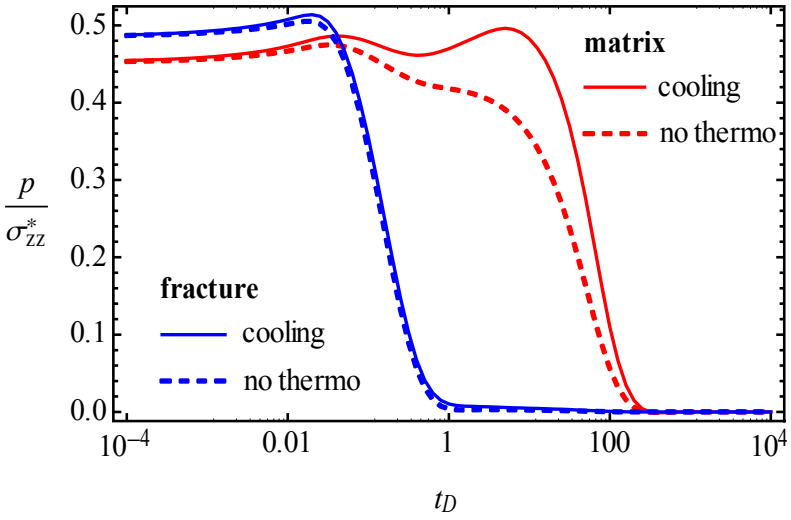

(b)

Fig. 4.14—History of normalized pore-pressure developed at the center (x/a = 0) under the effect of (a) heating and (b) cooling, in conjunction with no-thermo effect (dashed lines).

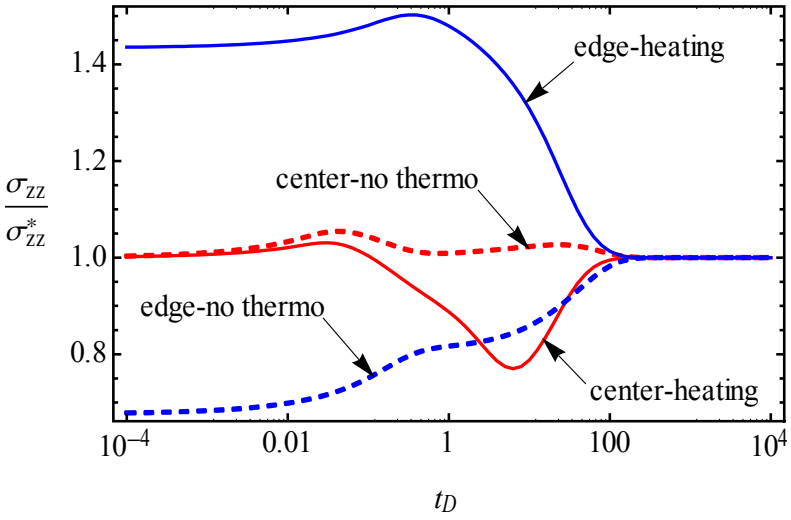

(a)

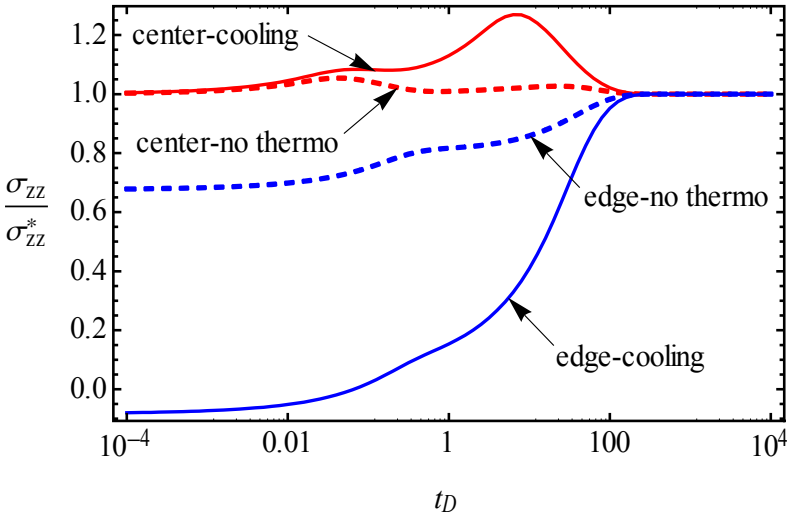

(b)

Fig. 4.15—History of normalized vertical stress developed at the center (x/a = 0) and at the edge (x/a = 1) under the effect of (a) heating and (b) cooling, in conjunction with no-thermo effect (dashed lines).

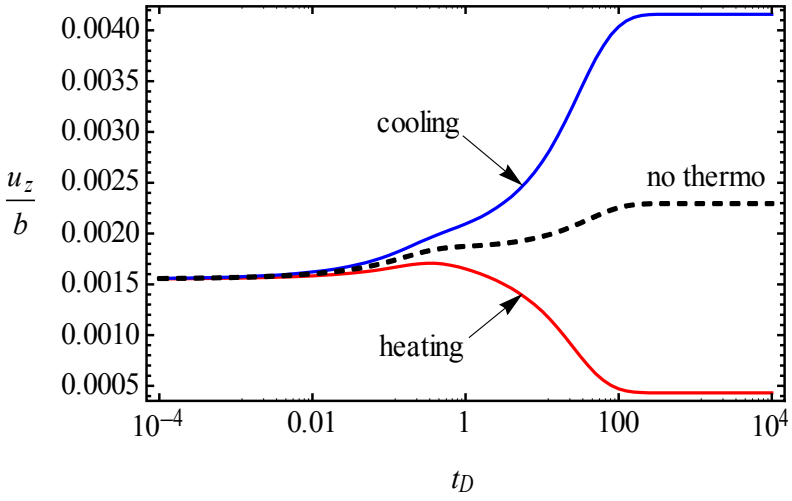

Fig. 4.16—History of normalized vertical displacement at the top (z/b = 1) under the effect of heating and cooling, in conjunction with no-thermo effect (dashed lines).

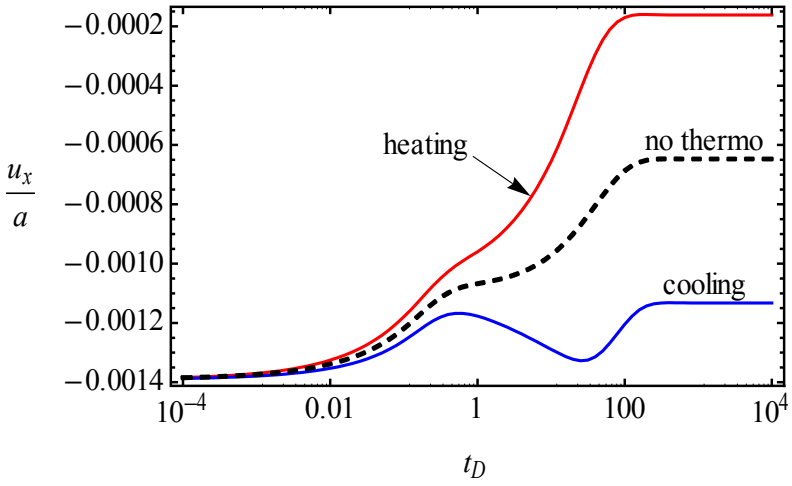

Fig. 4.17—History of normalized lateral displacement at the edges (x/a = +/-1) under the effect of heating and cooling, in conjunction with no-thermo effect (dashed lines).

4.5 Summary

In this chapter, the dual-porothermoelastic analytical model and solutions for the responses of two problem geometries, inclined wellbore and rectangular strip, have been derived and illustrated. Coupling of temperature effects for non-isothermal condition is incorporated by adopting a "single-temperature" approach in which a single representative thermodynamic continuum is adopted for naturally fractured rock formations.

The inclined wellbore results demonstrate that thermal loading induces significant concentration of stress and pore pressure that controls near-wellbore stability. The effect of thermal expansion coefficients of solid and fluid on stress and pore pressure was shown, in addition to the anisotropic impact of varying the ratio, $\overline{\alpha}_3^s / \overline{\alpha}_1^s$. Numerical examples employing finite difference method are also shown accounting for heat convection.

The results for rectangular strip displayed the canonical responses of the coupled dual-porothermoelastic process which lend insight into the impact of thermal loading and the triple time scales among dual fluid flow and single heat diffusion in naturally fractured porous rock formations under non-isothermal condition.

Chapter 5

Applications

5.1 Introduction

This chapter is dedicated to the applications to the solutions presented in previous chapters. The inclined wellbore solution is used to perform wellbore stability analysis for drilling through chemically active fractured rock formations under non-isothermal conditions. The hollow cylinder solution is applied to study elastic consolidation of a producing reservoir and its implications on porosity and permeability reduction in the near wellbore region. Finally, the cylinder solutions are used to demonstrate the dual-poromechanics responses under some realistic experimental loading conditions such as cyclic, linear ramping, and exponentially decayed.

5.2 Wellbore Stability[7]

In oil-and-gas operations, the majority of drilling footage is carried out through low-permeability rock formations such as shale, chalk, granite, etc. Many of these subsurface

[7] Part of this work was published in *SPEJ* **14**(2): 282-301 (Nguyen et al. 2009) and presented at SPE ATCE (Nguyen and Abousleiman, SPE 123901, October 2009, New Orleans).

intervals are in-situ fractured and may be treated as such when it comes to drilling operations and wellbore-stability planning. The ultralow-permeability rock matrix is highly fractured not only at the macroscale as observed in many wellbore formation microscanner images (FMI) but also at the microscale as seen on thin sections and scanning electron microscopy (SEM) images (Han et al. 2009).

When the shale is fractured, it is mechanically weakened and exhibits high-permeability fluid-flow paths within the low-permeability intact shale matrix. Because of different fluid-diffusion rates between the fractures and shale matrix, there are two distinct pore-pressure fields in saturated fractured shale when subjected to stress and/or fluid-pressure perturbation. For example, in overbalanced drilling through a fractured-shale formation, the drilling mud penetrates the fractures immediately and there is no significant leakoff of fluid from the wellbore or from the fractures into the intact shale matrix. In other words, the fracture network with high permeability provides preferential flow paths for mud invasion into the formation. Consequently, we risk losing mud circulation and damaging the formation. In addition, the fluid invasion into the fractures weakens the mechanical strength of the shale such as cohesion and friction angle, as observed in laboratory shale testing. Furthermore, the communication between the fluid pressure in the fractures and wellbore mud pressure makes the formation more sensitive to every activity in the drilling operation such as stopping circulation, tripping, or drillstring impact. These events could create significant pressure variation in the fractures, leading to collapse failure consequences such as cavings and hole erosion.

As a result, the natural fractures of the shale, necessitate an unconventional approach to

assess wellbore instabilities. The basic approach consists of applying the dual-poromechanics equations to calculate the time-dependent pore-pressure and effective stress redistributions in and around the wellbore to compute subsequently the time-dependent mud-weight windows to prevent wellbore collapse or to avoid wellbore fracturing.

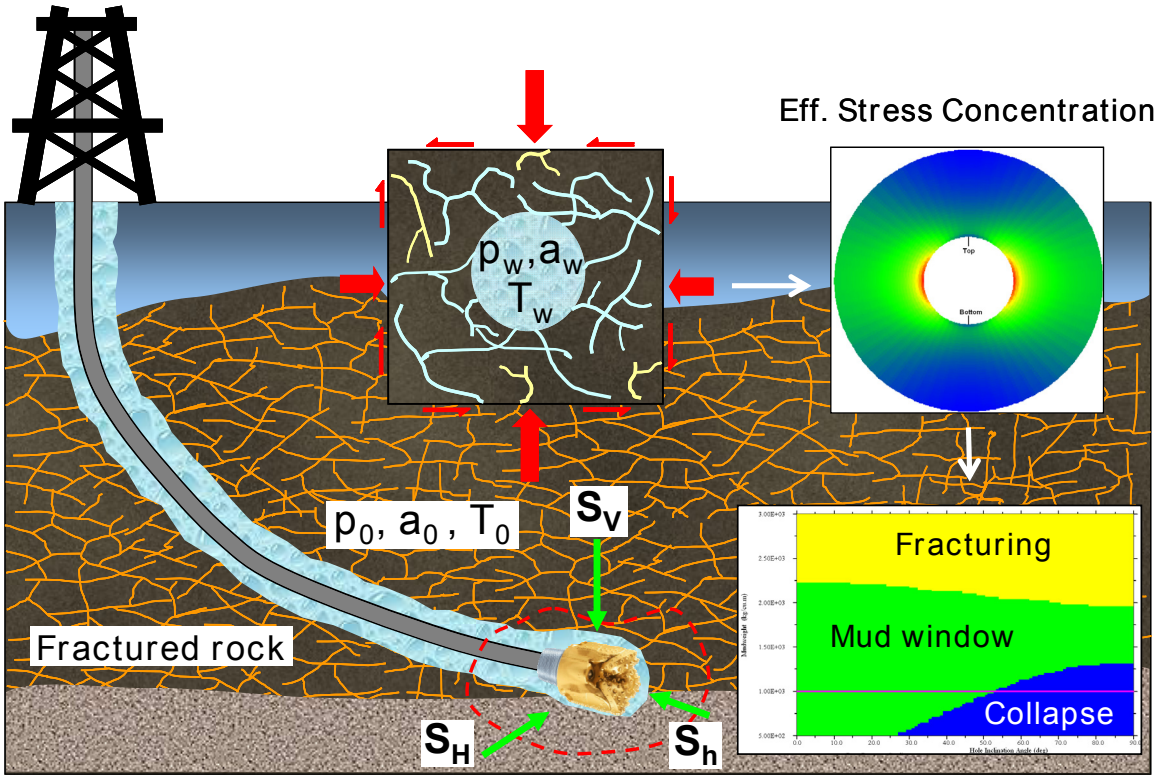

Fig. 5.1—The field problem of simulating and predicting wellbore stability.

Rocks generally fail when the effective stress state (total stress less the pore pressure: σ_{ij} - p) exceed the formation strength's either in tension or compression. The tensile strength of subsurface formations is generally very weak due to preexisting fractures or bedding planes in the rock. Thus, it is conservatively taken to be zero in stability calculation. The compressive strength is described using any two of the three strength parameters: friction angle, Φ; cohesion, C; and/or uniaxial compressive strength, UCS.

These compressive strength parameters are related by UCS = $2C\times\tan(\Phi/2+\pi/4)$. All tensile and compressive strength parameters can be measured from rock testing or correlated from well-log data.

In this section, the individual and combined time-dependent effects of shale's fractures, mud chemistry, and temperature will be analyzed through simulated downhole drilling condition. A wellbore is assumed to be drilled in a fractured shale formation at a true vertical depth (TVD) of 3281 ft (1000 m). The values for in-situ conditions and wellbore geometry are listed **Table 5**. Other modeling material parameters for fracture and chemical effects are given in **Table 6.**

TABLE 5—IN-SITU CONDITIONS AND WELLBORE GEOMETRY

In-situ Conditions	
Overburden stress (S_V)	1.050 psi/ft (23.75 kPa/m or 2.42 SG)
Maximum Horizontal stress (S_H)	0.880 psi/ft (19.90 kPa/m or 2.03 SG)
Minimum Horizontal stress (S_h)	0.800 psi/ft (18.10 kPa/m or 1.85 SG)
Formation pore pressure (p_o)	0.433 psi/ft (9.80 kPa/m or 1.00 SG)
Formation temperature (T_o)	40°C (104°F)
Formation water activity (a_o)	0.88 (~ 150K $CaCl_2$ = 0.034 mole fraction)
Wellbore Parameters	
Well depth (true vertical depth)	3281 ft (1000 m)
Wellbore diameter ($2R_w$)	4.0 in (0.1 m)
Well azimuth	0° clockwise from North
Well inclination	varying from vertical (0°) to horizontal(90°)
Rock Strength Parameters	
Formation cohesion (C_o)	1200 psi (8.27 MPa)
Formation friction angle (Φ_o)	20 degrees
Formation tensile strength	0 psi (0 MPa)
Bedding Plane Strength Parameters	
Bedding plane cohesion (C_b)	600 psi (4.14 MPa)
Bedding plane friction angle (Φ_b)	10°
Bedding plane dip (β_d)	80° from horizontal plane*
Bedding plane strike (β_a)	150° clockwise from North*

TABLE 6—MODELING PARAMETERS	
Single-Poroelastic Analysis (Intact Rock)	
Compressibility (c^I)	6.2×10^{-6} psi^{-1} (9.1×10^{-4} Mpa^{-1})
Poisson's ratio (ν^I)	0.22
Effective stress coeff. (α^I)	0.96
Storage coeff. ($1/M^I$)	7.6×10^{-7} psi^{-1} (1.1×10^{-4} Mpa^{-1})
Porosity (ϕ^I)	0.14
Permeability (k^I)	1.0×10^{-5} md (~ 1.0×10^{-20} m^2)
Fluid viscosity (μ)	1 cp (0.01 Pa·s)
Drilling-mud weight (p_w)	10.00 lb/gal (1120 kg/m^3 or 1.258 SG)
Dual-Poroelastic Analysis (Fractured Rock)	
Fracture's compressibility (c^{II})	6.2×10^{-5} psi^{-1} (9.1×10^{-3} Mpa^{-1})
Fracture's bulk volume fraction (ν^{II})	0.05
Fracture's effective stress coeff. (α^{II})	1.00
Fracture's storage coeff. ($1/M^{II}$)	7.6×10^{-6} psi^{-1} (1.1×10^{-3} Mpa^{-1})
Fracture's local porosity (ϕ^{II})	0.95
Fracture's permeability (k^{II})	1.0 md (~ 1.0×10^{-15} m^2)
Interporosity geometric factor (λ)	~ 3.87 in^{-2} (6.0×10^{3} m^{-2})
Overall fractured rock compressibility ($\bar{c}$)	9.1×10^{-6} psi^{-1} (1.31×10^{-3} MPa^{-1})†
Overall fractures rock Poisson's ratio ($\bar{\nu}$)	0.22
Overall matrix's effective stress coeff. ($\bar{\alpha}^I$)	0.21†
Overall fracture's effective stress coeff. ($\bar{\alpha}^{II}$)	0.76†
Dual-Porochemoelastic Analysis (Fractured Shale)	
Matrix's membrane efficiency (χ^I)	0.2
Fracture's membrane efficiency (χ^{II})	0.0 (no membrane behavior)
Solute diffusion coeff. in free solution (D_0^s)	0.27 in^2/day (1.75×10^{-4} m^2/day)
Matrix's effective solute diffusion coeff. ($D_{eff}^{sI} = D_0^s(\phi^I)^2$)	5.33×10^{-3} in^2/day (3.43×10^{-6} m^2/day)†
Fracture's effective solute diffusion coeff. ($D_{eff}^{sII} = D_0^s\phi^{II}$)	0.25 in^2/day (1.58×10^{-4} m^2/day)†
Drilling-mud activity (a_w^f)	0.986 (~ 50K $CaCl_2$ = 0.008 mole fraction)
Dual-Porothermoelastic Analysis (Fractured Rock under Non-isothermal Condition)	
Solid volumetric thermal expansion coeff. ($\bar{\alpha}^s$)	3.0×10^{-5} °C^{-1}
Fluid volumetric thermal expansion coeff. ($\bar{\alpha}^f$)	3.0×10^{-4} °C^{-1}
Bulk heat capacity ($\bar{C}$)	2732 kJ/m^3 -°C
Thermal conductivity (λ^T)	353 kJ/m-day-°C
† Computed	

Time-Dependent Analyses for Fractured Rock: Dual-Poroelastic Analyses. The impacts of natural fracture network on mud-weight window are illustrated in here. The mud-weight window at the borehole wall (r/R = 1) for compact shale formation as determined by the single-poroelastic solution, which neglects the effects of flow and deformation in the fracture is shown in **Fig. 5.2(top)**.

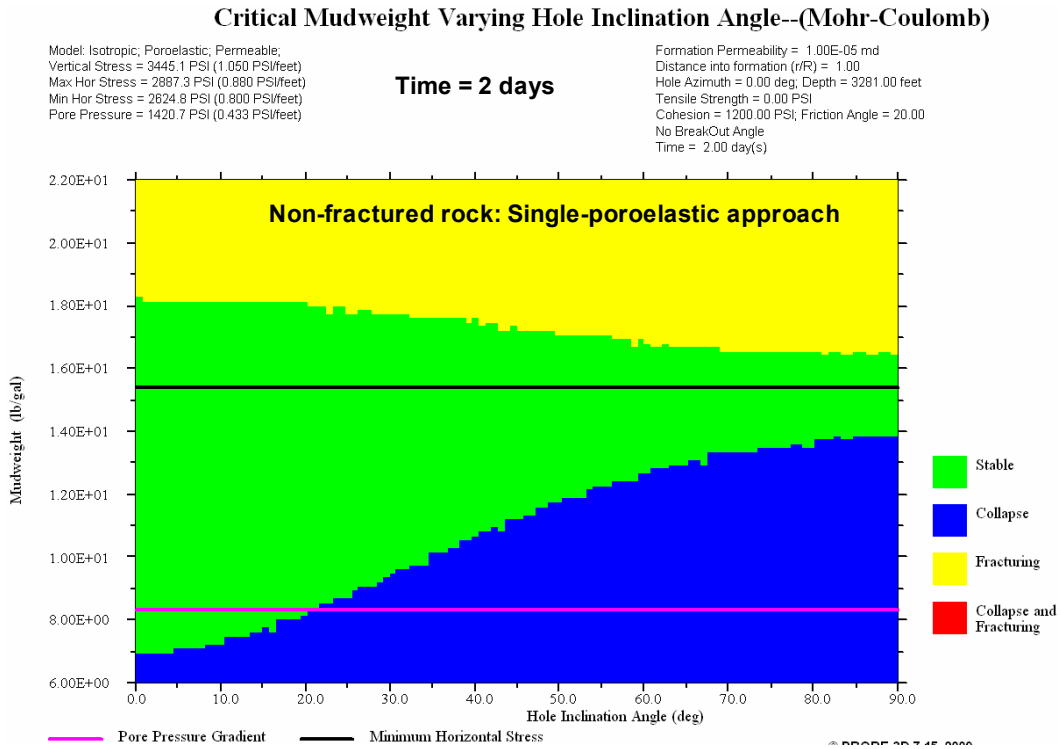

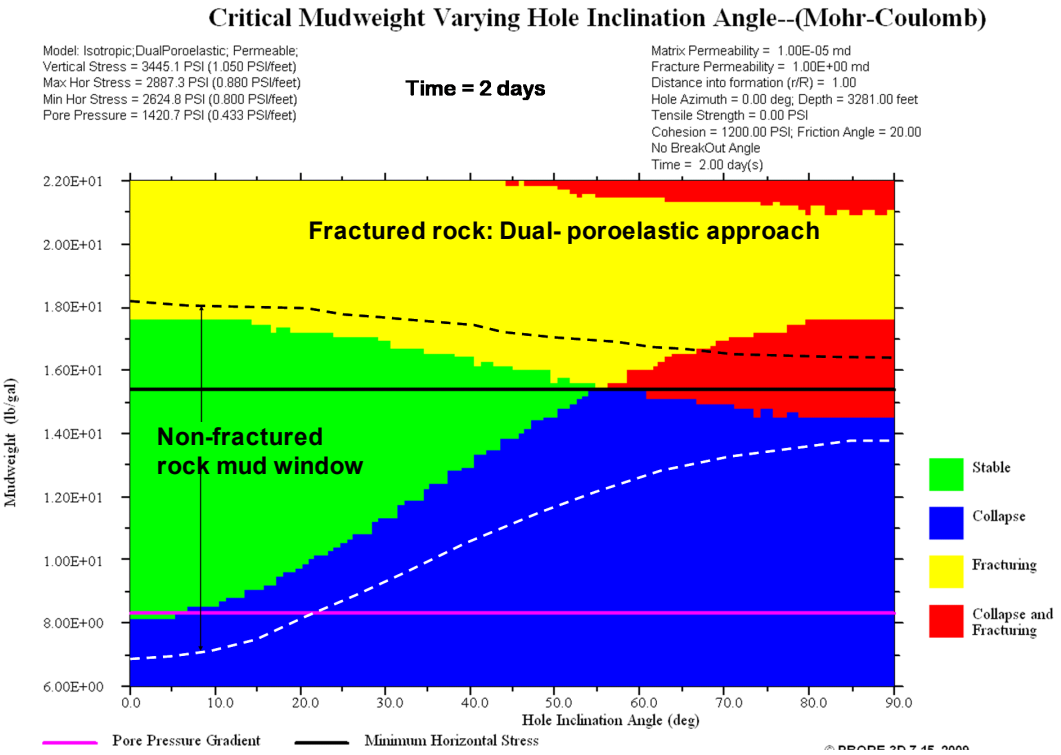

Fig. 5.2—Mud-weight windows at the borehole wall (*r*/*R* = 1) for different modeling approaches: (top) non-fractured rock, i.e., single-poroelastic and (bottom) fractured rock, i.e., dual-poroelastic.

The corresponding mud-weight window as predicted by the dual-porosity and dual-permeability solution is shown in **Fig. 5.2(bottom)**. In these figures, the green color indicates safe drilling mud-weights whereas the red color implies that the mud-weight to prevent collapse is higher than the allowable mud-weight to avoid fracturing the formation. At high wellbore mud pressure, flow in fracture network will quickly increase the pore pressure and decrease the effective stress, allowing more mud support to prevent collapse but also promoting tensile/fracturing failure (lower fracturing mud weight). On the other hand, at low mud weight, flow in fracture system will reduce mud support considerably and, thus, increase collapse potential (higher collapse mud weight). It is obvious that the non-fractured-shale approach and solution without coupling the fracture's contribution falls short in simulating wellbore stability in fractured shale because it predicts a wider mud-weight window for drilling operations. For example, drilling from a non-fractured shale section to fractured one will not tolerate high-angle wells, e.g., with borehole inclination greater than 55 degrees.

Time-Dependent Analyses for Fractured Shale with Mud Chemistry Effects: Dual-Porochemoelastic Analyses. Because the effective stress states are the same at the wellbore (Fig. 2), chemical effects on mud-weight windows only manifest inside the wellbore wall. In fact, the mud-weight window at r/R = 1.05 in **Fig. 5.3** reveals that low mud salinity (50K) and being fractured will shrink the mud-weight window. It is also important to note the time dependency of failure through the progression of the mud-weight window. In this case, it is observed that the mud-weight window shrinks from both ends (collapse and fracturing), approximately 1.50 lbm/gal after drilling for 1 day, resulting in a

total mud-weight-window contraction of 3.0 lbm/gal for high-angle wells. This trend suggests that borehole-instability potential increases with time.

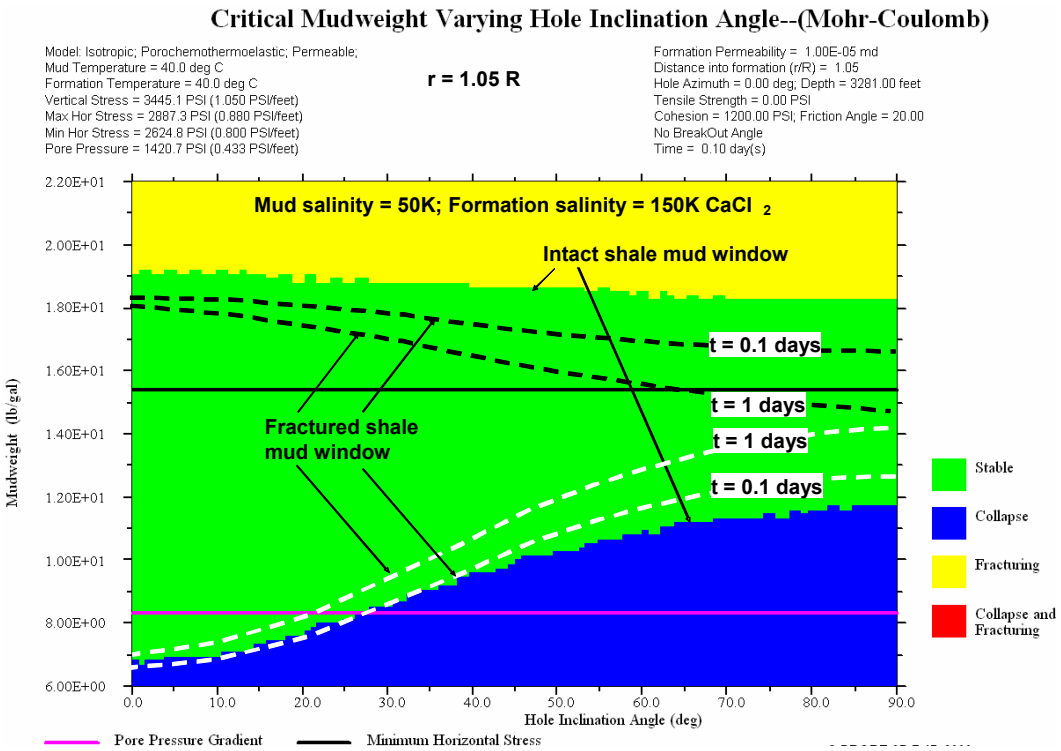

Fig. 5.3—Mud chemistry effect on mud-weight window at r/R = 1.05 after 0.1 day into drilling with low mud salinity (50K).

Time-Dependent Analyses for Fractured Shale with Mud Temperature Effects: Dual-Porothermoelastic Analyses. A mud/shale temperature gradient will increase or decrease the normal effectieve stress at the wellbore. As a result, the mud temperature can shift the allowable mudweight window either up or down. In **Fig. 5.4**, cooling will shift the mud window down, i.e., reducing the maximum mud density below which to avoid fracturing the wellbore while also decreasing the mud density required to prevent borehole collapse shear failures.

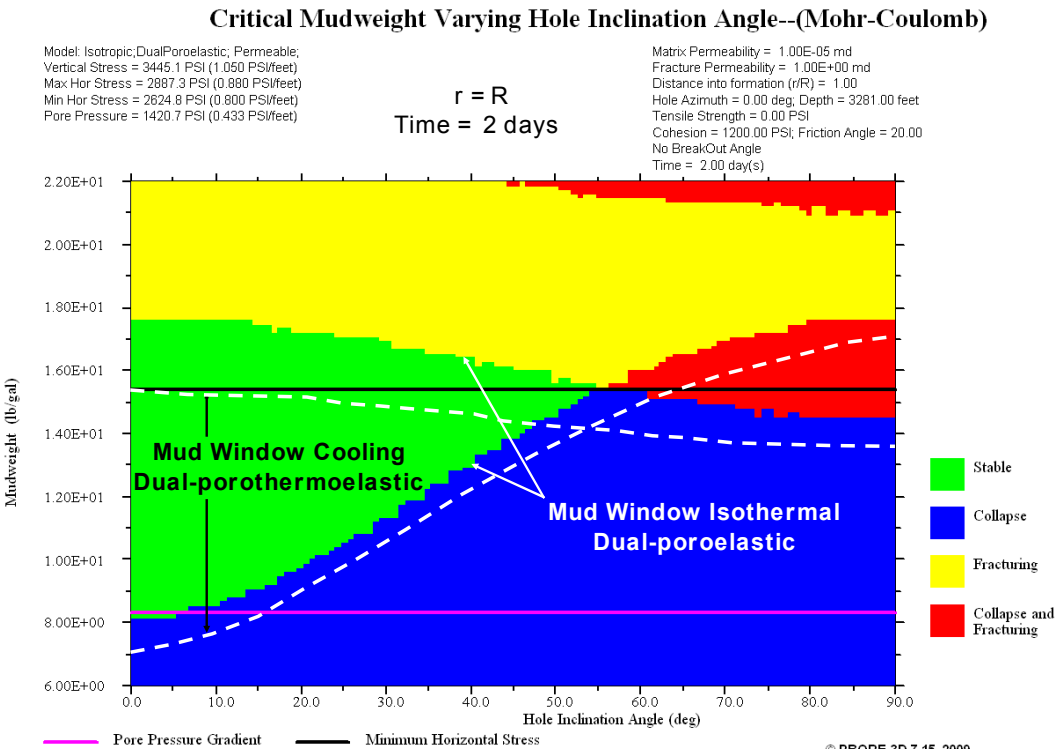

Fig. 5.4—Mud temperature effect on mud-weight window at r/R = 1.00 after 2 day into drilling for cooling.

5.3 Reservoir Consolidation[8]

Hydrocarbon production from naturally fractured reservoirs is susceptible to unwanted compaction and adverse pressure depletion. Compaction and depletion can be significant in "soft" and "highly permeable" reservoirs such as naturally fractured formations. In geomechanics reservoir modeling, the production induced reduction in reservoir pressure is fully coupled with the changes in total stress state in and around the reservoir. In other word, the reservoir porosity and permeability depends on the effective stress (total stress less fluid pressure) or deformation of the porous rock formation. Hence, knowledge of the

[8] Part of this work was presented at the SPE ATCE (Nguyen and Abousleiman, SPE 123900, October 2009, New Orleans).

effective stress histories and distributions during production and depletion can help estimate porosity and permeability change, predict and manage solid production, stress on casing, as well as near-wellbore formation mechanical stability.

In field development, it is desirable to establish the order of magnitude of the reservoir consolidation effect. Unfortunately, there are no simple tools available when it comes to analyzing the complex behaviors of fractured reservoirs. Geertsma's (1957) early analytical model used a nucleus-of-strain approach to simulate the elastic deformation of an infinitely thin disk-shaped reservoir with uniform pressure depletion. This approach provides estimate of deformation outside of the reservoir, e.g., subsidence, while giving no information about the fluid flow and/or deformation within the reservoir. Analytical approaches that consider deformation within the reservoir approximate the reservoir compaction as uniaxial elastic deformation with uniform pressure depletion (Settari 2002; Settari et al. 2005). In other word, the fluid flow and deformation field are uncoupled and solved separately. Recently, the fully coupled geomechanics approach to reservoir simulation has been incorporated in various numerical codes (Lewis et al. 2003, Phillips and Wheeler 2007). These numerical modeling identifies significant contribution of compaction drive mechanism during the life of a producing reservoir which required proper coupling between fluid flow and deformation in reservoir simulation. For homogeneous rock formation, Kanj and Abousleiman (2005, 2007) provided the analytical solutions for assessing compaction effect under the effects of stress, pressure, thermal and chemical perturbation. Recently, the analytical solution for inclined wellbore drilled in naturally fractured rock formation modeled as dual-porosity and dual-permeability continuum was

provided (Abousleiman and Nguyen 2005) and later extended to include chemical effect for analyses in fractured shale formation (Nguyen et al. 2009), thus systematically modeling the stresses and pore pressures in the fractures as well as in the matrix structure. These fully coupled solutions provide the groundwork for studying the compaction problem in naturally fractured reservoir since they can approximate the response of a finite boundary reservoir when the reservoir lateral extent is much larger than the wellbore radius or formation vertical thickness.

In this work, the reservoir is ideally modeled as a cylindrical disk-shape of large lateral extent of radius R_o compared to its vertical thickness, h ($R_o >> h$), buried at large depth (TVD $>>h$). A vertical well with wellbore radius of R_w ($R_w << R_o$) is completed in the center of the reservoir throughout the whole thickness which renders the problem geometry a hollow cylinder as depicted in **Fig. 5.5**. The reservoir behavior is linear poroelastic so that all material parameters such as compressibility are constant. The changes in reservoir effective stresses, displacements, and pore volume due to wellbore production/injection can be computed explicitly and analytically if the following assumptions and restrictions regarding boundary conditions are made (Fig. 5.5b):

- The reservoir is surrounded on all sides by non-depleting and much stiffer rock formations.
- At the outer boundary of the reservoir ($r = R_o$), there is no normal displacement ($u_r = 0$) and no flow ($q_r^{\mathrm{I}} = q_r^{\mathrm{II}} = 0$).
- At the wellbore ($r = R_w$), the casing support is assumed to enforce zero normal displacement ($u_r = 0$). For a prescribed production/injection rate, the total flow rate

across the wellbore wall is the sum of individual flow through the matrix and fracture network ($q_r = q_r^{I} + q_r^{II}$). In addition, hydraulic continuity requires that matrix and fracture fluid pressures are the same at the well ($p^{I} = p^{II}$).

- The bottom (z = 0) of the reservoir has a zero vertical displacement ($u_z = 0$) and no flow ($q_z^{I} = q_z^{II} = 0$) constraint.
- At the top (z = h) of the reservoir, the vertical stress applied on the reservoir by the overburden remains constant ($\Delta S_V = 0$) during production/injection. There is also no flow across this boundary ($q_z^{I} = q_z^{II} = 0$).

The boundary conditions imply that no axial fluid discharge occurs ($q_z^{I} = q_z^{II} = 0$) in the reservoir and fluid flow is in the radial direction only. The assumption of soft reservoir encased in stiffer rock formation render the reservoir's edge effects of shear stress and torsion negligible. This estimate will always yield a uniform vertical consolidation at the top of the reservoir. In reality, the vertical displacement is smaller at the edges of the reservoir as shown in Fig. 5.5a. Fortunately, for reservoir with large lateral extent, this assumption provides good approximation for vertical compaction (Setarri 2005). As a result, the problem geometry and boundary conditions allow the use of a generalized plane strain condition in which all quantities, except for vertical displacement (u_z), are z-independent. Due to the uniformity of lateral boundary conditions, the problem is obviously axisymetric (θ–independent). Here, we are interested in the changes of vertical displacement and effective stresses distribution in the reservoir due to production/injection (post-drilling and -completion processes) only. Therefore, the analytical solutions for these quantities are sought in reference to the pre-production stress state. The corresponding

analytical solution has been presented and details of the solution derivation can be obtained from Nguyen and Abousleiman (2009b).

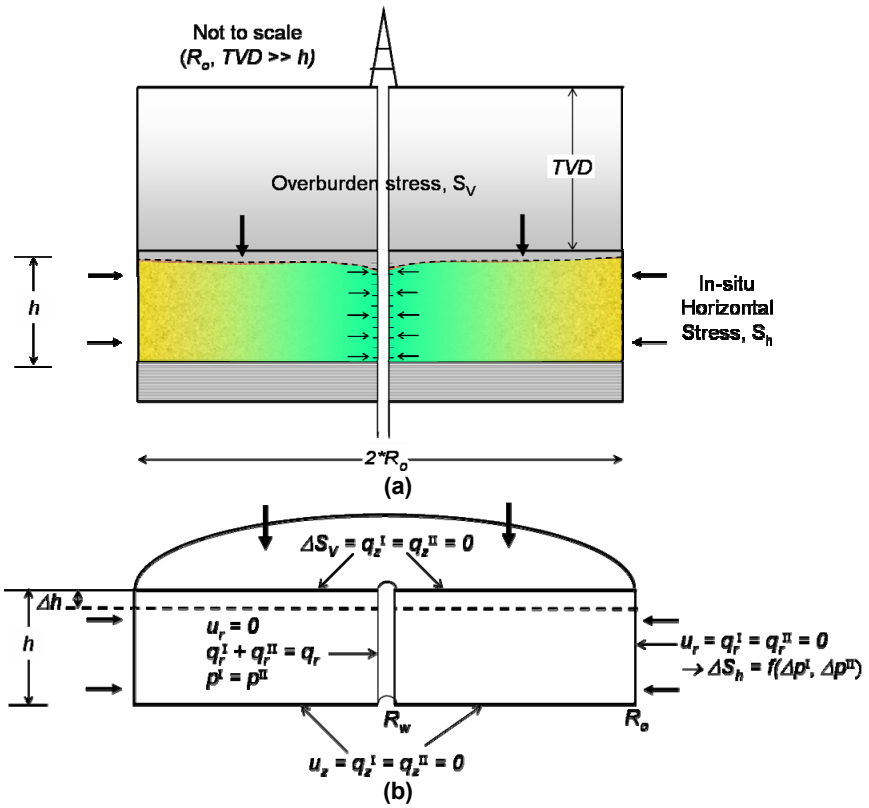

Fig. 5.5—Reservoir consolidation and compaction: (a) real behavior and (b) idealized model for fractured reservoirs.

In this section, the analytical solution is used to simulate the production and depletion of a fractured reservoir in the Ghawar field, Saudi Arabia and the subsequent impact on compaction, solid production and casing stress. The reservoir formation is predominantly carbonate rock with widespread dolomization and anhydrite pore-filling material. In some places, dolostones are responsible for producing permeability barriers, whereas in other places they are associated with zones of very high production (Meyer et al. 2000). These zones of very high flow have been termed ‘‘super-k’’ zones which can sustain up to 500 barrels per day per foot thickness. The average permeability varies from 1 md (matrix) to

400 md (fracture network). Therefore, the reservoir is a good candidate for dual-porosity and dual-permeability poroelastic modeling. Other formation material data include porosity = 20%, Young's modulus = 2×10^6 psi, and Poisson's ratio = 0.30.

A vertical well of radius R_w = 4 inches is assumed to be completed in a fractured reservoir with thickness h = 200 ft and lateral extent R_o = 3280 ft (1000 m) at 12,000 ft depth. The pre-production reservoir pressure is 6700 psi (1.30 SG). The in-situ stresses acting on the reservoir outer boundaries are the overburden S_V = 12,600 psi (2.42 SG) and horizontal in-situ stress $S_H = S_h$ = 9000 psi (1.73 SG). These are not the pre-production stress distribution in the reservoir because the original uniform in-situ stress state in the reservoir was altered due to wellbore drilling. The well is set to produce at constant flow rate of 10,000 STB/day for two years.

Consolidation and Implications on Porosity/Permeability Reduction. The current model and solution can be applied to simulate the effects of elastic-dominated deformation on porosity/permeability reduction due to reservoir depletion. The developed vertical consolidation is indicative of the pore volume reduced. However, it includes contribution from the bulk compressibility of the rock, the fluid as well as the pore volume. For small variation of the porosity, the change in apparent porosities, $v^I\phi^I$ and $v^{II}\phi^{II}$, are correctly captured by back calculating from the variation of fluid contents, Eqs. 2.10 and 2.11. Based on the porosity changes, the corresponding variations in permeability are computed. Assuming that the bulk volume fraction of the matrix (v^I) and fracture network (v^{II}) does not change during elastic deformation, the induced reduction in the intrinsic or local porosity of the matrix and fractured can be estimated. Since the fracture's intrinsic porosity

is usually a large number close to 1.0 but its bulk volume fraction is small, a small reduction in the total porosity can lead to a significant change in the fracture's intrinsic/local porosity ($\phi^{(N)}$) and subsequently the fracture's local permeability ($k^{(N)}$).

Isotropic Reservoir. The histories of vertical displacement between fractured and non-fractured isotropic reservoir as a result of production for up to 2 years are compared in **Fig. 5.6**. For constant production rate, the volumes of fluid withdrawn are the same for both non-fractured and fractured reservoir modeling. Therefore, the difference in the vertical displacement of 0.20 ft (2.4 in) clearly isolates the impact of fracture compressibility on reservoir deformation.

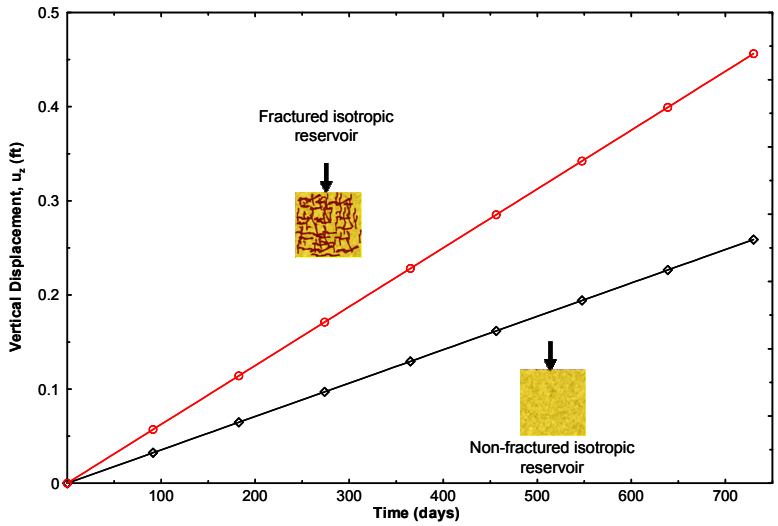

Fig. 5.6—Vertical consolidation due to constant production rate, Q_w = 10,000 stb/day, for isotropic reservoir.

Fig. 5.7 illustrates percent reduction in total porosity and equivalent permeability for constant production rate Q_w. The local permeability reductions (Δk^{I} and Δk^{II}) are estimated separately for the reservoir matrix block and fracture network and then combined to arrive at the equivalent permeability change. The results show up to 1.5% reduction in total

porosity and 6% decrease in the overall permeability. Ignoring the contribution of fracture's deformation and fluid flow could substantially underestimate the damage in reservoir flow quality.

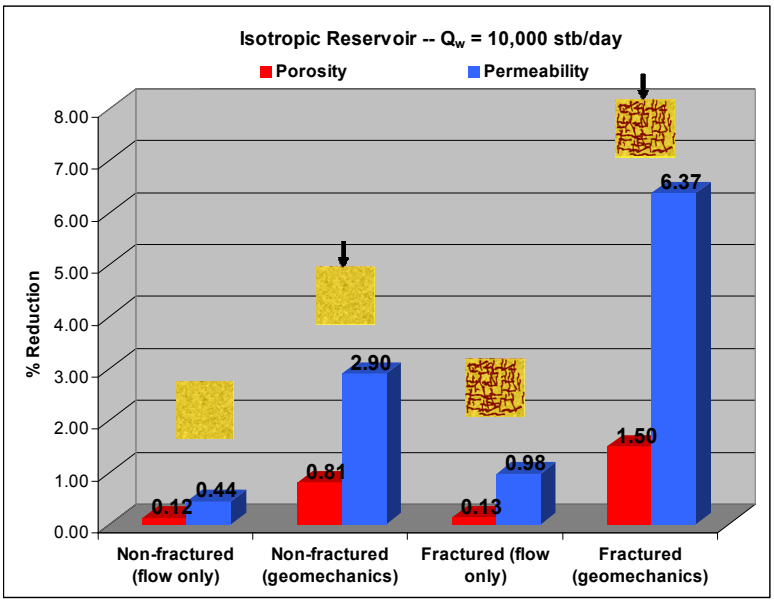

Fig. 5.7—Near-wellbore total porosity and equivalent permeability reductions due to constant production rate (Q_w = 10,000 stb/day) after 2 years.

Transversely Isotropic Reservoir. One potential application of the transversely isotropic model and solution is that the orientation of the fracture system in the reservoir can be partially simulated by modifying the ratios of material properties in the transverse direction (vertical) compared to those in the isotropic plane (horizontal). For example, a reservoir with horizontally oriented fracture system can be represented as being more compliant in the vertical direction ($(C_z/C_x)^{fracture} > 1$). Analogously, a randomly oriented fracture system can be modeled with isotropic properties, $(C_z/C_x)^{fracture} = 1$, whereas a vertically oriented fracture network can be represented as having $(C_z/C_x)^{fracture} < 1$. **Figs. 5.8 and 5.9** show the simulated vertical displacement and reduction in porosity and permeability for the three

fracture's representation discussed in here. The results are significantly different and demonstrate the impact of fractures' orientations, density, porosity and permeability on the overall reservoir flow and deformation responses.

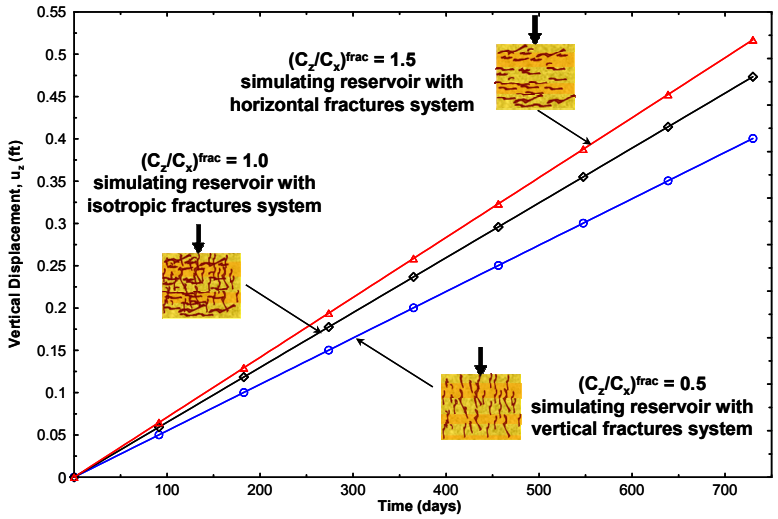

Fig. 5.8—Vertical consolidation of fractured reservoir. Fracture's orientation is simulated by varying the ratios of fracture's compressibility between the vertical direction and horizontal plane.

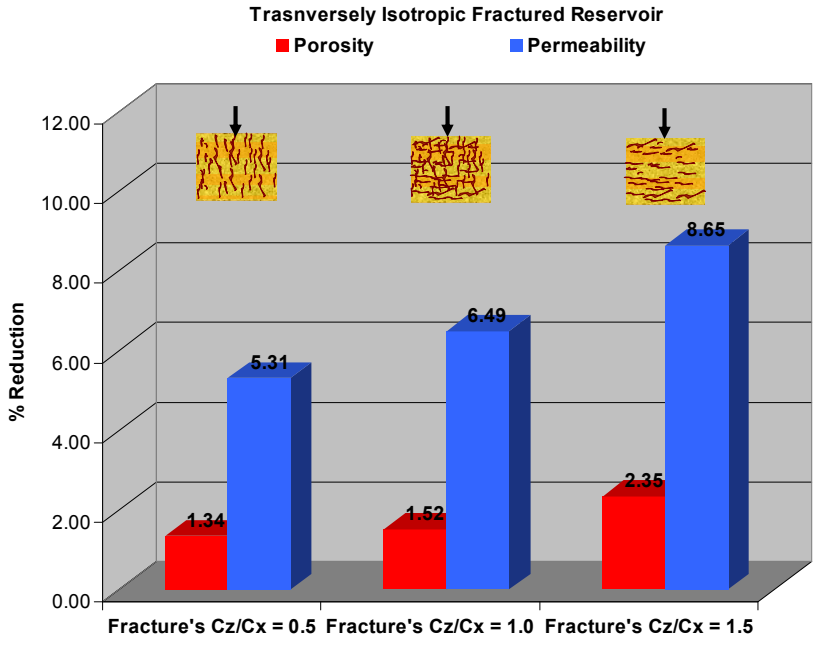

Fig. 5.9—Simulating near-wellbore porosity and permeability reductions for some fracture's orientations.

5.4 Time-dependent Load Applications

So far, the results are shown only for step loading condition. In this section, the responses due to time-dependent loading situations such as cyclic loading, linear ramp loading and/or combination are briefly demonstrated for cylinder geometry to illustrate the capability of the analytical solutions presented in this dissertation.

The material data and sample dimension are the same as listed for solid cylinder in Chapter 2, section 2.4.1.4. **Fig. 5.10** shows the pressure evolution at the center of the specimens under a low-frequency cyclic axial stress with magnitude of 1 MPa and a period of 2 seconds (0.5 Hz) for the first 5 cycles. As expected, the pore pressures also show cyclic behaviors in which the pressure in the fracture is the highest because the loading period is smaller than the characteristic time scale for fluid diffusion in the fracture network (~ 4 sec). On the other hand, **Fig. 5.11** demonstrates the pore pressure response due to a linear ramp loading for three different buildup rates with characteristic times to of 10, 100, and 1000 seconds. The pressurization process is such that the average axial stress reaches 10 MPa at to time and remains constant at this level afterward. Evidently, the fast diffusion speed in fractured medium together with inter-porosity flow allow significantly less pore pressure build up in the sample. Finally, superposition of the basic loading solutions allows modeling of more complex loading processes. For example, combination of the above cyclic and linear ramp results yields the pore pressure fluctuation during the first 28 seconds for the loading functions depicted in the inset of **Fig. 5.12**.

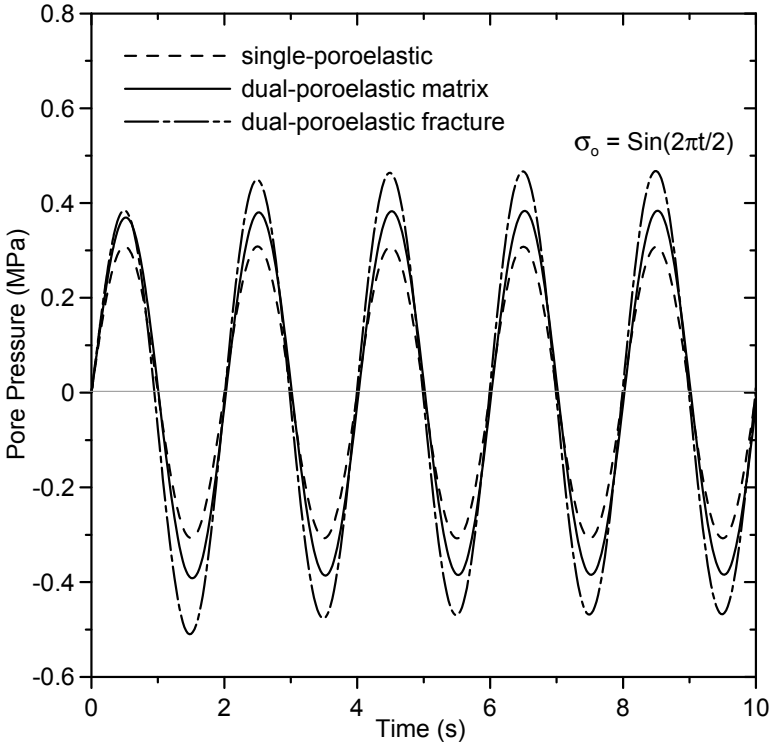

Fig. 5.10— Pore pressures histories at the cylinder's center *r* = 0 under cyclic loading.

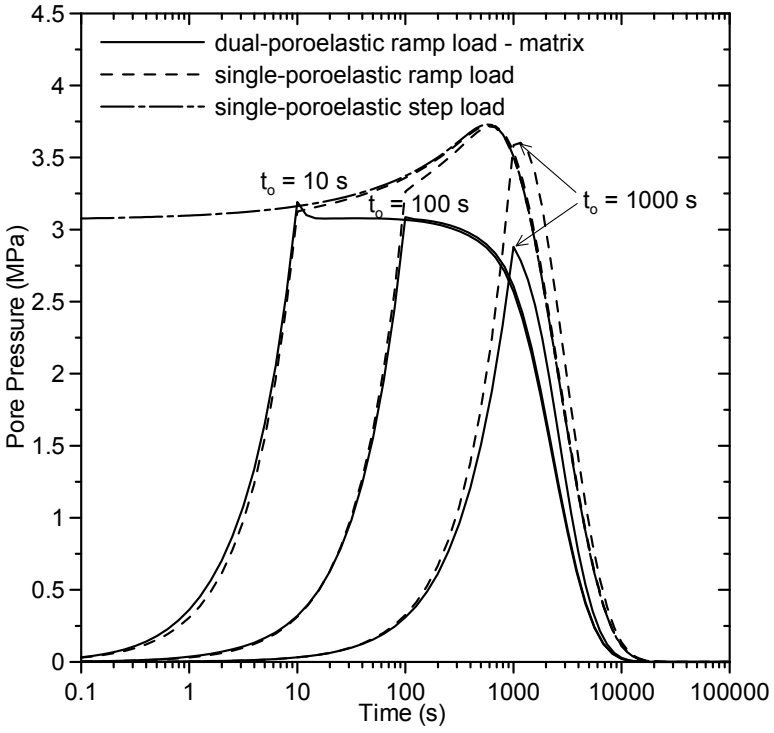

Fig. 5.11—Pore pressures histories at the cylinder's center *r* = 0 varying linear ramp loading rates.

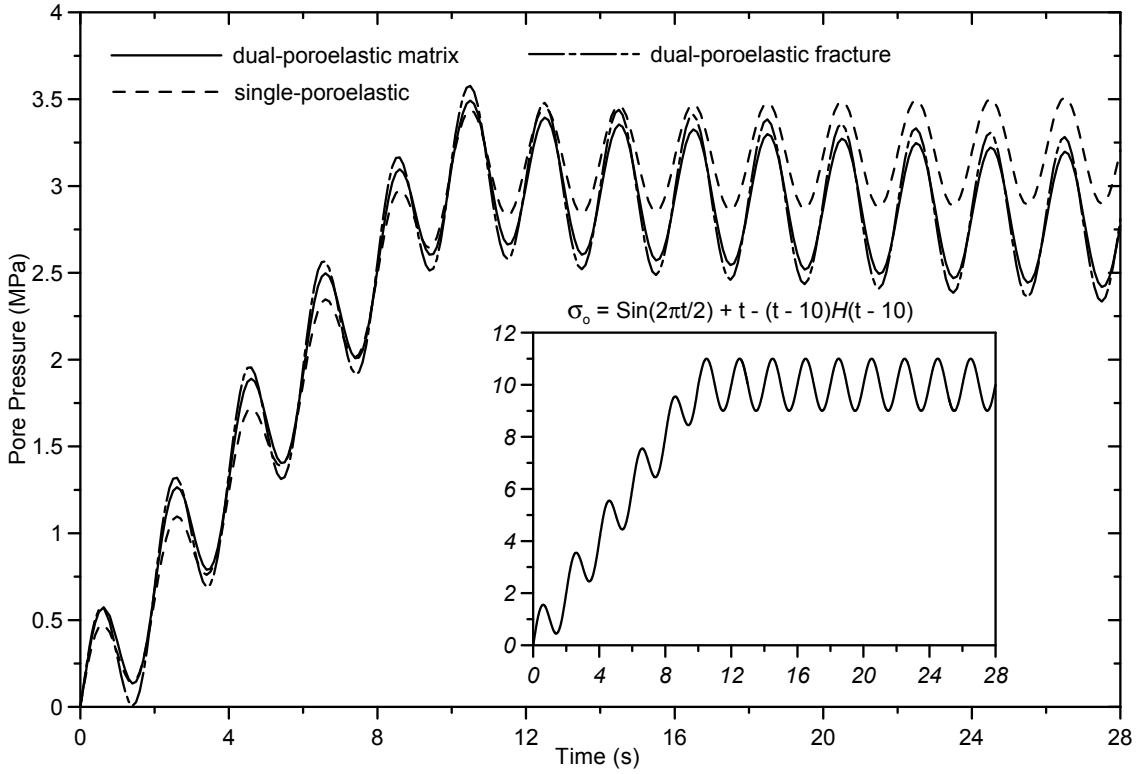

Fig. 5.12—Pore pressure fluctuations at the cylinder's center (r = 0) through times under combined cyclic and linear ramp loading (the cyclic loading period is T = 2 seconds and ramping characteristic time is t_o = 10 seconds).

5.5 Summary

The inclined wellbore solution has been applied to assess wellbore stability for a simulated downhole drilling condition. Analyses that neglect the naturally fractured nature of the shale fall short in simulating wellbore instability since they predicted a wider mud-weight window for the drilling operation, while mud salinity and temperature can be utilized as a stabilizing factor if calibrated previously. These analytical analyses can be applied directly to real-case drilling analyses in fractured-shale formations.

General anisotropic dual-porosity and dual-permeability analytical formulation and solution to simulate naturally fractured reservoir geomechanics due to production/injection

have been presented. The analytical model is easy to implement and can be used for sensitivity analyses among extreme cases of reservoir representation and management. The anisotropic representation of the fracture framework allows quick calculation of the effect of fractures on the overall geomechanical responses. Applications of the fractured model and solutions include estimation of consolidation and porosity and permeability reduction, all of which are important to the overall field development plan including recovery forecast and management, platform and well design, future stimulation programs (hydraulic fracturing). Furthermore, the analytical solution can be used to validate reservoir simulation numerical codes.

Finally, some realistic quasi-static loading conditions commonly encountered in experimental testing and field applications such as cyclic, linear ramping, and combination have been demonstrated via the solutions of solid cylinder geometry.

Chapter 6

Conclusions and Recommendations

6.1 Conclusions

A complete study of anisotropic dual-porosity and dual-permeability poromechanics is presented through generalized analytical solutions of problem geometries for laboratory and field applications. The behaviors of naturally fractured rock formations or the responses of the well known dual-porosity bone structure are modeled as dual-porosity and dual-permeability poroelastic media that fully couples fracture's deformation, fluid flow and interporosity exchange processes. For chemically active fractured media, e.g., clay, shale, or biomaterial, chemical interaction effects including osmotic and solute transport in both the porous matrix and fracture network is addressed based on non-equilibrium thermodynamics. Thermohydromechanical coupling under non-isothermal condition is incorporated by adopting a "single-temperature" approach in which a global representative thermodynamic continuum is argued to be sufficient to describe the thermally induced responses of a naturally fractured rock formation. The mathematical models are used to

find the poromechanical analytical solutions to selected problem geometries, including inclined wellbore, rectangular strip, and solid and hollow cylinder. The solutions are derived to include general time-dependent boundary conditions that can be tailored to specific field problems or laboratory testing setups. These solutions are expressed in closed forms in Laplace transform domain and can be easily inversed to obtain results in time domain.

Generic dual-poromechanics results are plotted and compared with single-poromechanics counterpart for a homogenous medium where applicable. Parametric analyses are also carried out to evaluate the effect of fracture network on the overall response. The inclined wellbore solution is used to perform comprehensive time-dependent wellbore stability analysis for drilling through chemically active fractured rock formations under non-isothermal conditions. The hollow cylinder is applied to study elastic consolidation of a producing naturally fractured reservoir and associated implications on porosity and permeability reduction in the near-wellbore region. Finally, the solid cylinder solution is used to demonstrate the dual-poromechanics responses under some realistic experimental loading conditions such as cyclic, linear ramping.

The following conclusions can be drawn based on the results of this study:

1. The inclined wellbore analytical solutions with various fluid boundary conditions can be applied directly to real-case drilling analyses in fractured-shale formations under non-isothermal condition.

2. Dual-poromechanics modeling of fractured rock formation predicts a narrower mudweight window for operations.

3. The mud chemistry and temperature can be used as stabilizing factor for wellbore stability if calibrated previously.

4. The analytical solutions for solid and hollow cylinder geometries can be used in both geomechanics and biomechanics for purposes of rock and bio-tissue characterization.

5. In addition, the anisotropic hollow cylinder solution can be easily implemented to simulate naturally fractured reservoir geomechanics due to production/injection through sensitivity analyses among extreme cases of reservoir representation and management.

6. Results show that analyses neglecting the effects of fracture, chemical salinity, and/or temperature in modeling approach can lead to erroneous laboratory test's results or interpretation as well as misleading the optimization of field operations.

7. Finally, the analytical solutions presented in this work can be used as benchmark for validating the integrity of numerical codes for reservoir simulation.

6.2 Recommendations

The developed model involves many assumptions and simplifications, including linear elastic medium, constant material coefficients, single-phase fluid flow, etc. During operations such as wellbore drilling, these simplifications may not apply, and their effects should be assessed properly. Therefore, experiments and more field case studies are needed to validate the analytical models.

Numerical analyses of realistic problem geometry and boundary conditions can be carried out using the analytical solutions presented in this dissertation as validation results.

References

Abdallah, G., Thoraval, A., Sfeir, A., and Piguet, J.P. 1995. Thermal Convection of Fluid in Fractured Media. *Int. J. Rock Mech. Min. Sci. & Geomech. Abstr.*, **32** (5): 481–490.

Abousleiman, Y., Cheng, A.H.-D., Cui, L., Detournay, E., and Roegiers, J.-C. 1996. Mandel's Problem Revisited. *Geotechnique*, **46**(2): 187-195.

Abousleiman, Y., and Cui, L. 1998. Poroelastic Solutions in Transversely Isotropic Media for Wellbore and Cylinder. *Int. J. Solids Struct.*, **35**(34–35): 4905–4929.

Abousleiman, Y., Ekbote, S., and Tare, U. 2001. Time-Dependent Wellbore Stability Predictions. *J. Pet. Technol.* February, 29–30.

Abousleiman, Y. and Ekbote, S. 2004. Solutions for the Inclined Borehole in a Porothermoelastic Transversely Isotropic Medium. *J. Appl. Mech.* **72**: 102–114.

Abousleiman, Y.N. and Kanj. M.Y. 2004. The Generalized Lamé Problem-Part II: Applications in Poromechanics. *J. Appl. Mech.*, **71**(3): 180–189. doi:10.1115/1.683800.

Abousleiman, Y. and Nguyen, V. 2005. PoroMechanics Response of Inclined Wellbore Geometry in Fractured Porous Media. *J. Eng. Mech*. **131**(11): 1170–1183. doi:10.1061/(ASCE)0733-9399(2005)131:11(1170).

Aguilera, D. 1995. Geologic Aspects. In *Naturally Fractured Reservoirs*, second edition, Chap. 1, 4-20. Tulsa, Oklahoma: PennWell Books.

Aifantis, E.C. 1977. Introducing a Multi-Porous Medium. *Developments in Mechanics*, **8**: 209-211.

Aifantis, E.C. and Beskos, D.E. 1980. Heat Extraction from Hot Dry Rocks. *Mech. Res. Comm.*, **7**(3): 165-170.

Alassi, H.T.I., Li, L., and Holt, R.M. 2006. Discrete Element Modeling of Stress and Strain Evolution Within and Outside a Depleting Reservoir. *Pure Appl. Geophys.*, **163**: 1131-1151. doi: 10.1007/s00024-006-0067-5.

Al-Tahini, A.M., Abousleiman, Y.N., and Brumley, J.L. 2005. Acoustic and Quasistatic Laboratory Measurement and Calibration of the Pore Pressure Prediction Coefficient

in the Poroelastic Theory. Paper SPE 95825 presented at the SPE Annual Technical Conference and Exhibition, Dallas, 9–12 October. doi: 10.2118/95825-MS.

Amadei, B. 1983. *Rock Anisotropy and the Theory of Stress Measurement*, Springer-Verlag.

Armstrong, C.G., Lai, W.M., and Mow, V.C. 1984. An Analysis of the Unconfined Compression of Articular Cartilage. *J. Biomech. Eng.*, **106**(5): 165–173.

Bader, S. and Kooi, H. 2005. Modeling Solute and Water Transport in Semi-Permeable Clay Membranes: Comparison with Experiment." *Adv. Water Resour.* **28**: 203-214.

Bagheri, M.A. and Settari, A. 2006. Effects of Fractures on Reservoir Deformation and Flow Modeling. *Can. Geotech. J.*, **43**: 574-586. doi:10.1139/T06-024.

Barenblatt, G.I., Zheltov, I.P., and Kochina, I.N. 1960. Basic Concept in the Theory of Seepage of Homogeneous Liquid in Fissured Rocks. *J. Appl. Math. Mech.*, **24**(5): 1286–1303.

Bear, J. 1972. *Dynamics of Fluids in Porous Media*, third edition, Chap. 1. New York City: American Elsevier.

Bear, J., and Corapcioglu, M.Y. 1981. A Mathematical Model for Consolidation in a Thermoelastic Aquifer Due to Hot Water Injection or Pumping. *Water Resour. Res.* **17(**3): 723–736.

Berryman, J.G. and Wang, H.F. 1995. Some Elastic Coefficients of Double-Porosity Models for Fluid Transport in Jointed Rocks. *J. Geophys. Res.* **100**(812): 24611-24627.

Berryman, J.G. and Pride, S.R. 2002. Models for Computing Geomechanical Constants of Double-Porosity Materials from the Constituents' Properties. *J. Geophys. Res.* **107**(B3): ECV2-1-ECV2-14.

Berryman, J.G. 2002. Extension of Poroelastic Analysis to Double-Porosity Materials: New Technique in Microgeomechanics. *J. Eng. Mech.* **128**(8): 840–847. doi:10.1061/(ASCE)0733-9399(2002)128:8(840).

Beskos, D.E. and Aifantis, E.C. 1986. On the Theory of Consolidation with Double Porosity – II. *Int. J. Engng. Sci.*, **24**: 1697-1716.

Bevillon, D., Bouteca, M.J., Longuemare, P., and Shahrour, I. 2000. Contribution of the Coupled HydroMechanical Theory in the Estimate of Reservoir Production. Paper SPE 65175 presented at the SPE European Petroleum Conference, Paris, France, 24-25 October.

Billaux, D., Chiles, J.P., Hestir, K., and Long, J. 1989. Three-Dimensional Statistical Modeling of a Fractured Rock Mass—An Example from the Fanay-Augeres Mine. *Int. J. Rock Mech. Min. Sci. & Geomech. Abstr.*, **26**(3–4): 281–299. doi:10.1016/0148-9062(89)91977-3.

Biot, M.A. 1941. General Theory of Three Dimensional Consolidation. *J. Appl. Phys.*, **12**: 155–164. doi: 10.1063/1.1712886.

Biot, M.A. 1955. Theory of Elasticity and Consolidation for a Porous Anisotropic Solid. *J. Appl. Phys.*, **26**(2): 182-185.

Bird, F., et.al. 1968. Experimental Determination of the Mechanical Properties of Bone. *Aerospace Medicine*, **39**(1): 44-48.

Booker, J.R. and Savvidou, C. 1985. Consolidation Around a Point Heat Source. *Int. J. Num. Anal. Meth. Geomech.*, **9**: 173-184.

Boresi, A.P. and Chong, K.P. 2000. *Elasticity in Engineering Mechanics*, second edition. New York City: John Wiley & Sons Inc.

Bowen, R.M. 1976. Theory of Mixtures. In *Continuum Physics*, Vol. III, ed. Eringen, A.C., 1-127. New York City: Academic Press.

Bradley, W.B. 1979. Failure of Inclined Boreholes. *J. Energy Resources Tech.*, **101**: 232–239.

Buschmann, M.D., Soulhat, J., Shirazi-Ald, A., Jurvelin, J.S., and Hunziker, E. B. 1998. Confined Compression of Articular Cartilage: Linearity in Ramp and Sinusoidal Tests and the Importance of Interdigitation and Incomplete Confinement. *J. Biomech*., **31**(2): 171–178.

Carter, J.P. and Booker, J.R. 1982. Elastic Consolidation Around a Deep Circular Tunnel. *Int. J. Solids Struct.*, **18**(12): 1059–1074.

Chen, G., Chenevert, M.E., Sharma, M.M., and Yu, M. 2003. A Study of Wellbore Instability in Shales Including Poroelastic, Chemical, and Thermal Effects. *J.Pet. Sci. Eng.* **38**: 167-176.

Chen, G. and Ewy, R.T. 2005. Thermoporoelastic Effects on Wellbore Stability. *SPEJ*, **10**(2): 121-129.

Chen, H.Y., Poston, S.W., and Raghavan, R. 1990. The Well Response in a Naturally Fractured Reservoir: Arbitrary Fracture Connectivity and Unsteady Fluid Transfer. Paper SPE 20566 presented 65th Annual Technical Conference and Exhibition of SPE held in New Orleans, LA, 23-26 September.

Chen, H.Y. 1990. Well Behaviors in Naturally Fractured Reservoirs. Ph.D. dissertation, Texas A&M U., College Station, Texas.

Chen, Z.-X and You, J. 1987. The Behavior of Naturally Fractured Reservoirs Including Fluid Flow in Matrix Blocks. *Transp. Porous Media*, **2**: 145–163.

Chen, Z.-X. 1989. Transient Flow of Slightly Compressible Fluids through Double-Porosity, Double-Permeability Systems – A State-of-the-Art Review. *Transp. Porous Media*, **4**: 147–184.

Cheng, A.H.-D. et al. 1992. Source Solution for a Generalized Dual Porosity Model. In *Structure et Comportement Mécanique des Géomatériaux*. eds. F. Homand, F. Masrouri, and J-P. Tisot, 109-116. Colloque René Houpert, Nancy, France.

Cheng, A.H.-D., Sidauruk, P., and Abousleiman, Y. 1994. Approximate Inversion of Laplace Transform. *Math. J.*, **4**(2): 76–82.

Cheng, A.H.-D. 1997. Material Coefficients of Anisotropic Poroelasticity. *Int. J. Rock Mech. Min. Sci.*, **34**: 183-193.

Chin, L.Y., Raghavan, R., and Thomas, L.K. 2000. Fully Coupled Geomechanics and Fluid-Flow Analysis of Wells with Stress-Dependent Permeability. *SPE J.*, **5**(1): 32-44.

Cho, T.F., Plesha, M.E., and Haimson, B.C. 1991. Continuum Modeling of Jointed Porous Rock. *Int. J. Numer. Analyt. Meth. Geomech.*, **15**: 333–353.

Choi, E.S., Cheema, T., and Islam, M.R. 1997. A New Dual-Porosity/Dual-Permeability Model with Non-Darcian Flow through Fractures. *J. Pet. Sci. Eng.*, **17**: 331-344.

Churchill, R.V. 1972. *Operational Mathematics*, . New York City: McGraw-Hill.

Christian, J.T. and Boehmer, J.W. 1970. Plane Strain Consolidation by Finite Elements. *J. Soil Mech. Found. Div.*, **96**(4): 1435–1457.

Cohen, B., et.al. 1998. A Transversely Isotropic Biphasic Model for Unconfined Compression of Growth Plate and Chondroepiphysis. *J. Biomech. Eng.*, **120**: 491–496.

Cook, N.G.W. 1992. Natural Joints in Rocks: Mechanical, Hydraulic and Seismic Behavior and Properties under Normal Stress. *Int. J. Rock Mech. Min. Sci. & Geomech. Abstr.*, **29**(3): 198-223.

Coussy, O. 1989. A General Theory of Thermoporoelastoplasticity for Saturated Porous Materials. *Transp. Porous Media*, **4**: 281–293.

Coussy, O. 2004. *Poromechanics*, John Wiley & Sons, Chichester, England, 37-61.

Cowin, S.C. 1999. Bone Poroelasticity. *J. Biomech.*, **32**(3): 217 – 238.

Cowin, S.C. and Mehrabadi, M.M. 2007. Compressible and Incompressible Constituents in Anisotropic Poroelasticity: The Problem of Unconfined Compression of a Disk. *J. Mech. Phys. Solids*, **55**: 161–193.

Cowin, S.C., Gailani, G., and Benalla, M. 2009. Hierarchical Poroelasticity: Movement of Interstitial Fluid Between Porosity Levels in Bones. *Phil. Trans. R. Soc. A*, **367**: 1-44.

Cryer, C.W. 1963. A Comparison of the Three-Dimensional Consolidation Theories of Biot and Terzaghi. *Quart. J. Mech. Appl. Math.*, **16**: 401-412.

Cui, L., Abousleiman, Y., Cheng, A.H.-D., and Kaliakin, V. 1996. Finite Element Analyses of Anisotropic Poroelasticity: A Generalized Mandel's Problem and an Inclined Borehole Problem. *Int. J. Numer. Analyt. Meth. Geomech.*, **20**(6): 381–401.

Cui, L., Cheng, A.H-D., and Abousleiman, Y. 1997. Poroelastic Solution for an Inclined Borehole. *J. Appl. Mech.*, **64**(1): 32–38. doi:10.1115/1.2787291.

Cui, L. et al. 1998. Borehole Stability Analysis in Fluid Saturated Formations with Impermeable Boundary. *Int. J. Rock Mech. & Min. Sci.*, **35**(4-5): 741.

Cui, L. and Abousleiman, Y.N. 2001. Time-Dependent Poromechanical Responses of Saturated Cylinders. *J. Eng. Mech.*, **127**(4): 391-398.

de Swaan, O.A. 1976. Analytic Solutions for Determining Naturally Fractured Reservoir Properties by Well Testing. *SPE J.*, **16**(2):117-122; *Trans.,* AIME, **261.** SPE-426-PA.

Dean, R.H., Gai, X., Stone, C.M., and Minkoff, S.E. 2006. A Comparison of Techniques for Coupling Porous Flow and Geomechanics. *SPE J.*, **11**(1): 132-140.

Dempster, W.T. and Liddicoat. 1952. Compact Bone as a Non-Isotropic Material. *Amer. J. Anat.*, **91**(3): 331-362.

Dershowitz, W. and Miller, I. 1995. Dual Porosity Fracture Flow and Transport. *Geophys. Resear. Let.*, **22**(11): 1441-1444.

Detournay, E., and Cheng, A.H.-D. 1988. Poroelastic Response of a Borehole in a Nonhydrostatic Stress Field. *Int. J. Rock Mech. Min. Sci. & Geomech. Abstr.*, **25**(3): 171-182.

Detournay, E. and Carvalho, J.L. 1989. Application of the Pressurized Hollow Poroelastic Cylinder Solution to the Intepretation of Laboratory Rock Burst

Experiments. In *Rock Mechanics as a Guide for Efficient Utilization of Natural Resources*, ed. A.W. Khair, 377-383. A.A. Balkema, Rotterdam, Neitherland.

Detournay, E., and Cheng, A.H.-D. 1993. Fundamentals of Poroelasticity. In *Comprehensive Rock Engineering: Principles, Practice and Projects*, Vol. 2, ed. Hudson, J.A., 113-171. Oxford, UK: Pergamon Press.

Dickey, J.W., Ladd, C.C., and Ringer, J.J. 1968. A Plane Strain Device for Testing Clays. Civil Engineering Research Report No. R68-3.

Duguid, J.O. and Lee, P.C.Y. 1977. Flow in Fractured Porous Media. *Water Resour. Res.*, **13**(3): 558-566.

Ekbote, S.M. 2002. Anisotropic Poromechanics of the Wellbore Coupled with Thermal and Chemical Gradients. Ph.D. Dissertation, The University of Oklahoma.

Ekbote, S. and Abousleiman, Y. 2003. Incorporating Chemical Effects in a Porothermoelastic Formulation and Application to Inclined Boreholes. *The 2003 IUTAM Symposium on the Mechanics of Physicochemical and Electromechanical Interactions in Porous Media*, Rolduc, Kerkrade, the Netherlands.

Ekbote, S., Abousleiman, Y., Cui, L., and Zaman, M. 2004. Analyses of Inclined Boreholes in Poroelastic Media. *Int. J. Geomech.*, **4**(3): 178-190.

Ekbote, S., Abousleiman, Y. 2005. Porochemothermoelastic Solution for an Inclined Borehole in a Transversely Isotropic Formation. *J. Eng. Mech.*, **131**: 522-533.

Ekbote, S., Abousleiman, Y. 2006. Porochemoelastic Solution for an Inclined Borehole in a Transversely Isotropic Formation. *J. Eng. Mech.*, **132**: 754-763.

Ewy, R.T., and Cook, N.G.W. 1990. Deformation and Fracture around Cylindrical Openings in Rock. I: Observations and Analysis of Deformations. *Int. J. Rock Mech. Min. Sci. Geomech. Abstr.,* **27**(5): 387–407.

Finol, A. and Farouq Ali, S.M. 1975. Numerical Simulation of Oil Production with Simultaneous Ground Subsidence. *SPEJ* (October 1975): 411-424.

Fritz, S.J. and Marine, I.W. 1983. Experimental Support for a Predictive Osmotic Model of Clay Membranes. *Geochim Cosmochim Acta.*, **47**: 1515–1522.

Gailani, G.B. and Cowin, S.C. 2008. The Unconfined Compression of a Poroelastic Annular Cylindrical Disk. *Mech. Mater.*, **40**: 507-523.

Geertsma, J. 1957. The Effect of Fluid Pressure Decline on Volumetric Changes of Porous Rocks. *Trans.,* AIME, **210:** 331–340.

Geertsma, J. 1973. Land Subsidence Above Compacting Oil and Gas Reservoir. *J. Petro. Technol.*, **25**: 734.

Gibson, R.E. and McNamee, J. 1963. A Three-Dimensional Problem of the Consolidation of a Semi-Infinite Clay Stratum. *Quar. J. Mech. and Appl. Math.*, **16**:115-127.

Gillham, R. W. and Cherry, J. A. 1982. Contaminant Migration in Saturated Consolidated Geologic Deposits. *Trends in Hydrogeology*, Geological Society of America Special Paper, **189**: 31-62.

Goulty, N.R. 2003. Reservoir Stress Path During Depletion of Norwegian Chalk Oilfields. *Petroleum Geoscience.*, **9**: 233-241.

Gutierrez, M. and Lewis R.W. 1998. The Role of Geomechanics in Reservoir Simulation. Paper SPE presented at the SPE/ISRM Eurock'98, Trondheim, Norway, 8-10 July.

Hale, A.H., Mody, F.K., and Salisbury, D.P. 1992. The Influence of Chemical Potential on Wellbore Stability. *SPEDC*, **8**(3): 207-216. SPE-23885-PA. doi: 10.2118/23885-PA

Hanshaw, B.B. 1964. Cation-Exchange Constants for Clays from Electrochemical Measurements. In *Proc. Natl. Conf. on Clays and Clay Minerals*, ed. W.F. Bradley, 397-421. Pergamon Press, New York, USA.

Heidug, W. K. and Wong, S. W. 1996. Hydration Swelling of Water Absorbing Rocks: A Constitutive Model. *Intl. J. Numer. Analyt. Meth. Geomech.*, **20**: 403-430.

Hemphill, T., Abousleiman, Y., Tran, M, Hoang, S. and Nguyen, V. 2008. Direct Strength Measurements of Shale Interaction with Drilling Fluids. Paper SPE 117851 presented at the 2008 Abu Dhabi International Petroleum Exhibition and Conference, Abu Dhabi, UAE, 3-6 November.

Hiramatsu, Y. and Oka, Y. 1968. Determination of the Stress in Rock Unaffected by Boreholes or Drifts, from Measured Strains or Deformations. *Int. J. Rock Mech. Min. Sci.*, **5**: 337–353.

Hoang, S.K., and Abousleiman, Y.N. 2009. Poroviscoelastic Two-Dimensional Anisotropic Solution With Application to Articular Cartilage Testing. *J. Eng. Mech.*, **135**(5): 367–374.

Huyghe, J.M. 1999. Intra-Extrafibrillar Mixture Formulation of Soft Charged Tissues. *J. Appl. Theor. Mech.*, **37**: 519-536.

Huyghe, J.M. and Janssen, J.D. 1999. Thermo-Chemo-Electro-Mechanical Formulation of Saturated Charged Porous Solids. *Transp. Porous Media.*, **24**: 129-141.

Jourine, S., Valkó, P.P., and Kronenberg, A.K. 2004. Modeling Poroelastic Hollow Cylinder Experiments with Realistic Boundary Conditions. *Intl. J. Numer. Analyt. Meth. Geomech.*, **28**: 1189-1205. doi: 10.1002/nag.383.

Kameo, Y., Adachi, T., and Hojo, M. 2008. Transient Response of Fluid Pressure in a Poroelastic Material Under Uniaxial Cyclic Loading. *J. Mech. Phys. Solids*, **56**: 1794-1805.

Kanj. M.Y., Abousleiman, Y.N., and Ghanem, R. 2003. Poromechanics of Anisotropic Hollow Cylinder. *J. Eng. Mech.*, **129**(11):1277-1287. doi: 10.1061/(ASCE)0733-9399 (2003)129:11(1277).

Kanj. M.Y. and Abousleiman, Y.N. 2004. The Generalized Lamé Problem-Part I: Couped Poromechanical Solutions. *J. Appl. Mech.*, **71**(3): 168–179. doi:10.1115/1.683751.

Kanj, M.Y. and Abousleiman, Y.N. 2005. Porothermoelastic analyses of anisotropic hollow cylinders with applications. *Int. J. Numer. Anal. Meth. Geomech.*, **29, 2**: 103-126.

Kanj, M.Y. and Abousleiman, Y.N. 2007. Taming Complexities of Coupled Geomechanics in Rock Testing: From Assessing Reservoir Compaction to Analyzing Stability of Expandable Sand Screens and Solid Tubulars. *SPE J.*, **12** (3): 293–304.

Katchalsky, A. and Curran, P. F. 1967. *Nonequilibrium Thermodynamics in Biophysics*, 95-123. Cambridge, MA: Harvard University Press.

Kazemi, H. 1969. Pressure Transient Analysis of Naturally Fracrured Reservoirs with Uniform Fracture Distribution. *SPEJ*., 451-462. Paper SPE 2156A.

Kazemi, H., Merrill, L.S., Porterfield, K.L., and Zeman, P.R. 1976. Numerical Simulation of Water-Oil Flow in Naturally Fractured Reservoirs. *SPEJ*., 317-326. Paper SPE 5719.

Kenyon, D.E. 1979. Consolidation in Transversely Isotropic Solids. *J. Appl. Mech.*, **46**(1): 65–70.

Kirsch 1898. Die Theorie der Elastizität und die Bedürfnisse der Festigkeitslehre. Zeitschrift des Vereines deutscher Ingenieure **42**: 797–807.

Kodashima, T. and Kurashige, M. 1996. Thermal Stresses of a Fluid-Saturated Poroelastic Hollow Sphere. *J. Thermal Stresses*, **19**: 139-151.

Kurashige, M. 1992. Thermal Stresses of a Fluid-Saturated Poroelastic Hollow Cylinder. *JSME Int. J. Series I*, **35**(4): 386-391.

Lewallen, K.T. and Wang, H.F. 1998. Consolidation of a Double-Porosity Medium. *Int. J. Solids Struc.* **35**(34-35): 4845-4867.

Lewis, R.W., Makurat, A., and Pao, W.K.S. 2003. Fully Coupled Modeling of Seabed Subsidence and Reservoir Compaction of North Sea Oil Field. *Hydrogeology Journal*, **11**(1): 142-161. doi: 10.1007/s10040-002-0239-z.

Li, X. 2003. Consolidation Around a Borehole in a Media with Double Porosity under Release of Geostatic Stresses." *Mech. Res. Commun.*, 30, 95-100.

Mandel, J. 1953. Consolidation des Sols étude Mathématique. *Geotechnique*, **3**(7): 287–299.

Masters, I., Pao, W.K.S., and Lewis, R.W. 2000. Coupling Temperature to a Double-Porosity Model of Deformable Porous Media. *Int. J. Num. Meth. Eng.*, **49**: 421-438.

Mattax, C.C. and Kyte 1962. Imbibition Oil Recovery from Fractured Water-Drive Reservoir. *SPEJ*., 177-184. Paper SPE 187.

McTigue, D. F. 1986. Thermoelastic Response of Fluid-Saturated Porous Rock. *J. Geophys. Res.*, **91**(B9): 9533–9542.

McTigue, D. F. 1990. Flow to a Heated Borehole in Porous, Thermoelastic Rock: Analysis. *Water Resour. Res.*, **26**(8): 1763–1774.

Meyer, F., Price, R., and Al-Raimi, S.M. 2000. Stratigraphic and Petrophysical Characteristics of Cored Arab-D Super-k Intervals, Hawiyah Area, Ghawar Field, Saudi Arabia. *Geo-Arabia*, **5**: 355–384.

Millard, A., Durin, M., Stietel, A., Thoraval, A., Vuillod, E., Baroudi, H., Plas F., Bougnoux, A., Vouille, G., Kobayashi, A., Hara, K., Fujita, T., and Ohnishi, Y. 1995. Discrete and Continuum Approaches to Simulate the Thermo-Hydro-Mechanical Couplings in a Large, Fractured Rock Mass. *Int. J. Rock Mech. Min. Sci. & Geomech. Abstr.* **32** (5): 409–434.

Nair, R.S. 2003. The Poromechanics of Naturally Fractured Rock Formations: A Finite Element Approach. PhD dissertation, Oklahoma U., Norman, Oklahoma.

Nair, R.S., Abousleiman, Y.N., and Zaman, M. 2004. A Finite Element Porothermoelastic Model for Dual-Porosity Media. *Int. J. Numer. Anal. Meth. Geomech.* **28**(9): 875-898.

Nguyen, V.X., Abousleiman, Y.N., and Hoang, S.K. 2009. Analyses of Wellbore Instability in Drilling Through Chemically Active Fractured Rock Formations. *SPE J.*, **14**(2): 283-301. SPE-105383-PA.

Nguyen, V.X. and Abousleiman, Y.N. 2009a. PoroMechanics Response of Inclined Wellbore Geometry in Chemically Active Fractured Porous Media. *J. Eng. Mech.*, **135**(11): 1-14.

Nguyen, V.X. and Abousleiman, Y.N. 2009b. Dual-Porosity and Dual-Permeability Poromechanics Solutions of Isotropic Hollow Cylinders.In *Poro-Mechanics IV*. eds. H. I. Ling, A. Smyth, and R. Betti, 850-857. Pennsylvania: DEStech Publications, Inc. Paper presented at the 4th Biot Conference on Poromechanics held at Columbia University, New York 8-10 June.

Nguyen, V.X. and Abousleiman, Y.N. 2010a. Poromechanics Solutions to Plane Strain and Axisymmetric Mandel-type Problems in Dual-Porosity and Dual-Permeability Porous Medium. *J. Appl. Mech.*, **77**(1): 011002-1-011002-18.

Nguyen, V.X. and Abousleiman, Y.N. 2010b. Incorporating Electrokinetic Effects in the PoroChemoelastic Inclined Wellbore Formulation and Solution. *An.Acad.Bras. Cienc.*, **82**(1): 195-222.

Nguyen, T.S. and Selvadurai, A.P.S. 1995. Coupled Thermal-Mechanical-Hydrological Behavior of Sparsely Fractured Rock: Implications for Nuclear Fuel Waste Disposal. *Int. J. Rock Mech. Min. Sci. & Geomech. Abstr.* **32** (5): 465–479.

Nowinski, J.L. and Davis, C.F. 1970. A Model of the Human Skull as a Poroelastic Spherical Shell Subjected to a Quasistatic Load. *Mathematical Biosciences*, **8**: 397-416.

Odgaard, A., and Linde, F., 1991. The Underestimation of Young's Modulus in Compressive Testing of Cancellous Bone Specimens. *J. Biomech.*, **24**(8): 691–698.

Papamichos, E., Vardoulakis, I., Tronvoll, J., and Skjrstein, A. 2001. Volumetric Sand Production Model and Experiment. *Int. J. Numer. Anal. Meth. Geomech.* **25**: 789-808. doi: 10.1002/nag.154.

Pariseau, W.G. 1993. Equivalent Properties of a Jointed Biot Material. *Int. J. Rock Mech. Min. Sci. & Geomech. Abstr.* **30** (7): 1151–1157. doi:10.1016/0148-9062(93)90085-R.

Phillips, P.J. and Wheeler, M.F. 2007. A Coupling of Mixed and Continuous Galerkin Finite Element Methods for Poroelasticity I: The Continuous Time Case. *Computational GeoSciences*, **11**(2): 131-144.

Polyanin, A.D., and Manzhirov, A.V. 1998. *Handbook of Integral Equations*, first edition, Sect. 2.2.1, formula #19. Boca Raton Florida: CRC Press.

Rahman, M.S., El-Zahaby, K., and Nooker, J. 1994. A Semi-Analytical Method for the Wave-Induced Seabed Response. *Int. J.Num. & Ana. Meth. Geomech.*, **18**: 213-236.

Rémond, A. and Naili, S. 2005. Transverse Isotropic Poroelastic Osteon Model Under Cyclic Loading. *Mech. Res. Commun.*, **32**: 645-651.

Saada, A.S. 1974. *Elasticity: Theory and Applications*, second edition (1993), Chap. 8. Malabar, Florida: Krieger Publishing Company.

Sachs J.R. and Grodzinsky A.J. 1987. An Electromechanically Coupled Poroelastic Medium Driven by an Applied Electrical Current: Surface Detection of Bulk Material Parameters. *Phys. Chem. Hydrodynamics*, **11**: 585-614.

Schutjens, P, Hanssen, T.H., Hettema, M.H.H., Merour, J., de Bree, P., Coremans, J.W.A., and Helliesen, G. 2004. Compaction-Induced Porosity/Permeability Reduction in Sandstone Reservoirs: Data and Model for Elasticity-Dominated Deformation. *SPE Reservoir Eval. & Eng.*, **7**(3): 202-216.

Schutjens, P., Kuvshinov, B., Dunayevsky, V., Rambow, F., Knowles, D., Love, K., Fehler, D., Khodaverdian, M., Frazer, S., and Leeftink, G. 2007. Wellbore Stress change due to Drawdown and Depletion: An Analytical Model and Its Application. Paper SPE 11536 presented at the International Petroleum Technology Conference, Dubai, U.A.E., 4–6 December.

Settari, A. 2002. Reservoir Compaction. *J. Petrol. Technol.*, **54**(8): 62-69. SPE-76805.

Settari, A.T., Bachman, R.C., and Walters, D.A. 2005. How to Approximate Effects of Geomechanics in Conventional Reservoir Simulation. Paper SPE 97155 presented at the SPE ATCE, Dallas, Texas, U.S.A., 9-12 October.

Sherwood, J.D. 1993. Biot Poroelasticity of a Chemically Active Shale. *Proc.Royal Soc. Lond. A*, **440**: 365-377.

Sherwood, J.D. and Bailey, L. 1994. Swelling Shale Around a Cylindrical Wellbore. *Proc. Royal Soc. Lond. A*, **444:** 161-184.

Sherwood, J. D. 1994. A Model of Hindered Solute Transport in a Poroelastic Shale." *Proc. Royal. Soc. Lond. A*, **445**: 679–692.

Schmitt, D.R., Tait, R.J., and Spann, H. 1993. Solution for Pore Pressure and Stress in a Porous Hollow Cylinder: Application to a Laboratory Experiment. *Int. J. Rock Mech. Min. Sci. & Geomech. Abstr.*, **30**(7): 1057–1060.

Simoes, F.M.F. and Loret, B. 2003. A Chemo-mechanical Model for Articular Cartilage: The Role of Intra- and Extrafibrillar Water. Proc., *IUTAM Symp. on Physicochemical*

and Electromechanical Interactions in Porous Media, eds., J.M. Huyghe, P.A.A. Raats, and S.C. Cowin, Springer, Berlin.

Stehfesh, H. 1970. Numerical Inversion of Laplace Transforms. *Commun. ACM.*, **13**: 47-49.

Terzaghi, K. 1943. *Theoretical Soil Mechanics*. New York City: Wiley.

Timoshenko, S. and Goodier, J.N. 1951. *Theory of Elasticity*, second edition. New York City: McGraw-Hill.

Thomas, L.K., Dixon, T.N., and Pierson, R.G. 1983. Fractured Reservoir Simulation. *SPEJ.*, 42-54. Paper SPE 9305.

Thompson, M. and Willis, J.R. 1991. A Reformulation of the Equations of Anisotropic Poroelasticity. *J. Appl. Mech.* ASME **58**: 612-616.

Tom, B., Dao, C.V., Nguyen, Q.V., Nguyen, D.V., Paul, G., David, H., Bingjian, L., Richard, M., Satyaki, R., Bernard, M., Ron, N., Davis, S., and Lars, S. 2006. The Nature of Naturally Fractured Reservoirs. *Oil Field Review*, **18**(2): 4-23.

Urban, J. P. G., Maroudas, A., Bayliss, M. T., and Dillon, J. 1979. Swelling Pressures of Proteoglycans at the Concentrations Found in Cartilagenous Tissues.*Biorheology*, **16**: 447–464.

Valliappan, S. and Khalili-Naghadeh, N. 1990. Flow through Fissured Porous Media with Deformable Matrix. *Int. J. Num. Meth. Engr.*, **29**: 1079-1094.

Van Oort E. 1994. A Novel Technique for the Investigation of Drilling Fluid Induced Borehole Instability in Shales. Paper SPE/ISRM 28064 presented at the 1994 SPE/ISRM Rock Mechanics in Petroleum Engineering Conference, Netherlands.

Vikram, S. and Settari, A.T. 2007. Simulation of Permeability and Geomechanical Anisotropy in Fractured Reservoirs. *The Leading Edge*, **26**(9): 1128–1133.

Wang, H. 2000. *Theory of Poroelasticity With Applications to Geomechanics and Hydrology*, Chap. 7-8. Princeton, New Jersey: Princeton University Press.

Wang, C., Chahine, N., Hung, C., and Ateshian, G., 2003. Optical Determination of Anisotropic Material Properties of Bovine Articular Cartilage in Compression. *J. Biomech.*, **36**: 339–353.

Wang, Y.L. and Papamichos, E. 1994. Conductive Heat Flow and Thermally Induced Fluid Flow around Wellbore in a Poroelastic Medium. *Water Resour. Res.*, **30**(12): 3375-3382.

Warren, J.E. and Root, P.J. 1963. The Behavior of Naturally Fractured Reservoirs. *SPE J.*, **3** (3): 245–255; *Trans.,* AIME, **228.** SPE-426-PA. doi: 10.2118/426-PA.

Wilson, R.K. and Aifantis, E.C. 1982. On the Theory of Consolidation with Double Porosity. *Int. J. Engng Sci.*, **20**(9): 1009-1035.

Wu, Y.S. and Pruess, K.A. 1988. A Multiple-Porosity Method for Simulation of Naturally Fractured Petroleum Reservoirs. *SPE Res. Eng.*, 327-336.

Yeung, A.T. and Mitchell, J.K. 1993. Coupled Fluid, Electrical and Chemical Flows in Soil. *Geotechnique*, **43**(1): 121-134.

Yeung, A.T. and Datla, S. 1995. Fundamental Formulation of Electrokinetic Extraction of Contaminants from Soil. *Can. Geotech. J.*, **32**(4): 569-583.

Yew, C.H., Chenevert, M.E., Wang, C.L., and Osisanya, S.O. 1990. Wellbore Stress Distribution Produced by Moisture Adsorption. *SPEDE*, **5**: 311-316.

Yin, S., Rothenburg, L., and Dusseault, M.B. 2006. 3D Coupled Displacement Discontinuity and Finite Element Analysis of Reservoir Behavior During Production in Semi-Infinite Domain. *Transp. Porous Media*, **65**(3): 425–441.

Yudovich, A., Chin, L.Y., Morgan, D.R. 1988. Casing Deformation in Ekofisk. Paper SPE 17856 presented at the Offshore Technology Conference, Houston, 2-5 May.

Zhang, D., Weinbaum, S., and Cowin, S.C. 1998. On the Calculation of Bone Pore Water Pressure due to Mechanical Loading. *Int. J. Solids Struc.*, **35**(34-35): 4981-4997.

Zhang, Jianguo, Rojas, J.C., and Clark, D.E. 2008. Stressed-Shale Drilling Strategy Water Activity Design Improves Drilling Performance. *SPEDC*, **23**(4): 385-393. SPE-102498-PA.

Appendix A Material Coefficients for Dual-Porosity and Dual-Permeability Poroelasticity

A.1 Transversely Isotropic Case

The individual drained elastic modulus tensor is expressed in matrix notation as

$$\mathbf{M}^{(\mathrm{N})} = \begin{bmatrix} M_{11}^{(\mathrm{N})} & M_{12}^{(\mathrm{N})} & M_{13}^{(\mathrm{N})} & 0 & 0 & 0 \\ M_{12}^{(\mathrm{N})} & M_{11}^{(\mathrm{N})} & M_{13}^{(\mathrm{N})} & 0 & 0 & 0 \\ M_{13}^{(\mathrm{N})} & M_{13}^{(\mathrm{N})} & M_{33}^{(\mathrm{N})} & 0 & 0 & 0 \\ 0 & 0 & 0 & M_{44}^{(\mathrm{N})} & 0 & 0 \\ 0 & 0 & 0 & 0 & M_{55}^{(\mathrm{N})} & 0 \\ 0 & 0 & 0 & 0 & 0 & M_{55}^{(\mathrm{N})} \end{bmatrix}, \quad \text{(A1.1)}$$

For engineering applications, it is more practical to use the familiar drained Young's moduli $E_1^{(\mathrm{N})}$ and $E_3^{(\mathrm{N})}$, Poisson's ratios $v_{12}^{(\mathrm{N})}$ and $v_{13}^{(\mathrm{N})}$, and the shear modulus $G_3^{(\mathrm{N})}$ to express the components of the transversely isotropic drained elastic modulus matrix $\mathbf{M}^{(\mathrm{N})}$ by the following relations (Abousleiman and Cui 1998)

$$M_{11}^{(\mathrm{N})} = \frac{E_1^{(\mathrm{N})}[E_3^{(\mathrm{N})} - E_1^{(\mathrm{N})}(v_{13}^{(\mathrm{N})})^2]}{(1+v_{12}^{(\mathrm{N})})[E_3^{(\mathrm{N})} - E_3^{(\mathrm{N})}v_{12}^{(\mathrm{N})} - 2E_1^{(\mathrm{N})}(v_{13}^{(\mathrm{N})})^2]}, \quad \text{(A1.2a)}$$

$$M_{12}^{(\mathrm{N})} = \frac{E_1^{(\mathrm{N})}[E_3^{(\mathrm{N})}v_{12}^{(\mathrm{N})} + E_1^{(\mathrm{N})}(v_{13}^{(\mathrm{N})})^2]}{(1+v_{12}^{(\mathrm{N})})[E_3^{(\mathrm{N})} - E_3^{(\mathrm{N})}v_{12}^{(\mathrm{N})} - 2E_1^{(\mathrm{N})}(v_{13}^{(\mathrm{N})})^2]}, \quad \text{(A1.2b)}$$

$$M_{13}^{(\mathrm{N})} = \frac{E_1^{(\mathrm{N})}E_3^{(\mathrm{N})}v_{13}^{(\mathrm{N})}}{E_3^{(\mathrm{N})} - E_3^{(\mathrm{N})}v_{12}^{(\mathrm{N})} - 2E_1^{(\mathrm{N})}(v_{12}^{(\mathrm{N})})^2}, \quad \text{(A1.2c)}$$

$$M_{33}^{(\mathrm{N})} = \frac{(E_3^{(\mathrm{N})})^2(1-v_{12}^{(\mathrm{N})})}{E_3^{(\mathrm{N})} - E_3^{(\mathrm{N})}v_{12}^{(\mathrm{N})} - 2E_1^{(\mathrm{N})}(v_{12}^{(\mathrm{N})})^2}, \quad \text{(A1.2d)}$$

$$M_{44}^{(\mathrm{N})} = G_1^{(\mathrm{N})} = (M_{11}^{(\mathrm{N})} - M_{12}^{(\mathrm{N})})/2; \qquad M_{55}^{(\mathrm{N})} = M_{66}^{(\mathrm{N})} = G_3^{(\mathrm{N})}, \quad \text{(A1.2e)}$$

And the compliance matrix $\mathbf{C}^{(\mathrm{N})}$ which is the inverse of the drained elastic moduli $\mathbf{M}^{(\mathrm{N})}$ is given as follows

$$\mathbf{C}^{(\mathrm{N})} = \begin{bmatrix} C_{11}^{(\mathrm{N})} & C_{12}^{(\mathrm{N})} & C_{13}^{(\mathrm{N})} & 0 & 0 & 0 \\ C_{12}^{(\mathrm{N})} & C_{11}^{(\mathrm{N})} & C_{13}^{(\mathrm{N})} & 0 & 0 & 0 \\ C_{13}^{(\mathrm{N})} & C_{13}^{(\mathrm{N})} & C_{33}^{(\mathrm{N})} & 0 & 0 & 0 \\ 0 & 0 & 0 & C_{44}^{(\mathrm{N})} & 0 & 0 \\ 0 & 0 & 0 & 0 & C_{55}^{(\mathrm{N})} & 0 \\ 0 & 0 & 0 & 0 & 0 & C_{55}^{(\mathrm{N})} \end{bmatrix}, \quad \text{(A1.3a)}$$

$$C_{11}^{(\mathrm{N})} = 1/E_1^{(\mathrm{N})}; \qquad C_{12}^{(\mathrm{N})} = -v_{12}^{(\mathrm{N})}/E_1^{(\mathrm{N})}; \qquad C_{13}^{(\mathrm{N})} = -v_{13}^{(\mathrm{N})}/E_3^{(\mathrm{N})}, \quad \text{(A1.3b)}$$

$$C_{33}^{(\mathrm{N})} = 1/E_3^{(\mathrm{N})}; \qquad C_{44}^{(\mathrm{N})} = 1/G_1^{(\mathrm{N})}; \qquad C_{55}^{(\mathrm{N})} = 1/G_3^{(\mathrm{N})}, \quad \text{(A1.3c)}$$

Based on microhomogeneity and microisotropy arguments, the constituents' pore-pressure-coefficient matrix and Biot moduli are given by

$$\boldsymbol{\alpha}^{(\mathrm{N})} = [\,\alpha_1^{(\mathrm{N})} \quad \alpha_1^{(\mathrm{N})} \quad \alpha_3^{(\mathrm{N})} \quad 0 \quad 0 \quad 0\,]^{\mathrm{T}}, \quad \text{(A1.4a)}$$

$$\alpha_1^{(\mathrm{N})} = 1 - \frac{M_{11}^{(\mathrm{N})} + M_{12}^{(\mathrm{N})} + M_{13}^{(\mathrm{N})}}{3K_s^{(\mathrm{N})}}, \quad \text{(A1.4b)}$$

$$\alpha_3^{(\mathrm{N})} = 1 - \frac{2M_{13}^{(\mathrm{N})} + M_{33}^{(\mathrm{N})}}{3K_s^{(\mathrm{N})}}, \quad \text{(A1.4c)}$$

$$M^{(\mathrm{N})} = \frac{(K_s^{(\mathrm{N})})^2}{K_s^{(\mathrm{N})}[1+\phi^{(\mathrm{N})}(K_s^{(\mathrm{N})}/K_f^{(\mathrm{N})} - 1)] - \overline{\overline{M}}^{(\mathrm{N})}}, \quad \text{(A1.5)}$$

where the superscript $^{\mathrm{T}}$ denotes matrix's transpose operation. $K_s^{(\mathrm{N})}$ is the solid grain bulk modulus and $K_f^{(\mathrm{N})}$ is the fluid bulk modulus of the porous matrix and fracture network, respectively. $\phi^{(\mathrm{N})} = V_{pore}^{(\mathrm{N})} / V^{(\mathrm{N})}$ is the local porosity. $\overline{\overline{M}}^{(\eta)}$ is a lumped modulus given as

$$\overline{\overline{M}}^{(\mathrm{N})} = (2M_{11}^{(\mathrm{N})} + M_{33}^{(\mathrm{N})} + 2M_{12}^{(\mathrm{N})} + 4M_{13}^{(\mathrm{N})})/9, \quad \text{(A1.6)}$$

Following Berryman and Pride (2002), the effective constitutive coefficients for dual-poroelastic composite material can be identified in terms of the individual constituent's properties as

$$\overline{\boldsymbol{\alpha}}^{(\mathrm{N})} = -\overline{\mathbf{M}}\,(\mathbf{b}^{(\mathrm{N})})^{\mathrm{T}}, \quad \text{(A1.7)}$$

$$1/\overline{M}^{\mathrm{I}} = r^{\mathrm{I}} - \mathbf{b}^{\mathrm{I}}\,\overline{\mathbf{M}}\,(\mathbf{b}^{\mathrm{I}})^{\mathrm{T}}, \quad \text{(A1.8a)}$$

$$1/\overline{M}^{\mathrm{I,II}} = r^{\mathrm{I,II}} - \mathbf{b}^{\mathrm{I}}\,\overline{\mathbf{M}}\,(\mathbf{b}^{\mathrm{II}})^{\mathrm{T}}, \quad \text{(A1.8b)}$$

$$1/\overline{M}^{\mathrm{II}} = r^{\mathrm{II}} - \mathbf{b}^{\mathrm{II}}\,\overline{\mathbf{M}}\,(\mathbf{b}^{\mathrm{II}})^{\mathrm{T}}, \quad \text{(A1.8c)}$$

where $\overline{\mathbf{M}}$ is the overall drained elastic modulus matrix. Other matrixes and scalars are expressed as

$$\overline{\boldsymbol{\alpha}}^{(\mathrm{N})} = [\,\overline{\alpha}_1^{(\mathrm{N})} \quad \overline{\alpha}_1^{(\mathrm{N})} \quad \overline{\alpha}_3^{(\mathrm{N})} \quad 0 \quad 0 \quad 0\,]^{\mathrm{T}}, \quad \text{(A1.9)}$$

$$\mathbf{b}^{\mathrm{I}} = -(\boldsymbol{\alpha}^{\mathrm{I}})^{\mathrm{T}}\,\mathbf{C}^{\mathrm{I}}\left(\mathbf{C}^{\mathrm{I}} - \mathbf{C}^{\mathrm{II}}\right)^{-1}\left(\overline{\mathbf{C}} - \mathbf{C}^{\mathrm{II}}\right), \quad \text{(A1.10a)}$$

$$\mathbf{b}^{\mathrm{II}} = -(\boldsymbol{\alpha}^{\mathrm{II}})^{\mathrm{T}}\,\mathbf{C}^{\mathrm{II}}\left(\mathbf{C}^{\mathrm{I}} - \mathbf{C}^{\mathrm{II}}\right)^{-1}\left(\mathbf{C}^{\mathrm{I}} - \overline{\mathbf{C}}\right), \quad \text{(A1.10b)}$$

$$r^{(\mathrm{N})} = \mathrm{v}^{(\mathrm{N})}\overline{\overline{C}}^{(\mathrm{N})} - \mathrm{v}^{(\mathrm{N})}(\boldsymbol{\alpha}^{(\mathrm{N})})^{\mathrm{T}}\,\mathbf{C}^{(\mathrm{N})}\left(\mathbf{C}^{\mathrm{I}} - \mathbf{C}^{\mathrm{II}}\right)^{-1}\mathbf{C}^{(\mathrm{N})}\left(\mathbf{I} - \mathbf{Q}^{(\mathrm{N})}\right)\boldsymbol{\alpha}^{(\mathrm{N})}, \quad \text{(A1.11a)}$$

$$\begin{aligned} r^{\mathrm{I,II}} &= -\mathrm{v}^{\mathrm{II}}(\boldsymbol{\alpha}^{\mathrm{I}})^{\mathrm{T}}\,\mathbf{C}^{\mathrm{I}}\left(\mathbf{C}^{\mathrm{I}} - \mathbf{C}^{\mathrm{II}}\right)^{-1}\mathbf{C}^{\mathrm{II}}\left(\mathbf{I} - \mathbf{Q}^{\mathrm{II}}\right)\boldsymbol{\alpha}^{\mathrm{II}} \\ &= -\mathrm{v}^{\mathrm{I}}(\boldsymbol{\alpha}^{\mathrm{II}})^{\mathrm{T}}\,\mathbf{C}^{\mathrm{II}}\left(\mathbf{C}^{\mathrm{I}} - \mathbf{C}^{\mathrm{II}}\right)^{-1}\mathbf{C}^{\mathrm{I}}\left(\mathbf{I} - \mathbf{Q}^{\mathrm{I}}\right)\boldsymbol{\alpha}^{\mathrm{I}} \end{aligned}, \quad \text{(A1.11b)}$$

in which the superscripts $^{-1}$ denotes matrix's inverse operation and

$$\mathrm{v}^{\mathrm{I}}\mathbf{Q}^{\mathrm{I}} = \left(\mathbf{C}^{\mathrm{I}} - \mathbf{C}^{\mathrm{II}}\right)^{-1}\left(\overline{\mathbf{C}} - \mathbf{C}^{\mathrm{II}}\right), \quad \text{(A1.12a)}$$

$$\mathrm{v}^{\mathrm{II}}\mathbf{Q}^{\mathrm{II}} = \left(\mathbf{C}^{\mathrm{I}} - \mathbf{C}^{\mathrm{II}}\right)^{-1}\left(\mathbf{C}^{\mathrm{I}} - \overline{\mathbf{C}}\right), \quad \text{(A1.12b)}$$

$$\overline{\overline{C}}^{(\mathrm{N})} = (\boldsymbol{\alpha}^{(\mathrm{N})})^{\mathrm{T}}\mathbf{C}^{(\mathrm{N})}\boldsymbol{\alpha}^{(\mathrm{N})} + 1/M^{(\mathrm{N})}, \quad \text{(A1.13)}$$

The above approach requires the estimation of the overall drained elastic modulus $\overline{\mathbf{M}}$ or compliance $\overline{\mathbf{C}}$ matrixes. Generally, the overall moduli $\overline{\mathbf{M}}$ are functions of fractures volume/spacing and geometries which can be estimated by some averaging schemes or homogenization techniques. Values of elastic moduli, however, should be bounded between the fracture network's moduli $\mathbf{M}^{\mathrm{II}}$ and the matrix's ones $\mathbf{M}^{\mathrm{I}}$. One reasonable estimate could be the geometric mean of the constituents' moduli ($\overline{\mathbf{M}}^{(\mathrm{N})} = (\mathbf{M}^{\mathrm{I}})^{\mathrm{v}^{\mathrm{I}}}(\mathbf{M}^{\mathrm{II}})^{\mathrm{v}^{\mathrm{II}}}$) assuming that the fracture network is sufficiently developed and randomly distributed to form a homogeneous and transversely isotropic continuum on its own.

A.2 Isotropic Case

For isotropic case in which $E_1^{(\mathrm{N})} = E_3^{(\mathrm{N})} = E^{(\mathrm{N})}$, $v_{12}^{(\mathrm{N})} = v_{13}^{(\mathrm{N})} = v^{(\mathrm{N})}$, and $G_1^{(\mathrm{N})} = G_3^{(\mathrm{N})} = G^{(\mathrm{N})}$, the individual moduli and compliance simplify to

$$M_{11}^{(\mathrm{N})} = M_{33}^{(\mathrm{N})} = \frac{E^{(\mathrm{N})}(1 - v^{(\mathrm{N})})}{(1 + v^{(\mathrm{N})})(1 - 2v^{(\mathrm{N})})}, \quad \text{(A2.1a)}$$

$$M_{12}^{(\mathrm{N})} = M_{13}^{(\mathrm{N})} = \frac{E^{(\mathrm{N})}v^{(\mathrm{N})}}{(1 + v^{(\mathrm{N})})(1 - 2v^{(\mathrm{N})})}, \quad \text{(A2.1b)}$$

$$M_{44}^{(\mathrm{N})} = M_{55}^{(\mathrm{N})} = G^{(\mathrm{N})} = \frac{E^{(\mathrm{N})}}{2(1+v^{(\mathrm{N})})}, \quad \text{(A2.1b)}$$

$$C_{11}^{(\mathrm{N})} = C_{33}^{(\mathrm{N})} = 1/E^{(\mathrm{N})}; \qquad C_{12}^{(\mathrm{N})} = C_{13}^{(\mathrm{N})} = -v^{(\mathrm{N})}/E^{(\mathrm{N})}; \qquad C_{44}^{(\mathrm{N})} = C_{55}^{(\mathrm{N})} = 1/G^{(\mathrm{N})}, \quad \text{(A2.2)}$$

The corresponding constituents' pore-presure coefficients and Biot's moduli become

$$\alpha_1^{(\mathrm{N})} = \alpha_3^{(\mathrm{N})} = 1 - \frac{K^{(\mathrm{N})}}{K_s^{(\mathrm{N})}} = 1 - \frac{E^{(\mathrm{N})}}{3(1-2v^{(\mathrm{N})})K_s^{(\mathrm{N})}}, \quad \text{(A2.3)}$$

$$M^{(\mathrm{N})} = \frac{(K_s^{(\mathrm{N})})^2}{K_s^{(\mathrm{N})}[1+\phi^{(\mathrm{N})}(K_s^{(\mathrm{N})}/K_f^{(\mathrm{N})}-1)] - K^{(\mathrm{N})}}, \quad \text{(A2.4)}$$

$$\overline{\overline{M}}^{(\mathrm{N})} = K^{(\mathrm{N})} = E^{(\mathrm{N})}/[3(1-2v^{(\mathrm{N})})], \quad \text{(A2.5a)}$$

$$\overline{\overline{C}}^{(\mathrm{N})} = \frac{(\alpha^{(\mathrm{N})})^2}{K^{(\mathrm{N})}} + \frac{1}{M^{(\mathrm{N})}}, \quad \text{(A2.5b)}$$

The dual-poroelastic coefficients reduce to

$$\overline{\alpha}^{\mathrm{I}} = \alpha^{\mathrm{I}} \frac{\overline{K} - K^{\mathrm{II}}}{K^{\mathrm{I}} - K^{\mathrm{II}}}, \quad \text{(A2.6a)}$$

$$\overline{\alpha}^{\mathrm{II}} = \alpha^{\mathrm{II}} \frac{K^{\mathrm{I}} - \overline{K}}{K^{\mathrm{I}} - K^{\mathrm{II}}}, \quad \text{(A2.6b)}$$

$$\frac{1}{\overline{M}^{\mathrm{I}}} = \mathrm{v}^{\mathrm{I}}\overline{\overline{C}}^{\mathrm{I}} - \left(\frac{\alpha^{\mathrm{I}}K^{\mathrm{II}}}{K^{\mathrm{I}} - K^{\mathrm{II}}}\right)^2 \left(\frac{\mathrm{v}^{\mathrm{I}}}{K^{\mathrm{I}}} + \frac{\mathrm{v}^{\mathrm{II}}}{K^{\mathrm{II}}} - \frac{1}{\overline{K}}\right) - \frac{(\overline{\alpha}^{\mathrm{I}})^2}{\overline{K}}, \quad \text{(A2.7a)}$$

$$\frac{1}{\overline{M}^{\mathrm{I,II}}} = \frac{\alpha^{\mathrm{I}}\alpha^{\mathrm{II}}K^{\mathrm{I}}K^{\mathrm{II}}}{(K^{\mathrm{I}} - K^{\mathrm{II}})^2} \left(\frac{\mathrm{v}^{\mathrm{I}}}{K^{\mathrm{I}}} + \frac{\mathrm{v}^{\mathrm{II}}}{K^{\mathrm{II}}} - \frac{1}{\overline{K}}\right) - \frac{\overline{\alpha}^{\mathrm{I}}\overline{\alpha}^{\mathrm{II}}}{\overline{K}}, \quad \text{(A2.7b)}$$

$$\frac{1}{\overline{M}^{\mathrm{II}}} = \mathrm{v}^{\mathrm{II}}\overline{\overline{C}}^{\mathrm{II}} - \left(\frac{\alpha^{\mathrm{II}}K^{\mathrm{I}}}{K^{\mathrm{I}} - K^{\mathrm{II}}}\right)^2 \left(\frac{\mathrm{v}^{\mathrm{I}}}{K^{\mathrm{I}}} + \frac{\mathrm{v}^{\mathrm{II}}}{K^{\mathrm{II}}} - \frac{1}{\overline{K}}\right) - \frac{(\overline{\alpha}^{\mathrm{II}})^2}{\overline{K}}, \quad \text{(A2.7c)}$$

$K^{(\mathrm{N})}$ and $\overline{K}$ are the individual and overall bulk moduli, repectively. It can be seen that

when the secondary porosity medium vanishes, i.e., $v^{II} \rightarrow 0$, the material coefficients reduce naturally to the single-porosity counterparts.

Appendix B Dual-Poroelastic Rectangular Strip's Solutions

The boundary conditions for fluid pressures at the two edges $x_D = 1$ and vertical loading at the top $z_D = 2$ are

Load Controlled.

$$\widetilde{p}^{\mathrm{I}}\Big|_{x_D=1} = \widetilde{P}_c f^{\mathrm{I}} + \widetilde{C}_1 g^{\mathrm{I}} + C_2^{\mathrm{I}} \cosh(\xi^{\mathrm{I}}) + C_2^{\mathrm{II}} \cosh(\xi^{\mathrm{II}}) = \widetilde{p}_o \,, \quad \text{(B.1)}$$

$$\widetilde{p}^{\mathrm{II}}\Big|_{x_D=1} = \widetilde{P}_c f^{\mathrm{II}} + \widetilde{C}_1 g^{\mathrm{II}} + m^{\mathrm{I}} C_2^{\mathrm{I}} \cosh(\xi^{\mathrm{I}}) + m^{\mathrm{II}} C_2^{\mathrm{II}} \cosh(\xi^{\mathrm{II}}) = \widetilde{p}_o \,, \quad \text{(B.2)}$$

$$\int_{-1}^{1} \widetilde{\sigma}_{zz} dx_D = 2\left[A_0 \widetilde{P}_c + A_1 \widetilde{C}_1 + A_2^{\mathrm{I}} C_2^{\mathrm{I}} \frac{\sinh(\xi^{\mathrm{I}})}{\xi^{\mathrm{I}}} + A_2^{\mathrm{II}} C_2^{\mathrm{II}} \frac{\sinh(\xi^{\mathrm{II}})}{\xi^{\mathrm{II}}} \right] = \frac{2\widetilde{F}}{a} \,, \quad \text{(B.3)}$$

Equations B1 to B3 are solved simultaneously for $\widetilde{C}_1$, C_2^{I} and C_2^{II} as

$$\begin{aligned} \widetilde{C}_1 = {} & \left\{ \begin{matrix} -A_2^{\mathrm{I}}(1-m^{\mathrm{II}})\xi^{\mathrm{II}} \sinh(\xi^{\mathrm{I}}) \cosh(\xi^{\mathrm{II}}) \\ +A_2^{\mathrm{II}}(1-m^{\mathrm{I}})\xi^{\mathrm{I}} \cosh(\xi^{\mathrm{I}}) \sinh(\xi^{\mathrm{II}}) \end{matrix} \right\} \frac{\widetilde{p}_o}{d_{strip}} \\ & + \left\{ \begin{matrix} A_2^{\mathrm{I}}(f^{\mathrm{II}} - f^{\mathrm{I}} m^{\mathrm{II}})\xi^{\mathrm{II}} \sinh(\xi^{\mathrm{I}}) \cosh(\xi^{\mathrm{II}}) \\ -A_2^{\mathrm{II}}(f^{\mathrm{II}} - f^{\mathrm{I}} m^{\mathrm{I}})\xi^{\mathrm{I}} \cosh(\xi^{\mathrm{I}}) \sinh(\xi^{\mathrm{II}}) \end{matrix} \right\} \frac{\widetilde{P}_c}{d_{strip}} \\ & + (m^{\mathrm{I}} - m^{\mathrm{II}})\xi^{\mathrm{I}}\xi^{\mathrm{II}} \cosh(\xi^{\mathrm{I}}) \cosh(\xi^{\mathrm{II}})(\widetilde{F}/a - A_0 \widetilde{P}_c)/d_{strip} \end{aligned} \,, \quad \text{(B.4)}$$

$$\begin{aligned} C_2^{\mathrm{I}} = {} & \left\{ \begin{matrix} A_1 (1-m^{\mathrm{II}})\xi^{\mathrm{I}}\xi^{\mathrm{II}} \cosh(\xi^{\mathrm{II}}) \\ -A_2^{\mathrm{II}}(g^{\mathrm{I}} - g^{\mathrm{II}})\xi^{\mathrm{I}} \sinh(\xi^{\mathrm{II}}) \end{matrix} \right\} \frac{\widetilde{p}_o}{d_{strip}} \\ & + \left\{ \begin{matrix} -A_1 (f^{\mathrm{II}} - f^{\mathrm{I}} m^{\mathrm{II}})\xi^{\mathrm{I}}\xi^{\mathrm{II}} \cosh(\xi^{\mathrm{II}}) \\ +A_2^{\mathrm{II}}(f^{\mathrm{II}} g^{\mathrm{I}} - f^{\mathrm{I}} g^{\mathrm{II}})\xi^{\mathrm{I}} \sinh(\xi^{\mathrm{II}}) \end{matrix} \right\} \frac{\widetilde{P}_c}{d_{strip}} \\ & - (g^{\mathrm{II}} - g^{\mathrm{I}} m^{\mathrm{II}})\xi^{\mathrm{I}}\xi^{\mathrm{II}} \cosh(\xi^{\mathrm{II}})(\widetilde{F}/a - A_0 \widetilde{P}_c)/d_{strip} \end{aligned} \,, \quad \text{(B.5)}$$

$$C_2^{\mathrm{II}} = \begin{Bmatrix} -A_1(1-m^{\mathrm{I}})\xi^{\mathrm{I}}\xi^{\mathrm{II}}\cosh(\xi^{\mathrm{I}}) \\ +A_2^{\mathrm{I}}(g^{\mathrm{I}}-g^{\mathrm{II}})\xi^{\mathrm{II}}\sinh(\xi^{\mathrm{I}}) \end{Bmatrix} \frac{\widetilde{p}_o}{d_{strip}} + \begin{Bmatrix} A_1(f^{\mathrm{II}}-f^{\mathrm{I}}m^{\mathrm{I}})\xi^{\mathrm{I}}\xi^{\mathrm{II}}\cosh(\xi^{\mathrm{I}}) \\ -A_2^{\mathrm{I}}(f^{\mathrm{II}}g^{\mathrm{I}}-f^{\mathrm{I}}g^{\mathrm{II}})\xi^{\mathrm{II}}\sinh(\xi^{\mathrm{I}}) \end{Bmatrix} \frac{\widetilde{P}_c}{d_{strip}} + (g^{\mathrm{II}}-g^{\mathrm{I}}m^{\mathrm{I}})\xi^{\mathrm{I}}\xi^{\mathrm{II}}\cosh(\xi^{\mathrm{I}})(\widetilde{F}/a - A_0\widetilde{P}_c)/d_{strip} \quad , \text{(B.6)}$$

$$d_{strip} = -A_2^{\mathrm{I}}(g^{\mathrm{II}}-g^{\mathrm{I}}m^{\mathrm{II}})\xi^{\mathrm{II}}\sinh(\xi^{\mathrm{I}})\cosh(\xi^{\mathrm{II}}) + A_2^{\mathrm{II}}(g^{\mathrm{II}}-g^{\mathrm{I}}m^{\mathrm{I}})\xi^{\mathrm{I}}\cosh(\xi^{\mathrm{I}})\sinh(\xi^{\mathrm{II}}) + A_1(m^{\mathrm{I}}-m^{\mathrm{II}})\xi^{\mathrm{I}}\xi^{\mathrm{II}}\cosh(\xi^{\mathrm{I}})\cosh(\xi^{\mathrm{II}}) \quad , \text{(B.7)}$$

Displacement Control

Instead of Eq. B3, the vertical strain at the top of the strip ($z_D = 2$) is imposed as

$$\widetilde{\varepsilon}_{zz} = \frac{\overline{M}_{11}\widetilde{C}_1 - \overline{M}_{13}\widetilde{P}_c}{\overline{M}_{11}\overline{M}_{33} - \overline{M}_{13}^2} = \widetilde{\varepsilon}_{zz}^* = \frac{\widetilde{u}_z^*}{2b} \quad , \text{(B.8)}$$

Solving Eqs. B1, B2, and B8 for $\widetilde{C}_1$, C_2^{I}, and C_2^{II} as

$$\widetilde{C}_1 = \frac{\overline{M}_{11}\overline{M}_{33} - \overline{M}_{13}^2}{\overline{M}_{11}}\widetilde{\varepsilon}_{zz}^* + \frac{\overline{M}_{13}}{\overline{M}_{11}}\widetilde{P}_c \quad , \text{(B.9)}$$

$$C_2^{\mathrm{I}} = \frac{(1-m^{\mathrm{II}})\widetilde{p}_o - (f^{\mathrm{II}}-f^{\mathrm{I}}m^{\mathrm{II}})\widetilde{C}_1}{(m^{\mathrm{I}}-m^{\mathrm{II}})\cosh(\xi^{\mathrm{I}})} \quad , \text{(B.10)}$$

$$C_2^{\mathrm{II}} = -\frac{(1-m^{\mathrm{I}})\widetilde{p}_o - (f^{\mathrm{II}}-f^{\mathrm{I}}m^{\mathrm{I}})\widetilde{C}_1}{(m^{\mathrm{I}}-m^{\mathrm{II}})\cosh(\xi^{\mathrm{II}})} \quad , \text{(B.11)}$$

Appendix C Dual-Poroelastic Solid Cylinder's Solutions

First, it is convenient to show the derivations for stress and strain/displacement

components. The stress equilibrium in polar coordinate is

$$\frac{\partial \sigma_{rr}}{\partial r_D} + \frac{\sigma_{rr} - \sigma_{\theta\theta}}{r_D} = 0$$

Combining the above with Eq. 2.92 yields

$$\sigma_{rr} = \frac{1}{r_D^2}\int_0^{r_D} (\bar{\gamma}^{\mathrm{I}} p^{\mathrm{I}} + \bar{\gamma}^{\mathrm{II}} p^{\mathrm{II}}) r dr + \frac{C_1}{2}, \quad \text{(C.1)}$$

$$\sigma_{\theta\theta} = \bar{\gamma}^{\mathrm{I}} p^{\mathrm{I}} + \bar{\gamma}^{\mathrm{II}} p^{\mathrm{II}} - \frac{1}{r_D^2}\int_0^{r_D} (\bar{\gamma}^{\mathrm{I}} p^{\mathrm{I}} + \bar{\gamma}^{\mathrm{II}} p^{\mathrm{II}}) r dr + \frac{C_1}{2}, \quad \text{(C.2)}$$

Summation of the in-plane strain components is expressed in terms of stresses as

$$\varepsilon_{rr} + \varepsilon_{\theta\theta} = \frac{\sigma_{rr} + \sigma_{\theta\theta} - 2(\overline{\alpha}_1^{\mathrm{I}} p^{\mathrm{I}} + \overline{\alpha}_1^{\mathrm{II}} p^{\mathrm{II}}) - 2\overline{M}_{13}\varepsilon_{zz}}{\overline{M}_{11} + \overline{M}_{12}}, \quad \text{(C.3)}$$

Substituting Eqs. C1 to C3 into the constitutive equation gives the axial stress as

$$\begin{aligned}\sigma_{zz} = &\left(\overline{\alpha}_3^{\mathrm{I}} - \overline{\alpha}_1^{\mathrm{I}} \frac{\overline{M}_{13}}{\overline{M}_{11}}\right) p^{\mathrm{I}} + \left(\overline{\alpha}_3^{\mathrm{II}} - \overline{\alpha}_1^{\mathrm{II}} \frac{\overline{M}_{13}}{\overline{M}_{11}}\right) f^{\mathrm{I}} p^{\mathrm{II}} \\ &+ \left(1 - \frac{2\overline{M}_{13}^2}{\overline{M}_{33}(\overline{M}_{11} + \overline{M}_{12})}\right) S_{zz} + \frac{\overline{M}_{13} C_1}{\overline{M}_{11} + \overline{M}_{12}}\end{aligned}, \quad \text{(C.4)}$$

The radial displacement is obtained by integration noting that $\varepsilon_{rr} + \varepsilon_{\theta\theta} = (1/r)\partial(r u_r)/\partial r$

$$\frac{u_r}{R} = -\frac{1}{r_D}\int_0^{r_D} \frac{(\overline{\alpha}_1^{\mathrm{I}} p^{\mathrm{I}} + \overline{\alpha}_1^{\mathrm{II}} p^{\mathrm{II}})}{\overline{M}_{11}} r dr + \frac{1}{\overline{M}_{11} + \overline{M}_{12}}\left(C_1 - \frac{2\overline{M}_{13}}{\overline{M}_{33}} S_{zz}\right)\frac{r_D}{2}, \quad \text{(C.5)}$$

And the strain components are

$$\begin{aligned}\varepsilon_{rr} = &-\frac{1}{r_D^2}\int_0^{r_D} \frac{(\overline{\alpha}_1^{\mathrm{I}} p^{\mathrm{I}} + \overline{\alpha}_1^{\mathrm{II}} p^{\mathrm{II}})}{\overline{M}_{11}} r dr - \frac{(\overline{\alpha}_1^{\mathrm{I}} p^{\mathrm{I}} + \overline{\alpha}_1^{\mathrm{II}} p^{\mathrm{II}})}{\overline{M}_{11}} \\ &+ \frac{1}{\overline{M}_{11} + \overline{M}_{12}}\left(C_1 - \frac{2\overline{M}_{13}}{\overline{M}_{33}} S_{zz}\right)/2\end{aligned}, \quad \text{(C.6)}$$

$$\varepsilon_{\theta\theta} = -\frac{1}{r_D^2}\int_0^{r_D} \frac{(\overline{\alpha}_1^{\mathrm{I}} p^{\mathrm{I}} + \overline{\alpha}_1^{\mathrm{II}} p^{\mathrm{II}})}{\overline{M}_{11}} r dr + \frac{1}{\overline{M}_{11} + \overline{M}_{12}}\left(C_1 - \frac{2\overline{M}_{13}}{\overline{M}_{33}} S_{zz}\right)/2 , \quad \text{(C.7)}$$

Substitution of the pressure expressions (Eqs. 2.95 and 2.96) leads to the explicit general solutions of stress and displacements (Eqs. 2.97 to 2.102). The applicable boundary conditions for this geometry are the fluid pressure and confining stress boundary conditions at the cylinder's outer surface $r_D = 1$, and the axial loading condition at the top $z_D = 2$.

Load Controlled.

$$\widetilde{p}^{\mathrm{I}}\big|_{r_D=1} = \widetilde{S}_{zz} f^{\mathrm{I}} + \widetilde{C}_1 g^{\mathrm{I}} + C_2^{\mathrm{I}} \mathrm{I}_0(\xi^{\mathrm{I}}) + C_2^{\mathrm{II}} \mathrm{I}_0(\xi^{\mathrm{II}}) = \widetilde{p}_o , \quad \text{(C.8)}$$

$$\widetilde{p}^{\mathrm{II}}\big|_{r_D=1} = \widetilde{S}_{zz} f^{\mathrm{II}} + \widetilde{C}_1 g^{\mathrm{II}} + m^{\mathrm{I}} C_2^{\mathrm{I}} \mathrm{I}_0(\xi^{\mathrm{I}}) + m^{\mathrm{II}} C_2^{\mathrm{II}} \mathrm{I}_0(\xi^{\mathrm{II}}) = \widetilde{p}_o , \quad \text{(C.9)}$$

$$\widetilde{\sigma}_{rr}\big|_{r_D=1} = A_0 \widetilde{S}_{zz} + A_1 \widetilde{C}_1 + A_2^{\mathrm{I}} C_2^{\mathrm{I}} \frac{\mathrm{I}_1(\xi^{\mathrm{I}})}{\xi^{\mathrm{I}}} + A_2^{\mathrm{II}} C_2^{\mathrm{II}} \frac{\mathrm{I}_1(\xi^{\mathrm{I}})}{\xi^{\mathrm{I}}} = \widetilde{P}_c , \quad \text{(C.10)}$$

$$\int_0^1 \widetilde{\sigma}_{zz} r_D dr_D = \frac{B_0 \widetilde{S}_{zz} + B_1 \widetilde{C}_1}{2} + B_2^{\mathrm{I}} C_2^{\mathrm{I}} \frac{\mathrm{I}_1(\xi^{\mathrm{I}})}{\xi^{\mathrm{I}}} + B_2^{\mathrm{II}} C_2^{\mathrm{II}} \frac{\mathrm{I}_1(\xi^{\mathrm{II}})}{\xi^{\mathrm{II}}} = \frac{\widetilde{F}}{2\pi R^2} , \quad \text{(C.11)}$$

Equations C8 to C11 are solved simultaneously for $\widetilde{C}_1$, C_2^{I}, C_2^{II}, and $\widetilde{S}_{zz}$ as

$$\begin{aligned}
\widetilde{C}_1 = &-\begin{bmatrix} 2(f^{\mathrm{II}} - f^{\mathrm{I}} m^{\mathrm{II}})(A_2^{\mathrm{I}} \widetilde{F}/(2\pi R^2) - B_2^{\mathrm{I}} \widetilde{P}_c) \\ + (2A_0 B_2^{\mathrm{I}} - A_2^{\mathrm{I}} B_0)(1 - m^{\mathrm{II}})\,\widetilde{p}_o \end{bmatrix} \frac{\xi^{\mathrm{II}}\,\mathrm{I}_0(\xi^{\mathrm{II}})\,\mathrm{I}_1(\xi^{\mathrm{I}})}{d_{cylinder}} \\
&+ \begin{bmatrix} 2(f^{\mathrm{II}} - f^{\mathrm{I}} m^{\mathrm{I}})(A_2^{\mathrm{II}} \widetilde{F}/(2\pi R^2) - B_2^{\mathrm{II}} \widetilde{P}_c) \\ + (2A_0 B_2^{\mathrm{II}} - A_2^{\mathrm{II}} B_0)(1 - m^{\mathrm{I}}) \end{bmatrix} \frac{\xi^{\mathrm{I}}\,\mathrm{I}_0(\xi^{\mathrm{I}})\,\mathrm{I}_1(\xi^{\mathrm{II}})}{d_{cylinder}} \\
&- 2(A_2^{\mathrm{I}} B_2^{\mathrm{II}} - A_2^{\mathrm{II}} B_2^{\mathrm{I}})(f^{\mathrm{I}} - f^{\mathrm{II}})\,\mathrm{I}_1(\xi^{\mathrm{I}})\,\mathrm{I}_1(\xi^{\mathrm{II}})\,\widetilde{p}_o / d_{cylinder} \\
&+ (m^{\mathrm{I}} - m^{\mathrm{II}})\xi^{\mathrm{I}}\,\xi^{\mathrm{II}}\,\mathrm{I}_0(\xi^{\mathrm{I}})\,\mathrm{I}_0(\xi^{\mathrm{II}})[2A_0 \widetilde{F}/(2\pi R^2) - B_0 \widetilde{P}_c]/d_{cylinder}
\end{aligned} , \quad \text{(C.12)}$$

$$C_2^{\mathrm{I}} = \begin{bmatrix} (f^{\mathrm{II}} - f^{\mathrm{I}} m^{\mathrm{II}})(2A_1 \widetilde{F}/(2\pi R^2) - B_1 \widetilde{P}_c) \\ -(g^{\mathrm{II}} - g^{\mathrm{I}} m^{\mathrm{II}})(2A_0 \widetilde{F}/(2\pi R^2) - B_0 \widetilde{P}_c) \\ +(A_0 B_1 - A_1 B_0)(1 - m^{\mathrm{II}})\widetilde{p}_o \end{bmatrix} \frac{\xi^{\mathrm{I}} \xi^{\mathrm{II}} \mathrm{I}_0(\xi^{\mathrm{II}})}{d_{cylinder}}$$
$$- \begin{bmatrix} 2(f^{\mathrm{II}} g^{\mathrm{I}} - f^{\mathrm{I}} g^{\mathrm{II}})(2A_2^{\mathrm{II}} \widetilde{F}/(2\pi R^2) - B_2^{\mathrm{II}} \widetilde{P}_c) \\ -(f^{\mathrm{I}} - f^{\mathrm{II}})(2A_1 B_2^{\mathrm{II}} - A_2^{\mathrm{II}} B_1)\widetilde{p}_o \\ +(g^{\mathrm{I}} - g^{\mathrm{II}})(2A_0 B_2^{\mathrm{II}} - A_2^{\mathrm{II}} B_0)\widetilde{p}_o \end{bmatrix} \frac{\xi^{\mathrm{I}} \mathrm{I}_1(\xi^{\mathrm{II}})}{d_{cylinder}} \quad \text{,.....(C.13)}$$

$$C_2^{\mathrm{II}} = -\begin{bmatrix} (f^{\mathrm{II}} - f^{\mathrm{I}} m^{\mathrm{I}})(2A_1 \widetilde{F}/(2\pi R^2) - B_1 \widetilde{P}_c) \\ -(g^{\mathrm{II}} - g^{\mathrm{I}} m^{\mathrm{I}})(2A_0 \widetilde{F}/(2\pi R^2) - B_0 \widetilde{P}_c) \\ +(A_0 B_1 - A_1 B_0)(1 - m^{\mathrm{I}})\widetilde{p}_o \end{bmatrix} \frac{\xi^{\mathrm{I}} \xi^{\mathrm{II}} \mathrm{I}_0(\xi^{\mathrm{I}})}{d_{cylinder}}$$
$$+ \begin{bmatrix} 2(f^{\mathrm{II}} g^{\mathrm{I}} - f^{\mathrm{I}} g^{\mathrm{II}})(2A_2^{\mathrm{I}} \widetilde{F}/(2\pi R^2) - B_2^{\mathrm{I}} \widetilde{P}_c) \\ -(f^{\mathrm{I}} - f^{\mathrm{II}})(2A_1 B_2^{\mathrm{I}} - A_2^{\mathrm{I}} B_1)\widetilde{p}_o \\ +(g^{\mathrm{I}} - g^{\mathrm{II}})(2A_0 B_2^{\mathrm{I}} - A_2^{\mathrm{I}} B_0)\widetilde{p}_o \end{bmatrix} \frac{\xi^{\mathrm{II}} \mathrm{I}_1(\xi^{\mathrm{I}})}{d_{cylinder}} \quad \text{,.....(C.14)}$$

$$d_{cylinder} = \begin{bmatrix} (f^{\mathrm{II}} - f^{\mathrm{I}} m^{\mathrm{II}})(2A_1 B_2^{\mathrm{I}} - A_2^{\mathrm{I}} B_1) \\ -(g^{\mathrm{II}} - g^{\mathrm{I}} m^{\mathrm{II}})(2A_0 B_2^{\mathrm{I}} - A_2^{\mathrm{I}} B_0) \end{bmatrix} \xi^{\mathrm{II}} \mathrm{I}_0(\xi^{\mathrm{II}}) \mathrm{I}_1(\xi^{\mathrm{I}})$$
$$- \begin{bmatrix} (f^{\mathrm{II}} - f^{\mathrm{I}} m^{\mathrm{I}})(2A_1 B_2^{\mathrm{II}} - A_2^{\mathrm{II}} B_1) \\ -(g^{\mathrm{II}} - g^{\mathrm{I}} m^{\mathrm{I}})(2A_0 B_2^{\mathrm{II}} - A_2^{\mathrm{II}} B_0) \end{bmatrix} \xi^{\mathrm{I}} \mathrm{I}_0(\xi^{\mathrm{I}}) \mathrm{I}_1(\xi^{\mathrm{II}}), \quad \text{.....(C.15)}$$
$$+ (A_0 B_1 - A_1 B_0)(m^{\mathrm{I}} - m^{\mathrm{II}}) \xi^{\mathrm{I}} \xi^{\mathrm{II}} \mathrm{I}_0(\xi^{\mathrm{I}}) \mathrm{I}_0(\xi^{\mathrm{II}})$$
$$- 2(f^{\mathrm{II}} g^{\mathrm{I}} - f^{\mathrm{I}} g^{\mathrm{II}})(2A_2^{\mathrm{II}} B_2^{\mathrm{I}} - A_2^{\mathrm{I}} B_2^{\mathrm{II}}) \mathrm{I}_1(\xi^{\mathrm{I}}) \mathrm{I}_1(\xi^{\mathrm{II}})$$

$$A_0 \widetilde{S}_{zz} = \widetilde{P}_c - A_1 \widetilde{C}_1 - A_2^{\mathrm{I}} C_2^{\mathrm{I}} \frac{\mathrm{I}_1(\xi^{\mathrm{I}})}{\xi^{\mathrm{I}}} - A_2^{\mathrm{II}} C_2^{\mathrm{II}} \frac{\mathrm{I}_1(\xi^{\mathrm{I}})}{\xi^{\mathrm{I}}}, \quad \text{.....(C.16)}$$

Displacement Controlled

Instead of Eq. C11, the vertical displacement or strain at the top of the cylinder ($z_D = 2$) is imposed as $\widetilde{S}_{zz} = \overline{M}_{33} \widetilde{\varepsilon}_{zz} = u_z^* / 2h$. Solving Eqs. C8 to C10 for $\widetilde{C}_0$, C_1^{I}, and C_1^{II} as

$$\widetilde{C}_1 = \left[A_2^{\mathrm{I}}(f^{\mathrm{II}} - f^{\mathrm{I}}m^{\mathrm{II}})\widetilde{S}_{zz} - A_2^{\mathrm{I}}(1-m^{\mathrm{II}})\widetilde{p}_o\right]\frac{\xi^{\mathrm{II}}\,\mathrm{I}_0(\xi^{\mathrm{II}})\mathrm{I}_1(\xi^{\mathrm{I}})}{d_{cylinder}}$$
$$+\left[-A_2^{\mathrm{II}}(f^{\mathrm{II}} - f^{\mathrm{I}}m^{\mathrm{I}})\widetilde{S}_{zz} + A_2^{\mathrm{II}}(1-m^{\mathrm{I}})\widetilde{p}_o\right]\frac{\xi^{\mathrm{I}}\,\mathrm{I}_0(\xi^{\mathrm{I}})\mathrm{I}_1(\xi^{\mathrm{II}})}{d_{cylinder}}, \quad \text{(C.17)}$$
$$-(m^{\mathrm{I}} - m^{\mathrm{II}})(A_0\widetilde{S}_{zz} - \widetilde{P}_c)\frac{\xi^{\mathrm{I}}\xi^{\mathrm{II}}\,\mathrm{I}_0(\xi^{\mathrm{I}})\mathrm{I}_0(\xi^{\mathrm{II}})}{d_{cylinder}}$$

$$C_2^{\mathrm{I}} = \begin{bmatrix} -A_1(f^{\mathrm{II}} - f^{\mathrm{I}}m^{\mathrm{II}})\widetilde{S}_{zz} + A_1(1-m^{\mathrm{II}})\widetilde{p}_o \\ +(g^{\mathrm{II}} - g^{\mathrm{I}}m^{\mathrm{II}})(A_0\widetilde{S}_{zz} - \widetilde{P}_c) \end{bmatrix}\frac{\xi^{\mathrm{I}}\,\xi^{\mathrm{II}}\,\mathrm{I}_0(\xi^{\mathrm{II}})}{d_{cylinder}}$$
$$+A_2^{\mathrm{II}}\left[(f^{\mathrm{II}}g^{\mathrm{I}} - f^{\mathrm{I}}g^{\mathrm{II}})\widetilde{S}_{zz} - (g^{\mathrm{I}} - g^{\mathrm{II}})\widetilde{p}_o\right]\frac{\xi^{\mathrm{I}}\,\mathrm{I}_1(\xi^{\mathrm{II}})}{d_{cylinder}}, \quad \text{(C.18)}$$

$$C_2^{\mathrm{II}} = \begin{bmatrix} A_1(f^{\mathrm{II}} - f^{\mathrm{I}}m^{\mathrm{I}})\widetilde{S}_{zz} - A_1(1-m^{\mathrm{I}})\widetilde{p}_o \\ -(g^{\mathrm{II}} - g^{\mathrm{I}}m^{\mathrm{I}})(A_0\widetilde{S}_{zz} - \widetilde{P}_c) \end{bmatrix}\frac{\xi^{\mathrm{I}}\,\xi^{\mathrm{II}}\,\mathrm{I}_0(\xi^{\mathrm{I}})}{d_{cylinder}}$$
$$+A_2^{\mathrm{I}}\left[-(f^{\mathrm{II}}g^{\mathrm{I}} - f^{\mathrm{I}}g^{\mathrm{II}})\widetilde{S}_{zz} + (g^{\mathrm{I}} - g^{\mathrm{II}})\widetilde{p}_o\right]\frac{\xi^{\mathrm{II}}\,\mathrm{I}_1(\xi^{\mathrm{I}})}{d_{cylinder}}, \quad \text{(C.19)}$$

$$d_{cylinder} = -A_2^{\mathrm{I}}(g^{\mathrm{II}} - g^{\mathrm{I}}m^{\mathrm{II}})\xi^{\mathrm{II}}\,\mathrm{I}_0(\xi^{\mathrm{II}})\mathrm{I}_1(\xi^{\mathrm{I}})$$
$$+A_2^{\mathrm{II}}(g^{\mathrm{II}} - g^{\mathrm{I}}m^{\mathrm{I}})\xi^{\mathrm{I}}\,\mathrm{I}_0(\xi^{\mathrm{I}})\mathrm{I}_1(\xi^{\mathrm{II}}) \quad \text{(C.20)}$$
$$+A_1(m^{\mathrm{I}} - m^{\mathrm{II}})\xi^{\mathrm{I}}\,\xi^{\mathrm{II}}\,\mathrm{I}_0(\xi^{\mathrm{I}})\mathrm{I}_0(\xi^{\mathrm{II}})$$

Appendix D Dual-Poroelastic Inclined Wellbore Solutions

The complete dual-poroelastic inclined wellbore solution for naturally fractured formations is given by Eqs. 2.63a to 2.63h. The boundary conditions and associated expressions for contributing axisymmetric loading case ($p^{\mathrm{I}(1)}$, $p^{\mathrm{II}(1)}$, $\sigma_{rr}^{(1)}$, $\sigma_{\theta\theta}^{(1)}$) and deviatoric loading case ($p^{\mathrm{I}(2)}$, $p^{\mathrm{II}(2)}$, $\sigma_{rr}^{(2)}$, $\sigma_{\theta\theta}^{(2)}$, $\sigma_{r\theta}^{(2)}$) are given in the following section.

D.1 Pressure Boundary Condition (Permeable)

Assuming full hydraulic communication across the borehole wall, the corresponding boundary conditions and solutions are

Case 1 – Axisymmetric Loading

The perturbed boundary condition at the borehole wall ($r_D = 1$) are

$$\sigma_{rr}^{(1)} = -\sigma_m + p_w(t_D); \quad \sigma_{r\theta}^{(1)} = 0, \qquad \text{(D1.1)}$$

$$p^{\mathrm{I}(1)} = p^{\mathrm{II}(1)} = p_w(t_D) - p_0, \qquad \text{(D1.2)}$$

This is an axisymmetric ($n = 0$) radial stress and hydraulic loading problem. The stress has contribution from the mud pressure, p_w, and the hydrostatic part of the released in-situ stress, σ_m. Meanwhile, the fluid flow is due to pressure gradient between the wellbore mud and the formation fluid. Bounded solution at far field requires that $\widetilde{C}_1$ vanishes. The solution is transient and given in Laplace transform domain which could be inverted to the

time domain using the Stehfest's algorithm (Stehfest 1970)

$$\widetilde{p}^{\,\mathrm{I}(1)} = \Delta^{\mathrm{I}}\Phi(\xi^{\mathrm{I}} r_D) + \Delta^{\mathrm{II}}\Phi(\xi^{\mathrm{II}} r_D)\,, \quad \text{(D1.3)}$$

$$\widetilde{p}^{\,\mathrm{II}(1)} = m^{\mathrm{I}}\Delta^{\mathrm{I}}\Phi(\xi^{\mathrm{I}} r_D) + m^{\mathrm{II}}\Delta^{\mathrm{II}}\Phi(\xi^{\mathrm{II}} r_D)\,, \quad \text{(D1.4)}$$

$$\widetilde{\sigma}_{rr}^{(1)} = -A_2^{\mathrm{I}}\Delta^{\mathrm{I}}\Pi(\xi^{\mathrm{I}} r_D) - A_2^{\mathrm{II}}\Delta^{\mathrm{II}}\Pi(\xi^{\mathrm{II}} r_D) + \Delta\widetilde{\sigma}/r_D^2\,, \quad \text{(D1.5)}$$

$$\widetilde{\sigma}_{\theta\theta}^{(1)} = A_2^{\mathrm{I}}\Delta^{\mathrm{I}}[\Pi(\xi^{\mathrm{I}} r_D) + \Phi(\xi^{\mathrm{I}} r_D)] + A_2^{\mathrm{II}}\Delta^{\mathrm{II}}[\Pi(\xi^{\mathrm{II}} r_D) + \Phi(\xi^{\mathrm{II}} r_D)] - \Delta\widetilde{\sigma}/r_D^2\,, \quad \text{(D1.6)}$$

in which

$$\Delta^{\mathrm{I}} = \frac{1-m^{\mathrm{II}}}{m}\Delta\widetilde{p}; \quad \Delta^{\mathrm{II}} = -\frac{1-m^{\mathrm{I}}}{m}\Delta\widetilde{p}; \quad m = m^{\mathrm{I}} - m^{\mathrm{II}}\,, \quad \text{(D1.7)}$$

$$\Delta\widetilde{p} = (\widetilde{p}_w - p_0/s); \quad \Delta\widetilde{\sigma} = (\widetilde{p}_w - \sigma_m/s)\,, \quad \text{(D1.8)}$$

$$\Phi(x\,r_D) = \frac{\mathrm{K}_0(x\,r_D)}{\mathrm{K}_0(x)}; \quad \Pi(x\,r_D) = \frac{\mathrm{K}_1(x\,r_D)}{x\,r_D\,\mathrm{K}_0(x)} - \frac{\mathrm{K}_1(x)}{x\,r_D^2\,\mathrm{K}_0(x)}\,, \quad \text{(D1.9)}$$

where the superscript $^{(1)}$ denotes the loading case and only non-zero solutions are listed.

Case 2 – Deviatoric Loading

The perturbed boundary condition at the borehole wall ($r_D = 1$) are

$$\sigma_{rr}^{(2)} = -\sigma_d \cos(2(\theta-\theta_r)); \qquad \sigma_{r\theta}^{(2)} = \sigma_d \sin(2(\theta-\theta_r))\,, \quad \text{(D1.10)}$$

$$p^{\mathrm{I}(2)} = p^{\mathrm{II}(2)} = 0\,, \quad \text{(D1.11)}$$

This is an asymmetric (n = 2) stress loading problem accounting for the release of the deviatoric part of the in-plane in-situ stresses, σ_d. The solutions in Laplace transform domain are

$$s\,\widetilde{p}^{\,\mathrm{I}(2)} = \sigma_d[\,C_2^{\mathrm{I}}\mathrm{K}_2(\xi^{\mathrm{I}} r_D) + C_2^{\mathrm{II}}\mathrm{K}_2(\xi^{\mathrm{II}} r_D) + g^{\mathrm{I}}\widetilde{C}_1 r_D^{-2}]\cos(2(\theta-\theta_r))\,, \quad \text{(D1.12)}$$

$$s\,\tilde{p}^{\mathrm{II}(2)} = \sigma_d[\,C_2^{\mathrm{I}} m^{\mathrm{I}} \mathrm{K}_2(\xi^{\mathrm{I}} r_D) + C_2^{\mathrm{II}} m^{\mathrm{II}} \mathrm{K}_2(\xi^{\mathrm{II}} r_D) + g^{\mathrm{II}} \widetilde{C}_1 r_D^{-2}]\cos(2(\theta-\theta_r))\,, \quad \text{(D1.13)}$$

$$\begin{aligned} s\,\tilde{\sigma}_{rr}^{(2)} = -\sigma_d[&A_2^{\mathrm{I}} C_2^{\mathrm{I}} \Theta(\xi^{\mathrm{I}} r_D) + A_2^{\mathrm{II}} C_2^{\mathrm{II}} \Theta(\xi^{\mathrm{II}} r_D) \\ &- 2A_1 \widetilde{C}_1 r_D^{-2} - C_0 r_D^{-4}]\cos(2(\theta-\theta_r)) \end{aligned}, \quad \text{(D1.14)}$$

$$s\,\tilde{\sigma}_{\theta\theta}^{(2)} = \sigma_d[A_2^{\mathrm{I}} C_2^{\mathrm{I}} \Omega(\xi^{\mathrm{I}} r_D) + A_2^{\mathrm{II}} C_2^{\mathrm{II}} \Omega(\xi^{\mathrm{II}} r_D) - C_0 r_D^{-4}]\cos(2(\theta-\theta_r))\,, \quad \text{(D1.15)}$$

$$\begin{aligned} s\,\tilde{\sigma}_{r\theta}^{(2)} = -\sigma_d[&A_2^{\mathrm{I}} C_2^{\mathrm{I}} \Xi(\xi^{\mathrm{I}} r_D) + A_2^{\mathrm{II}} C_2^{\mathrm{II}} \Xi(\xi^{\mathrm{II}} r_D) \\ &- A_1 \widetilde{C}_1 r_D^{-2} - C_0 r_D^{-4}]\sin(2(\theta-\theta_r)) \end{aligned}, \quad \text{(D1.16)}$$

where the coefficients C_0, $\widetilde{C}_1$, C_2^{I}, and C_2^{II} are given as

$$\widetilde{C}_1 = -2mD_2^{\mathrm{I}} D_2^{\mathrm{II}} / D_3\,, \quad \text{(D1.17)}$$

$$C_2^{\mathrm{I}} = 2(g^{\mathrm{II}} - g^{\mathrm{I}} m^{\mathrm{II}})\xi^{\mathrm{I}} D_2^{\mathrm{II}} / D_3\,, \quad \text{(D1.18)}$$

$$C_2^{\mathrm{II}} = -2(g^{\mathrm{II}} - g^{\mathrm{I}} m^{\mathrm{I}})\xi^{\mathrm{II}} D_2^{\mathrm{I}} / D_3\,, \quad \text{(D1.19)}$$

$$\begin{aligned} C_0 = \frac{3}{D_3}\Bigg[&A_1 m D_2^{\mathrm{I}} D_2^{\mathrm{II}} + A_2^{\mathrm{I}}(g^{\mathrm{II}} - g^{\mathrm{I}} m^{\mathrm{II}}) D_2^{\mathrm{II}}\left(D_1^{\mathrm{I}} + \frac{4D_2^{\mathrm{I}}}{(\xi^{\mathrm{I}})^2}\right) \\ &- A_2^{\mathrm{II}}(g^{\mathrm{II}} - g^{\mathrm{I}} m^{\mathrm{I}}) D_2^{\mathrm{I}}\left(D_1^{\mathrm{II}} + \frac{4D_2^{\mathrm{II}}}{(\xi^{\mathrm{II}})^2}\right)\Bigg] \end{aligned}, \quad \text{(D1.20)}$$

in which $m = m^{\mathrm{I}} - m^{\mathrm{II}}$ and

$$D_1^{\mathrm{I}} = \mathrm{K}_1(\xi^{\mathrm{I}}); \quad D_1^{\mathrm{II}} = \mathrm{K}_1(\xi^{\mathrm{II}}); \quad D_2^{\mathrm{I}} = \xi^{\mathrm{I}} \mathrm{K}_2(\xi^{\mathrm{I}}); \quad D_2^{\mathrm{II}} = \xi^{\mathrm{II}} \mathrm{K}_2(\xi^{\mathrm{II}})\,, \quad \text{(D1.21)}$$

$$D_3 = A_1 m D_2^{\mathrm{I}} D_2^{\mathrm{II}} - A_2^{\mathrm{I}}(g^{\mathrm{II}} - g^{\mathrm{I}} m^{\mathrm{II}}) D_1^{\mathrm{I}} D_2^{\mathrm{II}} + A_2^{\mathrm{II}}(g^{\mathrm{II}} - g^{\mathrm{I}} m^{\mathrm{I}}) D_2^{\mathrm{I}} D_1^{\mathrm{II}}\,, \quad \text{(D1.22)}$$

And Θ, Ω, and Ξ are functions defined as

$$\Theta(xr_D) = \frac{\mathrm{K}_1(xr_D)}{xr_D} + \frac{6\mathrm{K}_2(xr_D)}{(xr_D)^2}\,, \quad \text{(D1.23)}$$

$$\Omega(xr_D) = \Theta(xr_D) + \mathrm{K}_2(xr_D)\,, \quad \text{(D1.24)}$$

$$\Xi(xr_D) = \frac{\mathrm{K}_1(xr_D)}{x\,r_D} + \frac{3\mathrm{K}_2(xr_D)}{(xr_D)^2}, \quad \text{(D1.25)}$$

D.2 Flux Boundary Condition

Assuming a flux boundary condition at the borehole wall which simulates fluid injection or withdrawal, the boundary conditions and solutions for the two contributing loading cases are given as

Case 1 – Axisymmetric Loading

The perturbed boundary condition at the borehole wall ($r_D = 1$) are

$$\sigma_{rr}^{(1)} = p_w(q_w(t_D)) - \sigma_m; \quad \sigma_{r\theta}^{(1)} = 0, \quad \text{(D2.1)}$$

$$\int_0^{2\pi} \left(q_r^{\mathrm{I}(1)} + q_r^{\mathrm{II}(1)}\right) d\theta = -(1-\bar{\kappa}_D)\frac{\partial p^{\mathrm{I}(1)}}{\partial r_D} - \bar{\kappa}_D \frac{\partial p^{\mathrm{II}(1)}}{\partial r_D} = q_w(t_D), \quad \text{(D2.2)}$$

$$p^{\mathrm{I}(1)} = p^{\mathrm{II}(1)} = p_w(q_w(t_D)), \quad \text{(D2.3)}$$

Again, this axisymmetric flux loading case requires n = 0 and $\widetilde{C}_1$ = 0 for bounded solutions at far field. The fluid discharge at the wellbore wall (r_D = 1) is $q_w(t_D)$ = $Q_w(t_D)/[2\pi(\bar{\kappa}_1^{\mathrm{I}} + \bar{\kappa}_1^{\mathrm{II}})]$ where $Q_w(t_D)$ is the flow rate (positive for injection) per unit formation thickness. As a result, the wellbore pressure is a function of the flow rate imposed across the borehole wall, i.e., $p_w(t_D) = p_w(q_w(t_D))$ as shown in Eq. 2.128a and 2.128c. Due to hydraulic communication at the borehole wall, continuity condition requires that the fluid pressure in the matrix and fractures are the same and equal to the wellbore fluid pressure (Eq. 2.128c). The corresponding solutions in Laplace transform domain are

given as

$$\widetilde{p}^{\mathrm{I}(1)} = \frac{\widetilde{q}_w}{m}[(1-m^{\mathrm{II}})\mathrm{K}_0(\xi^{\mathrm{II}})\mathrm{K}_0(\xi^{\mathrm{I}} r_D) - (1-m^{\mathrm{I}})\mathrm{K}_0(\xi^{\mathrm{I}})\mathrm{K}_0(\xi^{\mathrm{II}} r_D)], \quad \text{(D2.4)}$$

$$\widetilde{p}^{\mathrm{II}(1)} = \frac{\widetilde{q}_w}{m}[m^{\mathrm{I}}(1-m^{\mathrm{II}})\mathrm{K}_0(\xi^{\mathrm{II}})\mathrm{K}_0(\xi^{\mathrm{I}} r_D) - m^{\mathrm{II}}(1-m^{\mathrm{I}})\mathrm{K}_0(\xi^{\mathrm{I}})\mathrm{K}_0(\xi^{\mathrm{II}} r_D)], \quad \text{(D2.5)}$$

$$\widetilde{\sigma}_{rr}^{(1)} = -\frac{\widetilde{q}_w}{m}\begin{bmatrix} A_2^{\mathrm{I}}(1-m^{\mathrm{II}})\mathrm{K}_0(\xi^{\mathrm{II}})\,\Phi(\xi^{\mathrm{I}} r_D) \\ -A_2^{\mathrm{II}}(1-m^{\mathrm{I}})\mathrm{K}_0(\xi^{\mathrm{I}})\,\Phi(\xi^{\mathrm{II}} r_D) \end{bmatrix} + \frac{\Delta\widetilde{\sigma}}{r_D^2}, \quad \text{(D2.6)}$$

$$\widetilde{\sigma}_{\theta\theta}^{(1)} = \frac{\widetilde{q}_w}{m}\begin{Bmatrix} A_1^{\mathrm{I}}(1-m^{\mathrm{II}})\mathrm{K}_0(\xi^{\mathrm{II}})\,[\,\Phi(\xi^{\mathrm{I}} r_D) + \mathrm{K}_0(\xi^{\mathrm{I}} r_D)] \\ -A_1^{\mathrm{II}}(1-m^{\mathrm{I}})\mathrm{K}_0(\xi^{\mathrm{I}})[\,\Phi(\xi^{\mathrm{II}} r_D) + \mathrm{K}_0(\xi^{\mathrm{II}} r_D)] \end{Bmatrix} - \frac{\Delta\widetilde{\sigma}}{r_D^2}, \quad \text{(D2.7)}$$

where $\Delta\widetilde{\sigma} = \widetilde{p}_w - \sigma_m / s$ and

$$\begin{aligned} m = {} & (1-m^{\mathrm{II}})(1-\overline{\kappa}_D + \overline{\kappa}_D m^{\mathrm{I}})\,\xi^{\mathrm{I}}\mathrm{K}_1(\xi^{\mathrm{I}})\mathrm{K}_0(\xi^{\mathrm{II}}) \\ & -(1-m^{\mathrm{I}})(1-\overline{\kappa}_D + \overline{\kappa}_D m^{\mathrm{II}})\,\xi^{\mathrm{II}}\mathrm{K}_1(\xi^{\mathrm{II}})\mathrm{K}_0(\xi^{\mathrm{I}}) \end{aligned}, \quad \text{(D2.8)}$$

$$\widetilde{p}_w = \widetilde{p}^{\mathrm{I}}_{r_D=1} = \widetilde{p}^{\mathrm{II}}_{r_D=1} = \frac{\widetilde{q}_w}{m}(m^{\mathrm{I}} - m^{\mathrm{II}})\mathrm{K}_0(\xi^{\mathrm{I}})\mathrm{K}_0(\xi^{\mathrm{II}}), \quad \text{(D2.9)}$$

$$\Phi(x r_D) = \frac{\mathrm{K}_1(x r_D)}{x\, r_D} - \frac{\mathrm{K}_1(x)}{x\, r_D^2}, \quad \text{(D2.10)}$$

Case 2 – Deviatoric Loading

The perturbed boundary condition at the borehole wall ($r_D = 1$) are

$$\sigma_{rr}^{(2)} = -\sigma_d \cos(2(\theta - \theta_r)); \qquad \sigma_{r\theta}^{(2)} = \sigma_d \sin(2(\theta - \theta_r)), \quad \text{(D2.11)}$$

$$\int_0^{2\pi}\left(q_r^{\mathrm{I}(2)} + q_r^{\mathrm{II}(2)}\right)d\theta = \int_0^{2\pi}\left[-(1-\overline{\kappa}_D)\frac{\partial p^{\mathrm{I}(2)}}{\partial r_D} - \overline{\kappa}_D\frac{\partial p^{\mathrm{II}(2)}}{\partial r_D}\right]d\theta = 0, \quad \text{(D2.12)}$$

$$p^{\mathrm{I}(2)} = p^{\mathrm{II}(2)} = 0, \quad \text{(D2.13)}$$

It should be noted that the zero total flux boundary condition Eq. D2.12 is automatically satisfied regardless of the expressions for p^{I} and p^{II}. Because there is full hydraulic communication and fluid pressure at the wall is dictated by the total flowrate as calculated in the above axisymmetric loading, it is logical to set pore-pressure perturbation at the wellbore wall for the current deviatoric loading to be zero. The solutions and associated coefficients in Laplace transform domain are the same as Case 2 for pressure-boundary condition, i.e., Eqs. D1.12 to D1.25.

D.3 No-Flow Boundary Condition (Impermeable)

In the special case of impermeable borehole wall, there is no hydraulic communication between the wellbore and the formation. Hence, the dual pore pressures at the borehole wall are generally different from each other as well as are independent from the applied wellbore pressure: $p^{\mathrm{I}}_{r_D=1}(t_D) \neq p^{\mathrm{II}}_{r_D=1}(t_D) \neq p_w(t_D)$. The applied wellbore pressure in this case is simply the hydraulic head exerted by the fluid column in the borehole.

Case 1 – Axisymmetric Loading

The perturbed boundary condition at the borehole wall ($r_D = 1$) are

$$\sigma_{rr}^{(1)} = p_w(t_D) - \sigma_m; \quad \sigma_{r\theta}^{(1)} = 0, \qquad \text{(D3.1)}$$

$$q_r^{\mathrm{I}(1)} = q_r^{\mathrm{II}(1)} = 0, \qquad \text{(D3.2)}$$

Because no fluid flow is allowed, the solution for the perturbed dual pore pressure fields are trivial and identically zero: $p^{\mathrm{I}(1)} = p^{\mathrm{II}(1)} = 0$. The solution for stresses due to radial hydrostatic loading is purely elastic as given by the classical Lamé solution

$$\sigma_{rr}^{(1)} = [p_w(t_D) - \sigma_m]/r_D^2; \qquad \sigma_{\theta\theta}^{(1)} = -[p_w(t_D) - \sigma_m]/r_D^2, \quad \text{(D3.3)}$$

Case 2 – Deviatoric Loading

The perturbed boundary condition at the borehole wall ($r_D = 1$) are

$$\sigma_{rr}^{(2)} = -\sigma_d \cos(2(\theta - \theta_r)); \qquad \sigma_{r\theta}^{(2)} = \sigma_d \sin(2(\theta - \theta_r)), \quad \text{(D3.4)}$$

$$q_r^{\mathrm{I}(2)} = q_r^{\mathrm{II}(2)} = 0 \qquad \forall\theta \in [0, 2\pi], \quad \text{(D3.5)}$$

Note that in this case, the fluid pressures in the matrix and fracture network are not the same at the wellbore wall as in the cases of permeable or flux boundary conditions (Eq. D1. or D2.) because no hydraulic communication is allowed. The corresponding coefficients, C_0, $\widetilde{C}_1$, C_2^{I}, and C_2^{II} are

$$\widetilde{C}_1 = -2D_4/D_5; \qquad C_2^{\mathrm{I}} = 2\xi^{\mathrm{I}} D_3^{\mathrm{I}}/D_5; \qquad C_2^{\mathrm{II}} = -2\xi^{\mathrm{II}} D_3^{\mathrm{II}}/D_5, \quad \text{(D3.6)}$$

$$C_0 = \frac{3}{D_5}\left[A_1 D_4 + A_2^{\mathrm{I}} D_3^{\mathrm{I}}\left(D_1^{\mathrm{I}} + \frac{4D_2^{\mathrm{I}}}{(\xi^{\mathrm{I}})^2}\right) - A_2^{\mathrm{II}} D_3^{\mathrm{II}}\left(D_1^{\mathrm{II}} + \frac{4D_2^{\mathrm{II}}}{(\xi^{\mathrm{II}})^2}\right)\right], \quad \text{(D3.7)}$$

in which D_1^{I}, D_1^{II}, D_2^{I}, and D_2^{II} are given in Eqs. D1.21 and

$$D_3^{\mathrm{I}} = 2(g^{\mathrm{II}} - g^{\mathrm{I}} m^{\mathrm{II}})[(\xi^{\mathrm{II}})^2 D_1^{\mathrm{II}} + 2D_2^{\mathrm{II}}], \quad \text{(D3.8)}$$

$$D_3^{\mathrm{II}} = 2(g^{\mathrm{II}} - g^{\mathrm{I}} m^{\mathrm{I}})[(\xi^{\mathrm{I}})^2 D_1^{\mathrm{I}} + 2D_2^{\mathrm{I}}], \quad \text{(D3.9)}$$

$$D_4 = (m^{\mathrm{I}} - m^{\mathrm{II}})[(\xi^{\mathrm{I}})^2 D_1^{\mathrm{I}} + 2D_2^{\mathrm{I}}][(\xi^{\mathrm{II}})^2 D_1^{\mathrm{II}} + 2D_2^{\mathrm{II}}], \quad \text{(D3.10)}$$

$$D_5 = A_1 D_4 - A_2^{\mathrm{I}} D_1^{\mathrm{I}} D_3^{\mathrm{I}} + A_2^{\mathrm{II}} D_1^{\mathrm{II}} D_3^{\mathrm{II}}, \quad \text{(D3.11)}$$

D.4 Impermeable Matrix and Permeable Fracture Boundary Condition

In extremely low permeability formation, the intact rock matrix can be considered as impermeable to fluid flow, i.e., requiring the wellbore pressure to exceed certain capillary entry pressure, whereas there is full hydraulic communication between the wellbore fluid the fracture network in the formation. Mathematically, the boundary conditions and solutions simulating this case are

Case 1 – Axisymmetric Loading

The perturbed boundary condition at the borehole wall ($r_D = 1$) are

$$\sigma_{rr}^{(1)} = p_w(t_D) - \sigma_m; \quad \sigma_{r\theta}^{(1)} = 0, \qquad \text{(D4.1)}$$

$$q_r^{\mathrm{I}(1)} = 0; \qquad p^{\mathrm{II}(1)} = p_w(t_D) - p_0, \qquad \text{(D4.2)}$$

The solutions in Laplace transform domain are

$$\widetilde{p}^{\mathrm{I}(1)} = \frac{\Delta\widetilde{p}}{m}[\xi^{\mathrm{II}}\mathrm{K}_1(\xi^{\mathrm{II}})\mathrm{K}_0(\xi^{\mathrm{I}}r_D) - \xi^{\mathrm{I}}\mathrm{K}_1(\xi^{\mathrm{I}})\mathrm{K}_0(\xi^{\mathrm{II}}r_D)], \qquad \text{(D4.3)}$$

$$\widetilde{p}^{\mathrm{II}(1)} = \frac{\Delta\widetilde{p}}{m}[m^{\mathrm{I}}\xi^{\mathrm{II}}\mathrm{K}_1(\xi^{\mathrm{II}})\mathrm{K}_0(\xi^{\mathrm{I}}r_D) - m^{\mathrm{II}}\xi^{\mathrm{I}}\mathrm{K}_1(\xi^{\mathrm{I}})\mathrm{K}_0(\xi^{\mathrm{II}}r_D)], \qquad \text{(D4.4)}$$

$$\widetilde{\sigma}_{rr}^{(1)} = -\frac{\Delta\widetilde{p}}{m}\begin{bmatrix} A_2^{\mathrm{I}}\xi^{\mathrm{II}}\mathrm{K}_1(\xi^{\mathrm{II}})\,\Pi(\xi^{\mathrm{I}}r_D) \\ -A_2^{\mathrm{II}}\xi^{\mathrm{I}}\mathrm{K}_1(\xi^{\mathrm{I}})\,\Pi(\xi^{\mathrm{II}}r_D) \end{bmatrix} + \frac{\Delta\widetilde{\sigma}}{r_D^2}, \qquad \text{(D4.5)}$$

$$\widetilde{\sigma}_{\theta\theta}^{(1)} = \frac{\Delta\widetilde{p}}{m}\begin{Bmatrix} A_2^{\mathrm{I}}\xi^{\mathrm{II}}\mathrm{K}_1(\xi^{\mathrm{II}})\,[\Pi(\xi^{\mathrm{I}}r_D) + \mathrm{K}_0(\xi^{\mathrm{I}}r_D)] \\ -A_2^{\mathrm{II}}\xi^{\mathrm{I}}\mathrm{K}_1(\xi^{\mathrm{I}})\,[\Pi(\xi^{\mathrm{II}}r_D) + \mathrm{K}_0(\xi^{\mathrm{II}}r_D)] \end{Bmatrix} - \frac{\Delta\widetilde{\sigma}}{r_D^2}, \qquad \text{(D4.6)}$$

where $\Delta\widetilde{p}$ and $\Delta\widetilde{\sigma}$ are given in Eq. D1.8; the function Π is defined in Eq. D1.9 and

$$m = m^{\mathrm{I}}\xi^{\mathrm{II}}\mathrm{K}_0(\xi^{\mathrm{I}})\mathrm{K}_1(\xi^{\mathrm{II}}) - m^{\mathrm{II}}\xi^{\mathrm{I}}\mathrm{K}_0(\xi^{\mathrm{II}})\mathrm{K}_1(\xi^{\mathrm{I}}), \qquad \text{(D4.7)}$$

Case 2 – Deviatoric Loading

The perturbed boundary condition at the borehole wall ($r_D = 1$) are

$$\sigma_{rr}^{(2)} = -\sigma_d \cos(2(\theta - \theta_r)); \qquad \sigma_{r\theta}^{(2)} = \sigma_d \sin(2(\theta - \theta_r)) \,, \quad \text{(D4.8)}$$

$$q_r^{\mathrm{I}(2)} = p^{\mathrm{II}(2)} = 0 \qquad \forall \theta \in [0, 2\pi] \,, \quad \text{(D4.9)}$$

The coefficients C_0, $\widetilde{C}_1$, C_2^{I}, C_2^{II} are

$$\widetilde{C}_1 = -2D_4 / D_5; \qquad C_2^{\mathrm{I}} = 2\xi^{\mathrm{I}} D_3^{\mathrm{I}} / D_5; \qquad C_2^{\mathrm{I}} = -2\xi^{\mathrm{II}} D_3^{\mathrm{II}} / D_5 \,, \quad \text{(D4.10)}$$

$$C_0 = \frac{3}{D_5}\left[A_1 D_4 + A_2^{\mathrm{I}} D_3^{\mathrm{I}} \left(D_1^{\mathrm{I}} + \frac{4D_2^{\mathrm{I}}}{(\xi^{\mathrm{I}})^2} \right) - A_2^{\mathrm{II}} D_3^{\mathrm{II}} \left(D_1^{\mathrm{II}} + \frac{4D_2^{\mathrm{II}}}{(\xi^{\mathrm{II}})^2} \right) \right], \quad \text{(D4.11)}$$

in which D_1^{I}, D_1^{II}, D_2^{I}, and D_2^{II} were given in Eq. D1.12 and

$$D_3^{\mathrm{I}} = g^{\mathrm{II}} (\xi^{\mathrm{II}})^2 D_1^{\mathrm{II}} + 2(g^{\mathrm{II}} - g^{\mathrm{I}} m^{\mathrm{II}}) D_2^{\mathrm{II}} \,, \quad \text{(D4.12)}$$

$$D_3^{\mathrm{II}} = g^{\mathrm{II}} (\xi^{\mathrm{I}})^2 D_1^{\mathrm{I}} + 2(g^{\mathrm{II}} - g^{\mathrm{I}} m^{\mathrm{I}}) D_2^{\mathrm{I}} \,, \quad \text{(D4.13)}$$

$$D_4 = m^{\mathrm{I}} (\xi^{\mathrm{II}})^2 D_1^{\mathrm{II}} D_2^{\mathrm{I}} - m^{\mathrm{II}} (\xi^{\mathrm{I}})^2 D_1^{\mathrm{I}} D_2^{\mathrm{II}} + 2(m^{\mathrm{I}} - m^{\mathrm{II}}) D_2^{\mathrm{I}} D_2^{\mathrm{II}} \,, \quad \text{(D4.14)}$$

$$D_5 = A_1 D_4 - A_2^{\mathrm{I}} D_1^{\mathrm{I}} D_3^{\mathrm{I}} + A_2^{\mathrm{II}} D_1^{\mathrm{II}} D_3^{\mathrm{II}} \,, \quad \text{(D4.15)}$$

Appendix E Hollow Cylinder's Dual-Poroelastic Solutions

E.1 Case 1

The following lateral boundary conditions are enforced

$$\widetilde{\sigma}_{rr}\Big|_{r_{\mathrm{D}}=r_{\mathrm{iD}}}=\widetilde{P}_{\mathrm{i}};\qquad \widetilde{p}^{\mathrm{I}}\Big|_{r_{\mathrm{D}}=r_{\mathrm{iD}}}=\widetilde{p}^{\mathrm{II}}\Big|_{r_{\mathrm{D}}=r_{\mathrm{iD}}}=\widetilde{p}_{\mathrm{i}}\,,\qquad\text{(E1.1a)}$$

$$\widetilde{\sigma}_{rr}\Big|_{r_{\mathrm{D}}=r_{\mathrm{oD}}}=\widetilde{P}_{\mathrm{o}};\qquad \widetilde{p}^{\mathrm{I}}\Big|_{r_{\mathrm{D}}=r_{\mathrm{oD}}}=\widetilde{p}^{\mathrm{II}}\Big|_{r_{\mathrm{D}}=r_{\mathrm{oD}}}=\widetilde{p}_{\mathrm{o}}\,,\qquad\text{(E1.1b)}$$

And the resulting coefficients are

Displacement-controlled.

$$\begin{Bmatrix} C_1^{\mathrm{I}} \\ C_1^{\mathrm{II}} \\ C_2^{\mathrm{I}} \\ C_2^{\mathrm{II}} \end{Bmatrix} = \begin{bmatrix} d_{11}^{\mathrm{I}} & d_{11}^{\mathrm{II}} & d_{12}^{\mathrm{I}} & d_{12}^{\mathrm{II}} \\ d_{21}^{\mathrm{I}} & d_{21}^{\mathrm{II}} & d_{22}^{\mathrm{I}} & d_{22}^{\mathrm{II}} \\ d_{31}^{\mathrm{I}} & d_{31}^{\mathrm{II}} & d_{32}^{\mathrm{I}} & d_{32}^{\mathrm{II}} \\ d_{41}^{\mathrm{I}} & d_{41}^{\mathrm{II}} & d_{42}^{\mathrm{I}} & d_{42}^{\mathrm{II}} \end{bmatrix}^{-1} \begin{Bmatrix} \widetilde{p}_{\mathrm{i}} - f^{\mathrm{I}}\widetilde{S}_{zz} - g^{\mathrm{I}}\widetilde{\sigma}_{\mathrm{io}}^{*} \\ \widetilde{p}_{\mathrm{i}} - f^{\mathrm{II}}\widetilde{S}_{zz} - g^{\mathrm{II}}\widetilde{\sigma}_{\mathrm{io}}^{*} \\ \widetilde{p}_{\mathrm{o}} - f^{\mathrm{I}}\widetilde{S}_{zz} - g^{\mathrm{I}}\widetilde{\sigma}_{\mathrm{io}}^{*} \\ \widetilde{p}_{\mathrm{o}} - f^{\mathrm{II}}\widetilde{S}_{zz} - g^{\mathrm{II}}\widetilde{\sigma}_{\mathrm{io}}^{*} \end{Bmatrix},\qquad\text{(E1.2)}$$

$$\widetilde{C}_1 = \widetilde{\sigma}_{\mathrm{io}}^{*} - \sum_{(\mathrm{N})=\mathrm{I},\mathrm{II}} A_3^{(\mathrm{N})}\left[C_2^{(\mathrm{N})}\,\Phi(\xi^{(\mathrm{N})}) - C_3^{(\mathrm{N})}\,\Theta(\xi^{(\mathrm{N})})\right],\qquad\text{(E1.3)}$$

$$C_4 = \widetilde{\sigma}_{\mathrm{io}}^{**} + \sum_{(\mathrm{N})=\mathrm{I},\mathrm{II}} A_2^{(\mathrm{N})}\left[C_2^{(\mathrm{N})}\,\Omega(\xi^{(\mathrm{N})}) - C_3^{(\mathrm{N})}\,\Xi(\xi^{(\mathrm{N})})\right],\qquad\text{(E1.4)}$$

where Φ, Θ, Ω, and Ξ are functions defined as

$$\Phi(\xi^{(\mathrm{N})}) = \rho\left[\frac{1}{r_{\mathrm{iD}}^2}\frac{\mathrm{I}_1(\xi^{(\mathrm{N})}\,r_{\mathrm{oD}})}{\xi^{(\mathrm{N})}r_{\mathrm{oD}}} - \frac{1}{r_{\mathrm{oD}}^2}\frac{\mathrm{I}_1(\xi^{(\mathrm{N})}\,r_{\mathrm{iD}})}{\xi^{(\mathrm{N})}r_{\mathrm{iD}}}\right],\qquad\text{(E1.5a)}$$

$$\Theta(\xi^{(\mathrm{N})}) = \rho\left[\frac{1}{r_{\mathrm{iD}}^2}\frac{\mathrm{K}_1(\xi^{(\mathrm{N})}\,r_{\mathrm{oD}})}{\xi^{(\mathrm{N})}r_{\mathrm{oD}}} - \frac{1}{r_{\mathrm{oD}}^2}\frac{\mathrm{K}_1(\xi^{(\mathrm{N})}\,r_{\mathrm{iD}})}{\xi^{(\mathrm{N})}r_{\mathrm{iD}}}\right],\qquad\text{(E1.5b)}$$

$$\Omega(\xi^{(\mathrm{N})}) = \rho\left[\frac{\mathrm{I}_1(\xi^{(\mathrm{N})} r_{\mathrm{oD}})}{\xi^{(\mathrm{N})} r_{\mathrm{oD}}} - \frac{\mathrm{I}_1(\xi^{(\mathrm{N})} r_{\mathrm{iD}})}{\xi^{(\mathrm{N})} r_{\mathrm{iD}}}\right], \quad \text{(E1.5c)}$$

$$\Xi(\xi^{(\mathrm{N})}) = \rho\left[\frac{\mathrm{K}_1(\xi^{(\mathrm{N})} r_{\mathrm{oD}})}{\xi^{(\mathrm{N})} r_{\mathrm{oD}}} - \frac{\mathrm{K}_1(\xi^{(\mathrm{N})} r_{\mathrm{iD}})}{\xi^{(\mathrm{N})} r_{\mathrm{iD}}}\right], \quad \text{(E1.5d)}$$

The coefficients $d_{ij}^{(\mathrm{N})}$ in Eq. E1.2 are expressed as

$$d_{11}^{(\mathrm{N})} = \mathrm{I}_0(\xi^{(\mathrm{N})} r_{\mathrm{iD}}) - g^{\mathrm{I}} A_3^{(\mathrm{N})}\, \Phi(\xi^{(\mathrm{N})}), \quad \text{(E1.6a)}$$

$$d_{12}^{(\mathrm{N})} = \mathrm{K}_0(\xi^{(\mathrm{N})} r_{\mathrm{iD}}) + g^{\mathrm{I}} A_3^{(\mathrm{N})}\, \Theta(\xi^{(\mathrm{N})}), \quad \text{(E1.6b)}$$

$$d_{21}^{(\mathrm{N})} = m^{(\mathrm{N})}\mathrm{I}_0(\xi^{(\mathrm{N})} r_{\mathrm{iD}}) - g^{\mathrm{II}} A_3^{(\mathrm{N})}\Phi(\xi^{(\mathrm{N})}), \quad \text{(E1.6c)}$$

$$d_{22}^{(\mathrm{N})} = m^{(\mathrm{N})}\mathrm{K}_0(\xi^{(\mathrm{N})} r_{\mathrm{iD}}) + g^{\mathrm{II}} A_3^{(\mathrm{N})}\Theta(\xi^{(\mathrm{N})}), \quad \text{(E1.6d)}$$

$$d_{31}^{(\mathrm{N})} = \mathrm{I}_0(\xi^{(\mathrm{N})} r_{\mathrm{oD}}) - g^{\mathrm{I}} A_3^{(\mathrm{N})}\Phi(\xi^{(\mathrm{N})}), \quad \text{(E1.6e)}$$

$$d_{32}^{(\mathrm{N})} = \mathrm{K}_0(\xi^{(\mathrm{N})} r_{\mathrm{oD}}) + g^{\mathrm{I}} A_3^{(\mathrm{N})}\, \Theta(\xi^{(\mathrm{N})}), \quad \text{(E1.6f)}$$

$$d_{41}^{(\mathrm{N})} = m^{(\mathrm{N})}\mathrm{I}_0(\xi^{(\mathrm{N})} r_{\mathrm{oD}}) - g^{\mathrm{II}} A_3^{(\mathrm{N})}\Phi(\xi^{(\mathrm{N})}), \quad \text{(E1.6g)}$$

$$d_{42}^{(\mathrm{N})} = m^{(\mathrm{N})}\mathrm{K}_0(\xi^{(\mathrm{N})} r_{\mathrm{oD}}) + g^{\mathrm{II}} A_3^{(\mathrm{N})}\Theta(\xi^{(\mathrm{N})}), \quad \text{(E1.6h)}$$

The lumped coefficients $\widetilde{\sigma}_{\mathrm{io}}^{*}$, $\widetilde{\sigma}_{\mathrm{io}}^{**}$, ρ, and $A_3^{(\mathrm{N})}$ are defined as

$$\widetilde{\sigma}_{\mathrm{io}}^{*} = \frac{\rho}{A_1}\left(\frac{\widetilde{P}_{\mathrm{o}} - A_0\widetilde{S}_{zz}}{r_{\mathrm{iD}}^2} - \frac{\widetilde{P}_{\mathrm{i}} - A_0\widetilde{S}_{zz}}{r_{\mathrm{oD}}^2}\right); \qquad \widetilde{\sigma}_{\mathrm{io}}^{**} = \rho(\widetilde{P}_{\mathrm{i}} - \widetilde{P}_{\mathrm{o}}), \quad \text{(E1.7)}$$

$$\rho = \frac{r_{\mathrm{iD}}^2 r_{\mathrm{oD}}^2}{r_{\mathrm{oD}}^2 - r_{\mathrm{iD}}^2}; \qquad A_3^{(\mathrm{N})} = A_2^{(\mathrm{N})} / A_1, \quad \text{(E1.8)}$$

Load-controlled.

$$\begin{Bmatrix} C_1^{\mathrm{I}} \\ C_1^{\mathrm{II}} \\ C_2^{\mathrm{I}} \\ C_2^{\mathrm{II}} \end{Bmatrix} = \begin{bmatrix} d_{11}^{\mathrm{I}} & d_{11}^{\mathrm{II}} & d_{12}^{\mathrm{I}} & d_{12}^{\mathrm{II}} \\ d_{21}^{\mathrm{I}} & d_{21}^{\mathrm{II}} & d_{22}^{\mathrm{I}} & d_{22}^{\mathrm{II}} \\ d_{31}^{\mathrm{I}} & d_{31}^{\mathrm{II}} & d_{32}^{\mathrm{I}} & d_{32}^{\mathrm{II}} \\ d_{41}^{\mathrm{I}} & d_{41}^{\mathrm{II}} & d_{42}^{\mathrm{I}} & d_{42}^{\mathrm{II}} \end{bmatrix}^{-1} \begin{Bmatrix} \widetilde{p}_{\mathrm{i}} - [f^{\mathrm{I}}\widetilde{\sigma}_{zz}^{*} + (-B_1 f^{\mathrm{I}} + g^{\mathrm{I}})\widetilde{\sigma}_{\mathrm{io}}^{*}]/B_0 \\ \widetilde{p}_{\mathrm{i}} - [f^{\mathrm{II}}\widetilde{\sigma}_{zz}^{*} + (-B_1 f^{\mathrm{II}} + g^{\mathrm{II}})\widetilde{\sigma}_{\mathrm{io}}^{*}]/B_0 \\ \widetilde{p}_{\mathrm{o}} - [f^{\mathrm{I}}\widetilde{\sigma}_{zz}^{*} + (-B_1 f^{\mathrm{I}} + g^{\mathrm{I}})\widetilde{\sigma}_{\mathrm{io}}^{*}]/B_0 \\ \widetilde{p}_{\mathrm{o}} - [f^{\mathrm{II}}\widetilde{\sigma}_{zz}^{*} + (-B_1 f^{\mathrm{II}} + g^{\mathrm{II}})\widetilde{\sigma}_{\mathrm{io}}^{*}]/B_0 \end{Bmatrix}, \quad \text{..... (E1.9)}$$

The constants $\widetilde{C}_1$ and C_4 are the same as defined in Eqs. E1.3 and E1.4. The coefficients $d_{ij}^{(\mathrm{N})}$ are rewritten as

$$d_{11}^{(\mathrm{N})} = \mathrm{I}_0(\xi^{(\mathrm{N})} r_{\mathrm{iD}}) + [f^{\mathrm{I}}(A_3^{(\mathrm{N})} B_1 - 2B_2^{(\mathrm{N})})/B_0 - g^{\mathrm{I}} A_3^{(\mathrm{N})}]\Phi(\xi^{(\mathrm{N})}), \quad \text{.....(E1.10a)}$$

$$d_{12}^{(\mathrm{N})} = \mathrm{K}_0(\xi^{(\mathrm{N})} r_{\mathrm{iD}}) - [f^{\mathrm{I}}(A_3^{(\mathrm{N})} B_1 - 2B_2^{(\mathrm{N})})/B_0 - g^{\mathrm{I}} A_3^{(\mathrm{N})}]\Theta(\xi^{(\mathrm{N})}), \quad \text{..... (E1.10b)}$$

$$d_{21}^{(\mathrm{N})} = m^{(\mathrm{N})}\mathrm{I}_0(\xi^{(\mathrm{N})} r_{\mathrm{iD}}) + [f^{\mathrm{II}}(A_3^{(\mathrm{N})} B_1 - 2B_2^{(\mathrm{N})})/B_0 - g^{\mathrm{II}} A_3^{(\mathrm{N})}]\Phi(\xi^{(\mathrm{N})}), \quad \text{.....(E1.10c)}$$

$$d_{22}^{(\mathrm{N})} = m^{(\mathrm{N})}\mathrm{K}_0(\xi^{(\mathrm{N})} r_{\mathrm{iD}}) - [f^{\mathrm{II}}(A_3^{(\mathrm{N})} B_1 - 2B_2^{(\mathrm{N})})/B_0 - g^{\mathrm{II}} A_3^{(\mathrm{N})}]\,\Theta(\xi^{(\mathrm{N})}), \quad \text{..... (E1.10d)}$$

$$d_{31}^{(\mathrm{N})} = \mathrm{I}_0(\xi^{(\mathrm{N})} r_{\mathrm{oD}}) + [f^{\mathrm{I}}(A_3^{(\mathrm{N})} B_1 - 2B_2^{(\mathrm{N})})/B_0 - g^{\mathrm{I}} A_3^{(\mathrm{N})}]\Phi(\xi^{(\mathrm{N})}), \quad \text{.....(E1.10e)}$$

$$d_{32}^{(\mathrm{N})} = \mathrm{K}_0(\xi^{(\mathrm{N})} r_{\mathrm{oD}}) - [f^{\mathrm{I}}(A_3^{(\mathrm{N})} B_1 - 2B_2^{(\mathrm{N})})/B_0 - g^{\mathrm{I}} A_3^{(\mathrm{N})}]\,\Theta(\xi^{(\mathrm{N})}), \quad \text{.....(E1.10f)}$$

$$d_{41}^{(\mathrm{N})} = m^{(\mathrm{N})}\mathrm{I}_0(\xi^{(\mathrm{N})} r_{\mathrm{oD}}) + [f^{\mathrm{II}}(A_3^{(\mathrm{N})} B_1 - 2B_2^{(\mathrm{N})})/B_0 - g^{\mathrm{II}} A_3^{(\mathrm{N})}]\Phi(\xi^{(\mathrm{N})}), \quad \text{..... (E1.10g)}$$

$$d_{42}^{(\mathrm{N})} = m^{(\mathrm{N})}\mathrm{K}_0(\xi^{(\mathrm{N})} r_{\mathrm{oD}}) - [f^{\mathrm{II}}(A_3^{(\mathrm{N})} B_1 - 2B_2^{(\mathrm{N})})/B_0 - g^{\mathrm{II}} A_3^{(\mathrm{N})}]\Theta(\xi^{(\mathrm{N})}), \quad \text{..... (E1.10h)}$$

in which the functions Φ, Θ, Ω, and Ξ are the same as defined in Eqs. E1.5a to E1.5d. The lumped coefficients $\widetilde{\sigma}_{\mathrm{io}}^{*}$ and $A_3^{(\mathrm{N})}$ are redefined as

$$\widetilde{\sigma}_{\mathrm{io}}^{*} = \frac{\rho}{A_1 B_0 - A_0 B_1}\left(\frac{B_0 \widetilde{P}_{\mathrm{o}} - A_0 \widetilde{\sigma}_{zz}^{*}}{r_{\mathrm{iD}}^2} - \frac{B_0 \widetilde{P}_{\mathrm{i}} - A_0 \widetilde{\sigma}_{zz}^{*}}{r_{\mathrm{oD}}^2}\right), \quad \text{..... (E1.11)}$$

$$A_3^{(\mathrm{N})} = \frac{(A_2^{(\mathrm{N})} B_0 - 2A_0 B_2^{(\mathrm{N})})}{(A_1 B_0 - A_0 B_1)}, \quad \text{..... (E1.12)}$$

E.2 Case 2

The following lateral boundary conditions are enforced

$$\widetilde{\sigma}_{rr}\Big|_{r_{\mathrm{D}}=r_{\mathrm{iD}}} = \widetilde{P}_{\mathrm{i}}; \qquad \widetilde{q}_r^{\mathrm{I}} + \widetilde{q}_r^{\mathrm{II}}\Big|_{r_{\mathrm{D}}=r_{\mathrm{iD}}} = \widetilde{q}_{\mathrm{i}}; \qquad \widetilde{p}^{\mathrm{I}}\Big|_{r_{\mathrm{D}}=r_{\mathrm{iD}}} = \widetilde{p}^{\mathrm{II}}\Big|_{r_{\mathrm{D}}=r_{\mathrm{iD}}}, \quad \text{.....(E2.1a)}$$

$$\widetilde{\sigma}_{rr}\Big|_{r_{\mathrm{D}}=r_{\mathrm{oD}}} = \widetilde{P}_{\mathrm{o}}; \qquad \widetilde{p}^{\mathrm{I}}\Big|_{r_{\mathrm{D}}=r_{\mathrm{oD}}} = \widetilde{p}^{\mathrm{II}}\Big|_{r_{\mathrm{D}}=r_{\mathrm{oD}}} = \widetilde{p}_{\mathrm{o}}, \quad \text{..... (E2.1b)}$$

where $\widetilde{q}_{\mathrm{i}} = \widetilde{Q}_{\mathrm{i}} / [2\pi r_{\mathrm{iD}} (\overline{\kappa}_1^{\mathrm{I}} + \overline{\kappa}_1^{\mathrm{II}})]$ in which Q_{i} is the flow rate per unit thickness. And the resulting coefficients are

$$\begin{Bmatrix} C_1^{\mathrm{I}} \\ C_1^{\mathrm{II}} \\ C_2^{\mathrm{I}} \\ C_2^{\mathrm{II}} \end{Bmatrix} = \begin{bmatrix} d_{11}^{\mathrm{I}} & d_{11}^{\mathrm{II}} & d_{12}^{\mathrm{I}} & d_{12}^{\mathrm{II}} \\ d_{21}^{\mathrm{I}} & d_{21}^{\mathrm{II}} & d_{22}^{\mathrm{I}} & d_{22}^{\mathrm{II}} \\ d_{31}^{\mathrm{I}} & d_{31}^{\mathrm{II}} & d_{32}^{\mathrm{I}} & d_{32}^{\mathrm{II}} \\ d_{41}^{\mathrm{I}} & d_{41}^{\mathrm{II}} & d_{42}^{\mathrm{I}} & d_{42}^{\mathrm{II}} \end{bmatrix}^{-1} \begin{Bmatrix} \widetilde{q}_{\mathrm{i}} \\ (f^{\mathrm{II}} - f^{\mathrm{I}})\widetilde{\sigma}_{\mathrm{io}}^{*} \\ \widetilde{p}_{\mathrm{o}} - f^{\mathrm{I}}\widetilde{\sigma}_{\mathrm{io}}^{*} \\ \widetilde{p}_{\mathrm{o}} - f^{\mathrm{II}}\widetilde{\sigma}_{\mathrm{io}}^{*} \end{Bmatrix}, \quad \text{..... (E2.2)}$$

where the coefficients $d_{11}^{(\mathrm{N})}$, $d_{12}^{(\mathrm{N})}$, $d_{21}^{(\mathrm{N})}$, and $d_{22}^{(\mathrm{N})}$ are rewritten as

$$d_{11}^{(\mathrm{N})} = (1 - \overline{\kappa}_D + \overline{\kappa}_D m^{(\mathrm{N})}) \xi^{(\mathrm{N})} \mathrm{I}_0(\xi^{(\mathrm{N})} r_{\mathrm{iD}}), \quad \text{.....(E2.3a)}$$

$$d_{12}^{(\mathrm{N})} = -(1 - \overline{\kappa}_D + \overline{\kappa}_D m^{(\mathrm{N})}) \xi^{(\mathrm{N})} \mathrm{K}_0(\xi^{(\mathrm{N})} r_{\mathrm{iD}}), \quad \text{..... (E2.3b)}$$

$$d_{21}^{(\mathrm{N})} = (1 - m^{(\mathrm{N})}) \mathrm{I}_0(\xi^{(\mathrm{N})} r_{\mathrm{iD}}) - (f^{\mathrm{I}} - f^{\mathrm{II}}) \Phi(\xi^{(\mathrm{N})}), \quad \text{.....(E2.3c)}$$

$$d_{22}^{(\mathrm{N})} = (1 - m^{(\mathrm{N})}) \mathrm{K}_0(\xi^{(\mathrm{N})} r_{\mathrm{iD}}) + (f^{\mathrm{I}} - f^{\mathrm{II}}) \Theta(\xi^{(\mathrm{N})}), \quad \text{..... (E2.3d)}$$

The rest of the coefficients and functions are the same as previously defined for Case 1.

For the special case of no-flow or jacketed on the inner surface, the fluid boundary condition at this surface becomes

$$\widetilde{q}_r^{\mathrm{I}}\Big|_{r_{\mathrm{D}}=r_{\mathrm{iD}}} = \widetilde{q}_r^{\mathrm{II}}\Big|_{r_{\mathrm{D}}=r_{\mathrm{iD}}} = 0, \quad \text{..... (E2.4)}$$

The resulting coefficients are

$$\begin{Bmatrix} C_1^{\mathrm{I}} \\ C_1^{\mathrm{II}} \\ C_2^{\mathrm{I}} \\ C_2^{\mathrm{II}} \end{Bmatrix} = \begin{bmatrix} d_{11}^{\mathrm{I}} & d_{11}^{\mathrm{II}} & d_{12}^{\mathrm{I}} & d_{12}^{\mathrm{II}} \\ d_{21}^{\mathrm{I}} & d_{21}^{\mathrm{II}} & d_{22}^{\mathrm{I}} & d_{22}^{\mathrm{II}} \\ d_{31}^{\mathrm{I}} & d_{31}^{\mathrm{II}} & d_{32}^{\mathrm{I}} & d_{32}^{\mathrm{II}} \\ d_{41}^{\mathrm{I}} & d_{41}^{\mathrm{II}} & d_{42}^{\mathrm{I}} & d_{42}^{\mathrm{II}} \end{bmatrix}^{-1} \begin{Bmatrix} 0 \\ 0 \\ \widetilde{p}_{\mathrm{o}} - f^{\mathrm{I}} \widetilde{\sigma}_{\mathrm{io}}^{*} \\ \widetilde{p}_{\mathrm{o}} - f^{\mathrm{II}} \widetilde{\sigma}_{\mathrm{io}}^{*} \end{Bmatrix}, \quad \text{(E2.5)}$$

where the coefficients $d_{11}^{(\mathrm{N})}$, $d_{12}^{(\mathrm{N})}$, $d_{21}^{(\mathrm{N})}$, and $d_{22}^{(\mathrm{N})}$ are rewritten as

$$d_{11}^{(\mathrm{N})} = (1-\overline{\kappa}_D)\,\xi^{(\mathrm{N})}\mathrm{I}_0(\xi^{(\mathrm{N})} r_{\mathrm{iD}}), \quad \text{(E2.6a)}$$

$$d_{12}^{(\mathrm{N})} = -(1-\overline{\kappa}_D)\,\xi^{(\mathrm{N})}\mathrm{K}_0(\xi^{(\mathrm{N})} r_{\mathrm{iD}}), \quad \text{(E2.6b)}$$

$$d_{11}^{(\mathrm{N})} = \overline{\kappa}_D m^{(\mathrm{N})}\,\xi^{(\mathrm{N})}\mathrm{I}_0(\xi^{(\mathrm{N})} r_{\mathrm{iD}}), \quad \text{(E2.6c)}$$

$$d_{12}^{(\mathrm{N})} = -\overline{\kappa}_D m^{(\mathrm{N})}\xi^{(\mathrm{N})}\mathrm{K}_0(\xi^{(\mathrm{N})} r_{\mathrm{iD}}), \quad \text{(E2.6d)}$$

The rest of the coefficients and functions are the same as previously defined for Case 1.

E.3 Case 3

The following lateral boundary conditions are enforced

$$\widetilde{\sigma}_{rr}\Big|_{r_{\mathrm{D}}=r_{\mathrm{iD}}} = \widetilde{P}_{\mathrm{i}}; \qquad \widetilde{p}^{\mathrm{I}}\Big|_{r_{\mathrm{D}}=r_{\mathrm{iD}}} = \widetilde{p}^{\mathrm{II}}\Big|_{r_{\mathrm{D}}=r_{\mathrm{iD}}} = \widetilde{p}_{\mathrm{i}}, \quad \text{(E3.1a)}$$

$$\widetilde{\sigma}_{rr}\Big|_{r_{\mathrm{D}}=r_{\mathrm{oD}}} = \widetilde{P}_{\mathrm{o}}; \qquad \widetilde{q}_r^{\mathrm{I}} + \widetilde{q}_r^{\mathrm{II}}\Big|_{r_{\mathrm{D}}=r_{\mathrm{oD}}} = \widetilde{q}_{\mathrm{o}}; \qquad \widetilde{p}^{\mathrm{I}}\Big|_{r_{\mathrm{D}}=r_{\mathrm{oD}}} = \widetilde{p}^{\mathrm{II}}\Big|_{r_{\mathrm{D}}=r_{\mathrm{oD}}}, \quad \text{(E3.1b)}$$

where $\widetilde{q}_{\mathrm{o}} = \widetilde{Q}_{\mathrm{o}} / [2\pi r_{\mathrm{oD}}(\overline{\kappa}_1^{\mathrm{I}} + \overline{\kappa}_1^{\mathrm{II}})]$ in which Q_{o} is the flow rate per unit thickness. And the resulting coefficients are

$$\begin{Bmatrix} C_1^{\mathrm{I}} \\ C_1^{\mathrm{II}} \\ C_2^{\mathrm{I}} \\ C_2^{\mathrm{II}} \end{Bmatrix} = \begin{bmatrix} d_{11}^{\mathrm{I}} & d_{11}^{\mathrm{II}} & d_{12}^{\mathrm{I}} & d_{12}^{\mathrm{II}} \\ d_{21}^{\mathrm{I}} & d_{21}^{\mathrm{II}} & d_{22}^{\mathrm{I}} & d_{22}^{\mathrm{II}} \\ d_{31}^{\mathrm{I}} & d_{31}^{\mathrm{II}} & d_{32}^{\mathrm{I}} & d_{32}^{\mathrm{II}} \\ d_{41}^{\mathrm{I}} & d_{41}^{\mathrm{II}} & d_{42}^{\mathrm{I}} & d_{42}^{\mathrm{II}} \end{bmatrix}^{-1} \begin{Bmatrix} \widetilde{p}_{\mathrm{i}} - f^{\mathrm{I}} \widetilde{\sigma}_{\mathrm{io}}^{*} \\ \widetilde{p}_{\mathrm{i}} - f^{\mathrm{II}} \widetilde{\sigma}_{\mathrm{io}}^{*} \\ \widetilde{q}_{\mathrm{o}} \\ (f^{\mathrm{II}} - f^{\mathrm{I}}) \widetilde{\sigma}_{\mathrm{io}}^{*} \end{Bmatrix}, \quad \text{(E3.2)}$$

where the coefficients $d_{31}^{(\mathrm{N})}$, $d_{32}^{(\mathrm{N})}$, $d_{41}^{(\mathrm{N})}$, and $d_{42}^{(\mathrm{N})}$ are rewritten as

$$d_{31}^{(\mathrm{N})} = (1 - \overline{\kappa}_D + \overline{\kappa}_D m^{(\mathrm{N})}) \xi^{(\mathrm{N})} \mathrm{I}_0(\xi^{(\mathrm{N})} r_{\mathrm{oD}}), \quad \text{(E3.3a)}$$

$$d_{32}^{(\mathrm{N})} = -(1 - \overline{\kappa}_D + \overline{\kappa}_D m^{(\mathrm{N})}) \xi^{(\mathrm{N})} \mathrm{K}_0(\xi^{(\mathrm{N})} r_{\mathrm{oD}}), \quad \text{(E3.3b)}$$

$$d_{41}^{(\mathrm{N})} = (1 - m^{(\mathrm{N})}) \mathrm{I}_0(\xi^{(\mathrm{N})} r_{\mathrm{oD}}) - (f^{\mathrm{I}} - f^{\mathrm{II}}) \Phi(\xi^{(\mathrm{N})}), \quad \text{(E3.3c)}$$

$$d_{42}^{(\mathrm{N})} = (1 - m^{(\mathrm{N})}) \mathrm{K}_0(\xi^{(\mathrm{N})} r_{\mathrm{oD}}) + (f^{\mathrm{I}} - f^{\mathrm{II}}) \Theta(\xi^{(\mathrm{N})}), \quad \text{(E3.3d)}$$

The rest of the coefficients and functions are the same as previously defined for Case 1.

For the special case of no-flow or jacketed on the outer surface, the fluid boundary condition at this surface becomes

$$\widetilde{q}_r^{\mathrm{I}}\Big|_{r_{\mathrm{D}} = r_{\mathrm{oD}}} = \widetilde{q}_r^{\mathrm{II}}\Big|_{r_{\mathrm{D}} = r_{\mathrm{oD}}} = 0, \quad \text{(E3.4)}$$

The resulting coefficients are

$$\begin{Bmatrix} C_1^{\mathrm{I}} \\ C_1^{\mathrm{II}} \\ C_2^{\mathrm{I}} \\ C_2^{\mathrm{II}} \end{Bmatrix} = \begin{bmatrix} d_{11}^{\mathrm{I}} & d_{11}^{\mathrm{II}} & d_{12}^{\mathrm{I}} & d_{12}^{\mathrm{II}} \\ d_{21}^{\mathrm{I}} & d_{21}^{\mathrm{II}} & d_{22}^{\mathrm{I}} & d_{22}^{\mathrm{II}} \\ d_{31}^{\mathrm{I}} & d_{31}^{\mathrm{II}} & d_{32}^{\mathrm{I}} & d_{32}^{\mathrm{II}} \\ d_{41}^{\mathrm{I}} & d_{41}^{\mathrm{II}} & d_{42}^{\mathrm{I}} & d_{42}^{\mathrm{II}} \end{bmatrix}^{-1} \begin{Bmatrix} \widetilde{p}_{\mathrm{i}} - f^{\mathrm{I}} \widetilde{\sigma}_{\mathrm{io}}^{*} \\ \widetilde{p}_{\mathrm{i}} - f^{\mathrm{II}} \widetilde{\sigma}_{\mathrm{io}}^{*} \\ 0 \\ 0 \end{Bmatrix}, \quad \text{(E3.5)}$$

where the coefficients $d_{31}^{(\mathrm{N})}$, $d_{32}^{(\mathrm{N})}$, $d_{41}^{(\mathrm{N})}$, and $d_{42}^{(\mathrm{N})}$ are rewritten as

$$d_{31}^{(\mathrm{N})} = (1 - \overline{\kappa}_D) \xi^{(\mathrm{N})} \mathrm{I}_0(\xi^{(\mathrm{N})} r_{\mathrm{oD}}), \quad \text{(E3.6a)}$$

$$d_{32}^{(\mathrm{N})} = -(1 - \overline{\kappa}_D) \xi^{(\mathrm{N})} \mathrm{K}_0(\xi^{(\mathrm{N})} r_{\mathrm{oD}}), \quad \text{(E3.6b)}$$

$$d_{41}^{(\mathrm{N})} = \bar{\kappa}_D m^{(\mathrm{N})} \xi^{(\mathrm{N})} \mathrm{I}_0(\xi^{(\mathrm{N})} r_{\mathrm{oD}}), \quad \text{(E3.6c)}$$

$$d_{42}^{(\mathrm{N})} = -\bar{\kappa}_D m^{(\mathrm{N})} \xi^{(\mathrm{N})} \mathrm{K}_0(\xi^{(\mathrm{N})} r_{\mathrm{oD}}), \quad \text{(E3.6d)}$$

The rest of the coefficients and functions are the same as previously defined for Case 1.

E.4 Case 4

The following lateral boundary conditions are enforced

$$\widetilde{\sigma}_{rr}\Big|_{r_{\mathrm{D}}=r_{\mathrm{iD}}} = \widetilde{P}_{\mathrm{i}}; \qquad \widetilde{q}_r^{\mathrm{I}} + \widetilde{q}_r^{\mathrm{II}}\Big|_{r_{\mathrm{D}}=r_{\mathrm{iD}}} = \widetilde{q}_{\mathrm{i}}; \qquad \widetilde{p}^{\mathrm{I}}\Big|_{r_{\mathrm{D}}=r_{\mathrm{iD}}} = \widetilde{p}^{\mathrm{II}}\Big|_{r_{\mathrm{D}}=r_{\mathrm{iD}}}, \quad \text{(E4.1a)}$$

$$\widetilde{\sigma}_{rr}\Big|_{r_{\mathrm{D}}=r_{\mathrm{oD}}} = \widetilde{P}_{\mathrm{o}}; \qquad \widetilde{q}_r^{\mathrm{I}} + \widetilde{q}_r^{\mathrm{II}}\Big|_{r_{\mathrm{D}}=r_{\mathrm{oD}}} = \widetilde{q}_{\mathrm{o}}; \qquad \widetilde{p}^{\mathrm{I}}\Big|_{r_{\mathrm{D}}=r_{\mathrm{oD}}} = \widetilde{p}^{\mathrm{II}}\Big|_{r_{\mathrm{D}}=r_{\mathrm{oD}}}, \quad \text{(E4.1b)}$$

The resulting coefficients are

$$\begin{Bmatrix} C_1^{\mathrm{I}} \\ C_1^{\mathrm{II}} \\ C_2^{\mathrm{I}} \\ C_2^{\mathrm{II}} \end{Bmatrix} = \begin{bmatrix} d_{11}^{\mathrm{I}} & d_{11}^{\mathrm{II}} & d_{12}^{\mathrm{I}} & d_{12}^{\mathrm{II}} \\ d_{21}^{\mathrm{I}} & d_{21}^{\mathrm{II}} & d_{22}^{\mathrm{I}} & d_{22}^{\mathrm{II}} \\ d_{31}^{\mathrm{I}} & d_{31}^{\mathrm{II}} & d_{32}^{\mathrm{I}} & d_{32}^{\mathrm{II}} \\ d_{41}^{\mathrm{I}} & d_{41}^{\mathrm{II}} & d_{42}^{\mathrm{I}} & d_{42}^{\mathrm{II}} \end{bmatrix}^{-1} \begin{Bmatrix} \widetilde{q}_{\mathrm{i}} \\ (f^{\mathrm{II}} - f^{\mathrm{I}})\widetilde{\sigma}_{\mathrm{io}}^{*} \\ \widetilde{q}_{\mathrm{o}} \\ (f^{\mathrm{II}} - f^{\mathrm{I}})\widetilde{\sigma}_{\mathrm{io}}^{*} \end{Bmatrix}, \quad \text{(E4.2)}$$

where the coefficients $d_{11}^{(\mathrm{N})}$, $d_{12}^{(\mathrm{N})}$, $d_{21}^{(\mathrm{N})}$, and $d_{22}^{(\mathrm{N})}$ are rewritten as

$$d_{11}^{(\mathrm{N})} = (1 - \bar{\kappa}_D + \bar{\kappa}_D m^{(\mathrm{N})}) \xi^{(\mathrm{N})} \mathrm{I}_0(\xi^{(\mathrm{N})} r_{\mathrm{iD}}), \quad \text{(E4.3a)}$$

$$d_{12}^{(\mathrm{N})} = -(1 - \bar{\kappa}_D + \bar{\kappa}_D m^{(\mathrm{N})}) \xi^{(\mathrm{N})} \mathrm{K}_0(\xi^{(\mathrm{N})} r_{\mathrm{iD}}), \quad \text{(E4.3b)}$$

$$d_{21}^{(\mathrm{N})} = (1 - m^{(\mathrm{N})}) \mathrm{I}_0(\xi^{(\mathrm{N})} r_{\mathrm{iD}}) - (f^{\mathrm{I}} - f^{\mathrm{II}}) \Phi(\xi^{(\mathrm{N})}), \quad \text{(E4.3c)}$$

$$d_{22}^{(\mathrm{N})} = (1 - m^{(\mathrm{N})}) \mathrm{K}_0(\xi^{(\mathrm{N})} r_{\mathrm{iD}}) + (f^{\mathrm{I}} - f^{\mathrm{II}}) \Theta(\xi^{(\mathrm{N})}), \quad \text{(E4.3d)}$$

$$d_{31}^{(\mathrm{N})} = (1 - \bar{\kappa}_D + \bar{\kappa}_D m^{(\mathrm{N})}) \xi^{(\mathrm{N})} \mathrm{I}_0(\xi^{(\mathrm{N})} r_{\mathrm{oD}}), \quad \text{(E4.3e)}$$

$$d_{32}^{(\mathrm{N})} = -(1-\bar{\kappa}_D + \bar{\kappa}_D m^{(\mathrm{N})})\,\xi^{(\mathrm{N})}\mathrm{K}_0(\xi^{(\mathrm{N})} r_{\mathrm{oD}}), \quad \text{(E4.3f)}$$

$$d_{41}^{(\mathrm{N})} = (1-m^{(\mathrm{N})})\,\mathrm{I}_0(\xi^{(\mathrm{N})} r_{\mathrm{oD}}) - (f^{\mathrm{I}} - f^{\mathrm{II}})\,\Phi(\xi^{(\mathrm{N})}), \quad \text{(E4.3g)}$$

$$d_{42}^{(\mathrm{N})} = (1-m^{(\mathrm{N})})\,\mathrm{K}_0(\xi^{(\mathrm{N})} r_{\mathrm{oD}}) + (f^{\mathrm{I}} - f^{\mathrm{II}})\,\Theta(\xi^{(\mathrm{N})}), \quad \text{(E4.3h)}$$

The rest of the coefficients and functions are the same as previously defined for Case 1.

For the special case of no flow or jacketed on both the inner and outer surfaces, the condition is undrained and the solution simplifies to an elastic one with undrained parameters.

E.5 Case 5

The following lateral boundary conditions are enforced

$$\widetilde{\sigma}_{rr}\Big|_{r_{\mathrm{D}}=r_{\mathrm{iD}}} = \widetilde{P}_{\mathrm{i}}; \qquad \widetilde{p}^{\mathrm{I}}\Big|_{r_{\mathrm{D}}=r_{\mathrm{iD}}} = \widetilde{p}^{\mathrm{II}}\Big|_{r_{\mathrm{D}}=r_{\mathrm{iD}}} = \widetilde{p}_{\mathrm{i}}, \quad \text{(E5.1a)}$$

$$\widetilde{u}_r\Big|_{r_{\mathrm{D}}=r_{\mathrm{oD}}} = \widetilde{U}_{\mathrm{o}}; \qquad \widetilde{p}^{\mathrm{I}}\Big|_{r_{\mathrm{D}}=r_{\mathrm{oD}}} = \widetilde{p}^{\mathrm{II}}\Big|_{r_{\mathrm{D}}=r_{\mathrm{oD}}} = \widetilde{p}_{\mathrm{o}}, \quad \text{(E5.1b)}$$

The resulting coefficients $C_1^{(\mathrm{N})}$, $C_2^{(\mathrm{N})}$, $\widetilde{C}_0$ and C_3 are the same as given in Eqs. E1.2, E1.3 and E1.4. The lumped coefficients $\widetilde{\sigma}_{\mathrm{io}}^{*}$, $\widetilde{\sigma}_{\mathrm{io}}^{**}$, $\varphi_{\mathrm{i}}^{(\mathrm{N})}$, $\varphi_{\mathrm{o}}^{(\mathrm{N})}$, $\gamma_{\mathrm{i}}^{(\mathrm{N})}$, $\gamma_{\mathrm{o}}^{(\mathrm{N})}$, and ρ are rewritten as

Displacement-controlled.

$$\widetilde{\sigma}_{\mathrm{io}}^{*} = \frac{\rho}{r_{\mathrm{iD}}^2 r_{\mathrm{oD}}^2}\left[2(\widetilde{P}_{\mathrm{i}} r_{\mathrm{iD}}^2 + A_3 \widetilde{U}_{\mathrm{o}} r_{\mathrm{oD}}) + (A_3 r_{\mathrm{oD}}^2 - 2A_2 r_{\mathrm{iD}}^2)\,\widetilde{\varepsilon}_{zz}^{*}\right], \quad \text{(E5.2a)}$$

$$\widetilde{\sigma}_{\mathrm{io}}^{**} = \rho[2A_0 \widetilde{U}_{\mathrm{o}} / r_{\mathrm{oD}} + h\widetilde{P}_{\mathrm{i}} + (A_0 - A_3 h)\,\widetilde{\varepsilon}_{zz}^{*}], \quad \text{(E5.2b)}$$

$$\varphi_{\mathrm{i}}^{(\mathrm{N})} = 2A_1^{(\mathrm{N})}; \qquad \varphi_{\mathrm{o}}^{(\mathrm{N})} = 2A_3 h^{(\mathrm{N})}, \quad \text{(E5.3a)}$$

$$\gamma_{\mathrm{i}}^{(\mathrm{N})} = A_1^{(\mathrm{N})} h; \qquad \gamma_{\mathrm{o}}^{(\mathrm{N})} = 2A_0 h^{(\mathrm{N})}, \quad \text{(E5.3b)}$$

$$\rho = -\frac{r_{\mathrm{iD}}^2 r_{\mathrm{oD}}^2}{A_3 h\, r_{\mathrm{oD}}^2 - 2A_0 r_{\mathrm{iD}}^2}, \quad \text{.....(E5.3c)}$$

Load-controlled.

$$\widetilde{\sigma}_{\mathrm{io}}^{*} = \rho \frac{r_{\mathrm{oD}}^2 - r_{\mathrm{iD}}^2}{r_{\mathrm{iD}}^2 r_{\mathrm{oD}}^2}\left[2B_2(\widetilde{P}_{\mathrm{i}} r_{\mathrm{iD}}^2 + A_3 \widetilde{U}_{\mathrm{o}} r_{\mathrm{oD}}) + (A_3 r_{\mathrm{oD}}^2 - 2A_2 r_{\mathrm{iD}}^2)\,\widetilde{\sigma}_{zz}^{*}\right], \quad \text{.....(E5.4a)}$$

$$\widetilde{\sigma}_{\mathrm{io}}^{**} = \rho(r_{\mathrm{oD}}^2 - r_{\mathrm{iD}}^2)[2(A_0 B_2 - A_2 B_0)\widetilde{U}_{\mathrm{o}} / r_{\mathrm{oD}} + (A_0 - A_2 h)\,\widetilde{\sigma}_{zz}^{*} - (B_0 - B_2 h)\,\widetilde{P}_{\mathrm{i}}], \quad \text{.... (E5.4b)}$$

$$\varphi_{\mathrm{i}}^{(\mathrm{N})} = 2[(A_1^{(\mathrm{N})} B_2 - A_3 B_1^{(\mathrm{N})}) r_{\mathrm{oD}}^2 - (A_1^{(\mathrm{N})} B_2 - 2A_2 B_1^{(\mathrm{N})}) r_{\mathrm{iD}}^2], \quad \text{.....(E5.5a)}$$

$$\varphi_{\mathrm{o}}^{(\mathrm{N})} = 2[(A_3 B_2 h^{(\mathrm{N})} - A_3 B_1^{(\mathrm{N})}) r_{\mathrm{oD}}^2 - (A_3 B_2 h^{(\mathrm{N})} - 2A_2 B_1^{(\mathrm{N})}) r_{\mathrm{iD}}^2], \quad \text{..... (E5.5b)}$$

$$\gamma_{\mathrm{i}}^{(\mathrm{N})} = A_1^{(\mathrm{N})}(B_2 h - B_0) r_{\mathrm{oD}}^2 - [(A_1^{(\mathrm{N})} B_2 - 2A_2 B_1^{(\mathrm{N})}) h - (A_1^{(\mathrm{N})} B_0 - 2A_0 B_1^{(\mathrm{N})})]\, r_{\mathrm{iD}}^2, \quad \text{.....(E5.6a)}$$

$$\gamma_{\mathrm{o}}^{(\mathrm{N})} = 2[(A_0 B_2 - A_2 B_0) h^{(\mathrm{N})} + (A_2 h - A_0) B_1^{(\mathrm{N})}] r_{\mathrm{oD}}^2 - 2(A_0 B_2 - A_2 B_0) h^{(\mathrm{N})} r_{\mathrm{iD}}^2, \quad \text{..... (E5.6b)}$$

$$\rho = \frac{r_{\mathrm{iD}}^2 r_{\mathrm{oD}}^2 / (r_{\mathrm{oD}}^2 - r_{\mathrm{iD}}^2)}{A_3(B_0 - B_2 h) r_{\mathrm{oD}}^2 + 2(A_0 B_2 - A_2 B_0) r_{\mathrm{iD}}^2}, \quad \text{..... (E5.7)}$$

E.6 Case 6

The following lateral boundary conditions are enforced

$$\widetilde{\sigma}_{rr}\Big|_{r_{\mathrm{D}}=r_{\mathrm{iD}}} = \widetilde{P}_{\mathrm{i}}; \qquad \widetilde{q}_r^{\mathrm{I}} + \widetilde{q}_r^{\mathrm{II}}\Big|_{r_{\mathrm{D}}=r_{\mathrm{iD}}} = \widetilde{q}_{\mathrm{i}}; \qquad \widetilde{p}^{\mathrm{I}}\Big|_{r_{\mathrm{D}}=r_{\mathrm{iD}}} = \widetilde{p}^{\mathrm{II}}\Big|_{r_{\mathrm{D}}=r_{\mathrm{iD}}}, \quad \text{.....(E6.1a)}$$

$$\widetilde{u}_r\Big|_{r_{\mathrm{D}}=r_{\mathrm{oD}}} = \widetilde{U}_{\mathrm{o}}; \qquad \widetilde{p}^{\mathrm{I}}\Big|_{r_{\mathrm{D}}=r_{\mathrm{oD}}} = \widetilde{p}^{\mathrm{II}}\Big|_{r_{\mathrm{D}}=r_{\mathrm{oD}}} = \widetilde{p}_{\mathrm{o}}, \quad \text{..... (E6.1b)}$$

The coefficients $C_1^{(\mathrm{N})}$, $C_2^{(\mathrm{N})}$ are the same as given in Eq. E1.12 for Case 2. $\widetilde{C}_0$ and C_3 are given in Eqs. E1.3 and E1.4. The lumped coefficients $\widetilde{\sigma}_{\mathrm{io}}^{*}$, $\widetilde{\sigma}_{\mathrm{io}}^{**}$, $\varphi_{\mathrm{i}}^{(\mathrm{N})}$, $\varphi_{\mathrm{o}}^{(\mathrm{N})}$, $\gamma_{\mathrm{i}}^{(\mathrm{N})}$, $\gamma_{\mathrm{o}}^{(\mathrm{N})}$, and ρ are the same as written for Case 5.

For the special case of no-flow or jacketed on the inner surface, the fluid boundary condition at this surface becomes

$$\widetilde{q}_r^{\,\mathrm{I}}\Big|_{r_\mathrm{D}=r_\mathrm{iD}} = \widetilde{q}_r^{\,\mathrm{II}}\Big|_{r_\mathrm{D}=r_\mathrm{iD}} = 0\,, \qquad \text{(E6.2)}$$

The coefficients $C_1^{(\mathrm{N})}$, $C_2^{(\mathrm{N})}$ are the same as given in Eq. E1.21 for Case 5. $\widetilde{C}_0$ and C_3 are given in Eqs. E1.3 and E1.4. The lumped coefficients $\widetilde{\sigma}_{\mathrm{io}}^{*}$, $\widetilde{\sigma}_{\mathrm{io}}^{**}$, $\varphi_{\mathrm{i}}^{(\mathrm{N})}$, $\varphi_{\mathrm{o}}^{(\mathrm{N})}$, $\gamma_{\mathrm{i}}^{(\mathrm{N})}$, $\gamma_{\mathrm{o}}^{(\mathrm{N})}$, and ρ are the same as written for Case 5.

E.7 Case 7

The following lateral boundary conditions are enforced

$$\widetilde{\sigma}_{rr}\Big|_{r_\mathrm{D}=r_\mathrm{iD}} = \widetilde{P}_\mathrm{i}; \qquad \widetilde{p}^{\,\mathrm{I}}\Big|_{r_\mathrm{D}=r_\mathrm{iD}} = \widetilde{p}^{\,\mathrm{II}}\Big|_{r_\mathrm{D}=r_\mathrm{iD}} = \widetilde{p}_\mathrm{i}\,, \qquad \text{(E7.1a)}$$

$$\widetilde{u}_r\Big|_{r_\mathrm{D}=r_\mathrm{oD}} = \widetilde{U}_\mathrm{o}; \qquad \widetilde{q}_r^{\,\mathrm{I}} + \widetilde{q}_r^{\,\mathrm{II}}\Big|_{r_\mathrm{D}=r_\mathrm{oD}} = \widetilde{q}_\mathrm{o}; \qquad \widetilde{p}^{\,\mathrm{I}}\Big|_{r_\mathrm{D}=r_\mathrm{oD}} = \widetilde{p}^{\,\mathrm{II}}\Big|_{r_\mathrm{D}=r_\mathrm{oD}}\,, \qquad \text{(E7.1b)}$$

The coefficients $C_1^{(\mathrm{N})}$, $C_2^{(\mathrm{N})}$ are the same as given in Eq. E1.15 for Case 3. $\widetilde{C}_0$ and C_3 are given in Eqs. E1.3 and E1.4. The lumped coefficients $\widetilde{\sigma}_{\mathrm{io}}^{*}$, $\widetilde{\sigma}_{\mathrm{io}}^{**}$, $\varphi_{\mathrm{i}}^{(\mathrm{N})}$, $\varphi_{\mathrm{o}}^{(\mathrm{N})}$, $\gamma_{\mathrm{i}}^{(\mathrm{N})}$, $\gamma_{\mathrm{o}}^{(\mathrm{N})}$, and ρ are the same as written for Case 5.

For the special case of no-flow or jacketed on the outer surface, the fluid boundary condition at this surface becomes

$$\widetilde{q}_r^{\,\mathrm{I}}\Big|_{r_\mathrm{D}=r_\mathrm{oD}} = \widetilde{q}_r^{\,\mathrm{II}}\Big|_{r_\mathrm{D}=r_\mathrm{oD}} = 0\,, \qquad \text{(E7.2)}$$

The coefficients $C_1^{(\mathrm{N})}$, $C_2^{(\mathrm{N})}$ are the same as given in Eq. E1.24 for Case 6. $\widetilde{C}_0$ and C_3 are given in Eqs. E1.3 and E1.4. The lumped coefficients $\widetilde{\sigma}_{\mathrm{io}}^{*}$, $\widetilde{\sigma}_{\mathrm{io}}^{**}$, $\varphi_{\mathrm{i}}^{(\mathrm{N})}$, $\varphi_{\mathrm{o}}^{(\mathrm{N})}$, $\gamma_{\mathrm{i}}^{(\mathrm{N})}$, $\gamma_{\mathrm{o}}^{(\mathrm{N})}$, and ρ are the same as written for Case 5.

E.8 Case 8

The following lateral boundary conditions are enforced

$$\widetilde{\sigma}_{rr}\Big|_{r_{\mathrm{D}}=r_{\mathrm{iD}}} = \widetilde{P}_{\mathrm{i}}; \qquad \widetilde{q}_r^{\mathrm{I}} + \widetilde{q}_r^{\mathrm{II}}\Big|_{r_{\mathrm{D}}=r_{\mathrm{iD}}} = \widetilde{q}_{\mathrm{i}}; \qquad \widetilde{p}^{\mathrm{I}}\Big|_{r_{\mathrm{D}}=r_{\mathrm{iD}}} = \widetilde{p}^{\mathrm{II}}\Big|_{r_{\mathrm{D}}=r_{\mathrm{iD}}}, \quad \text{.....(E8.1a)}$$

$$\widetilde{u}_r\Big|_{r_{\mathrm{D}}=r_{\mathrm{oD}}} = \widetilde{U}_{\mathrm{o}}; \qquad \widetilde{q}_r^{\mathrm{I}} + \widetilde{q}_r^{\mathrm{II}}\Big|_{r_{\mathrm{D}}=r_{\mathrm{oD}}} = \widetilde{q}_{\mathrm{o}}; \qquad \widetilde{p}^{\mathrm{I}}\Big|_{r_{\mathrm{D}}=r_{\mathrm{oD}}} = \widetilde{p}^{\mathrm{II}}\Big|_{r_{\mathrm{D}}=r_{\mathrm{oD}}}, \quad \text{..... (E8.1b)}$$

The coefficients $C_1^{(\mathrm{N})}$, $C_2^{(\mathrm{N})}$ are the same as given in Eq. E1.18 for Case 4. $\widetilde{C}_0$ and C_3 are given in Eqs. E1.3 and E1.4. The lumped coefficients $\widetilde{\sigma}_{\mathrm{io}}^{*}$, $\widetilde{\sigma}_{\mathrm{io}}^{**}$, $\varphi_{\mathrm{i}}^{(\mathrm{N})}$, $\varphi_{\mathrm{o}}^{(\mathrm{N})}$, $\gamma_{\mathrm{i}}^{(\mathrm{N})}$, $\gamma_{\mathrm{o}}^{(\mathrm{N})}$, and ρ are the same as written for Case 5.

For the special case of no flow or jacketed on both the inner and outer surfaces, the condition is undrained and the solution simplifies to an elastic one with undrained parameters.

E.9 Case 9

The following lateral boundary conditions are enforced

$$\widetilde{u}_r\Big|_{r_{\mathrm{D}}=r_{\mathrm{iD}}} = \widetilde{U}_{\mathrm{i}}; \qquad \widetilde{p}^{\mathrm{I}}\Big|_{r_{\mathrm{D}}=r_{\mathrm{iD}}} = \widetilde{p}^{\mathrm{II}}\Big|_{r_{\mathrm{D}}=r_{\mathrm{iD}}} = \widetilde{p}_{\mathrm{i}}, \quad \text{.....(E9.1a)}$$

$$\widetilde{\sigma}_{rr}\Big|_{r_{\mathrm{D}}=r_{\mathrm{oD}}} = \widetilde{P}_{\mathrm{o}}; \qquad \widetilde{p}^{\mathrm{I}}\Big|_{r_{\mathrm{D}}=r_{\mathrm{oD}}} = \widetilde{p}^{\mathrm{II}}\Big|_{r_{\mathrm{D}}=r_{\mathrm{oD}}} = \widetilde{p}_{\mathrm{o}}, \quad \text{..... (E9.1b)}$$

The resulting coefficients $C_1^{(N)}$, $C_2^{(N)}$, $\widetilde{C}_0$ and C_3 are the same as given in Eqs. E1.2, E1.3 and E1.4. The lumped coefficients $\widetilde{\sigma}_{io}^{*}$, $\widetilde{\sigma}_{io}^{**}$, $\varphi_i^{(N)}$, $\varphi_o^{(N)}$, $\gamma_i^{(N)}$, $\gamma_o^{(N)}$, and ρ are rewritten as

Displacement-controlled.

$$\widetilde{\sigma}_{io}^{*} = \frac{\rho}{r_{iD}^2 r_{oD}^2}\left[2(\widetilde{P}_o r_{oD}^2 + A_3\widetilde{U}_i r_{iD}) - (2A_2 r_{oD}^2 - A_3 r_{iD}^2)\,\widetilde{\varepsilon}_{zz}^{*}\right], \quad \text{(E9.2a)}$$

$$\widetilde{\sigma}_{io}^{**} = \rho[2A_0\widetilde{U}_i / r_{iD} + h\widetilde{P}_o + (A_0 - A_2 h)\,\widetilde{\varepsilon}_{zz}^{*}], \quad \text{(E9.2b)}$$

$$\varphi_i^{(N)} = 2A_3 h^{(N)}; \qquad \varphi_o^{(N)} = 2A_1^{(N)}, \quad \text{(E9.3a)}$$

$$\gamma_i^{(N)} = 2A_0 h^{(N)}; \qquad \gamma_o^{(N)} = A_1^{(N)} h, \quad \text{(E9.3b)}$$

$$\rho = \frac{r_{iD}^2 r_{oD}^2}{2A_0\, r_{oD}^2 - A_3 h\, r_{iD}^2}, \quad \text{(E9.3c)}$$

Load-controlled.

$$\widetilde{\sigma}_{io}^{*} = \rho\frac{r_{oD}^2 - r_{iD}^2}{r_{iD}^2 r_{oD}^2}\left[2B_2(\widetilde{P}_o r_{oD}^2 + A_3\widetilde{U}_i r_{iD}) - (2A_2 r_{oD}^2 - A_3 r_{iD}^2)\,\widetilde{\sigma}_{zz}^{*}\right], \quad \text{(E9.4a)}$$

$$\widetilde{\sigma}_{io}^{**} = \rho(r_{oD}^2 - r_{iD}^2)[2(A_0B_2 - A_2B_0)\widetilde{U}_i / r_{iD} + (A_0 - A_2 h)\,\widetilde{\sigma}_{zz}^{*} - (B_0 - B_2 h)\,\widetilde{P}_o], \quad \text{(E9.4b)}$$

$$\varphi_i^{(N)} = 2[(A_3 B_2 h^{(N)} - 2A_2 B_1^{(N)})r_{oD}^2 - A_3(B_2 h^{(N)} - B_1^{(N)})r_{iD}^2], \quad \text{(E9.5a)}$$

$$\varphi_o^{(N)} = 2[(A_1^{(N)} B_2 - 2A_2 B_1^{(N)})r_{oD}^2 - (A_1^{(N)} B_2 - A_3 B_1^{(N)})r_{iD}^2], \quad \text{(E9.5b)}$$

$$\gamma_i^{(N)} = 2(A_0 B_2 - A_2 B_0)h^{(N)} r_{oD}^2 - 2[(A_0 B_2 - A_2 B_0)h^{(N)} + (A_2 h - A_0)B_1^{(N)}]r_{iD}^2, \quad \text{(E9.6a)}$$

$$\gamma_o^{(N)} = 2[(A_1^{(N)} B_2 - A_2 B_1^{(N)})h + A_0 B_1^{(N)} - A_1^{(N)} B_0]r_{oD}^2 - A_1^{(N)}(B_2 h - B_0)r_{iD}^2, \quad \text{(E9.6b)}$$

$$\rho = \frac{r_{iD}^2 r_{oD}^2 /(r_{oD}^2 - r_{iD}^2)}{2(A_0 B_2 - A_2 B_0)\, r_{oD}^2 - A_3(B_2 h - B_0)\, r_{iD}^2}, \quad \text{(E9.7)}$$

E.10 Case 10

The following lateral boundary conditions are enforced

$$\widetilde{u}_r\Big|_{r_D=r_{iD}} = \widetilde{U}_i; \qquad \widetilde{q}_r^{I} + \widetilde{q}_r^{II}\Big|_{r_D=r_{iD}} = \widetilde{q}_i; \qquad \widetilde{p}^{I}\Big|_{r_D=r_{iD}} = \widetilde{p}^{II}\Big|_{r_D=r_{iD}}, \quad \text{.....(E10.1a)}$$

$$\widetilde{\sigma}_{rr}\Big|_{r_D=r_{oD}} = \widetilde{P}_o; \qquad \widetilde{p}^{I}\Big|_{r_D=r_{oD}} = \widetilde{p}^{II}\Big|_{r_D=r_{oD}} = \widetilde{p}_o, \quad \text{..... (E10.1b)}$$

The coefficients $C_1^{(N)}$, $C_2^{(N)}$ are the same as given in Eq. E1.12 for Case 2. $\widetilde{C}_0$ and C_3 are given in Eqs. E1.3 and E1.4. The lumped coefficients $\widetilde{\sigma}_{io}^{*}$, $\widetilde{\sigma}_{io}^{**}$, $\varphi_i^{(N)}$, $\varphi_o^{(N)}$, $\gamma_i^{(N)}$, $\gamma_o^{(N)}$, and ρ are the same as written for Case 9.

For the special case of no-flow or jacketed on the inner surface, the fluid boundary condition at this surface becomes

$$\widetilde{q}_r^{I}\Big|_{r_D=r_{iD}} = \widetilde{q}_r^{II}\Big|_{r_D=r_{iD}} = 0, \quad \text{..... (E10.2)}$$

The coefficients $C_1^{(N)}$, $C_2^{(N)}$ are the same as given in Eq. E1.21 for Case 5. $\widetilde{C}_0$ and C_3 are given in Eqs. E1.3 and E1.4. The lumped coefficients $\widetilde{\sigma}_{io}^{*}$, $\widetilde{\sigma}_{io}^{**}$, $\varphi_i^{(N)}$, $\varphi_o^{(N)}$, $\gamma_i^{(N)}$, $\gamma_o^{(N)}$, and ρ are the same as written for Case 9.

E.11 Case 11

The following lateral boundary conditions are enforced

$$\widetilde{u}_r\Big|_{r_D=r_{iD}} = \widetilde{U}_i; \qquad \widetilde{p}^{I}\Big|_{r_D=r_{iD}} = \widetilde{p}^{II}\Big|_{r_D=r_{iD}} = \widetilde{p}_i, \quad \text{.....(E11.1a)}$$

$$\widetilde{\sigma}_{rr}\Big|_{r_D=r_{oD}} = \widetilde{P}_o; \qquad \widetilde{q}_r^{I} + \widetilde{q}_r^{II}\Big|_{r_D=r_{oD}} = \widetilde{q}_o; \qquad \widetilde{p}^{I}\Big|_{r_D=r_{oD}} = \widetilde{p}^{II}\Big|_{r_D=r_{oD}}, \quad \text{..... (E11.1b)}$$

The coefficients $C_1^{(N)}$, $C_2^{(N)}$ are the same as given in Eq. E1.15 for Case 3. $\widetilde{C}_0$ and C_3 are given in Eqs. E1.3 and E1.4. The lumped coefficients $\widetilde{\sigma}_{io}^{*}$, $\widetilde{\sigma}_{io}^{**}$, $\varphi_i^{(N)}$, $\varphi_o^{(N)}$, $\gamma_i^{(N)}$, $\gamma_o^{(N)}$, and ρ are the same as written for Case 9.

For the special case of no-flow or jacketed on the outer surface, the fluid boundary condition at this surface becomes

$$\widetilde{q}_r^{\,\mathrm{I}}\Big|_{r_D=r_{oD}} = \widetilde{q}_r^{\,\mathrm{II}}\Big|_{r_D=r_{iD}} = 0, \quad \text{(E11.2)}$$

The coefficients $C_1^{(N)}$, $C_2^{(N)}$ are the same as given in Eq. E1.24 for Case 6. $\widetilde{C}_0$ and C_3 are given in Eqs. E1.3 and E1.4. The lumped coefficients $\widetilde{\sigma}_{io}^{*}$, $\widetilde{\sigma}_{io}^{**}$, $\varphi_i^{(N)}$, $\varphi_o^{(N)}$, $\gamma_i^{(N)}$, $\gamma_o^{(N)}$, and ρ are the same as written for Case 9.

E.12 Case 12

The following lateral boundary conditions are enforced

$$\widetilde{u}_r\Big|_{r_D=r_{iD}} = \widetilde{U}_i; \qquad \widetilde{q}_r^{\,\mathrm{I}} + \widetilde{q}_r^{\,\mathrm{II}}\Big|_{r_D=r_{iD}} = \widetilde{q}_i; \qquad \widetilde{p}^{\,\mathrm{I}}\Big|_{r_D=r_{iD}} = \widetilde{p}^{\,\mathrm{II}}\Big|_{r_D=r_{iD}}, \quad \text{(E12.1a)}$$

$$\widetilde{\sigma}_{rr}\Big|_{r_D=r_{oD}} = \widetilde{P}_o; \qquad \widetilde{q}_r^{\,\mathrm{I}} + \widetilde{q}_r^{\,\mathrm{II}}\Big|_{r_D=r_{oD}} = \widetilde{q}_o; \qquad \widetilde{p}^{\,\mathrm{I}}\Big|_{r_D=r_{oD}} = \widetilde{p}^{\,\mathrm{II}}\Big|_{r_D=r_{oD}}, \quad \text{(E12.1b)}$$

The coefficients $C_1^{(N)}$, $C_2^{(N)}$ are the same as given in Eq. E1.18 for Case 4. $\widetilde{C}_0$ and C_3 are given in Eqs. E1.3 and E1.4. The lumped coefficients $\widetilde{\sigma}_{io}^{*}$, $\widetilde{\sigma}_{io}^{**}$, $\varphi_i^{(N)}$, $\varphi_o^{(N)}$, $\gamma_i^{(N)}$, $\gamma_o^{(N)}$, and ρ are the same as written for Case 9.

For the special case of no flow or jacketed on both the inner and outer surfaces, the condition is undrained and the solution simplifies to an elastic one with undrained

parameters.

E.13 Case 13

The following lateral boundary conditions are enforced

$$\widetilde{u}_r\Big|_{r_{\mathrm{D}}=r_{\mathrm{iD}}}=\widetilde{U}_{\mathrm{i}};\qquad \widetilde{p}^{\mathrm{I}}\Big|_{r_{\mathrm{D}}=r_{\mathrm{iD}}}=\widetilde{p}^{\mathrm{II}}\Big|_{r_{\mathrm{D}}=r_{\mathrm{iD}}}=\widetilde{p}_{\mathrm{i}}\,, \tag{E13.1a}$$

$$\widetilde{u}_r\Big|_{r_{\mathrm{D}}=r_{\mathrm{oD}}}=\widetilde{U}_{\mathrm{o}};\qquad \widetilde{p}^{\mathrm{I}}\Big|_{r_{\mathrm{D}}=r_{\mathrm{oD}}}=\widetilde{p}^{\mathrm{II}}\Big|_{r_{\mathrm{D}}=r_{\mathrm{oD}}}=\widetilde{p}_{\mathrm{o}}\,, \tag{E13.1b}$$

The resulting coefficients $C_1^{(\mathrm{N})}$, $C_2^{(\mathrm{N})}$, $\widetilde{C}_0$ and C_3 are the same as given in Eqs. E1.2, E1.3 and E1.4. The lumped coefficients $\widetilde{\sigma}_{\mathrm{io}}^{*}$, $\widetilde{\sigma}_{\mathrm{io}}^{**}$, $\varphi_{\mathrm{i}}^{(\mathrm{N})}$, $\varphi_{\mathrm{o}}^{(\mathrm{N})}$, $\gamma_{\mathrm{i}}^{(\mathrm{N})}$, $\gamma_{\mathrm{o}}^{(\mathrm{N})}$, and ρ are rewritten as

Displacement-controlled.

$$\widetilde{\sigma}_{\mathrm{io}}^{*}=\frac{2\rho}{r_{\mathrm{iD}}^2 r_{\mathrm{oD}}^2}\frac{\widetilde{U}_{\mathrm{o}}r_{\mathrm{oD}}-\widetilde{U}_{\mathrm{i}}r_{\mathrm{iD}}}{h}-\frac{\widetilde{\varepsilon}_{zz}^{*}}{h};\qquad \widetilde{\sigma}_{\mathrm{io}}^{**}=\rho\left(\frac{\widetilde{U}_{\mathrm{i}}}{r_{\mathrm{iD}}}-\frac{\widetilde{U}_{\mathrm{o}}}{r_{\mathrm{oD}}}\right), \tag{E1.51}$$

$$\varphi_{\mathrm{i}}^{(\mathrm{N})}=\varphi_{\mathrm{o}}^{(\mathrm{N})}=\frac{2h^{(\mathrm{N})}}{h};\qquad \gamma_{\mathrm{i}}^{(\mathrm{N})}=\gamma_{\mathrm{o}}^{(\mathrm{N})}=h^{(\mathrm{N})};\qquad \rho=\frac{r_{\mathrm{iD}}^2 r_{\mathrm{oD}}^2}{r_{\mathrm{oD}}^2-r_{\mathrm{iD}}^2}, \tag{E1.52}$$

Load-controlled.

$$\widetilde{\sigma}_{\mathrm{io}}^{*}=\frac{\rho}{r_{\mathrm{iD}}^2 r_{\mathrm{oD}}^2}\left[\frac{2B_2(\widetilde{U}_{\mathrm{o}}r_{\mathrm{oD}}-\widetilde{U}_{\mathrm{i}}r_{\mathrm{iD}})+(r_{\mathrm{oD}}^2-r_{\mathrm{iD}}^2)\,\widetilde{\sigma}_{zz}^{*}}{B_0-B_2h}\right], \tag{E1.53}$$

$$\varphi_{\mathrm{i}}^{(\mathrm{N})}=\varphi_{\mathrm{o}}^{(\mathrm{N})}=\frac{2(B_1^{(\mathrm{N})}-B_2h^{(\mathrm{N})})}{B_0-B_2h}, \tag{E1.54}$$

where $\widetilde{\sigma}_{\mathrm{io}}^{**}$, $\gamma_{\mathrm{i}}^{(\mathrm{N})}$, $\gamma_{\mathrm{o}}^{(\mathrm{N})}$, and ρ are the same as given in Eqs. E1.51 and E1.52.

E.14 Case 14

The following lateral boundary conditions are enforced

$$\widetilde{u}_r\Big|_{r_D=r_{iD}} = \widetilde{U}_i; \qquad \widetilde{q}_r^{I} + \widetilde{q}_r^{II}\Big|_{r_D=r_{iD}} = \widetilde{q}_i; \qquad \widetilde{p}^{I}\Big|_{r_D=r_{iD}} = \widetilde{p}^{II}\Big|_{r_D=r_{iD}}, \quad \text{.....(E14.1a)}$$

$$\widetilde{u}_r\Big|_{r_D=r_{oD}} = \widetilde{U}_o; \qquad \widetilde{p}^{I}\Big|_{r_D=r_{oD}} = \widetilde{p}^{II}\Big|_{r_D=r_{oD}} = \widetilde{p}_o, \quad \text{..... (E14.1b)}$$

The coefficients $C_1^{(N)}$, $C_2^{(N)}$ are the same as given in Eq. E1.12 for Case 2. $\widetilde{C}_0$ and C_3 are given in Eqs. E1.3 and E1.4. The lumped coefficients $\widetilde{\sigma}_{io}^{*}$, $\widetilde{\sigma}_{io}^{**}$, $\varphi_i^{(N)}$, $\varphi_o^{(N)}$, $\gamma_i^{(N)}$, $\gamma_o^{(N)}$, and ρ are the same as written for Case 13.

For the special case of no-flow or jacketed on the inner surface, the fluid boundary condition at this surface becomes

$$\widetilde{q}_r^{I}\Big|_{r_D=r_{iD}} = \widetilde{q}_r^{II}\Big|_{r_D=r_{iD}} = 0, \quad \text{..... (E14.2)}$$

The coefficients $C_1^{(N)}$, $C_2^{(N)}$ are the same as given in Eq. E1.21 for Case 5. $\widetilde{C}_0$ and C_3 are given in Eqs. E1.3 and E1.4. The lumped coefficients $\widetilde{\sigma}_{io}^{*}$, $\widetilde{\sigma}_{io}^{**}$, $\varphi_i^{(N)}$, $\varphi_o^{(N)}$, $\gamma_i^{(N)}$, $\gamma_o^{(N)}$, and ρ are the same as written for Case 13.

E.15 Case 15

The following lateral boundary conditions are enforced

$$\widetilde{u}_r\Big|_{r_D=r_{iD}} = \widetilde{U}_i; \qquad \widetilde{p}^{I}\Big|_{r_D=r_{iD}} = \widetilde{p}^{II}\Big|_{r_D=r_{iD}} = \widetilde{p}_i, \quad \text{.....(E15.1a)}$$

$$\widetilde{u}_r\Big|_{r_D=r_{oD}} = \widetilde{U}_o; \qquad \widetilde{q}_r^{I} + \widetilde{q}_r^{II}\Big|_{r_D=r_{oD}} = \widetilde{q}_o; \qquad \widetilde{p}^{I}\Big|_{r_D=r_{oD}} = \widetilde{p}^{II}\Big|_{r_D=r_{oD}}, \quad \text{..... (E15.1b)}$$

The coefficients $C_1^{(N)}$, $C_2^{(N)}$ are the same as given in Eq. E1.15 for Case 3. $\widetilde{C}_0$ and C_3 are given in Eqs. E1.3 and E1.4. The lumped coefficients $\widetilde{\sigma}_{io}^{*}$, $\widetilde{\sigma}_{io}^{**}$, $\varphi_i^{(N)}$, $\varphi_o^{(N)}$, $\gamma_i^{(N)}$, $\gamma_o^{(N)}$, and ρ are the same as written for Case 13.

For the special case of no-flow or jacketed on the outter surface, the fluid boundary condition at this surface becomes

$$\widetilde{q}_r^{\mathrm{I}}\Big|_{r_D=r_{oD}} = \widetilde{q}_r^{\mathrm{II}}\Big|_{r_D=r_{iD}} = 0, \quad \text{(E15.2)}$$

The coefficients $C_1^{(N)}$, $C_2^{(N)}$ are the same as given in Eq. E1.24 for Case 6. $\widetilde{C}_0$ and C_3 are given in Eqs. E1.3 and E1.4. The lumped coefficients $\widetilde{\sigma}_{io}^{*}$, $\widetilde{\sigma}_{io}^{**}$, $\varphi_i^{(N)}$, $\varphi_o^{(N)}$, $\gamma_i^{(N)}$, $\gamma_o^{(N)}$, and ρ are the same as written for Case 13.

E.16 Case 16

The following lateral boundary conditions are enforced

$$\widetilde{u}_r\Big|_{r_D=r_{iD}} = \widetilde{U}_i; \qquad \widetilde{q}_r^{\mathrm{I}} + \widetilde{q}_r^{\mathrm{II}}\Big|_{r_D=r_{iD}} = \widetilde{q}_i; \qquad \widetilde{p}^{\mathrm{I}}\Big|_{r_D=r_{iD}} = \widetilde{p}^{\mathrm{II}}\Big|_{r_D=r_{iD}}, \quad \text{(E16.1a)}$$

$$\widetilde{u}_r\Big|_{r_D=r_{oD}} = \widetilde{U}_o; \qquad \widetilde{q}_r^{\mathrm{I}} + \widetilde{q}_r^{\mathrm{II}}\Big|_{r_D=r_{oD}} = \widetilde{q}_o; \qquad \widetilde{p}^{\mathrm{I}}\Big|_{r_D=r_{oD}} = \widetilde{p}^{\mathrm{II}}\Big|_{r_D=r_{oD}}, \quad \text{(E16.1b)}$$

The coefficients $C_1^{(N)}$, $C_2^{(N)}$ are the same as given in Eq. E1.18 for Case 4. $\widetilde{C}_0$ and C_3 are given in Eqs. E1.3 and E1.4. The lumped coefficients $\widetilde{\sigma}_{io}^{*}$, $\widetilde{\sigma}_{io}^{**}$, $\varphi_i^{(N)}$, $\varphi_o^{(N)}$, $\gamma_i^{(N)}$, $\gamma_o^{(N)}$, and ρ are the same as written for Case 13. For the special case of no flow or jacketed on both the inner and outer surfaces, the condition is undrained and the solution simplifies to an elastic one with undrained parameters.

Appendix F Dual-Porochemoelastic Inclined Wellbore Solutions

The boundary conditions and associated expressions for contributing axisymmetric loading, Case 1, and deviatoric loading Case 2 are given in the following section.

Case 1 – Axisymmetric Loading

The perturbed boundary condition at the borehole wall ($r_D = 1$) are

$$\sigma_{rr}^{(1)} = -\sigma_m + p_w(t_D), \qquad \sigma_{r\theta}^{(1)} = 0, \quad \text{.....(F.1)}$$

$$p^{\mathrm{I}(1)} = p^{\mathrm{II}(1)} = p_w(t_D) - p_0, \quad \text{.....(F.2)}$$

$$p^{\mathrm{sI}} = p^{\mathrm{sII}} = (i\mathrm{RT}/V_0^f)[m_w^s(t_D) - m_0^s], \quad \text{.....(F.3)}$$

This is an axisymmetric ($n = 0$) loading problem. The stress has contribution from the mud pressure, p_w, and the hydrostatic part of the released in-situ stress, σ_m. The fluid and solute diffuse due to pressure and solute concentration gradient across the mud/rock interface. Bounded solution at far-field requires that $\widetilde{C}_0 = 0$. The solution is transient and given in Laplace transform domain as follows

$$\widetilde{p}^{\mathrm{I}(1)} = \sum_{j=1,2}\left[m_{1j}^{\mathrm{I}}\Delta_j^{\mathrm{I}}\Phi(\xi_j^{\mathrm{I}}r_D) + m_{1j}^{\mathrm{II}}\Delta_j^{\mathrm{II}}\Phi(\xi_j^{\mathrm{II}}r_D)\right] \quad \text{.....(F.4)}$$

$$\widetilde{p}^{\mathrm{sI}(1)} = \sum_{j=1,2}\left[m_{2j}^{\mathrm{I}}\Delta_j^{\mathrm{I}}\Phi(\xi_j^{\mathrm{I}}r_D) + m_{2j}^{\mathrm{II}}\Delta_j^{\mathrm{II}}\Phi(\xi_j^{\mathrm{II}}r_D)\right] \quad \text{.....(F.5)}$$

$$\widetilde{p}^{\mathrm{II}(1)} = \sum_{j=1,2}\left[m_{3j}^{\mathrm{I}}\Delta_j^{\mathrm{I}}\Phi(\xi_j^{\mathrm{I}}r_D) + m_{3j}^{\mathrm{II}}\Delta_j^{\mathrm{II}}\Phi(\xi_j^{\mathrm{II}}r_D)\right] \quad \text{.....(F.6)}$$

$$\widetilde{p}^{\,\mathrm{sII}(1)} = \sum_{j=1,2} \left[m_{4j}^{\mathrm{I}} \Delta_j^{\mathrm{I}} \Phi(\xi_j^{\mathrm{I}} r_D) + m_{4j}^{\mathrm{II}} \Delta_j^{\mathrm{II}} \Phi(\xi_j^{\mathrm{II}} r_D) \right] \quad \text{.....(F.7)}$$

$$\widetilde{\sigma}_{rr}^{(1)} = \Delta\widetilde{\sigma} / r_D^2 - \sum_{j=1,2} \sum_{(\mathrm{N})=\mathrm{I},\mathrm{II}} A_{1j}^{(\mathrm{N})} \Delta_j^{(\mathrm{N})} \, \Pi(\xi_j^{(\mathrm{N})} r_D) \,, \quad \text{.....(F.8)}$$

$$\widetilde{\sigma}_{\theta\theta}^{(1)} = -\Delta\widetilde{\sigma} / r_D^2 + \sum_{j=1,2} \sum_{(\mathrm{N})=\mathrm{I},\mathrm{II}} A_{1j}^{(\mathrm{N})} \Delta_j^{(\mathrm{N})} \left[\Pi(\xi_j^{(\mathrm{N})} r_D) + \Phi(\xi_j^{(\mathrm{N})} r_D) \right], \quad \text{.....(F.9)}$$

with

$$\begin{Bmatrix} \Delta_1^{\mathrm{I}} \\ \Delta_2^{\mathrm{I}} \\ \Delta_1^{\mathrm{II}} \\ \Delta_2^{\mathrm{II}} \end{Bmatrix} = \begin{bmatrix} m_{11}^{\mathrm{I}} & m_{12}^{\mathrm{I}} & m_{11}^{\mathrm{II}} & m_{12}^{\mathrm{II}} \\ m_{21}^{\mathrm{I}} & m_{22}^{\mathrm{I}} & m_{21}^{\mathrm{II}} & m_{22}^{\mathrm{II}} \\ m_{31}^{\mathrm{I}} & m_{32}^{\mathrm{I}} & m_{31}^{\mathrm{II}} & m_{32}^{\mathrm{II}} \\ m_{41}^{\mathrm{I}} & m_{42}^{\mathrm{I}} & m_{41}^{\mathrm{II}} & m_{42}^{\mathrm{II}} \end{bmatrix}^{-1} \begin{Bmatrix} \Delta\widetilde{p} \\ \Delta\widetilde{p}^{\,s} \\ \Delta\widetilde{p} \\ \Delta\widetilde{p}^{\,s} \end{Bmatrix}, \quad \text{.....(F.10)}$$

$$\Delta\widetilde{p} = \widetilde{p}_w - \frac{p_0}{s}, \qquad \Delta\widetilde{p}^{\,s} = \frac{i\mathrm{RT}}{V_0^f} \left(\widetilde{m}_w^s - \frac{m_0^s}{s} \right), \qquad \Delta\widetilde{\sigma} = \widetilde{p}_w - \frac{\sigma_m}{s}, \quad \text{.....(F.11)}$$

$$\Phi(x\, r_D) = \frac{\mathrm{K}_0(x\, r_D)}{\mathrm{K}_0(x)}, \qquad \Pi(x\, r_D) = \frac{\mathrm{K}_1(x\, r_D)}{x\, r_D\, \mathrm{K}_0(x)} - \frac{\mathrm{K}_1(x)}{x\, r_D^2\, \mathrm{K}_0(x)} \quad \text{.....(F.12)}$$

Case 2 – Deviatoric Loading

The perturbed boundary condition at the borehole wall ($r_D = 1$) are

$$\sigma_{rr}^{(2)} = -\sigma_d \cos(2(\theta - \theta_r)), \qquad \sigma_{r\theta}^{(2)} = \sigma_d \sin(2(\theta - \theta_r)) \quad \text{.....(F.13)}$$

$$p^{\mathrm{I}(2)} = p^{\mathrm{II}(2)} = p^{\mathrm{sI}(2)} = p^{\mathrm{sII}(2)} = 0 \quad \text{.....(F.14)}$$

This is an asymmetric (n = 2) stress loading problem accounting for the release of the deviatoric part of the in-plane in-situ stresses, σ_d. The solutions in Laplace transform domain are

$$s\, \widetilde{p}^{\,\mathrm{I}(2)} = \sigma_d \left\{ f_1^{\mathrm{I}} \widetilde{C}_0 r_D^{-2} + \sum_{j=1,2} \sum_{\mathrm{N}=\mathrm{I},\mathrm{II}} \left[m_{1j}^{(\mathrm{N})} C_j^{(\mathrm{N})} \mathrm{K}_2(\xi_j^{(\mathrm{N})} r_D) \right] \right\} \cos(2(\theta - \theta_r)) \quad \text{.....(F.15)}$$

$$s\,\widetilde{p}^{\mathrm{sI}(2)} = \sigma_d \left\{ f_2^{\mathrm{I}} \widetilde{C}_0 r_D^{-2} + \sum_{j=\mathrm{I},\mathrm{II}} \sum_{2\mathrm{N}=\mathrm{I},\mathrm{II}} \left[m_{2j}^{(\mathrm{N})} C_j^{(\mathrm{N})} \mathrm{K}_2(\xi_j^{(\mathrm{N})} r_D) \right] \right\} \cos(2(\theta - \theta_r)) \quad \text{.....(F.16)}$$

$$s\,\widetilde{p}^{\mathrm{II}(2)} = \sigma_d \left\{ f_1^{\mathrm{II}} \widetilde{C}_0 r_D^{-2} + \sum_{j=\mathrm{I},\mathrm{II}} \sum_{2\mathrm{N}=\mathrm{I},\mathrm{II}} \left[m_{3j}^{(\mathrm{N})} C_j^{(\mathrm{N})} \mathrm{K}_2(\xi_j^{(\mathrm{N})} r_D) \right] \right\} \cos(2(\theta - \theta_r)) \quad \text{.....(F.17)}$$

$$s\,\widetilde{p}^{\mathrm{sII}(2)} = \sigma_d \left\{ f_2^{\mathrm{II}} \widetilde{C}_0 r_D^{-2} + \sum_{j=\mathrm{I},\mathrm{II}} \sum_{2\mathrm{N}=\mathrm{I},\mathrm{II}} \left[m_{4j}^{(\mathrm{N})} C_j^{(\mathrm{N})} \mathrm{K}_2(\xi_j^{(\mathrm{N})} r_D) \right] \right\} \cos(2(\theta - \theta_r)) \quad \text{.....(F.18)}$$

$$s\,\widetilde{\sigma}_{rr}^{(2)} = -\sigma_d \left\{ \begin{array}{l} \displaystyle\sum_{j=\mathrm{I},\mathrm{II}} \sum_{2\mathrm{N}=\mathrm{I},\mathrm{II}} \left[A_{1j}^{(\mathrm{N})} C_j^{(\mathrm{N})} \Theta(\xi_j^{(\mathrm{N})} r_D) \right] \\ -2A_0 \widetilde{C}_0 r_D^{-2} - C_3 r_D^{-4} \end{array} \right\} \cos(2(\theta - \theta_r)) \quad \text{.....(F.19)}$$

$$s\,\widetilde{\sigma}_{\theta\theta}^{(2)} = \sigma_d \left\{ \sum_{j=\mathrm{I},\mathrm{II}} \sum_{2\mathrm{N}=\mathrm{I},\mathrm{II}} \left[A_{1j}^{(\mathrm{N})} C_j^{(\mathrm{N})} \Omega(\xi_j^{(\mathrm{N})} r_D) \right] - C_3 r_D^{-4} \right\} \cos(2(\theta - \theta_r)) \quad \text{.....(F.20)}$$

$$s\,\widetilde{\sigma}_{r\theta}^{(2)} = -\sigma_d \left\{ \begin{array}{l} \displaystyle\sum_{j=\mathrm{I},\mathrm{II}} \sum_{2\mathrm{N}=\mathrm{I},\mathrm{II}} \left[A_{1j}^{(\mathrm{N})} C_j^{(\mathrm{N})}\, \Xi(\xi_j^{(\mathrm{N})} r_D) \right] \\ -A_0 \widetilde{C}_0 r_D^{-2} - C_3 r_D^{-4} \end{array} \right\} \sin(2(\theta - \theta_r)) \quad \text{.....(F.21)}$$

where the coefficients $\widetilde{C}_0$, $C_j^{(\mathrm{N})}$,and C_3 are given as

$$\begin{Bmatrix} C_1^{\mathrm{I}} \\ C_2^{\mathrm{I}} \\ C_1^{\mathrm{II}} \\ C_2^{\mathrm{II}} \end{Bmatrix} = \frac{2}{A_0} \begin{bmatrix} d_{11}^{\mathrm{I}} & d_{12}^{\mathrm{I}} & d_{11}^{\mathrm{II}} & d_{12}^{\mathrm{II}} \\ d_{21}^{\mathrm{I}} & d_{22}^{\mathrm{I}} & d_{21}^{\mathrm{II}} & d_{22}^{\mathrm{II}} \\ d_{31}^{\mathrm{I}} & d_{32}^{\mathrm{I}} & d_{31}^{\mathrm{II}} & d_{32}^{\mathrm{II}} \\ d_{41}^{\mathrm{I}} & d_{42}^{\mathrm{I}} & d_{41}^{\mathrm{II}} & d_{42}^{\mathrm{II}} \end{bmatrix}^{-1} \begin{Bmatrix} f_1^{\mathrm{I}} \\ f_2^{\mathrm{I}} \\ f_1^{\mathrm{II}} \\ f_2^{\mathrm{II}} \end{Bmatrix}, \quad \text{.....(F.22)}$$

$$\widetilde{C}_0 = -\frac{2}{A_0} \left[1 + \sum_{j=\mathrm{I},\mathrm{II}} \sum_{2\mathrm{N}=\mathrm{I},\mathrm{II}} A_{1j}^{(\mathrm{N})} C_j^{(\mathrm{N})} \frac{\mathrm{K}_1(\xi_j^{(\mathrm{N})})}{\xi_j^{(\mathrm{N})}} \right], \quad \text{.....(F.23)}$$

$$C_3 = 3 \left[1 + \sum_{j=\mathrm{I},\mathrm{II}} \sum_{2\mathrm{N}=\mathrm{I},\mathrm{II}} A_{1j}^{(\mathrm{N})} C_j^{(\mathrm{N})}\, \Psi(\xi_j^{(\mathrm{N})}) \right], \quad \text{.....(F.24)}$$

with

$$d_{ij}^{(\mathrm{N})} = m_{ij}^{(\mathrm{N})}\mathrm{K}_2(\xi_j^{(\mathrm{N})}) - \frac{A_{1j}^{(\mathrm{N})}}{A_0} f_i^{(\mathrm{N})} \frac{\mathrm{K}_1(\xi_j^{(\mathrm{N})})}{\xi_j^{(\mathrm{N})}} \qquad i, j = 1,2; \quad (\mathrm{N}) = \mathrm{I}, \mathrm{II}, \ldots\ldots\ldots\ldots\ldots\ldots(\mathrm{F}.25)$$

$$d_{(i+2)j}^{(\mathrm{N})} = m_{(i+2)j}^{(\mathrm{N})}\mathrm{K}_2(\xi_j^{(\mathrm{N})}) - \frac{A_{1j}^{(\mathrm{N})}}{A_0} f_i^{(\mathrm{N})} \frac{\mathrm{K}_1(\xi_j^{(\mathrm{N})})}{\xi_j^{(\mathrm{N})}} \qquad i, j = 1,2; \quad (\mathrm{N}) = \mathrm{I}, \mathrm{II}, \ldots\ldots\ldots\ldots\ldots\ldots(\mathrm{F}.27)$$

$$\Theta(x\, r_D) = \frac{\mathrm{K}_1(x\, r_D)}{x\, r_D} + 6\frac{\mathrm{K}_2(x\, r_D)}{(x\, r_D)^2} \ldots\ldots\ldots\ldots\ldots\ldots(\mathrm{F}.28)$$

$$\Omega(x\, r_D) = \Theta(x\, r_D) + \mathrm{K}_2(x\, r_D) \ldots\ldots\ldots\ldots\ldots\ldots(\mathrm{F}.29)$$

$$\Xi(x\, r_D) = 2\frac{\mathrm{K}_1(x\, r_D)}{x\, r_D} + 6\frac{\mathrm{K}_2(x\, r_D)}{(x\, r_D)^2} \ldots\ldots\ldots\ldots\ldots\ldots(\mathrm{F}.30)$$

$$\Psi(x\, r_D) = \frac{\mathrm{K}_1(x\, r_D)}{x\, r_D} + 2\frac{\mathrm{K}_2(x\, r_D)}{(x\, r_D)^2} \ldots\ldots\ldots\ldots\ldots\ldots(\mathrm{F}.31)$$

Appendix G Dual-Porothermoelastic Finite Difference Solutions

The coefficient

$$[\mathbf{X}^{j+1}]=\begin{bmatrix} p_2^{\mathrm{I},j+1} \\ \vdots \\ \vdots \\ p_{nr-1}^{\mathrm{I},j+1} \\ p_2^{\mathrm{II},j+1} \\ \vdots \\ \vdots \\ p_{nr-1}^{\mathrm{II},j+1} \\ T_2^{j+1} \\ \vdots \\ \vdots \\ T_{nr-1}^{j+1} \end{bmatrix}; \qquad [\mathbf{BC}]=\begin{bmatrix} -2LL_{\mathrm{D},1}^{\mathrm{I}}(p_w-p_0) \\ 0 \\ \vdots \\ 0 \\ -2LL_{\mathrm{D},1}^{\mathrm{II}}(p_w-p_0) \\ 0 \\ \vdots \\ 0 \\ -2LL_{\mathrm{D},1}^{\mathrm{T}}(T_w-T_0) \\ 0 \\ \vdots \\ 0 \end{bmatrix}, \quad \text{.....(G.1)}$$

$$[\mathbf{L}^{j+1}]=\begin{bmatrix} \mathbf{LL}^{\mathrm{I}} & \mathbf{LL}^{\mathrm{I,II}} & \mathbf{LL}^{\mathrm{I},T} \\ \mathbf{LL}^{\mathrm{I,II}} & \mathbf{LL}^{\mathrm{II}} & \mathbf{LL}^{\mathrm{II},T} \\ \mathbf{0} & \mathbf{0} & \mathbf{LL}^{T,j+1} \end{bmatrix}; \qquad [\mathbf{R}^{j}]=\begin{bmatrix} \mathbf{RR}^{\mathrm{I}} & \mathbf{RR}^{\mathrm{I,II}} & \mathbf{RR}^{\mathrm{I},T} \\ \mathbf{RR}^{\mathrm{I,II}} & \mathbf{RR}^{\mathrm{II}} & \mathbf{RR}^{\mathrm{II},T} \\ \mathbf{0} & \mathbf{0} & \mathbf{RR}^{T,j} \end{bmatrix}, \quad \text{.....(G.2)}$$

in which the submatrices of $[\mathbf{L}^{j+1}]$ are given as

$$[\mathbf{LL}^{(\mathrm{N})}]=\begin{bmatrix} LL^{(\mathrm{N})} & LL_{\mathrm{U},1}^{(\mathrm{N})} & 0 & 0 \\ LL_{\mathrm{D},2}^{(\mathrm{N})} & LL^{(\mathrm{N})} & \ddots & 0 \\ 0 & \ddots & \ddots & LL_{\mathrm{U},nr-3}^{(\mathrm{N})} \\ 0 & 0 & LL_{\mathrm{D},nr-2}^{(\mathrm{N})} & LL^{(\mathrm{N})} \end{bmatrix}, \quad \text{.....(G.3)}$$

$$[\mathbf{LL}^{T,j+1}] = \begin{bmatrix} LL^{T} & LL_{\mathrm{U},1}^{T,j+1} & 0 & 0 \\ LL_{\mathrm{D},2}^{T,j+1} & LL^{T} & \ddots & 0 \\ 0 & \ddots & \ddots & LL_{\mathrm{U},nr-3}^{T,j+1} \\ 0 & 0 & LL_{\mathrm{D},nr-2}^{T,j+1} & LL^{T} \end{bmatrix}, \quad \text{(G.4)}$$

$$[\mathbf{LL}^{\mathrm{I,II}}] = \begin{bmatrix} LL^{\mathrm{I,II}} & 0 & 0 & 0 \\ 0 & LL^{\mathrm{I,II}} & \ddots & 0 \\ 0 & \ddots & \ddots & 0 \\ 0 & 0 & 0 & LL^{\mathrm{I,II}} \end{bmatrix}, \quad \text{(G.5)}$$

$$[\mathbf{LL}^{(\mathrm{N}),T}] = [\mathbf{RR}^{(\mathrm{N}),T}] = \begin{bmatrix} c_{hf}^{(\mathrm{N})} & 0 & 0 & 0 \\ 0 & c_{hf}^{(\mathrm{N})} & \ddots & 0 \\ 0 & \ddots & \ddots & 0 \\ 0 & 0 & 0 & c_{hf}^{(\mathrm{N})} \end{bmatrix}, \quad \text{(G.6)}$$

The submatrices of $\mathbf{R}^{j}$ ($\mathbf{RR}^{(\mathrm{N})}$, $\mathbf{RR}^{\mathrm{T},j+1}$, and $\mathbf{RR}^{\mathrm{I,II}}$) are defined similar to those of $\mathbf{L}^{j+1}$ with *LL* replaced by *RR*. The components of these submatrices are expressed as

$$LL_{\mathrm{D},i}^{\mathrm{I}} = (1-\overline{\kappa}_D)\left(\frac{\Delta t_D}{4\Delta r_D[1+(i+1)\Delta r_D]} - \frac{\Delta t_D}{2\Delta r_D^2}\right), \quad \text{(G.7)}$$

$$LL^{\mathrm{I}} = 1-\omega+(1-\overline{\kappa}_D)\frac{\Delta t_D}{\Delta r_D^2} + \lambda_D\frac{\Delta t_D}{2}, \quad \text{(G.8)}$$

$$LL_{\mathrm{U},i}^{\mathrm{I}} = -(1-\overline{\kappa}_D)\left(\frac{\Delta t_D}{4\Delta r_D[1+(i+1)\Delta r_D]} + \frac{\Delta t_D}{2\Delta r_D^2}\right), \quad \text{(G.9)}$$

$$LL_{\mathrm{D},i}^{\mathrm{II}} = \overline{\kappa}_D\left(\frac{\Delta t_D}{4\Delta r_D[1+(i+1)\Delta r_D]} - \frac{\Delta t_D}{2\Delta r_D^2}\right), \quad \text{(G.10)}$$

$$LL^{\mathrm{II}} = \omega + \overline{\kappa}_D \frac{\Delta t_D}{\Delta r_D^2} + \lambda_D \frac{\Delta t_D}{2}, \quad \text{(G.11)}$$

$$LL_{\mathrm{U},i}^{\mathrm{II}} = -\overline{\kappa}_D \left(\frac{\Delta t_D}{4\Delta r_D[1+(i+1)\Delta r_D]} + \frac{\Delta t_D}{2\Delta r_D^2} \right), \quad \text{(G.12)}$$

$$LL^{\mathrm{I,II}} = \omega_{12} - \lambda_D \frac{\Delta t_D}{2}, \quad \text{(G.13)}$$

$$LL_{\mathrm{D},i}^{\mathrm{T},j+1} = \overline{\kappa}_D^T \left(\frac{\Delta t_D}{4\Delta r_D[1+(i+1)\Delta r_D]} - \frac{\Delta t_D}{2\Delta r_D^2} \right) - \Delta p_{i+1}^{j+1} \frac{\Delta t_D}{8\Delta r_D^2}, \quad \text{(G.14)}$$

$$LL^T = 1 + \overline{\kappa}_D^T \frac{\Delta t_D}{\Delta r_D^2}, \quad \text{(G.15)}$$

$$LL_{\mathrm{U},i}^{\mathrm{II}} = -\overline{\kappa}_D^T \left(\frac{\Delta t_D}{4\Delta r_D[1+(i+1)\Delta r_D]} + \frac{\Delta t_D}{2\Delta r_D^2} \right) + \Delta p_{i+1}^{j+1} \frac{\Delta t_D}{8\Delta r_D^2}, \quad \text{(G.16)}$$

$$\Delta p_i^{j+1} = \frac{\overline{\kappa}_{hf}^{T,\mathrm{I}}}{2} \left(p_{i+1}^{\mathrm{I},j+1} - p_{i-1}^{\mathrm{I},j+1} + p_{i+1}^{\mathrm{I},j} - p_{i-1}^{\mathrm{I},j} \right) + \frac{\overline{\kappa}_{hf}^{T,\mathrm{II}}}{2} \left(p_{i+1}^{\mathrm{II},j+1} - p_{i-1}^{\mathrm{II},j+1} + p_{i+1}^{\mathrm{II},j} - p_{i-1}^{\mathrm{II},j} \right), \quad \text{(G.17)}$$

$$RR_{\mathrm{D},i}^{\mathrm{I}} = -LL_{\mathrm{D},i}^{\mathrm{I}}; \qquad RR^{\mathrm{I}} = 2(1-\omega) - LL^{\mathrm{I}}; \qquad RR_{\mathrm{U},i}^{\mathrm{I}} = -LL_{\mathrm{U},i}^{\mathrm{I}}, \quad \text{(G.18)}$$

$$RR^{\mathrm{I,II}} = 2\omega_{12} - LL^{\mathrm{I,II}}, \quad \text{(G.19)}$$

$$RR_{\mathrm{D},i}^{\mathrm{II}} = -LL_{\mathrm{D},i}^{\mathrm{II}}; \qquad RR^{\mathrm{II}} = 2\omega - LL^{\mathrm{II}}; \qquad RR_{\mathrm{U},i}^{\mathrm{II}} = -LL_{\mathrm{U},i}^{\mathrm{II}}, \quad \text{(G.20)}$$

$$RR_{\mathrm{D},i}^{\mathrm{T},j+1} = -LL_{\mathrm{D},i}^{\mathrm{T},j+1}; \qquad RR^{\mathrm{T},j+1} = 2 - LL^{\mathrm{T}}; \qquad RR_{\mathrm{U},i}^{\mathrm{T},j+1} = -LL_{\mathrm{D},i}^{\mathrm{T},j+1}, \quad \text{(G.21)}$$